2012

Geochemistry & Mineralogy of Fluvial Sediments in the Southern Alps, New Zealand

Emma Marie Kiekebosch-Fitt
University of Wollongong

Geochemistry & Mineralogy of Fluvial Sediments in the Southern Alps, New Zealand

Abstract

Silicate weathering acts as a global sink for the greenhouse gas carbon dioxide. In order to understand long-term climate change and the fluctuations in atmospheric carbon dioxide, it is paramount to investigate the regulators of chemical weathering. The controls of rainfall and uplift have been reported to either enhance or inhibit the extent of chemical weathering, and therefore their relationship is still being highly debated in literature. Investigation of this relationship in the Southern Alps of New Zealand has been modest in comparison to the Himalayas. These studies have either focused on solute geochemistry of rivers, and therefore do not integrate weathering history of the catchment, or have failed to investigate the interplay between the controls of uplift and precipitation. Fluvial sediments record conditions of chemical weathering at the catchment scale, whilst integrating its weathering history. Therefore, this study has been undertaken to improve the understanding of the response of chemical weathering to uplift and precipitation in the Southern Alps, utilising the geochemistry and mineralogy of fluvial sediments. Mineralogical analysis was performed through X-ray diffraction and optical microscopy, while geochemical techniques included X-ray fluorescence, uranium-series isotopes and strontium isotopic analysis. Geochemical results suggest that modern chemical weathering is low to moderate and is predominantly occurring within the weathering profile. In contrast, weathering during transport in the fluvial system appears to be dominated by physical abrasion, which contributes to downstream fining. Furthermore, 238U was shown to be leached with increased residence time in the fluvial system and its depletion enhanced by rainfall. Similarly, rainfall amplified Mg loss, while Na was leached regardless. High uplift rates, on the western coast, increase erosion and therefore reduce sediment residence time in the weathering profile. The extent of chemical weathering is consequently inhibited, whereby only the most mobile elements are depleted. Therefore, the Southern Alps are classified as a weathering limited setting, where the intensity of chemical weathering is largely controlled by the residence time of sediments (uplift) and rainfall.

Degree Type

Thesis

Degree Name

Bachelor of Science (Honours)

Department

School of Earth & Environmental Science

Advisor(s)

Tony Dosseto

Keywords

u-series, Sr isotopes, uplift

UNIVERSITY OF WOLLONGONG

Geochemistry & Mineralogy of Fluvial Sediments in the Southern Alps, NZ

The Influence of Climate & Tectonics on Chemical Weathering

Emma Marie Kiekebosch-Fitt

10th October, 2012

Submitted in part fulfillment of the requirements of the Honours degree of Bachelor of Science (Advanced) in the School of Earth and Environmental Sciences, University of Wollongong 2012

The information in this thesis is entirely the result of investigations conducted by the author, unless otherwise acknowledged and has not been submitted in part, or otherwise, for any other degree or qualification.

Emma Kiekebosch-Fitt

10/10/2012

Acknowledgements

I would like to extend my thanks to the numerous people who generously assisted me throughout the various life stages of my study. Without such assistance I would not have been able to undertake this study and for that I am grateful. I would firstly like to acknowledge, and give special thanks, to my supervisor Dr. Anthony Dosseto. Your guidance, expertise, enthusiasm, patience and feedback have been invaluable and I appreciate the time you spent introducing me to the research world. Furthermore, I would like to thank Associate Professor Brian Jones and Dr. Samuel Marx, for sharing valuable knowledge that aided in the development of my study. Thank you to all of the supporting staff at the School of Earth and Environmental Sciences, University of Wollongong, particularly José Abrantes and Michael Stevens.

To all my fellow honours students, whom I shared long days of laughter, tears, encouragement, chocolate and tea with, you have been such an amazing support network. To my friends and family, thank you for your continual support and encouragement, while helping me to keep life in perspective. Lastly to Dave, thank you for everything, you finally have the old me back!

Abstract

Silicate weathering acts as a global sink for the greenhouse gas carbon dioxide. In order to understand long-term climate change and the fluctuations in atmospheric carbon dioxide, it is paramount to investigate the regulators of chemical weathering. The controls of rainfall and uplift have been reported to either enhance or inhibit the extent of chemical weathering, and therefore their relationship is still being highly debated in literature. Investigation of this relationship in the Southern Alps of New Zealand has been modest in comparison to the Himalayas. These studies have either focused on solute geochemistry of rivers, and therefore do not integrate weathering history of the catchment, or have failed to investigate the interplay between the controls of uplift and precipitation.

Fluvial sediments record conditions of chemical weathering at the catchment scale, whilst integrating its weathering history. Therefore, this study has been undertaken to improve the understanding of the response of chemical weathering to uplift and precipitation in the Southern Alps, utilising the geochemistry and mineralogy of fluvial sediments. Mineralogical analysis was performed through X-ray diffraction and optical microscopy, while geochemical techniques included X-ray fluorescence, uranium-series isotopes and strontium isotopic analysis. Geochemical results suggest that modern chemical weathering is low to moderate and is predominantly occurring within the weathering profile. In contrast, weathering during transport in the fluvial system appears to be dominated by physical abrasion, which contributes to downstream fining. Furthermore, ^{238}U was shown to be leached with increased residence time in the fluvial system and its depletion enhanced by rainfall. Similarly, rainfall amplified Mg loss, while Na was leached regardless. High uplift rates, on the western coast, increase erosion and therefore reduce sediment residence time in the weathering profile. The extent of chemical weathering is consequently inhibited, whereby only the most mobile elements are depleted. Therefore, the Southern Alps are classified as a weathering limited setting, where the intensity of chemical weathering is largely controlled by the residence time of sediments (uplift) and rainfall.

Table of Contents

List of Figures

List of Tables

Chapter One: Introduction

1.1 Silicate Weathering – A Sink for CO_2

The existence of life on Earth is largely contributed to the presence of greenhouse gases, such as carbon dioxide (CO_2). Therefore atmospheric CO_2 is an important contributor to the regulation of Earth's climate and mean global temperatures. The level of CO_2 in the atmosphere is governed by mechanisms which cycle carbon between the atmosphere, hydrosphere and lithosphere. Negative feedback mechanisms ensure atmospheric CO_2 levels are maintained, which keep global climate at an optimal temperature, to sustain life. One important example is the consumption of atmospheric CO_2, over geological time, through the chemical weathering of silicate rocks.

Over geological timescales CO_2 is naturally released to the atmosphere by the natural process of degassing from volcanism. Once in the atmosphere, CO_2 combines with water vapour or dissolves into surface waters, forming an equilibrium with water molecules that produces carbonic acid. Percolation of precipitation, groundwater and runoff therefore facilitates the interaction between carbonic acid and bedrock. The presence of carbonic acid initiates the hydrolysis of silicate minerals, whereby for every mole of cations from silicate minerals (Ca^{2+}, for example) reacted, two moles of atmospheric CO_2 is consumed (Equation 1). During hydrolysis of silicate minerals, CO_2 is shown to be converted to the bicarbonate ion (HCO_3^-) which is transported to the ocean by rivers. In the marine environment, HCO_3^- combines with Ca^{2+}, precipitating calcium carbonate ($CaCO_3$) primarily forming limestone and coral reef platforms (Equation 2). During the precipitation of calcium carbonate, for every mole of $CaCO_3$ sequestered, one mole of CO_2 is released to the atmosphere as a by-product. Overall this generalised reaction series of silicate weathering demonstrates that the chemical weathering of one mole of silicate mineral, results in a net loss of one mole of atmospheric CO_2. In comparison to silicate weathering, the hydrolysis of carbonate minerals is the reverse reaction of the precipitation of calcium carbonate (Equation 3). Consequently the reaction series for the chemical weathering of carbonate

minerals, does not result in a net drawdown of $CO_2$and therefore does not have an overall effect on the concentration of atmospheric CO_2.

Equation 1 $2H_2CO_3 + CaSiO_3 \rightarrow Ca^{2+} + 2HCO_3^- + H_2O + SiO_2$

Equation 2 $Ca^{2+} + 2HCO_3^- \rightarrow CaCO_3 + CO_2 + H_2O$

Equation 3 $CaCO_3 + CO_2 + H_2O \rightarrow Ca^{2+} + 2HCO_3^-$

The theory that silicate weathering acted as a sink for atmospheric CO_2 was first proposed by Urey (1952) who demonstrated that the weathering of calcium and magnesium bearing silicate minerals sequesters atmospheric CO_2, through the ultimate precipitation of calcite and dolomite. Proceeding Urey's (1952) study, there have been a number of conceptual and numerical models that propose links and feedbacks between tectonics, atmospheric processes, climate, chemical weathering and physical erosion (Gabet *et al.* 2010).

In comparison to other major global reservoirs, the atmosphere stores relatively small proportion of carbon. For example, the ocean and the lithosphere respectively possess 50 and 10,000 times more carbon than the atmosphere (Jacobson 2001). As atmospheric CO_2 is proportionally quite small, disruptions of the balance between the mechanisms that regulate atmospheric CO_2 have the potential to greatly alter global climate. For instance, enhanced silicate weathering rates theoretically would increase the drawdown of atmospheric CO_2, leading to a reduction of the intensity of the greenhouse effect and ultimately resulting in a decreased global average temperature.

The coupling between global climate, atmospheric CO_2 levels and silicate weathering has been used to explain the shift of global climate over a geological timescale. For instance, Berner et al. (1983), devised the BLAG model which argues that the rate of CO_2 out gassing drives the global rate of silicate weathering. This hypothesis suggests a temperature weathering feedback, whereby global mean temperatures are raised by increased atmospheric CO_2, through the greenhouse effect. This increase in

temperature thus leads to an enhancement of silicate weathering rates, resulting in the reduction of atmospheric CO_2 and ultimately triggering global cooling (Gabet *et al.* 2010).

However, Raymo and Ruddiman (1992) disagreed with the BLAG model, suggesting that tectonics rather than climate, was more influential in global atmospheric CO_2 circulation. They proposed that tectonic collision and the subsequent uplift of the Tibetan plateau drove atmospheric CO_2 drawdown, overall leading to global cooling during the late Cenozoic (Raymo & Ruddiman 1992). This theory is based on the enhancement of mechanical erosion during tectonic uplift, which leads to increased chemical weathering. Mechanical erosion continually exposes fresh bedrock, by the removal of unconsolidated material, which ensures there is an abundance of material that is easily weathered (Raymo & Ruddiman 1992; Jacobson *et al.* 2003; Mortatti & Probst 2003; Lyons *et al.* 2005). Furthermore, the reactive surface area of minerals within the bedrock is increased, which enhances the rate of chemical breakdown (Raymo & Ruddiman 1992). Therefore Raymo and Ruddiman (1992) proposed that increased uplift rates enhanced chemical weathering, which consequently lowered atmospheric CO_2 concentrations and drove global cooling during the late Cenozoic (Raymo & Ruddiman 1992).

However, scepticism was placed on theories such as the BLAG and Raymo and Ruddiman (1992) models by Willenbring and von Blanckenburg (2010). They suggested chemical weathering rates do not reflect global temperature changes nor pulses in mountain uplift and therefore are not responsible for fluctuations in global mean temperatures. Willenbring and von Blanckenburg (2010) interpreted the $^{10}Be/^{9}Be$ record as a proxy of continental weathering and showed that this ratio has remained fairly constant over the last 10Ma. They concluded that the global flux of eroded material reaching the ocean remained fairly constant during the late Cenozoic, and therefore suggested that neither uplift nor climate change accelerated chemical weathering.

1.2 Main Factors Influencing Silicate Weathering

Silicate weathering is an important driver for global cooling and warming events. Therefore in order to understand long-term climate change and the fluctuations in atmospheric CO_2, it is paramount to investigate the regulators of chemical weathering. The controls of chemical weathering and their relative influence on atmospheric CO_2 drawdown are still being highly debated in literature. Debate has particularly been centred around the controls of tectonics, thus rock supply and climate on physical erosion and its relationship to chemical weathering (Hren 2007). For instance, Nesbitt and Young (1984) conclude that the degree of chemical weathering is predominantly determined by the rate of precipitation, which controls the amount of carbonic acid in contact with the bedrock. Harris and Mix (2002) support the importance of precipitation, arguing that tectonics and subsequent mountain building is a secondary factor and regional climatic conditions primary controls chemical weathering rates. However, there are a number of studies which suggest that tectonics is the dominant control of chemical weathering. For example, Riebe *et al.* (2001), observed a strong correlation between physical erosion rates and chemical weathering, arguing that weathering is strongly controlled by tectonics and only weakly influenced by climate. Therefore this study supported Raymo and Ruddiman's (1992) hypothesis that increased mountain uplift rates and subsequent erosion rates, will increase chemical weathering rates.

Mountain ranges provide a natural laboratory in which to examine the controls of chemical weathering, due to the large variations in temperature, precipitation, uplift and consequent erosion that are often present at both the catchment and mountain belt scale. Chemical weathering intensity can either be amplified or inhibited in these regions. Enhancement can occur firstly, by the continual exposure of fresh, fertile minerals and secondly, the increased reactive surface of minerals by the breakdown of mineral grains (Raymo & Ruddiman 1992; Jacobson *et al.* 2003; Mortatti & Probst 2003; Lyons *et al.* 2005). However, the combination of high rainfall and uplift rates can result in reduced residence in the weathering profile, which may result in sediments being subjected to minimal chemical weathering.The Himalayas is the world's highest and most extensive mountain range and therefore demonstrates

large scale weathering processes. Consequently, there has been a dominance of studies which investigate the control of tectonics and/or climate on chemical weathering, in the Himalayas (Raymo & Ruddiman 1992; Ahmad *et al.* 1998; Dalai *et al.* 2004).

In comparison, there have been minimal studies which investigate chemical weathering on the Southern Alps of New Zealand, a mountain range formed by the tectonic convergence between the Australian and Pacific plates (Jacobson *et al.* 2003; Robinson *et al.* 2004; Lyons *et al.* 2005; Kautz & Martin 2007). Raymo and Ruddiman's (1992) theory, that tectonic uplift accelerates mechanical erosion and thus chemical weathering, is supported by a study, conducted in the Southern Alps, by Jacobson *et al.* (2003). Jacobson *et al.* (2003) investigated solute geochemistry of streams and suggested that orogenic uplift enhances the rate of chemical weathering, however, the proportion of silicate to carbonate weathering decreases, due to low residence time of minerals in the soil. Though, Jacobson *et al.*'s (2003) study only focused on catchments to the east and west of the central Southern Alps, and consequently only investigated weathering in a relatively small geographic region. Kautz and Martin (2007) furthered Jacobson et al. (2003) work, by studying residual weathering products along two rivers draining opposing flanks of the Southern Alps. Therefore this study investigated the control of rainfall on silicate weathering intensity, whereby the adjacent catchment headwaters were subjected to similar uplift rates. Kautz and Martin (2007) reported that the intensity of silicate weathering did not differ between the opposing flanks of the Southern Alps and therefore rainfall intensity was not a dominant control. Therefore the study agreed with Jacobson et al.'s (2003) findings, concluding that uplift was the primary control of silicate weathering in regions characterised by high erosion rates.

However, Lyons *et al.* (2005) highlighted that it is the coupled relationship between high rates of precipitation and continuous supply of fresh, easily weatherable mineral surfaces, that has a strong influence on chemical weathering. Similarly to Jacobson *et al.* (2003), Lyons et al. (2005) analysed solute chemistry of flood-water

samples to estimate chemical weathering rates. This study concluded that enhanced chemical weathering rates were a consequence of the rapid production of fresh bedrock surfaces resulting from high physical erosion.

1.3 Aims and Objectives

Chemical weathering studies previously undertaken on the Southern Alps of New Zealand have predominantly investigated solute chemistry of rivers (Jacobson & Blum 2003; Lyons *et al.* 2005). This approach provides important constraints on the relationship between weathering and its controlling factors, however, it only reflects present day weathering conditions and does not integrate weathering over a timescale of drainage basin evolution (Gaillardet *et al.* 1999). In comparison, fluvial sediments record conditions of chemical weathering at the drainage basin scale, whilst integrating the weathering history of the catchment. In contrast to solute chemistry studies, there has been minimal research on the Southern Alps that have utilised sediment geochemistry and mineralogy to investigate chemical weathering (Kautz & Martin 2007). Furthermore, sediment geochemical studies on the Southern Alps of New Zealand, have failed to investigate the interplay between the controls of uplift and precipitation on chemical weathering over a variety of catchments (Kautz & Martin 2007).

The overall aim of this study is to use the geochemistry and mineralogy of fluvial sediments, to investigate how chemical weathering responds to climate and tectonic factors in mountain ranges. This will be achieved through the study of fluvial sediments from catchments draining the Southern Alps of New Zealand, which capture a climatic and tectonic matrix. Uplift and precipitation are employed in this study, as proxies for tectonics and climate, respectively. Therefore this study aims to determine if a relationship exists between rainfall, uplift and chemical weathering in the Southern Alps, New Zealand.

The objectives of this study address the overall aim are to investigate:

i. The influence of grain size distribution on the geochemistry and mineralogy of fluvial sediments.

ii. Downstream physical weathering trends.

iii. The intensity of chemical weathering in the weathering profile and during transport in the fluvial system.

iv. Sediment provenance by using the geochemical isotopic tracer, $^{87}Sr/^{86}Sr$.

v. The response of U-series isotopes to chemical weathering.

vi. Geochemistry of fluvial sediments to attempt to correlate the intensity of chemical weathering with rainfall and uplift rates.

Chapter Two: Literature Review

The purpose of this chapter is to briefly review the use of sediment geochemistry and mineralogy to study chemical weathering.

2.1 Sediment Composition & Geomorphology

The mineralogy and geochemistry of river sediments is a direct reflection of their physical and chemical history. Consequently the composition of sediments results from the cumulative effects of parent rock composition, chemical weathering, hydraulic sorting and physical abrasion (Nesbitt *et al.* 1997). Many studies have indicated that sediment grain size affects both modal composition and geochemistry (Johnsson 1990; Savage & Potter 1991; Nesbitt *et al.* 1997). Grain size effects can be varied and primarily result from the mechanical breakdown and chemical weathering of minerals, whereby minerals are preferentially concentrated in particular fractions (Johnsson & Basu 1993). Consequently, the degree of grain size variation of sediments is largely dependent upon the extent of physical and chemical weathering. Slatt and Eyles (1981) investigated the effects of mechanical breakdown in arctic environments, whereby chemical weathering was presumed to be slight. This study reported a dramatic decrease in polycrystalline lithic fragment abundance and increase in feldspar abundance between first and second cycle glacial sand. Slatt and Eyles (1981) explained this observation by the mechanical breakdown of lithic fragments, whereby strongly foliated lithic fragments were most severely affected.

When grain sizes of sediment differ markedly in composition, hydrodynamic sorting may have an effect upon sediment composition (Garzanti 1986). Hydrodynamic sorting is largely responsible for the large compositional variability between suspended sediments, dominated by clay minerals and monomineralic silt grains and the bedload, which contains primary minerals and lithic fragments (Johnsson & Basu 1993). Hydraulic sorting of the bedload results in compositional variations based upon density differences, whereby the most compositionally diverse sediments occurs in depositional environments characterised by rapid changes in hydraulic

velocity, such as on point bars, transverse bars and behind obstructions (Johnsson & Basu 1993). Studies have attempted to reduce the effect of grain size variability by studying specific size fractions or by employing normalisation techniques (Vital & Stattegger 2000; Dalai *et al.* 2004; Singh *et al.* 2005; Kautz & Martin 2007).

2.2 Sediment Composition & Chemical Weathering

River sediments can be described as the product or residue of weathering (Singh *et al.* 2005), whereby chemical weathering occurs during the physical erosion of source rocks, transport in fluvial systems and sediment recycling (Nesbitt & Young 1996; Nesbitt *et al.* 1997). Numerous studies have used this principle to relate the mineralogy and bulk composition of sediments to the intensity of chemical weathering to source bedrock.

Most minerals are unstable at the Earth's surface temperature and pressure conditions and therefore breakdown in order to attain chemical equilibrium with ambient conditions. Reestablishment of a mineral's equilibrium falls under the general term of pedogenesis (the formation of soil) and involves the chemical weathering of mineral grains (Nesbitt & Young 1996). Goldich (1938) showed that the common silicate minerals form a weathering stability series analogous to the Bowen's reactions series, whereby minerals that crystallise at higher temperatures are more prone to chemical weathering than those crystallised a lower temperatures. The process of chemical weathering is defined as the dissolution of primary minerals and the precipitation of secondary minerals (Eiriksdottir *et al.* 2011). This results in depleting the sediment of the more unstable minerals, causing a relative increase in the proportion of the more stable minerals. For example, it has been found that quartz is highly resistant to chemical weathering, whereas feldspars are particularly susceptible to degradation (Nesbitt *et al.* 1997). This conclusion is based on the abundance of quartz in sediment and sands, even though feldspars are much more common in the upper continental crust, as compared to quartz (Nesbitt & Young 1984). Therefore chemical weathering causes the degradation of feldspars, a primary mineral, from source rocks to produce secondary phase minerals such as clays.

Consequently as sediments reside within the fluvial system they are likely to become more quartz rich at the expense of feldspars and lithic fragments (Kautz & Martin 2007). Chemical weathering therefore can account for the mineralogical and geochemical differentiation between source rock and river sediments.

The dissolution of primary minerals, during chemical weathering, is coupled with cations being selectively leached based upon their chemical resistance (Limmer *et al.* 2012). This process leaves weathering products, or sediment, depleted in mobile elements and concentrated in immobile elements (Nesbitt & Young 1996). Ratios between mobile and immobile elements, consequently change during chemical weathering, as cations have different mobility's in aqueous fluids (Limmer *et al.* 2012). Laboratory and field studies have shown that labile major cations such as, sodium (Na), potassium (K), calcium (Ca) and manganese (Mg) ions are relatively leached from source rock and therefore are depleted in sediments (Roy *et al.* 2008). However, aluminium (Al) and titanium (Ti) ions are considered immobile and therefore concentrate in weathering products (Roy *et al.* 2008). In terms of trace elemental chemistry, studies how shown that strontium (Sr), barium (Ba), rubidium (Rb) and uranium (U) are generally lost during weathering, while zirconium (Zr), thorium (Th) and yttrium (Y) are conservative (Kamber *et al.* 2005; Marx & Kamber 2010). The varying mobilities of major and trace cations means that chemical weathering can greatly affect the geochemistry of siliciclastic sediments.

2.3 Elemental Ratios & Mobility

As sediments reside within the fluvial system they are likely to become more quartz rich at the expense of feldspars and lithic fragments, due to the chemical stability of quartz (Kautz & Martin 2007). Therefore elemental ratios are employed as proxies in geochemical weathering studies as they are independent of dilution effects which are produced by quartz enrichment in sediments (Bhuiyan *et al.* 2011). Since elements behave differently during chemical weathering, elemental ratios can be used to constrain conditions of chemical weathering (Rollinson 1993).

For example, Limmer *et al.* (2012)used Al as a relative reference phase in elemental ratios with Na, K and Mg to assess weathering of sediment. This simplistic geochemical weathering proxy assumes that Al remains immobile during chemical weathering and therefore its relative concentration will increase. Limmer *et al.* (2012) suggested that the K/Al ratio is the best suited weathering proxy, as it appears to not be affected by either grain size or carbonate content.

Elemental ratios, normalised to a source composition, can be used to semi-quantitatively express the chemical mobility of major and trace elements. Consequently the use of a conservative (immobile) element, in a normalised elemental ratio, can quantify the extent of chemical weathering or mass loss in solution (Merrill, 1906). One such parameter is termed the Chemical Depletion Fraction, which utilises the immobility of zirconium (Zr) as a reference element (Riebe *et al.,* 2003). Zr was identified by Green *et al.* (2006) as the most conservative element, in comparison to Ti, Ce, or Mn, as Zr was the only element to show mass accumulation in a weathering profile at all the sample location. The Chemical Depletion Fraction therefore highlights the relative enrichment (< 0) or depletion (> 0) of the element in the weathered rock/sediment from the source bedrock. The Chemical Depletion Fraction is expressed in wt% and is defined by Equation 4. Dosseto *et al.* (2008) used the Chemical Depletion Fraction to evaluate the mobility of elements in weathering profiles. This study reported that the depletion factor for mobile elements Na, Ca and K increased with depth, whereas the CDF value for less mobile of Fe, Ti, Th and Nb were fairly constant.

Equation 4:

$$\mathrm{CDF_X} = \left(1 - \frac{[\mathrm{X/Zr(sediment)}]}{[\mathrm{X/Zr(source)}]}\right) \times 100$$

Similar to Doesseto *et al.* (2008), Wang *et al.* (2011) reported low chemical mobility of Ti and Fe, moderate for K and higher for Na and Ca, in sediments which had been subjected to intense chemical weathering. However, this study utilised Al as an immobile reference element, calculating normalised elemental ratio as in Equation 5.

Equation 5:

$$\text{Normalised Elemental Ratio (X)} = \frac{[\text{X}/\text{Al}_2\text{O}_3(\text{sediment})]}{[\text{X}/\text{Al}_2\text{O}_3(\text{source})]}$$

2.4 Chemical Weathering Indices

Various geochemical proxies have been developed and employed to try to estimate the intensity of chemical weathering that has been subjected to a sediment (Price & Velbel 2003). The proxies are generally based on the varying mobility of cations during chemical weathering and therefore are calculated from the elemental composition of the sediment or aqueous fluid. Therefore these geochemical analysis methods can be broadly divided into proxies, based on data derived from the dissolved load in rivers or those that analyse the geochemistry of the sediment itself. Proxies, which are focused on the dissolved load, directly indicate the weathering intensity of a catchment at present and are therefore not able to reflect and integrate weathering history (Li & Yang 2010). In contrast, chemical weathering indices , quantify chemical weathering intensity by utilising the bulk major element oxide chemistry of the sediment (Price & Velbel 2003), therefore integrating the weathering history from bedrock to analysis. As proxies are based on the mobility of selected elements, increased chemical alteration reduces the relative proportion of mobile elements as compared to immobile elements. Weathering indices have been shown to generally change systematically with depth in weathering profiles (Parker 1970). Consequently chemical weathering indices have been used in a large number of sedimentary studies. For example, Roy et al. (2008) used geochemical data and subsequent triangular and scattered diagrams, in association with calculated weathering indices, to evaluate the chemical weathering intensity and provenance of siliciclastic sediments deposited in the Tecocomulco Lake basin in central Mexico.

2.4.1 Weathering Index of Parker

The Weathering Index of Parker (WIP) was proposed by Andrew Parker, as a weathering index for silicate rocks in 1970 (Equation 6). The chemical weathering proxy is based on studies, which suggest that alkali and alkaline earth metals are the most mobile elements (Price & Velbel 2003). The high mobility of these ions during chemical weathering implies that the relative concentration of these ions will decrease during chemical weathering. Therefore this will yield greater compositional variations relative to the unweathered bedrock, as compared to other less mobile elements. Therefore the index differentiates weathered sediments from the parent bedrock by only including the most mobile alkali and alkaline earth elements, Na, K, Mg and Ca (Price & Velbel 2003).

Equation 6:

$$\mathrm{WIP} = \left(\frac{2\mathrm{Na_2O}}{0.35} + \frac{\mathrm{MgO}}{0.9} + \frac{2\mathrm{K_2O}}{0.25} + \frac{\mathrm{CaO}}{0.7}\right) \times 100$$

An element's susceptibility to chemical weathering and thus mobility, is primarily based on its adhesion to the chemical lattice structure of the mineral (Parker 1970). This degree of mobility is accounted for in the Weathering Index of Parker, by including the weighting factor of the ionic bond strength of the element with oxygen (Parker 1970). In short ,this takes into consideration the energy required to break the respective element to oxygen bond, whereby a weaker bond corresponds to an increased likelihood that the element will be involved in weathering reactions (Parker 1970).

The primary difference between the Weathering Index of Parker and the majority of weathering indices is that it allows for aluminium to be mobile. Price and Velbel (2003) have reported aluminium mobilisation in weathering profiles over heterogeneous felsic metasedimentary bedrock, proposed that the WIP was the most appropriate index to use for heterogeneous bedrocks. Conversely, Bahlburg and Dobrzinski (2011) have suggested that WIP lacks consideration of a relatively

immobile reference phase (such as Al_2O_3), which would take into consideration of dilution effects and relative changes in elemental abundances. Furthermore, the calculation of WIP assumes that all CaO measured in a sample is derived from silicate minerals, which could introduce significant error where a considerable proportion of carbonate detritus or cements are present (Bahlburg & Dobrzinski 2011).

2.4.2 Chemical Index of Alteration

The Chemical Index of Alteration (CIA) is the most widely used chemical weathering index in studies which investigate and interpret the weathering history of modern and ancient sediments (Rollinson 1993; Bahlburg & Dobrzinski 2011). It was developed by Nesbitt and Young in 1982 and used the weathering of lutites to calculate a scale of weathering intensity (Price & Velbel 2003). The CIA is based on the breakdown of feldspars, which dominate the upper continental crust, to clays such as kaolinite, and is given as a ratio of immobile Al_2O_3 to the mobile cations Na^+, K^+ and Ca^{2+} expressed as oxides (Price & Velbel 2003; Bahlburg & Dobrzinski 2011). Essentially it measures the conversion of feldspar (CIA value near 50) through muscovite-illite (75) to gibbsite (100) during weathering (Roser *et al.* 1996). Therefore CIA values increase with chemical weathering intensity, whereby Fedo *et al.* (1995) has further defined CIA values as greater than 80 for extreme, 60-80 for moderate and below 60 for low intensity.

The calculation of CIA is give by Equation 7, whereby major element oxides are given in molecular proportions and CaO* represents Ca^{2+} in silicate bearing minerals only (Fedo *et al.* 1995). Therefore CIA values are normally corrected for biogenic calcium, however, where this data is unavailable the CaO^*/Na_2O ratio of plagioclase can be used instead of CaO* to give a good estimate of CIA (Singh *et al.* 2005).

Equation 7:

$$\mathrm{CIA} = \left(\frac{\mathrm{Al_2O_3}}{\mathrm{Al_2O_3 + Na_2O + K_2O + CaO^*}}\right) \times 100$$

The CIA proxy has been used in numerous studies to quantify the intensity of chemical weathering of modern and ancient sediments (Roy *et al.* 2008). For example, Bahlburg and Dobrzinski (2011) utilised a combination of the CIA proxy and a comprehensive facies analysis to assess changes in the relative contributions of chemical and physical weathering in the production of sedimentary detritus. Ahmad *et al.* (1998) calculated the CIA of bed sediments, from the Indus River in the Himalayas, to evaluate the intensity of weathering undergone by the source rocks in the catchment. Similarly, Dalai *et al.* (Dalai *et al.* 2004) considered CIA to assess the intensity of weathering within a catchment basin in the Himalayas. This study concluded that the low weathering intensity in the Yamuna River Basin was due to an enhancement of physical erosion caused by the steep gradient of the catchment (Dalai *et al.* 2004). High erosion rates imply a shorter residence time of sediments in the catchment meaning shorter duration of chemical weathering (Dalai *et al.* 2004).

CIA and corresponding weathering trends can be further developed through the use of an A-CN-K [(Al_2O_3) – $(CaO + Na_2O)$ – (K_2O)] ternary diagram (Nesbitt & Young 1984; 1989; Rollinson 1993). On a diagram of this type, the initial stages of weathering form a trend parallel to the Al_2O_3 – $(CaO + Na_2O)$ side of the diagram, whereas advanced weathering shows a marked loss in K_2O as compositions move towards the Al_2O_3 apex (Rollinson 1993). This reflects the removal of alkalis and Ca in solution during the breakdown of plagioclase first followed by potassium feldspar and ferromagnesian silicates (Rollinson 1993). This diagram therefore visually represents the loss of minerals during weathering.

A variation of the A-CN-K diagram is the A-CNK-FM [(Al_2O_3) – $(CaO + Na_2O + K_2O)$ – $(FeO + MgO)$] triangular plot. Rajamani *et al.* (2009) used these diagrams to study how differently felsic and mafic bedrock weather by showing the dissolution of plagioclase, amphibole and pyroxene during chemical weathering.

2. 5 Isotopic Fractionation & Chemical Weathering

With the development of technology, catalysing advancements in analytical techniques, instruments such as inductively coupled plasma mass spectrometry (ICP-MS) and thermal ionization mass spectrometry (TIMS), have allowed the accurate measurement of isotopes with an extremely high precision. These advancements have led to enhanced knowledge of isotopic ratios, which have emerged as a powerful tool to constrain the rates and timescale of geological processes.

2.5.1 Strontium- Isotopes

The strontium isotopic ratio ($^{88}Sr/^{86}Sr$) has been applied in a wide variety of sediment geochemical studies (Limmer *et al.* 2012). One geochemical use of the isotopic tracer, $^{87}Sr/^{86}Sr$, is in provenance studies, which link weathered material to its parent bedrock. As the geochemical and mineralogical of modern sediments are a reflection of the bedrock from which they are derived, the composition of the sediment is therefore a product of the provenances of the various tributaries in the fluvial system. Strontium isotopic ratios can be used to geochemically trace weathering reactions since the $^{87}Sr/^{86}Sr$ ratio of the weathering products is inherited from that of the weathered bedrock (Hren 2007). Consequently the $^{87}Sr/^{86}Sr$ isotopic ratio of the minerals in the weathered sediment will reflect the $^{87}Sr/^{86}Sr$ ratio of primary minerals in the source rock.

Strontium is an alkaline earth element, which has four naturally occurring isotopes with differing abundances ^{84}Sr (0.6%), ^{86}Sr (9.9%), ^{87}Sr (7.0%) and ^{88}Sr (82.6%) (Hren 2007). All of these isotopes are stable, however, as ^{87}Sr is radiogenic its concentration tends to increase over time due to the radioactive decay of ^{87}Rb ($t_{1/2}$ = 48.8 Ga) (Hren 2007; Liu *et al.* 2011). Therefore the $^{87}Sr/^{86}Sr$ ratio is a function of the initial $^{87}Rb/^{86}Sr$ ratio and the age of the minerals. Rocks containing minerals with a high concentration of rubidium will develop higher $^{87}Sr/^{86}Sr$ ratios over time, as compared to rocks with a low rubidium concentration. The use of $^{87}Sr/^{86}Sr$ ratio as a tracer is based on the fact that, in a closed system, the $^{87}Sr/^{86}Sr$ ratio of primary minerals will be the same as that in the original unweathered bedrock. As

fractionation is too recent during weathering to alter the $^{87}Sr/^{86}Sr$ ratio, the isotopic ratio of primary minerals in the sediment will reflect the source rock they are derived.

Therefore the $^{87}Sr/^{86}Sr$ ratio of sediments is utilised, in provenance studies, to determine and quantify regional sediment contributions to a river. For instance, Padoan (2011), used Sr isotopic ratios to reconstruct detrital fluxes and erosion patterns through the Nile drainage basin. Similarly, Bhushan and Singh (2008), determined sediment budget and spatial variability in physical erosion among the Ganga sub basins. These studies demonstrate that strontium isotopes are a useful geochemical tracer for assessing sediment provenance.

2.5.2 Uranium- Series

Uranium-series isotopes are being increasingly utilised in studies which assess chemical weathering in river sediments, at a catchment scale. Generally studies present U-series isotopes as daughter-parent activity ratios, using parenthenses to denote nuclide activities, such as ($^{234}U/^{238}U$) and ($^{230}Th/^{234}U$) (Dosseto *et al.* 2008). Analysis of these activity ratios are based on quantifying the fractionation between the parent and daughter nuclei, which are a function of duration and degree of weathering (Figure 1) (Dosseto *et al.* 2008). Isotopic fractionation of ^{238}U, ^{234}U and ^{230}Th nuclides during weathering processes occurs as U is more soluble than Th, causing radioactive disequilibria between the nuclides. In order to regain equilibrium, the daughter and parent nuclei will undergo radioactive decay until their activities are equal. This equilibrium state is defined as secular equilibrium and occurs when the geological system is closed for more than five to six half lives ($T_{1/2}$) of the daughter nuclei. Consequently, for bedrock to be in secular equilibrium for ($^{234}U/^{238}U$) and ($^{230}Th/^{234}U$) the geological system needs to be closed for approximately 1 Ma and 300 ka, respectively, assuming a discrete fractionation between ^{238}U, ^{234}U ($T_{1/2}$ = 244 ka) and ^{230}Th ($T_{1/2}$ = 75 ka) (Dosseto *et al.* 2008).

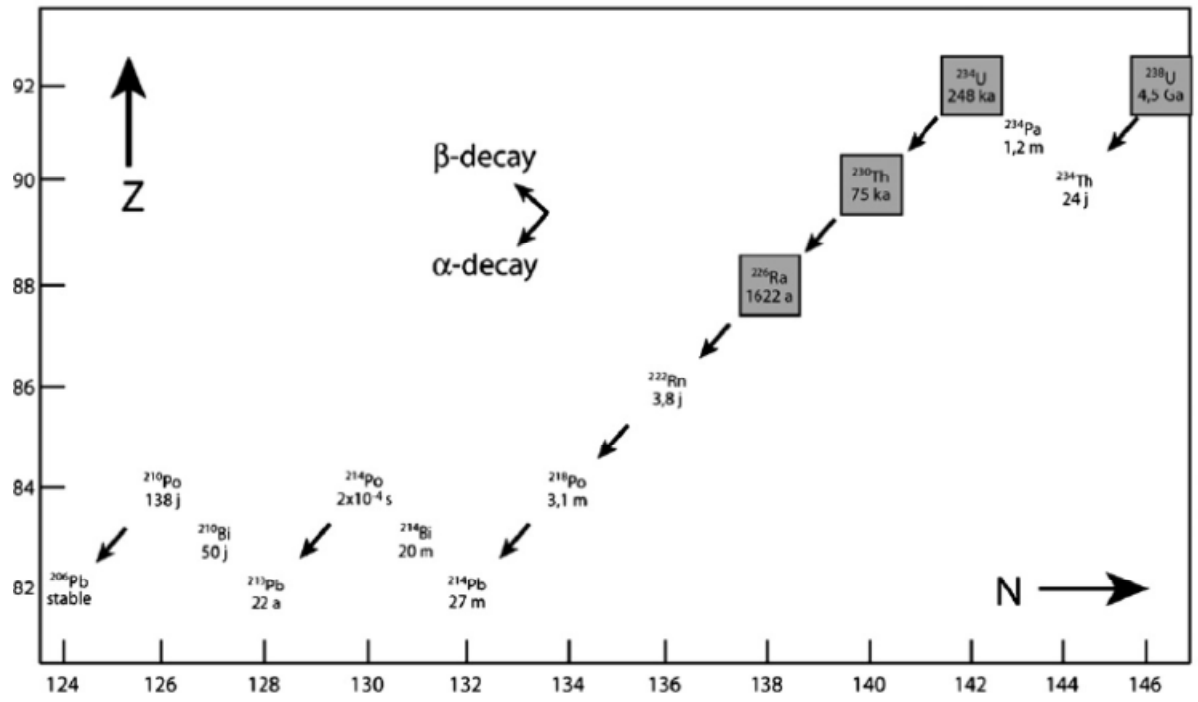

Figure 1: Diagram of the uranium-238 decay series in a proton number (Z) versus neutron number (N) (Dosseto et al. 2008).

Therefore bedrock is considered to be secular equilibrium for all nuclides, when the geological system has been closed for more than 1 Ma. However, when the bedrock becomes disturbed and begins to weather, mineral surfaces are exposed to an oxygenated environment leading to isotopic fractionation of ^{238}U, ^{234}U and ^{230}Th. Thorium (Th) naturally occurs in one oxidation state as Th^{4+}, which is considered to be relatively insoluble (Chabaux *et al.* 2003; Dosseto *et al.* 2008). However, uranium (U) is present in the environment in two oxidation states, which have varying degrees of solubility (Dosseto *et al.* 2008). Under reducing conditions of low oxygen concentration, such as below the Earth's surface, uranium is present as insoluble U^{4+} , whereas in high oxygenated conditions at the Earth's surface it's in the mobile U^{6+} state (Dosseto *et al.* 2008). Consequently, when minerals are beneath the Earth's surface their U concentration stays constant, however, when bedrock begins to weather, mineral surfaces are exposed to an oxygenated environment, which causes U to dissolve into the aqueous phase. Therefore the ($^{230}Th/^{234}U$) activity ratio is expected to be greater than one in the river sediment, soil and weathered rock, and less than one in the river water, soil pore waters and groundwater. However, there have been a number of studies which have reported river sediment ($^{230}Th/^{234}U$)

activity ratios to be less than one (Porcelli *et al.* 2001; Dosseto *et al.* 2006). For instance, Dosseto *et al.* (2006), documented ($^{230}Th/^{234}U$) < 1 in suspended sediments in the lowland rivers of the Amazon basin and attributed this anomaly to increased solubility of Th by highly dissolved organic carbon.

Additionally isotopic fractionation occurs between the ^{238}U and ^{234}U nuclei during weathering. This can occur when ^{238}U decays, the daughter nuclei ,^{234}Th, can be injected out of the mineral grain into solution, before rapidly decaying to ^{234}U (^{234}Th $T_{1/2}$ = 24 days) (Dosseto *et al.* 2008). However, ^{234}Th is only injected from the mineral grain if the distance to the grain boundary is smaller than the recoil distance of ^{234}Th (DePaolo *et al.* 2006). The recoil distance is dependent upon the radioactive decay, which emits high energy α – particles within the mineral, consequently displacing the daughter nuclei, ^{234}Th, from its original site (Figure 2) (Chabaux *et al.* 2003). For silicate and carbonate minerals, the recoil distance is approximately 30 nm (Chabaux *et al.* 2003; DePaolo *et al.* 2006). The release of high energy α – particles, during radioactive decay, can additionally damage the crystal lattice of the mineral (Dosseto *et al.* 2008). Therefore, the daughter nuclei, ^{234}Th, could be easily mobilized from the damaged crystal lattice of mineral grain and released into solution (Dosseto *et al.* 2008).

The combination of these processes results in the ($^{234}U/^{238}U$) activity ratio to be less than one in the river sediment, soil and weathered rock, and greater than one in the river water, soil pore waters and groundwater. However, sediments, in rivers, such as the Amazon (Dosseto *et al.* 2006) and organic rich rivers of Sweden (Porcelli *et al.* 2001), have been reported to have ($^{234}U/^{238}U$) activity ratios greater than one. The larger than expected activity ratio for sediments has been explained by ($^{234}U/^{238}U$)>1 from the waters, being absorbed onto Fe-oxides that have been precipitated on the sediment grain (Dosseto *et al.* 2008). Additionally, it is suspected that the mineral grain experienced minimal depletion of ^{234}U due to weathering (Dosseto *et al.* 2008). Therefore the combined effect of minimal depletion of ^{234}U and precipitation of Fe-oxides with higher ^{234}U than ^{238}U, means that the sediment grain has an overall

($^{234}U/^{238}U$)>1. This theory is supported by the study on a laterite deposit by Lowson *et al.* (1986) and von Gunten *et al.* (1999) who reported that Fe-oxides are the main U-bearing phases. Furthermore, they additionally found that amporhous Fe-oxides are in absorption/desorption equilibrium with surrounding waters.

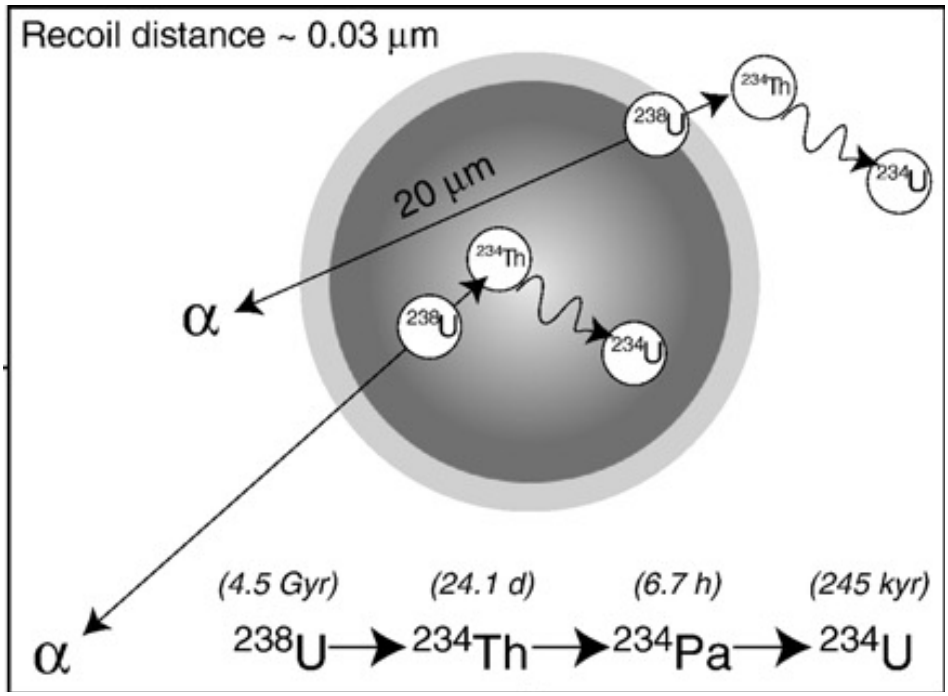

Figure 2: Schematic diagram of recoil ejection of ^{234}Th from a spherical grain as a result of alpha decay of ^{238}U, followed by beta decay of ^{234}Th to ^{234}U (Dosseto et al. 2008).

Chapter Three: Regional Settings

3.1 Tectonic Setting

For the past 5 Ma, the Indo-Australian and Pacific plates have been obliquely converging, resulting in the exposure of a small area of continental crust, which is known as the South Island of New Zealand (Williams 1991; Chamberlain *et al.* 2005). Convergence between the two plates operates as subduction zones, with trenches at the northern and southern ends of New Zealand, and a transverse fault connecting the two (Figure 3). The Indo-Australian Plate converges from the west, at a rate of 45 mm/yr in the southwest of the South Island, whereas off the east coast of the North Island sea floor spreading results in subduction of the Pacific Plate from the east, at a rate of 58 mm/yr (Williams 1991). Oblique crustal compression and dextral transpression on the fault is the consequence of this opposing relative movement. Therefore the fault is characterised by strike- and dip-slip rates of 27 mm/yr and 12 mm/yr, respectively, which account for nearly 75% of the total inter-plate velocity (Korup 2005b).

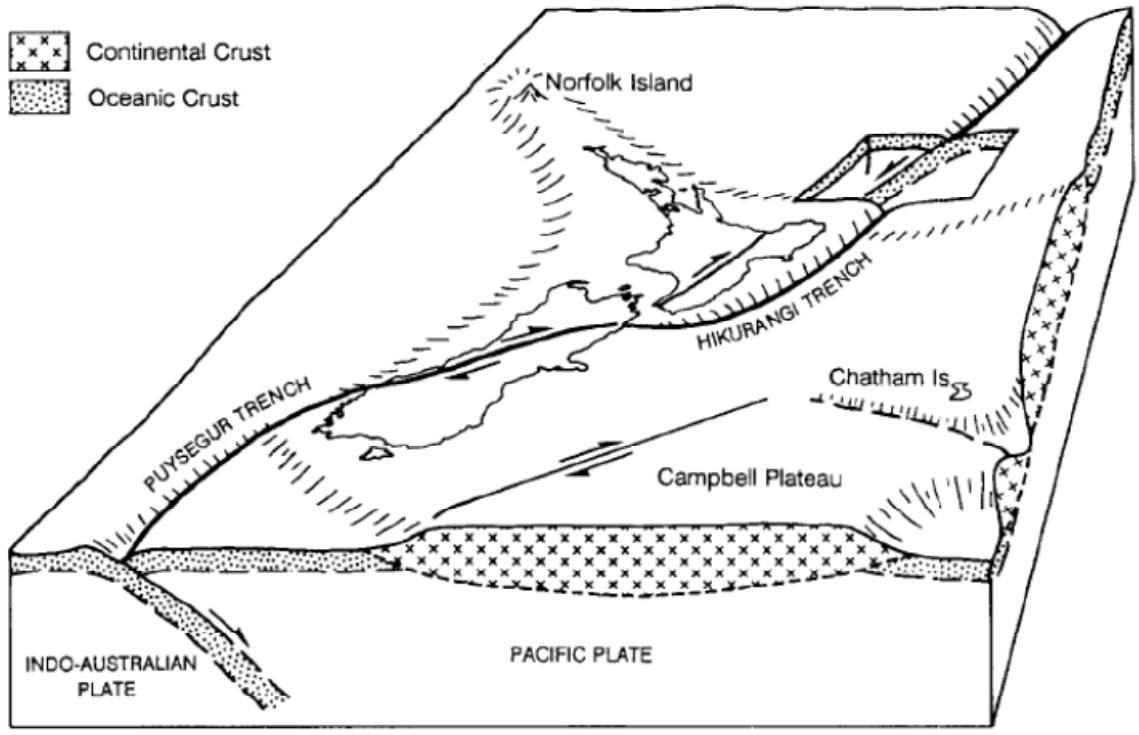

Figure 3: Tectonic setting of New Zealand, showing subduction trenches to the north-east and south-west and the transverse Alpine Fault connecting the two trenches (Williams, 1991).

This transverse fault is termed the Alpine Fault and has undergone approximately 500 km of strike slip motion and uplifting more than 20 km to give rise to the Southern Alps (Jacobson 2001; Chamberlain *et al.* 2005). The Southern Alps have an average elevation of approximately 2200 m and trend about 500 km in a north-easterly direction, parallel to the Alpine Fault (Koons 1990). Modern uplift rates vary greatly over the South Island, whereby uplift is at a maximum where convergence between the plates is the strongest. For the South Island, uplift rate is lowest around the Canterbury Plains region, whereby some zones are characterised by subsidence. Therefore a gradient of uplift rates is apparent over the South Island, whereby the western coast experiences rapid uplift rates, which then decrease easterly toward the Pacific Ocean (Figure 4).

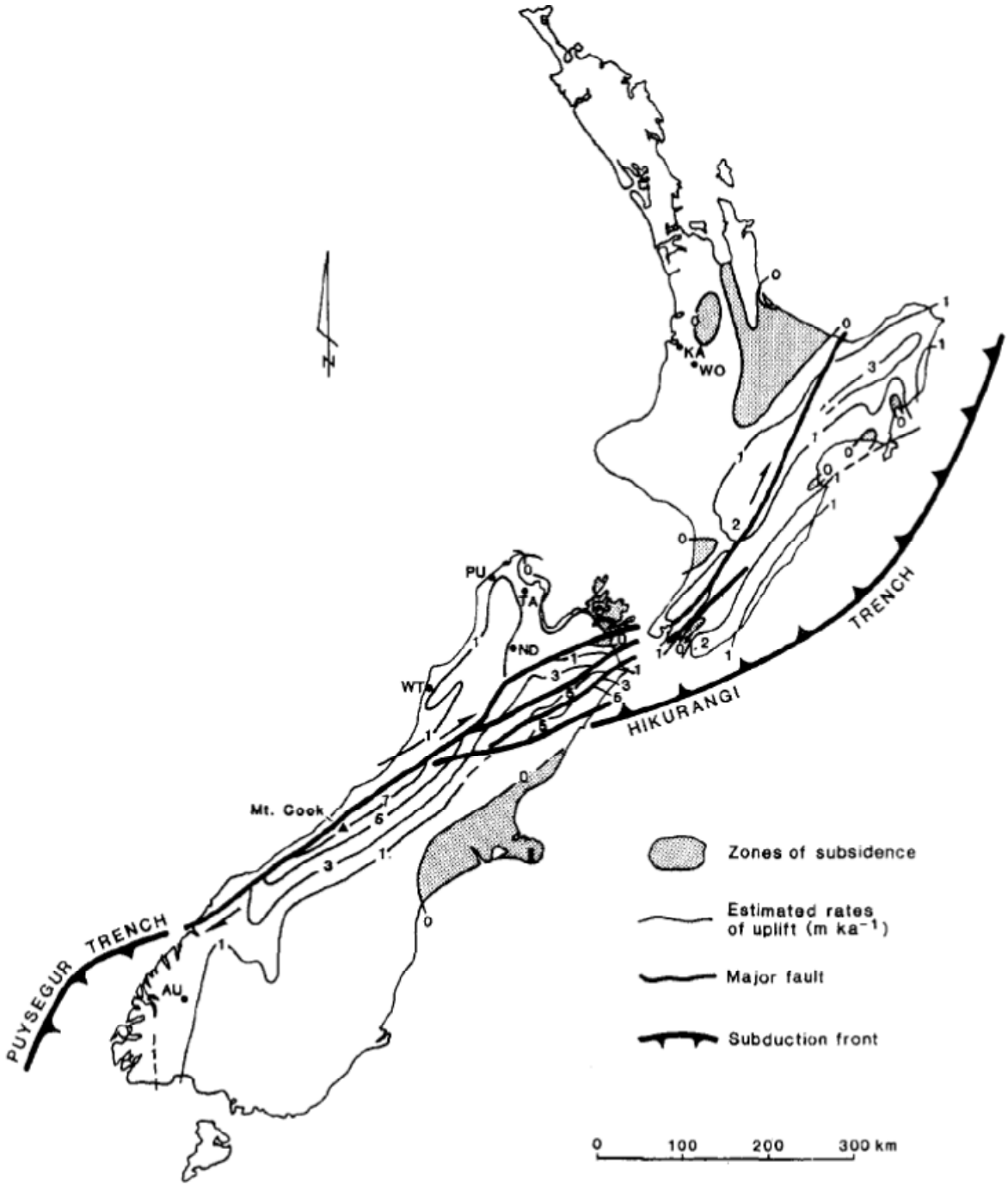

Figure 4: Late Quaternary annual uplift contour map of New Zealand (Williams, 1988).

3.2 Geology of the South Island

Geographical regions of the South Island are broken up into terranes, which are classified by similar geological characteristics (Figure 5). This thesis is focussed on the Torlesse (Pahua and Rakaia sub-terranes) and the Buller Terranes.

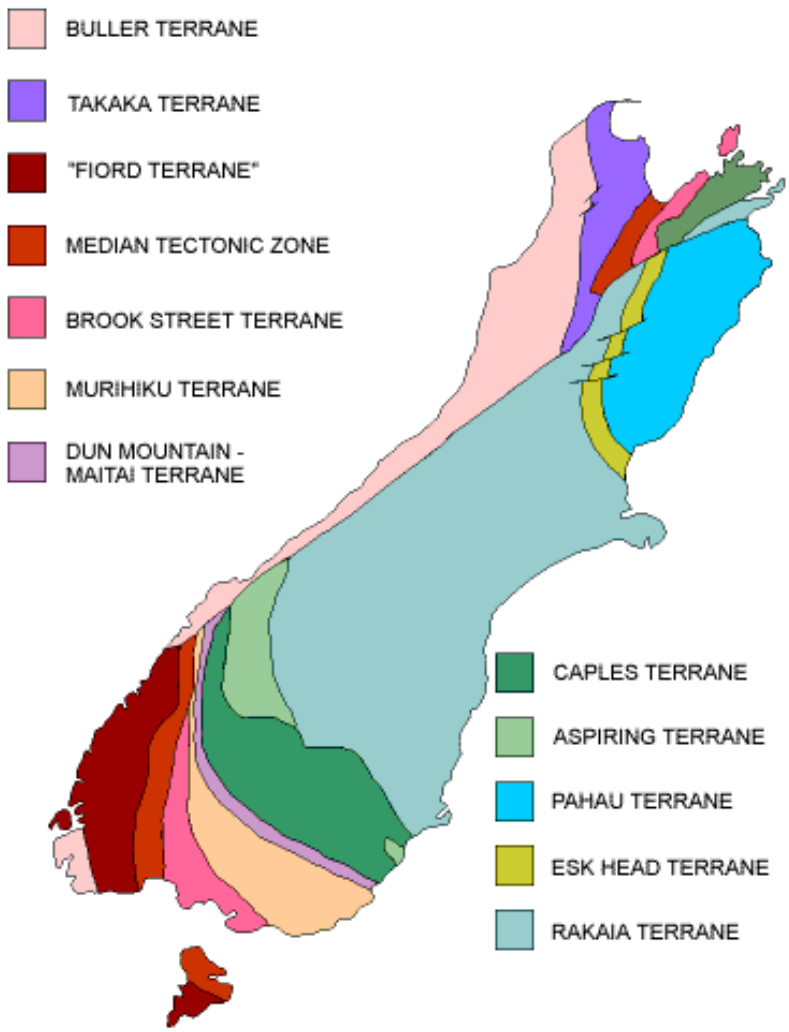

Figure 5: Tectonostratigraphic terranes that have been identified in South Island, New Zealand (University of Otago, 2011).

3.2.1 Torlesse Terrane

The Torlesse Terrane is made up of interbedded quartzofeldspathic greywacke and argillite, which outcrops east of the Southern Alps' Main Divide (Roser & Korsch 1999). The quartzofeldspathic greywacke is indurated, well-bedded and of a turbiditic nature (Mackinnon 1983). Compositionally the Torlesse Terrane greywacke is poorly to moderately well sorted with subangular grains and primarily contains Permian-Jurassic grains of undifferentiated quartz, plagioclase, muscovite and biotite mineral fragments derived from the erosion of granite, gneiss and schist (Suggate 1978; Mackinnon 1983). The sandstones are predominantly arkosic, with an average quartz-feldspar-lithic fragment ratio (Q:F:L) of 29:47:24, whereby the ratio of plagioclase to potassium feldspar is constant at approximately 5:1 (Mackinnon 1983). Plagioclase is largely albite-oligoclase, while K-feldspar is generally orthoclase with subordinate but conspicuous microcline (Mackinnon 1983). The lithic fragments are predominantly silicic volcanic however, quartzfeldspathic sandstone, mudstone and schist are additionally present. Heavy minerals are dominated by micas, titanite, epidote-clinozoisite, hornblende, apatite, zircon and garnet (Mackinnon 1983). Tectonic deformation of the hard greywacke and argillite basement rocks resulted in brittle fracture that has produced shearing, major faults and numerous associated joints (Suggate 1978).

There is a general acceptance that the Torlesse Terrane was deposited in an accretionary wedge at an active continental arc setting, which existed along the Gondwana margin (Suggate 1978; Wilson 1985; Mortimer 2004). It is thought that ocean deposits were scraped off the ocean floor on to the toe of an overriding plate where they were deposited with large amounts of sediments coming off the adjacent land (Suggate 1978). Whole rock geochemistry of the Torlesse Terranes suggests that sediment was derived from a relatively unweathered source, averaging near granodiorite composition (Roser & Korsch 1999). The Torlesse Terrane is subdivided into the northern Rakaia and southern Pahau Terranes, which have respective ages of Permian to Late Triassic and Late Jurassic to Early Cretaceous (Roser & Korsch 1999). A third sub-terrane, the Esk Head, additionally exists and is a melange zone separating the Rakaia and Pahau in the South Island (Suggate 1978).

Roser and Korsch (1999) have suggested, from geochemical evidences, that the Permain to Late Triassic Rakaia sediments are first-cycle erosion products of an active continental margin arc system, which has been identified as part of Gondwana (Wandres *et al.* 2004). Additionally, the Pahau Terrane is believed to have been derived in part from the same source, combined with material supplied from cannibalistic recycling of the Rakaia sediments, deposited during the Late Jurassic to Early Cretaceous (Figure 6) (Roser & Korsch 1999; Wandres *et al.* 2004). The more volcanogenic Mesozoic terranes, which lie to the west of the present Torlesse outcrop, may also have contributed a minor amount of detritus to the Pahau Terrane (Roser & Korsch 1999). Therefore the Torlesse Terrane is divided up into five petrofacies, with slightly different geochemical signatures (Figure 7) (Wandres *et al.* 2004).

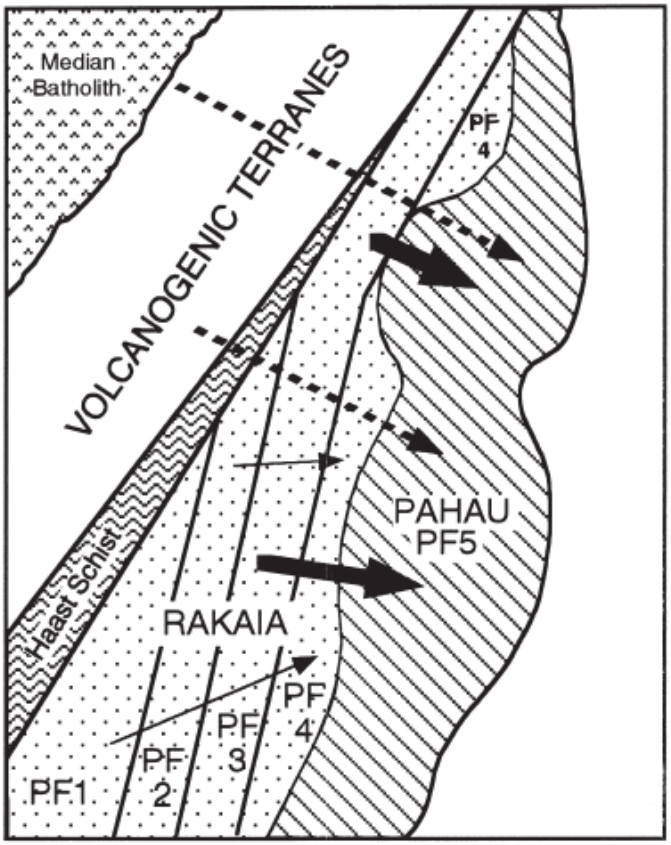

Figure 6: Schematic representation of deposition of the Pahau Terrane. The PF numbers represent Torlesse petrofacies. Arrows demonstrate erosion and subsequent deposition. PF4 is derived from PF1-PF3. Pahau source includes all Rakaia petrofacies, the volcanogenic terranes to the west and the intervening Haast Schist terrane.(Roser & Korsch 1999)

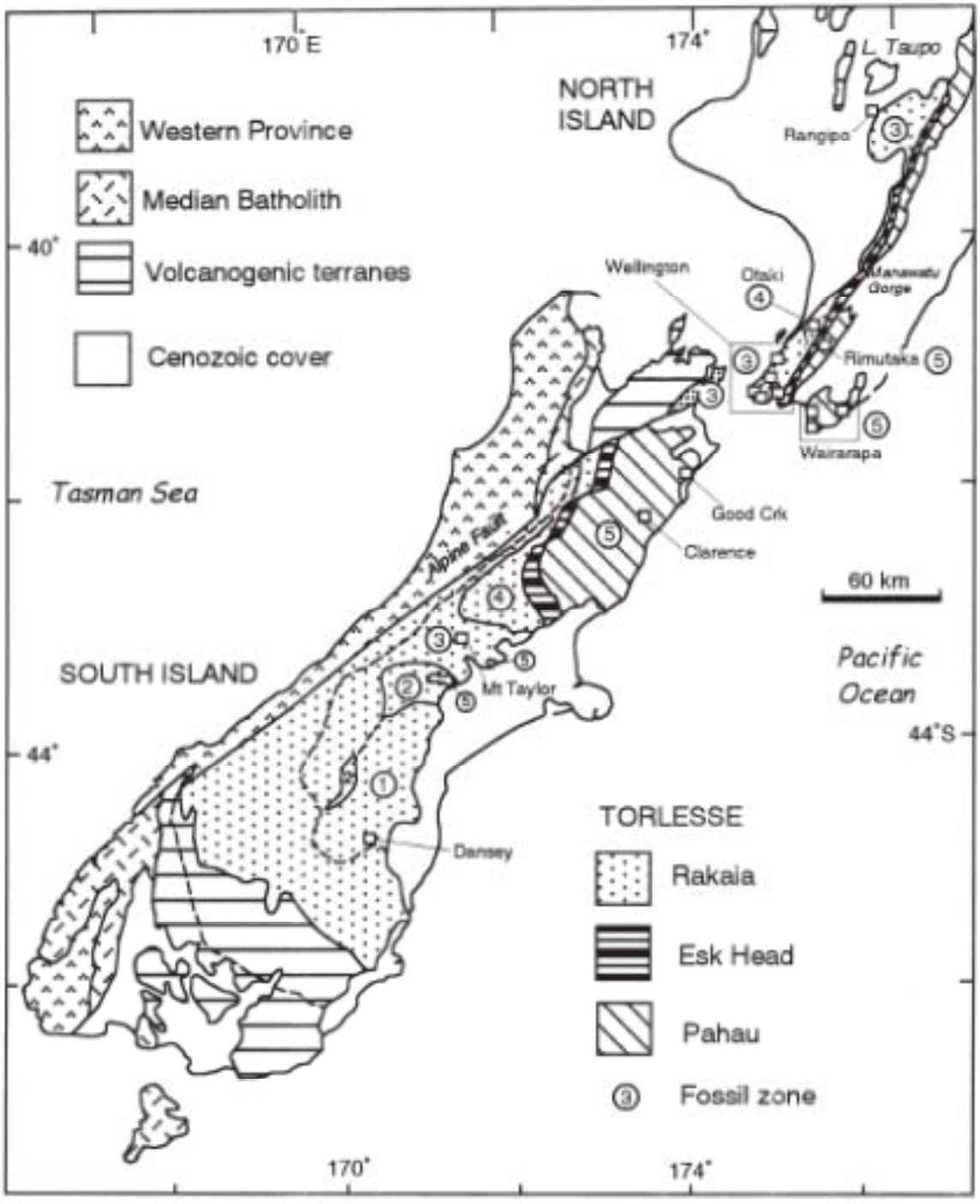

Figure 7: Map of central and southern New Zealand showing distribution of major geologic divisions, Torlesse sub-terranes and Torlesse petrofacies (Roser & Korsch 1999).

3.2.2 Buller Terrane - Haast Schist

The southern proportion of the Buller Terrane consists of the regional metamorphosed Rakaia Torlesse Terrane forming the Haast Schist Group, whereby the metamorphic belt is dominated (>95%) by altered greywacke and argillite (Vry *et al.* 2008). The alteration belt of Haast Schist is characterised by an increasing degree of metamorphism, from east to west, whereby the amphibolite metamorphic grade is highest along the Alpine Fault (Roser & Cooper 1990; Jacobson *et al.* 2003). The lower metamorphic grade, chlorite greenschist facies is divided into textural zones, based on the degree of schistosity (Suggate 1978; Tippett & Kamp 1993). The Chlorite II zone has cleavage but no distinct layering, Chlorite III is described as having distinct layering with aligned mica plates, whereas Chlorite IV is characterised as foliation, separating into marked white layers (mainly of quartz and feldspar) and dark layers of mica (Suggate 1978). The higher metamorphic grade schist can be classified into two groups, the higher garnet-oligoclase zone and its adjacent biotite zone. The mineralogy of the Haast Schist is characterised by a fine grained foliated matrix, mainly consisting of quartz and muscovite and small porphyroblasts, typically of plagioclase ± ilmenite ± titanate ± chlorite ± epidote and biotite ± tourmaline ± oligoclase ± garnet at higher grades (Mackinnon 1983; Roser & Cooper 1990; Vry *et al.* 2008). Hydrothermal activity, which has been associated with the uplifting of the Southern Alps, has led to the extensive deposition of centimetre to decimetre sized quartz-calcite veins, that are primarily evident in the biotite and garnet zones of the Haast River catchment (Jacobson *et al.* 2003; Kautz & Martin 2007).

3.3 Climate

For a large proportion of the year, New Zealand is located in the zone of westerly winds, which generally extend to latitudes of about 60 to 70 degrees (Tomlinson, 1992). These westerly weather systems travel across the Pacific Ocean uninterrupted and thus become moisture-laden. The Southern Alps are located almost perpendicular to these westerly weather systems and therefore intercept these moisture-laden air masses. Due to orographic processes, precipitation on the west coast of the South Island rapidly rises from 5,000 to a maximum of 12,000

mm/yr at the crest of the westernmost range (Tonkin & Basher 1990). By contrast ,the eastern coast is located in the rain shadow of the Southern Alps, whereby the annual rainfall dramatically decreases to less than 60 mm/yr, as shown in Figure 8 (Tonkin & Basher 1990; Chamberlain *et al.* 2005). Depending on the altitude, a variable proportion of this precipitation falls as snow (Tonkin & Basher 1990).

The South Island of New Zealand experiences relatively small variations between summer and winter temperatures, whereby mean annual summer air temperatures range between 12 – 22°C and decreasing to between 1 – 10°C in winter (NIWA, 2001). The mean annual temperature for the Southern Alps ranges from 2.1 – 6°C, where the temperature generally decreases, approximately 0.7°C every 100 m of altitude, as shown in Figure 8 (NIWA, 2001).

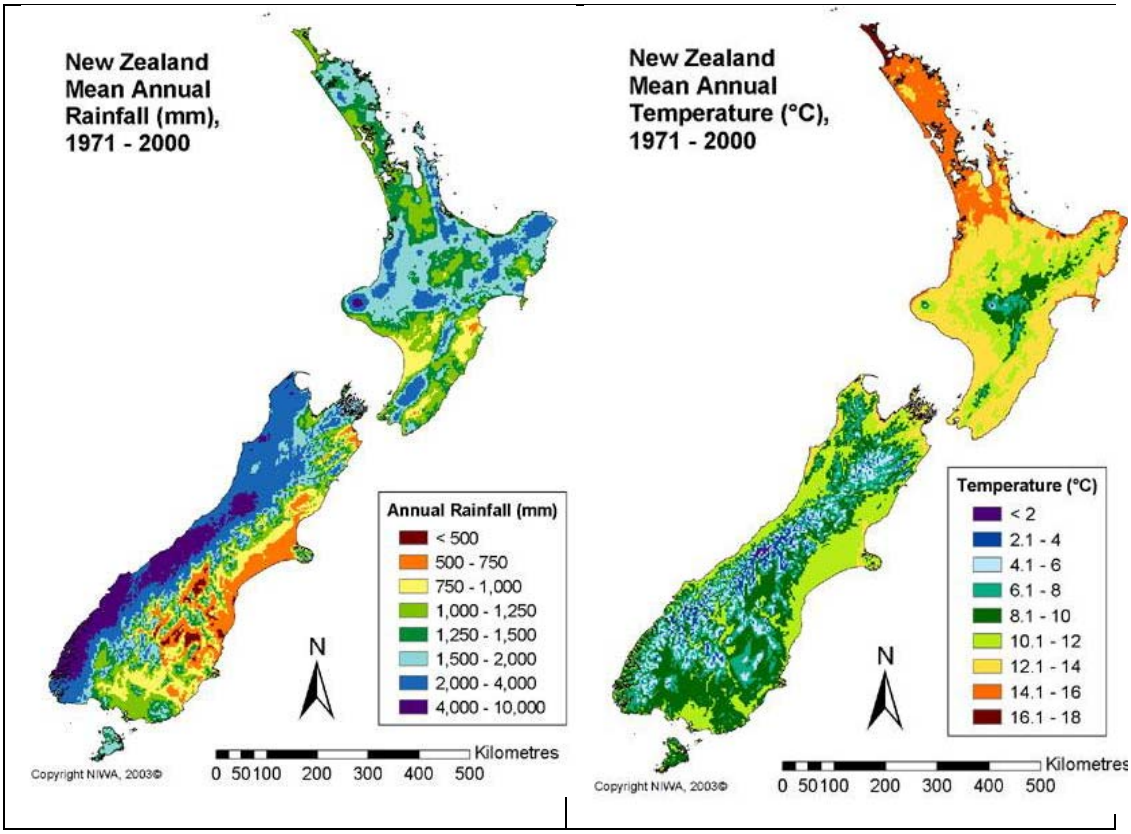

Figure 8: New Zealand mean annual (A) rainfall and (B) temperature based on the period 1971 - 2000 (NIWA, 2003).

3.4 Physical Erosion

In the South Island of New Zealand, the highest erosion rates and sediment yields are associated with the erodibility of the bedrock and precipitation rates (Hicks *et al.* 1996). The western Southern Alps are characterised by high erosion rates due to intense fluvial incision and debris avalanches, which have led to the development of highly dissected and steep slopes (Korup 2005b; Lyons *et al.* 2005). Hicks *et al.* (2011) demonstrated that sediment yields in New Zealand are primarily controlled by rainfall in the South Island. Due to the rapid uplift, high precipitation and consequent rapid erosion and steep slopes on the western side of the Southern Alps, the soil mantle is very thin (Tonkin & Basher 1990).

3.5 Hydrology

The western landscape, characterised by steep, rectilinear slopes and narrow ridge crests, results in rivers having steep channel gradients, often incised into bedrock, with a typically V-shaped channel (Tonkin & Basher 1990). In comparison, the eastern side of the Southern Alps decrease in height through a series of ranges and basins. Consequently eastern flowing rivers have a more gentle gradient and are characterised by broad-gravel filled valleys and braided channels (Tonkin & Basher 1990).

3.6 Vegetation

Vegetation patterns across the South Island of New Zealand are complex and reflect geographic variation of soil, microclimates, disturbance and drainage (Tonkin & Basher 1990). Areas of higher rainfall on the western side of the Southern Alps have a vegetation cover consisting of coniferous/broadleaved-hardwood and southern beech forests (Tonkin & Basher 1990; Hicks *et al.* 2011). East of the Southern Alps, vegetation in the mountainous regions is dominated by short and tall tussock grassland, scrubland and patches of native beech forest covered mountains (McWethy *et al.* 2009). The floodplains to the east of the mountain ranges are covered by introduced pastoral grasslands (Tonkin & Basher 1990; McWethy *et al.* 2009). Additionally the eastern region hosts patches of native beech forest (McWethy

et al. 2009). Overall there is a contrast of vegetation from the lush forest on the western coast to the pasturelands of the eastern region (Figure 9).

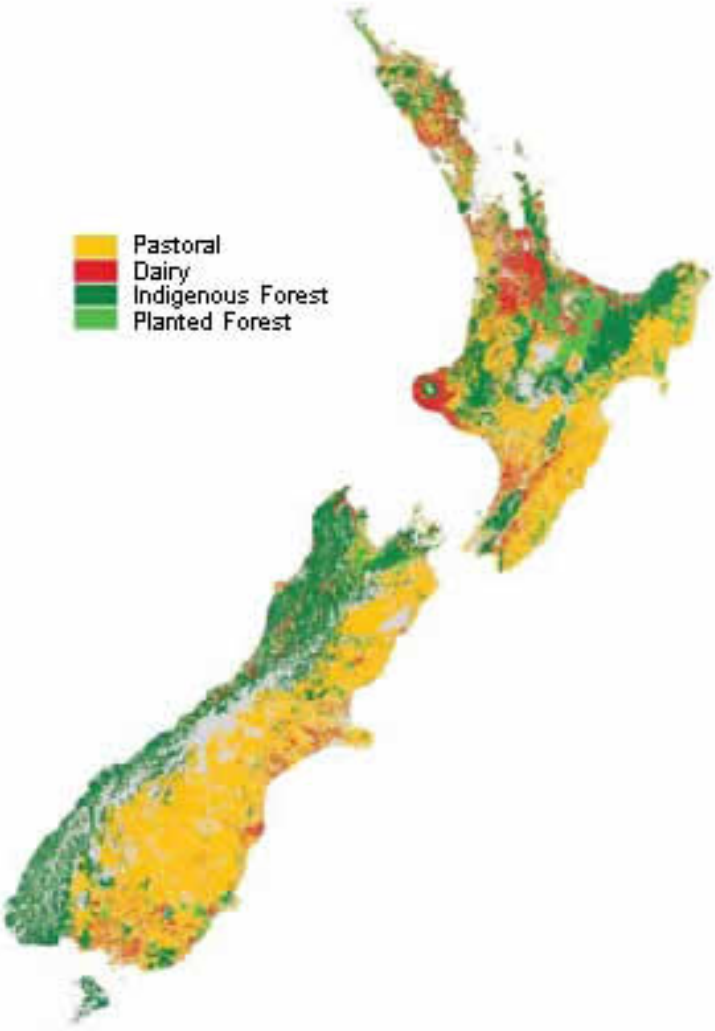

Figure 9: Prominent land use map of New Zealand (NZMAF, 2006)

3.7 Catchment Settings

Table 1 presents catchment settings for the river sediment samples, including drainage basin area, distance of the sample from headwaters, catchment average annual rainfall and uplift rates.

Table 1: Sample locations and catchment characteristics

River	Sample	Longitude	Latitude	Predominate Catchment Bedrock	Catchment Area (km^2)	Distance from headwaters (km)	Mean annual rainfall (mm/yr)	Mean annual uplift (mm/yr)[1]	Max Elevation - Headwaters (m)	Elevation - sample site (m)	Mean annual temp (°C)	Suspended Sediment Yield (Mt/yr)[2]
Awatere	**NZR24**	174°04'26"E	41°39'42"S	Greywacke	1525	88	939	3.6	1800	60	7.7	0.21
Clarence	**NZR19**	172°50'40"E	42°27'27"S	Greywacke	406	37	1580	2.1	1700	800	5.6	0.65
Clarence	**NZR19T**	172°50'40"E	42°27'27"S	Greywacke	406	37	1580	2.1	1700	800	5.6	-
Clarence	**NZR23**	173°50'30"E	42°06'41"S	Greywacke	3153	187	1446	3.7	1800	80	6.4	0.65
Conway	**NZR20**	173°16'32"E	42°27'44"S	Greywacke	81	12	1400	4.6	1500	300	7.8	0.22
Haast	**NZR14**	169°02'51"E	43°51'23"S	Schist	1287	80	6676	4.8	2700	10	6.3	5.93
Haast	**NZR15**	169°07'31"E	43°56'04"S	Schist	1287	73	6676	4.8	2700	20	6.3	5.93
Hapuku	**NZR22**	173°41'30"E	42°18'15"S	Greywacke	62	13	1693	6.5	2100	130	6.8	-
Kowhai	**NZR21**	173°37'11"E	42°23'16"S	Greywacke	69	20	1611	7.2	2000	50	6.8	-
Pareora	**NZR01**	171°11'54"E	44°29'35"S	Greywacke	542	43	661	0.1	1600	10	9.4	-
Poerua	**NZR12**	170°30'11"E	43°09'25"S	Schist	107	20	5197	7.4	2400	60	6.8	-
Rakaia	**NZR02**	172°01'54"E	43°44'60"S	Greywacke	2833	115	2043	2.1	2600	80	6.6	4.15
Rakaia	**NZR03**	172°02'42"E	43°44'16"S	Greywacke	2833	115	2043	2.1	2600	80	6.6	4.15
Rakaia	**NZR04**	171°39'20"E	43°31'06"S	Greywacke	2590	77	2155	2.1	2600	280	6.4	4.15
Andre (Rakaia tributary)	**NZR10**	171°39'12"E	43°19'32"S	Greywacke	1.8	2.5	1048	0.3	1600	900	7.5	-
Taramakau	**NZR08**	171°30'44"E	42°44'26"S	Schist	879	54	4476	6.6	2200	175	6.3	2.2
Taramakau	**NZR11**	171°11'53"E	42°37'43"S	Schist	461	82	5257	5.2	2200	30	7.9	2.2
Waimakariri	**NZR05**	171°35'56"E	43°01'14"S	Greywacke	284	18	4132	4.1	2200	755	4.7	3.14
Waimakariri	**NZR07**	171°33'46"E	42°56'25"S	Greywacke	24	5	4803	5.3	2400	630	4.2	3.14
Waimakariri	**NZR09**	172°03'5"E	43°21'39"S	Greywacke	2402	80	1925	1.8	2400	270	6.7	3.14
Wairau	**NZR25**	173°48'33"E	41°28'36"S	Greywacke	3556	118	1129	1.8	1700	40	8	0.78
Whataroa	**NZR13**	170°24'08"E	43°17'08"S	Schist	452	26	7584	7.4	3000	95	5.2	4.82

[1] *Uplift rates quoted from Robinson et al. (2004), except for NZR05, NZR07, & NZR10 which were derived from Wellman (1979).*

[2] *(Hicks et al. 2011)*

3.7.1 Catchments Draining Pahau Torlesse Terrane

The Wairau, Awatere, Clarence, Hapuku, Kowhai and Conway Rivers are located on the north-eastern edge of the South Island. The basement geology of these catchments is fairly uniform and predominantly consists of interbedded quartzofeldspahtic greywacke and argillite of the Pahau Torlesse Terrane. Overlying the basement geology are widely scattered alluvial deposits that have been redeposited during warmer interglacial periods. These occur amongst minor glacial deposits that are mainly concentrated to the upper Clarence and Wairau catchments (Figure 11) (Brown 1981). These glacial moraines and outwash deposits are remnants of ancient glaciers of Late Pleistocene Age (McCalpin 1992). The Awatere catchment additionally contains basaltic volcanic deposits, located along the valley and stretches, from the mid to lower catchment. Similarly the middle Clarence catchment contains minor basaltic volcanic deposits and minor limestone deposits in the middle to lower part of the catchment. A small pyroxenite pluton, intruded by syenite sills and dykes, is also located on the adjoining boundary of the Awatere and Clarence catchments (Figure 11). Similarly to the Clarence and Awatere, the Conway drainage basin includes a minor basaltic deposit, approximately 2 km from the sample site (Figure 10). Furthermore hillslope deposits are evident in the lower portion of the catchment that were also noted during field-work (Figure 10). The geological map of the area, shown in Figure 10, supports this observation, as hillslope deposits are located north of the shown sampling location.

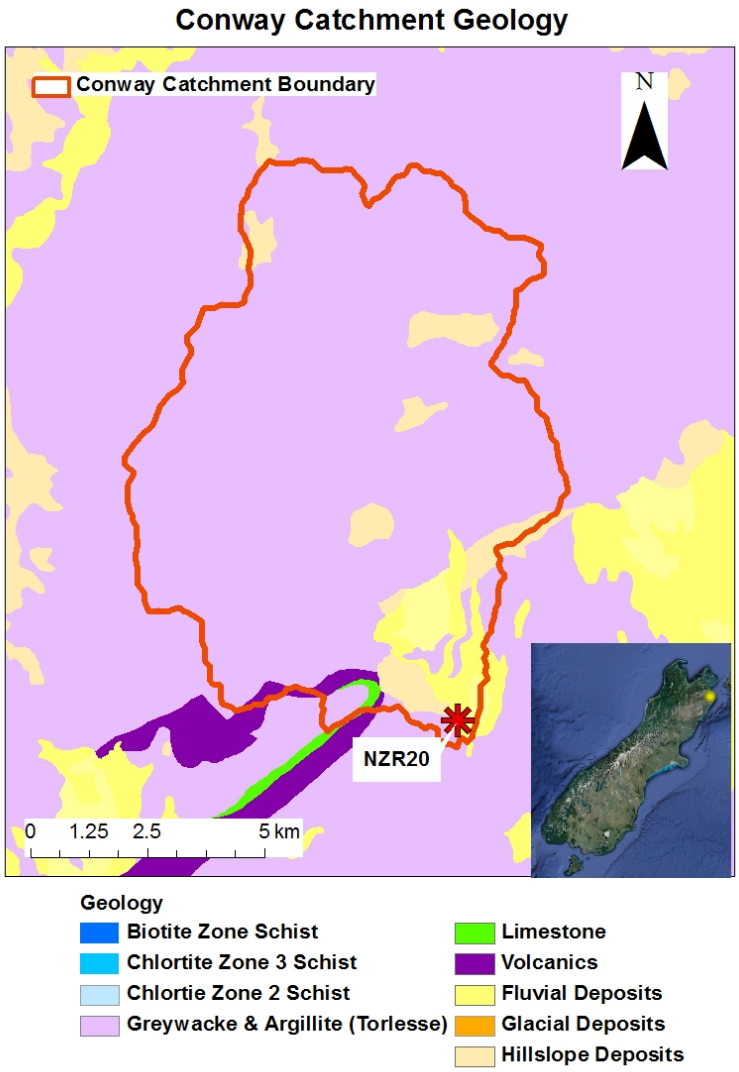

Figure 10: Simplified geological map of the Conway catchment, South Island, New Zealand. Drainage boundary is shown by the red line and the sampling location by the asterisk. Modified from Nathan (1993).

The Wairau and Clarence headwaters are located at the north-eastern extremity of the Southern Alps (Brown 1981). These rivers lie in the fault-angle depression formed along the Wairau and Clarence Faults, respectively, which are a continuation of the Alpine Fault (Brown 1981; Grapes & Wellman 1986; Christensen & Doscher 2010). The Wairau Fault separates the two sub-terranes of the Torlesse Terrane which make up the southern and northern parts of the Wairau catchment. South of the Wairau Fault, the bedrock consists of the characteristic interbedded Mesozoic greywacke and argillite of the Pahau sub-Terrane, whereas to the north the Rakaia sub-Terrane consists of Paleozoic greywacke and its metamorphic equivalent, schist (Suggate 1978; Christensen & Doscher 2010).

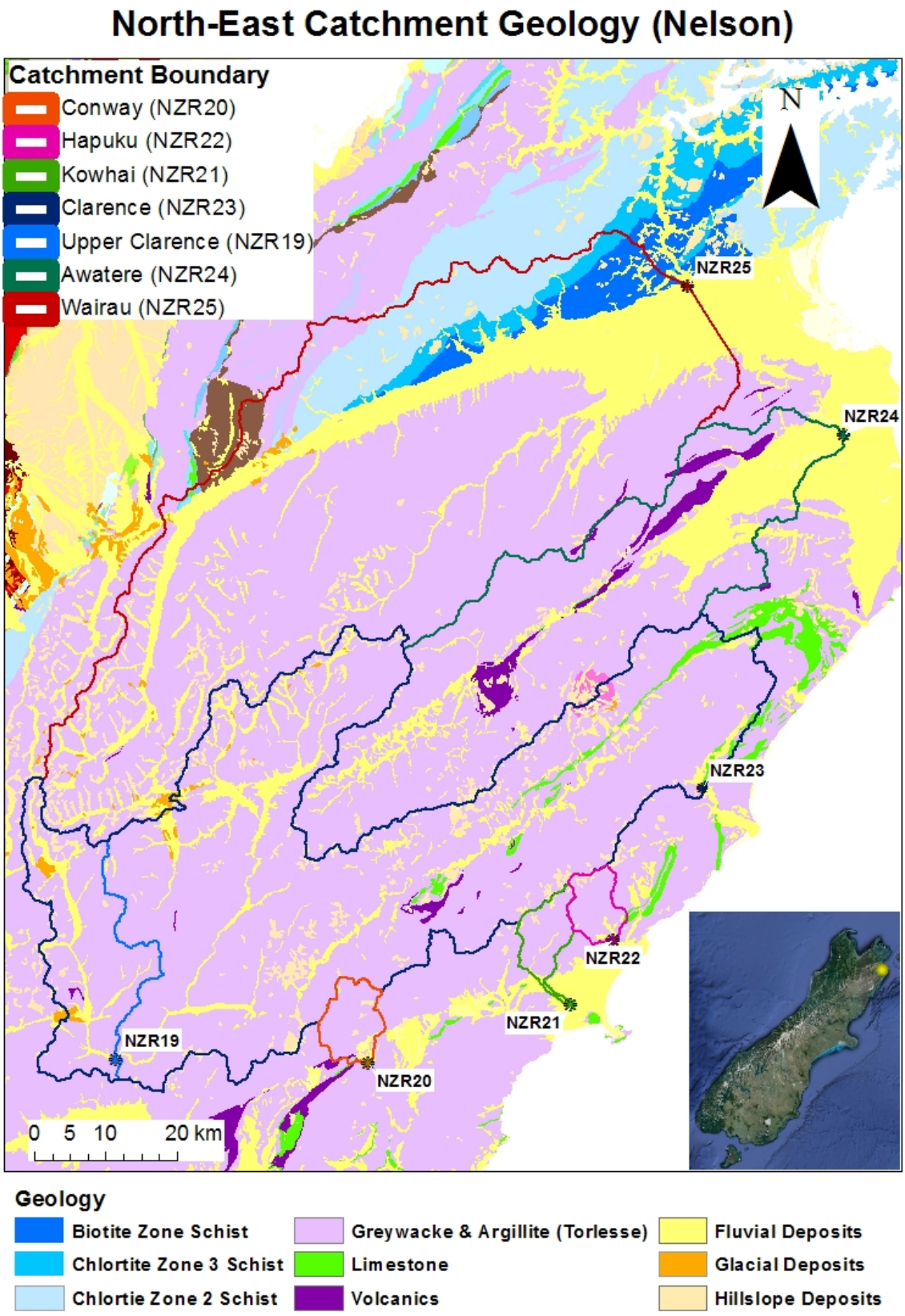

Figure 11: Simplified geological map for the north-east region of the South Island, New Zealand. Drainage boundary is shown by the solid lines and the sampling locations by the asterisk. Modified from Nathan (1993).

Similarly to the Wairau and Clarence, the Awatere flows down a fault line valley whose headwaters drain the Alpine region of the Inland Kaikoura Range. To the south, the Hapuku, Kowhai and Conway Rivers drain south-east from the Seaward Kaikoura Range. The Seaward Kaikoura Range is bounded by the extremely active Hope Fault which, Bellingham *et al.* (2005) report that, at the crest uplift rates range between 6-10 mm/yr. Consequently the Hapuku, Kowhai and Conway catchments are characterised by relatively high average uplift rates (Table 1). The plains surrounding the Kaikoura Range and the portions of the Wairau and Awatere are dominated by low-density farming (Hicks *et al.* 2011).

Figure 12: Satellite image of the Inland and Seaward Kaikoura Range separated by the Clarence Valley. Sample sites are indicated by yellow dots. Vertical exaggeration is equal to 2 (GoogleEarth, 2012).

3.7.2 Catchments Draining Rakaia Torlesse Terrane

Rakaia and Waimakariri Rivers

The Rakaia and Waimakariri Rivers are large braided alpine rivers that flow south-easterly from the topographic divide of the Southern Alps to the Pacific Ocean and are relict glacial systems (Griffiths 1979; Shulmeister *et al.* 2010). The upper portions of these catchments are characterised by mountainous topography where the headwaters flow through narrow glacial-moulded trough valleys (Griffiths 1979). The geology of the middle and upper Rakaia and Waimakariri consists of Rakaia Torlesse Terrane interbedded greywacke and argillite (Nathan 1993). Wilson (1985) has reported that discharge, sediment transport, aggradation and degradation of these rivers is controlled almost entirely by its area of catchment located on the slopes of the Southern Alps. The lower proportions of the Rakaia and Waimakariri catchments consist of fluvial deposits and are located in the Canterbury Plains (Figure 13 and Figure 14). Previous glaciations has deposited scattered glacial and glacio-fluvial deposits over the catchments (Griffiths 1979; Nathan 1993). Depositional landforms, such as moraines, terraces and fans, are additionally well developed in these basins (Tonkin & Basher 1990).

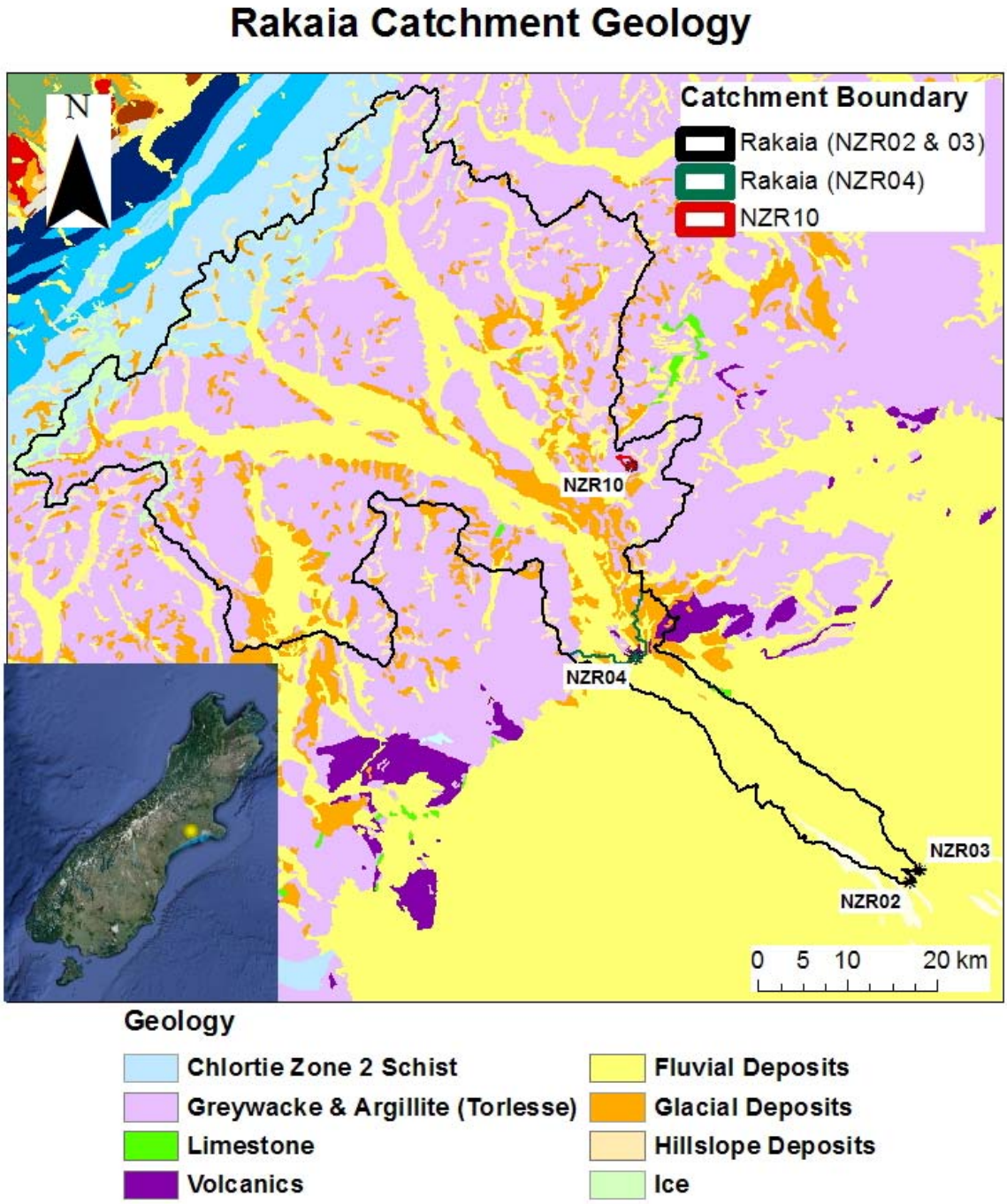

Figure 13: Simplified geological map for the Rakaia catchment, South Island, New Zealand. Drainage boundary is shown by the solid lines and the sampling locations by the asterisk. Modified from Nathan (1993).

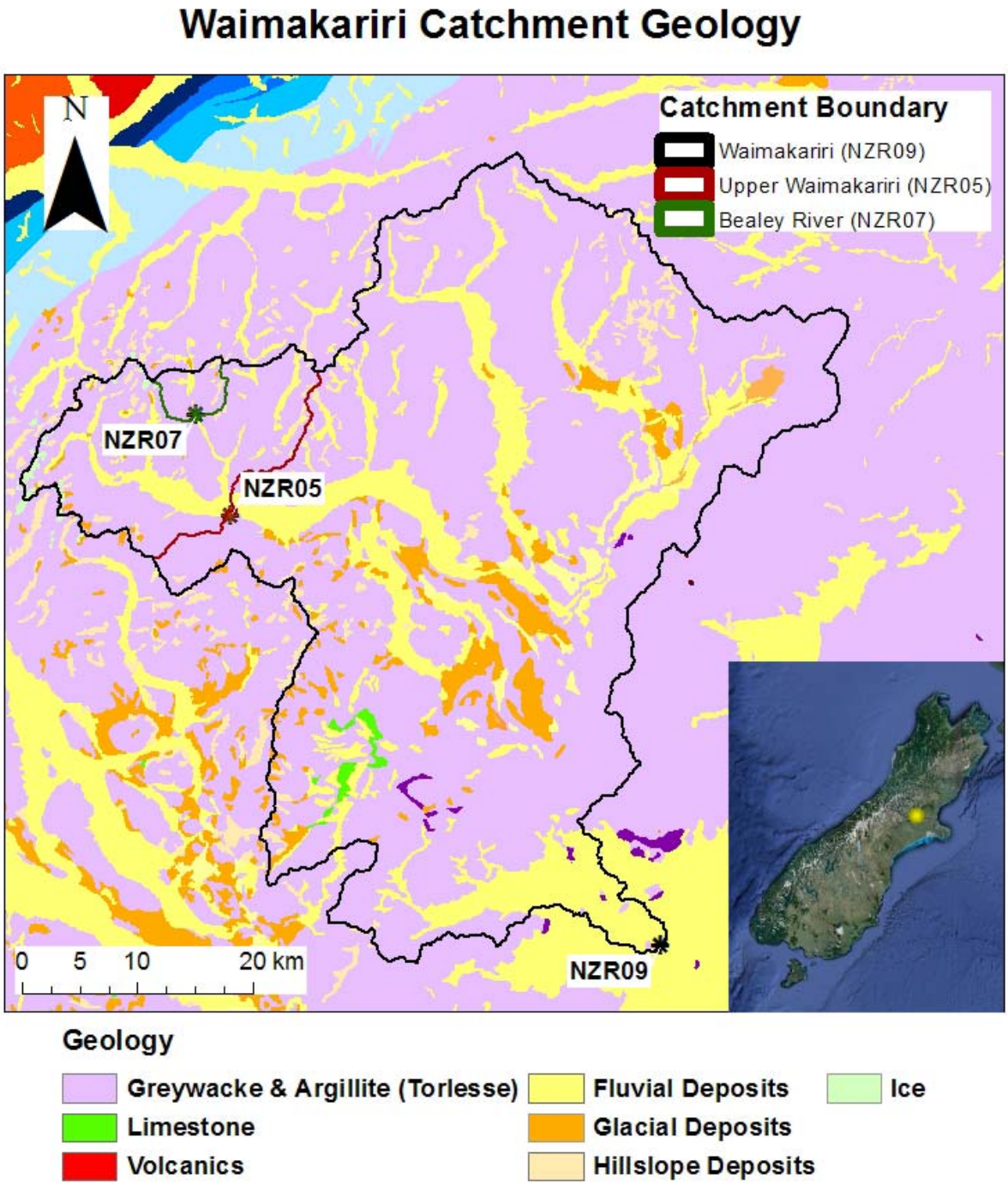

Figure 14: Simplified geological map for the Waimakariri catchment, South Island, New Zealand. Drainage boundary is shown by the solid lines and the sampling locations by the asterisk. Modified from Nathan (1993).

Pareora River

The Pareora River is a medium sized hill-fed river which flows through rolling hills in the upper and middle catchments, opening out into a flat alluvial valley in the lower catchment (LWNZ 2010). The underlying geology is predominantly moderate indurated greywacke and argillite of the Rakaia Torlesse Terrane (Figure 15) (Nathan 1993). This basement geology is overlain in the lower and middle catchment by Late Pleistocene to Holocene fluvial deposits, consisting of weathered greywacke and Middle Pleistocene loess deposits (Nathan 1993). Additionally the middle portion of the catchment contains scattered limestone deposits and low grade Chlorite zone 2 greenschist (Nathan 1993).

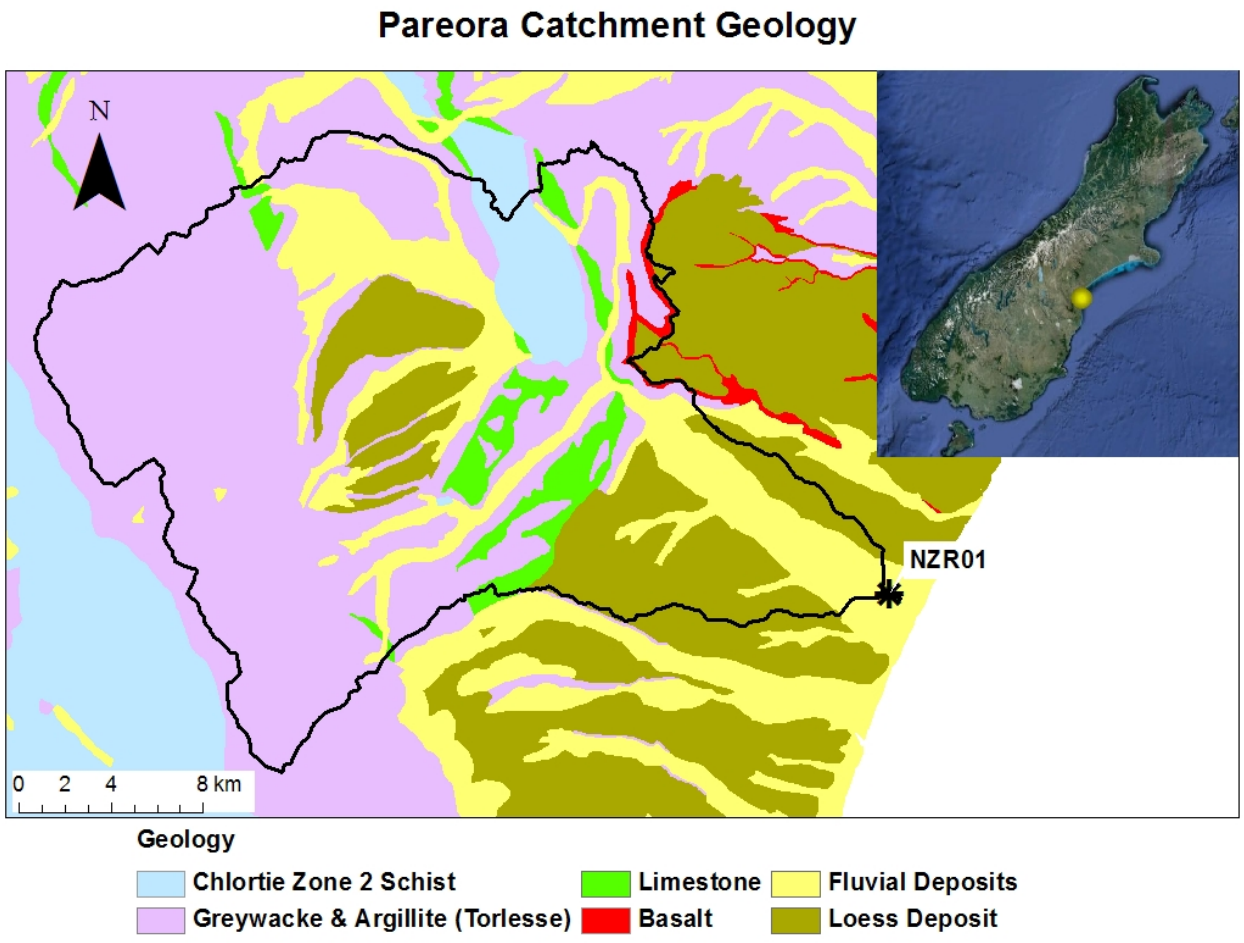

Figure 15: Simplified geological map for the Pareora catchment, South Island, New Zealand. Drainage boundary is shown by the solid black line and the sampling location by the asterisk. Modified from Nathan (1993).

3.7.3 Catchments Draining Haast Schist

Peorua and Whataroa Rivers

The Peorua and Whataroa Rivers are north-westerly draining fluvial systems whose headwaters are located at the Southern Alps. The geology of these drainage basins is defined as Haast Schist, however, the metamorphic grade varies between the two catchments (Figure 16) (Nathan 1993). The Peorua drains solely the higher metamorphic grade Biotite and Garnet-Oligoclase Zone schists. However, the lower portion of the sampled catchment passes through Holocene fluvial deposits, which are composed of unweathered schist-derived gravels (Nathan 1993). In contrast, the Whataroa drains all metamorphic grades of the Haast Schist (Figure 16). The basement geology of the lower Whataroa is located in the higher Garnet-Oligioclase Zone which grades into the Biotite Zone and then to the low grade Chlorite schist at the headwaters, as shown in Figure 16. Scattered throughout the Whataroa catchment are Holocene fluvial, hillslope and glacial deposits of predominantly an unweathered nature. At the Southern Alps ridge, the upper Whataroa catchment is influenced by current snow cover (Figure 16).

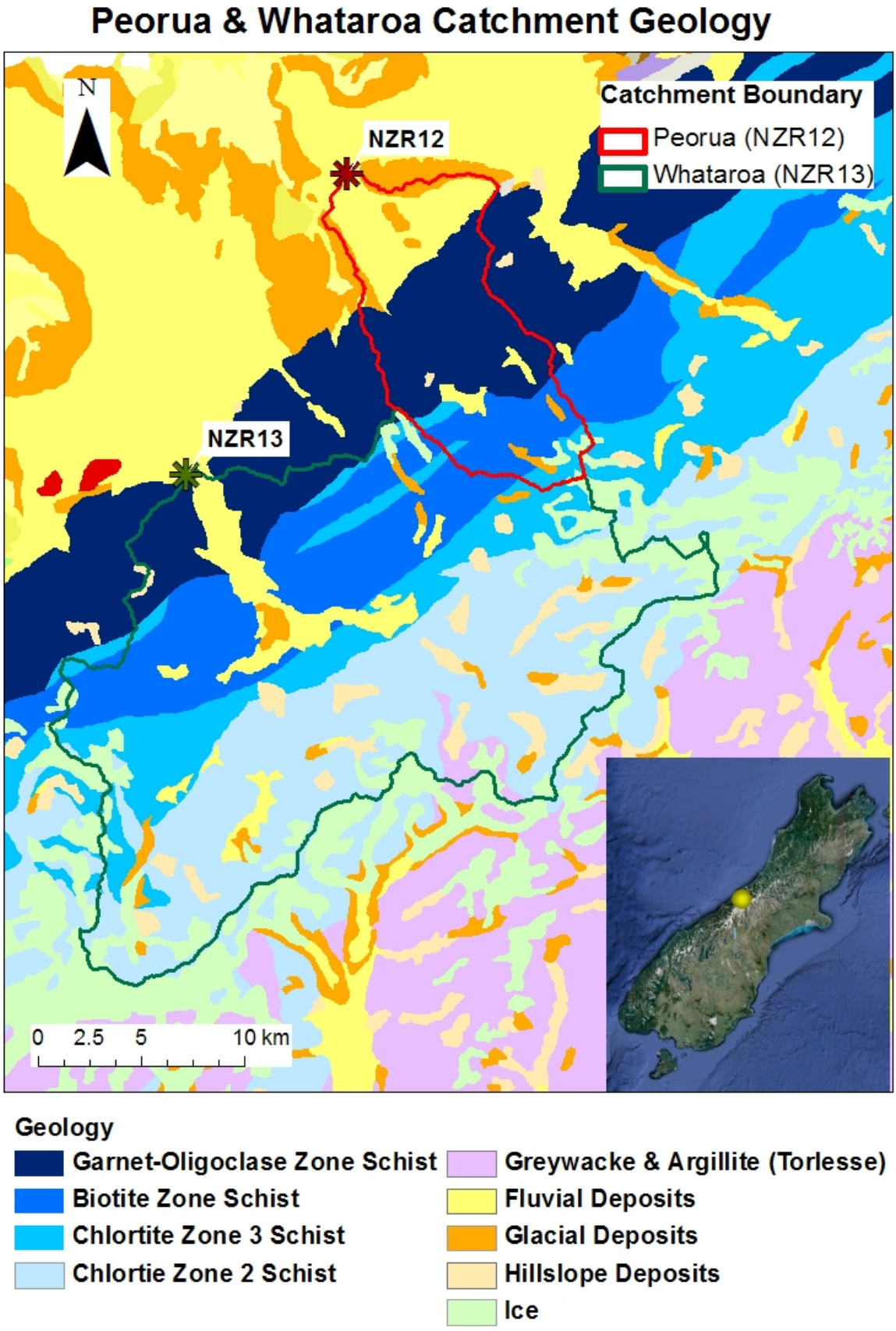

Figure 16: Simplified geological map for the Peorua and Whataroa catchments, South Island, New Zealand. Drainage boundary is shown by the solid lines and the sampling locations by the asterisk. Modified from Nathan (1993).

Taramakau River

Unlike the Whataroa or Peorua catchments, the Taramakau has more diverse basement geology. The headwaters of the Taramakau River drain Mesozoic interbedded quartzo-feldspathic greywacke and argillite of the Rakaia Torlesse Terrane (Figure 17). Downstream, the river drains the Haast Schist of predominantly chlorite grade, whereby higher grade Garnet to Oligoclase Zone schist occupies approximately a 2 km stretch of the 12-15 km wide metamorphic belt (Nathan 1993). The lower portion of the catchment hosts the granodiorite Hohonu Batholith intrusion which is located amongst Holocene postglacial alluvium gravel and sand deposits, as seen in Figure 17 (Waight *et al.* 1998). Near the sampling location of the Taramakau River are found anthropogenic dredge tailings and sluiced ground mining waste (Nathan 1993).

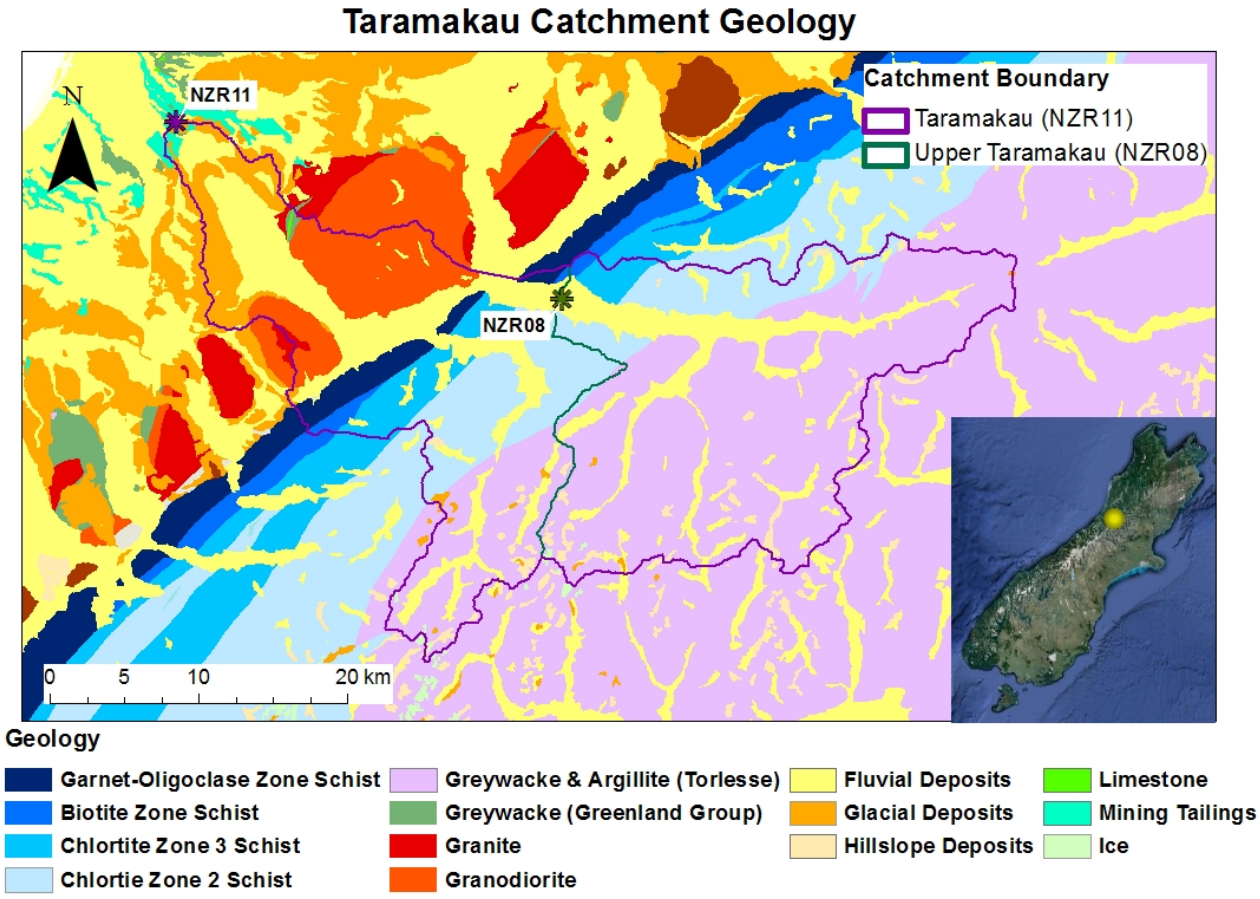

Figure 17: Simplified geological map for the Taramakau catchment, South Island, New Zealand. Drainage boundary is shown by the solid lines and the sampling locations by the asterisk. Modified from Nathan (1993).

Haast River

The Haast River is the steepest river on the South Island, whereby its tributaries drain towards the west from the central axis of the Southern Alps to the Tasman Sea (Kautz & Martin 2007). Similarly to the Whataroa River, the Haast River is hosted in the regionally metamorphosed quartofeldspathic Haast Schist. The headwaters of the Haast River are located in the Chlorite zone of the schist, whereas the lower regions of the valley are underlain by higher grade Biotite and Garnet-Oligoclase zone schists. The higher elevations in the Haast River headwaters have previously undergone glaciations and have scattered snow cover (Hicks *et al.* 2011).

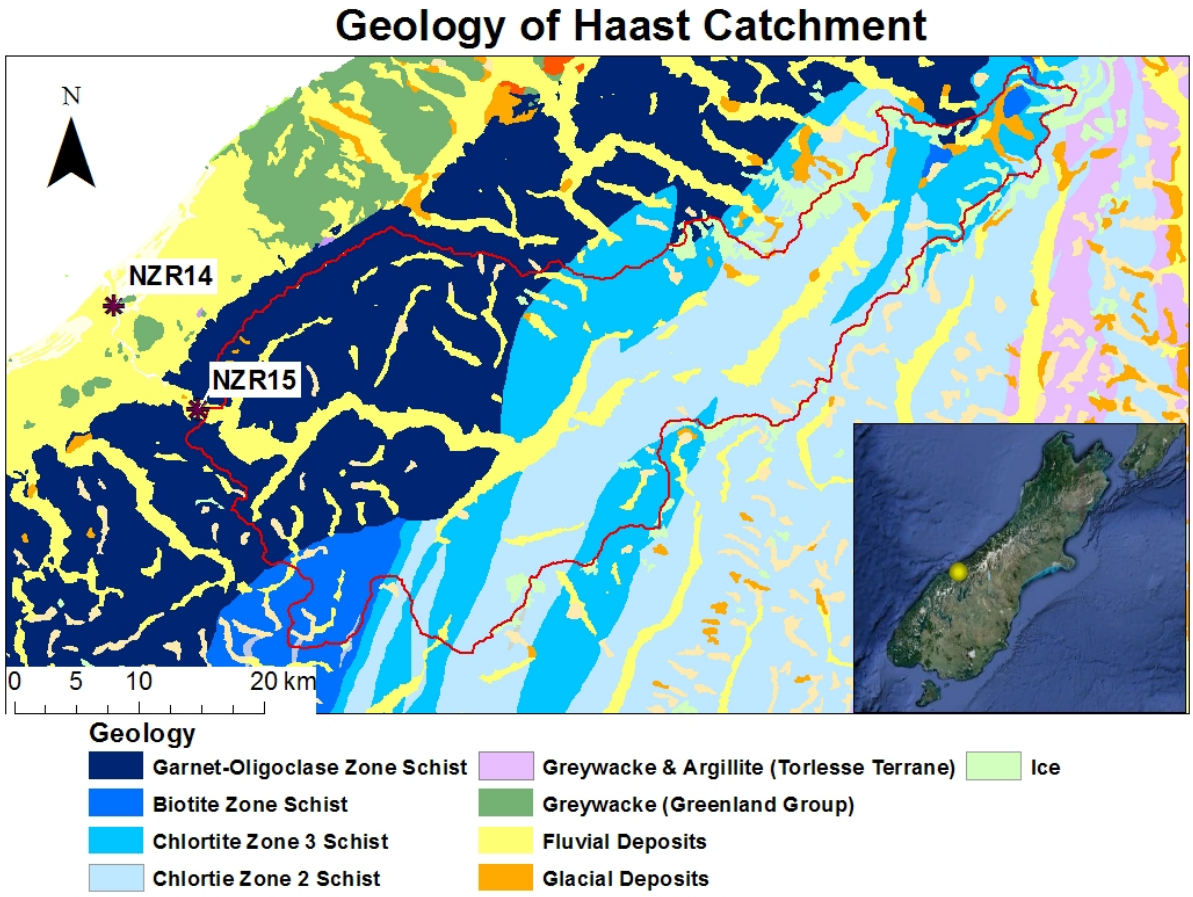

Figure 18: Simplified geological map for the Haast catchment, South Island, New Zealand. Drainage boundary is shown by the solid red line and the sampling locations by the asterisk. Modified from Nathan (1993).

Chapter Four: Methods

4.1 Site Selection and Sampling Technique

Field work and sample collection was conducted by Anthony Dosseto and Zachary Swander from the 5th to 13th of February 2011. Fluvial sediments were sampled from catchments, which captured a range of rainfall and uplift rates. 25 fluvial sediment samples were collected from sandy gravel point bars which are considered to be deposits at waning phase of high water flow and therefore are representative of active catchment scale erosion (Gaillardet *et al.* 1999). 21 of these samples were composite samples (approximately 1 kg of sediment) whereby handfuls were taken from 50 m to 200 m transects along and across point bars to ensure sediment was spatially representative. The other two samples, NZR02 and NZR03, were collected from alluvial flats of the sand bar, from a 10m by 10 m area. One alluvial terrace deposit (NZR19T) was sampled from a terrace adjacent to the upper Clarence River sediment (NZR19). This sample was collected below the vegetation trail, by digging out the first 10 cm in the deposit and collecting the sediment below. All sediment samples were stored in resealable LDPE plastic bags. Sample site locations are recorded in Table 1.

4.2 Sample Pre-Processing

The 25 sediment samples were firstly dried in an oven at 60°C. The sediment was homogenized and representative 20 g aliquots were obtained using a Civilab™ sample splitter with 12.7 mm chutes. For each sample, one 20 g aliquot was crushed to a fine powder, using a TEMA chromium-ring grinding mill at the School of Earth and Environmental Sciences, University of Wollongong. This ground aliquot was used for mineralogical (x-ray diffraction) and geochemical (major, trace elements, strontium and uranium-series isotopes) analyses. For each sample, another 20 g aliquot, was used for petrological and grain size analyses.

To investigate whether hydraulic sorting had an effect on the mineralogy of grain size fractions, another 20 g aliquot, for three samples, were sieved into six or seven grain size fractions and were individually analysed for mineralogical (x-ray diffraction) and trace geochemistry content. For further these analyses, NZR02, NZR15 and NZR25 were chosen as they covered a range of average rainfall and uplift rates of (2043 mm/yr & 2.1 mm/yr), (6676 mm/yr & 4.8 mm/yr) and (1129 mm/yr & 1.8 mm/yr) and are spread across the South Island, New Zealand. The NZR02 and NZR15 sediment samples were separated into <63 μm, 63 – 125 μm, 125 – 180 μm, 180 – 250 μm, 250 – 500 μm and >500 μm grain size fractions, using stainless steel sieves and a mechanical shaker. Whereas NZR25 was separated into <63 μm, 63 – 125 μm, 125 – 180 μm, 180 – 250 μm, 250 – 355 μm, 355 – 500 μm and >500 μm grain size fractions, using stainless steel sieves and a mechanical shaker. Sieves were cleaned with a combination of brushes and compressed air between each sample. These fractions were firstly weighed and then ground to a powder manually with an agar mortar and pestle. The mass of each grain size fraction is recorded in Appendix A, Table 5.

4.3 Grain Size Analysis

Grain size distribution was determined using a Malvern Mastersizer 2000 at the School of Earth and Environmental Sciences, University of Wollongong. Approximately 5 g of sediment sample was weighed and then passed through a 2 mm sieve. The mass of the grain size fraction >2 mm and <2 mm was recorded and then used to quantify the percentage of coarse sand (>2 mm). The sieved samples were firstly sonicated for 15 seconds, to breakup individual sediment clasts, before passing through the Malvern Mastersizer 2000. For each sample, grain size distribution was determined from the average of three consecutive measurements. Results were exported as percentage of sand (63 – 2000 μm), silt (3.9 – 63 μm) and clay (<3.9 μm). These percentages were then recalculated to include the sieved coarse sand (>2mm) fraction and are recorded in Appendix B.

4.4 Petrological Analysis

25 standard thin sections were prepared from the bulk sediment samples and three Haast Schist bedrock samples, at the School of Earth and Environmental Science, University of Wollongong. Sections were analysed on a Leica DM2500 petrologic microscope to identify and quantify primary minerals, mineral sorting and shape. Descriptions of individual thin sections were recorded and are tabulated in Appendix J. Photomicrographs were additionally taken of notable or characteristic features, using a Lecia DFC400 camera at the University of Wollongong.

200 points were counted in each thin section, using the Gazzi Dickinson point counting method (Dickinson 1970a; Dickinson *et al.* 1983; Suttner & Basu 1985) in order to quantify mineral composition. A slide advance mechanism was used at a 90 μm interval. Constituent fragments of the sediment were classified into monocrystalline quartz, polycrystalline quartz, metamorphic quartz, feldspar, plutonic fragments, volcanic fragments, sedimentary lithic fragments (further classified into mudstone, chert, siltstone and sandstone), schist, phylite, chlorite, biotite, amphibole, muscovite and calcite.

4.5 Mineralogical Analysis

Mineralogical analysis was performed by X-ray diffraction (XRD) whereby the powdered sample consists of fine grains of single crystalline minerals. This technique operates by emitting X-ray radiation of a fixed wavelength, onto a powdered sample. The radiation interacts with the electrons in the atoms resulting in scattering of the radiation. For crystalline minerals, when the distances between the atoms are of the same magnitude as the wavelength of the X-rays, the interference will be constructive and destructive, resulting in detraction at characteristic angles based on the inter-atomic spacing (Dutrow & Clark 2012). When the diffraction pattern and the intensity of the reflected radiation is recorded by a goniometer, it shows scattering peaks which correspond to the various atomic spacing in the crystal lattice (Barthelmy 2010; UCSB 2012). The positions and intensities of the peaks are then used to identify the mineral and weight percentage (wt%).

Preparation and analyses were performed at the School of Earth and Environmental Science, University of Wollongong, as per the school's Standard Operating Procedure for XRD (2012). The 25 bulk and 19 grain size fraction powdered samples were analysed using a Phillips 1150 PW Braggs-Brentano diffractometer with CuKα radiation. Mineralogical phases were identified from XRD data using TRACES4 software, which matches diffraction peaks to reference peaks. Quantitative analyses of the mineral phases in each sample were obtained using Siroquant™ software, with accuracy measured in chi-squared proportions and are presented in Appendix A and Appendix C.

4.6 Major and Trace Elemental Analysis

Major and trace element concentrations were determined using X-ray fluorescence (XRF) spectrometry. Preparation and analysis was performed at the School of Earth and Environmental Sciences, University of Wollongong, as per the school's Standard Operating Procedure for XRF Analysis (2012). The apparatus operates on the principles of wavelength-dispersive spectroscopy, similar to that of XRD, to determine both major and trace elements in the sediments. When the X-ray radiation interacts with the atoms, electrons from the inner shells are ejected (Blake 2012). Consequently the electrons from the outer shells move to the inner shells to occupy the vacant positions (Blake 2012). This results in the atom returning to a more stable (ground) state and in the process releases X-rays. Each element emits a characteristic X-ray that can be used for qualitative and quantitative compositional analysis of the sample (Blake 2012).

25 powdered bulk sediment samples, two duplicate samples, 19 powdered grain size fraction samples and three USCS standards were prepared into pressed pellets for trace element analysis. This was done by mixing approximately 5 g of sample with a PolyVinyl Acetate (PVA) binder and pressing into an aluminium cap, at approximately 2500 psi. Pressed pellets were dried in a 65°C oven for 24 hours to remove moisture before being weighed. Inefficient sediment weight was obtained for three grain size fractions (>500 for NZR15 and the <63 μm fraction for NZR02 and

NZR25). These three grain size fractions were therefore diluted with powdered 100% silica dioxide (SiO_2), before being mixed with the PVA binder to obtain sufficient weight for analysis. The grain size fractions, NZR25 <63 μm and NZR15 >500 μm, were diluted by a factor of two, to increase the sample weigh to approximately 3 g and 5 g respectively. The grain size fraction NZR02 <63 μm was diluted by factor of three to increase the sample weight to approximately 3 g.

23 powdered bulk sediment samples, two duplicate samples and three standards were prepared into glass buttons for major analysis. Glass buttons were fused using a pure 100% metaborate flux for high silica (>65% SiO_2) samples. Approximately 300 mg of sample was mixed with 2.4 g of flux. Samples were then heated from 600°C to 950°C gradually over one hour, in platinum crucibles. An iodine (NH_4I) pellet was added to the molten sample to reduce viscosity prior to pouring and pressing the sample on a graphite disc.

Analysis was performed using a SPECTRO XEPOS energy dispersive polarization XRF spectrometer, while deconvolution of the spectra and conversion of X-ray intensities was performed using Ametex Materials-Analysis Division proprietary software. Accuracy was controlled by calibration of the instrument against a wide range of natural rock standards and synthetic materials. Measurement of precision and accuracies, based on the three USCS standards are reported in Table 2 and Table 3.

The trace elemental data for the grain size fractions 250 – 355 μm and 355 – 500 μm for NZR25 were recalculated by mass into a 250 –500 μm fraction, in order to directly compare results with the 250 –500 μm fraction of NZR02 and NZR15.

Due to operational failure of the XRF spectrometer during the study, NZR12 and NZR19 were not analysed for major element content.

Table 2: Precision and accuracies for major element XRD analysis based on USCS standards. Bold values for standards indicate measurement is within error of the accepted value. Dash indicates that no value was suggested.

(wt%)	Na_2O	MgO	Al_2O_3	SiO_2	P_2O_5	K_2O	CaO	TiO_2	MnO	Fe_2O3
RSD (n=4)	1.57×10^{-1}	8.45×10^{-2}	2.75×10^{-2}	3.07×10^{-3}	1.05×10^{-1}	1.01×10^{-2}	5.83×10^{-3}	8.71×10^{-3}	1.32×10^{-2}	8.51×10^{-3}
BRC-2	2.96	**3.63**	14.62	**54.86**	0.43	**1.82**	**7.05**	**2.26**	0.18	13.31
	3.16 ± 0.11	**3.59 ± 0.05**	13.5 ± 0.02	**54.1 ± 0.8**	0.35 ± 0.02	**1.79 ± 0.05**	7.12 ± 0.11	**2.26 ± 0.05**	-	13.8 ± 0.2
W-2a	1.84	6.73	16.82	53.69	0.19	0.68	**10.93**	**1.06**	0.15	10.56
	2.2 ± 0.037	6.37 ± 0.058	15.45 ± 0.16	52.68 ± 0.29	0.14 ± 0.12	0.626± 0.012	**10.86 ± 0.078**	**1.06 ± 1.01**	0.167 ± 0.004	10.83 ± 0.21
QLO-1	3.16	0.92	17.94	66.92	0.30	**3.55**	**3.15**	**0.61**	0.09	4.19
	4.2 ± 0.13	1 ± 0.07	16.2 ± 0.19	65.6 ± 0.47	0.25 ± 0.02	**3.6 ± 0.12**	**3.17 ± 0.08**	**0.62 ± 0.03**	-	4.35 ± 0.14

Table 3: Precision and accuracies for trace element XRD analysis based on USCS standards. Bold values for standards indicate measurement is within error of the accepted value. Dash indicates that no value was suggested.

(ppm)	Ni	Zn	Rb	Sr	Y	Zr	Nb	Ba	Pb	Th	U
RSD (n=4)	5.15×10^{-2}	2.72×10^{-2}	4.97×10^{-3}	1.62×10^{-3}	3.24×10^{-3}	1.65×10^{-2}	1.20×10^{-2}	1.64×10^{-2}	7.08×10^{-2}	4.17×10^{-2}	1.89×10^{-1}
BCR-2	7	**126**	**50**	**344**	**39**	**188**	13	**682**	**10**	7.1	3.1
	-	**127 ± 9**	**48 ± 2**	**346 ± 14**	**37 ± 2**	**188 ± 16**	-	**683 ± 28**	**11 ± 2**	6.2 ± 0.7	1.69 ± 0.19
W-2a	62	77	**20**	198	**23**	91	7	**178**	8	1.9	2.1
	70 ± 2.5	80 ± 2	**21 ± 1.1**	190 ± 3	**23 ± 1.6**	100 ± 4	-	**170 ± 11**	-	2.4 ± 0.1	-
QLO-1	< 1	**64**	**72**	**340**	**26**	**195**	**10**	1496	23	3.7	3.7
	-	**61 ± 3**	**74 ± 3**	**340 ± 12**	**24 ± 3**	**185 ± 16**	**10 ± 1.3**	1370 ± 80	20 ± 0.8	4.5 ± 0.5	1.9 ± 0.12

4.7 Loss on Ignition

Loss on ignition was determined for the 25 powdered bulk samples and three USCS standards at the School of Earth and Environmental Sciences, University of Wollongong, as per the school's Standard Operating Procedure for LOI (2012). Approximately 1 g of powdered sample was ashed in a ceramic crucible for approximately two hours, in a temperature controlled furnace at 1050°C. During this process, volatile substances (hydrates, labile hydroxyl-compounds and carbon dioxide from carbonates) escape the sample (Donkin 1991). The loss of mass of sample was determined by weighing the samples in the crucible before and post ignition (after cooling). The difference in ashed and initial weight was converted to percentage loss on ignition.

4.8 Isotopic Analysis

Bulk sediment samples were prepared for U–series and Sr isotopic analysis in the Wollongong Isotope Geochronology Lab, University of Wollongong, as per the Laboratory Procedure for Uranium- and Strontium-Series Isotope Sample Preparation (Dosseto 2012). Isotopic analysis of primary minerals was performed for 25 powdered bulk sediment samples. Precision was assessed by duplicate analysis of two samples. Accuracy was assessed by duplicate analysis of USGS QLO-1 rock standard. Two total procedure blanks were also prepared for both U-series and Sr isotope sample preparation.

Approximately 5 g of sample was placed in a quartz crucible and ashed to 450°C overnight in a furnace, to burn off organic matter. This was performed to remove organic matter, as the primary mineral isotopic composition was required. The loss of mass of the ashed sample was determined by weighting the crucible and sample before and post-ignition. The samples were then leached with magnesian nitrate, rinsed with 18.2MΩ water and dried at 60°C to remove exchangeable cations which were previously bound to organic matter. In addition, aliquots of samples NZR03 and NZR23 underwent leaching with 1M sodium acetate to leach carbonates from the samples to ensure that the isotopic ratio which is measured, is of the primary minerals only.

Approximately 0.1 g of powder was weighed and a weighed amount of ^{236}U- ^{229}Th tracer solution (approximately 0.03 g) was added in order to determine U and Th concentrations. The sample-tracer mixture was then digested in PFA vials in 3 mL of 30% Merck Suprapur™ HCl, 2 mL of 65% Merck Suprapur™ HNO_3, 1 mL of 70% Merck Suprapur™ $HClO_4$ and 2 mL of 48% Merck Suprapur™ HF at 130°C overnight. Vials were then opened and left at 100°C to evaporate HCl, HNO_3, HF and drive off fluorides (mainly AlF_3, CaF_2 and MgF_2). The remaining solution was then dried down by stepwise heating at 150°C, 170°C and finally 200°C until incipient dryness occurred. Approximately 15 drops of 69% HNO_3 were then added and dried down at 100°C. This was performed twice before taking the sample up in 2 mL of 1.5M HNO_3 at 100°C for 30 minutes.

After acid digestion was performed, 16 samples and one of the QLO-1 standards still showed some suspension and therefore further digestion was performed. These samples were firstly dried down at 100°C, then heated for six hours at 96°C with 2 mL of 0.04M Merck Suprapur™ NH_2OH-HCl in 25% (v/v) acetic acid to dissolve Fe- and Mn-oxides. Dissolution was found to be complete for 11 of the samples and the QLO-1 standard, which were then taken up in 0.5 mL of 65% Merck Suprapur™ HNO_3 and dried down twice before re-dissolution in 2 mL of 1.5M Merck Suprapur™ HNO_3 . The five samples, which were not completely dissolved, were firstly dried down before 0.3 mL of 0.02 Merck Suprapur™ HNO_3, 0.5 mL 31% H_2O_2 and a drop of 65% Merck Suprapur™ HNO_3 were added, to remove any organic matter that may have not been volatised by ashing. The samples in solution were left at room temperature for approximately 15 minutes, while H_2O_2 reacted with the organic matter. The solution was then heated to 85°C for an hour and a half, after which dissolution was complete. 0.5 mL of 65% Merck Suprapur™ HNO_3 was then added to the samples before being dried down at 100°C. This was performed twice before taking the dried sample up in 2 mL of 1.5M Merck Suprapur™ HNO_3.

Once completely dissolved in 2 mL of 1.5M Merck Suprapur™ HNO_3, samples, standards and blanks were passed through 0.25 mL of Eichrom TRU resin to separate U and Th. The resin was firstly cleaned with 3M Merck Suprapur™ HCl, 0.2M Merck Suprapur™ HCl and 0.1M Merck Suprapur™ HCl – 0.3M HF and preconditioned with 1.5M Merck Suprapur™ HNO_3. While loading the sample, the solution containing all elements except REE, U and Th (i.e. including Sr) was collected. The next volume of 1.5M HNO_3 was also collected in the same vial. Th was then eluted in 0.2M Merck Suprapur™ HCl and U in 0.1M Merck Suprapur™ HCl – 0.3M HF.

The U and Th cuts were then dried down at 80°C, before 0.5 mL 31% H_2O_2 was added to eliminate any TRU resin that may have leaked with the U and Th cuts. The 31% H_2O_2 solution was then evaporated at 80°C. A drop of 65% Merck Suprapur™ HNO_3 was added before drying down at 80°C. Residues were then re-dissolved in 3 mL of 2% Merck Suprapur™ HNO_3 and sonicated for fifteen minutes to ensure complete re-dissolution. Solutions were screened for U and Th contents on an Agilent 7500 quadrupole ICP-MS at the University of Wollongong. Solutions were then diluted in order to obtain required concentrations of U and Th (typically 4 and 20 ppb, respectively) before isotopic analysis by multi-collector ICP-MS at the Australian National University. U and Th concentrations were determined by isotopic dilution and measurement of the $^{236}U/^{238}$ and $^{229}Th/^{232}Th$ ratios, respectively. $^{234}U/^{238}U$ and $^{230}Th/^{232}Th$ were also measured and the $^{230}Th/^{238}U$ ratio calculated using measured $^{230}Th/^{232}Th$ and U and Th concentrations. ^{234}U, ^{236}U, ^{230}Th and ^{229}Th were collected on a secondary ion multiplier (SEM) while ^{238}U, ^{235}U and ^{232}Th were collected on Faraday cups. Mass fractionation and SEM/Faraday cup yield were determined by measuring synthetic standards between each sample (New Brunswick Laboratory U010 for U and The Open University Th'U' for Th). ^{232}Th tail contribution on ^{230}Th was corrected using an offline exponential tail correction by measuring background signal at masses 231.5, 230.5, 229.5 and 228.5.

The solution collected from the U-Th column chromatography that contained all elements except REE, U and Th (i.e. including Sr) was dried down at 80°C and then taken up in 2 mL of 2M Merck Suprapur™ HNO_3. It was then passed through a column containing 0.2 mL of Eichrom Sr resin over 0.1 mL of Eichrom pre-filter resin. The resins were cleaned with 0.02M Merck Suprapur™ HNO_3, 8M Merck Suprapur™ HCl and 0.02M Merck Suprapur™ HNO_3 and preconditioned with 2M Merck Suprapur™ HNO_3, prior to sample loading. Sr was eluted in 0.02M Merck Suprapur™ HNO_3. Sr cuts were dried down at 80°C and then taken up in 3 mL of 2% Merck Suprapur™ HNO_3. They were then screened on an Agilent 7500 quadrupole-ICPMS at the University of Wollongong, in order to assess how much Ca and Rb remained in the Sr cut after chromatography. This analysis showed that column chromatography had removed 80% of Ca and 99.9% Rb. As these ions interfere with Sr analysis, Sr column chromatography was performed again to reduce the Ca and Rb content further (to 4% and 0.01%, respectively).

Blank measurement was undertaken on an Agilent 7500 quadrupole-ICPMS, at the University of Wollongong. The first blanks processed contained as much as 65 ng of Sr, although this would not impact our analyses because typically 25.5 µg (25,500 ng) of Sr were processed, it was decided to subsequently use Merck Ultrapur™ grade (ppt level) of reagents instead of the Merck Suprapur™ grade (ppb level), for the second Sr column chromatography. Blanks for Sr contributed typically 0.2% and were considered negligible. Blanks with a similar proportion of Sr were also reported by Goldstein and Jacobson (1988).

$^{87}Sr/^{86}Sr$ ratios were measured by multi-collector ICP-MS on a ThermoFisher Neptune at the Australian National University. Accuracy was checked by measuring synthetic standard SRM 987.

External analytical uncertainty is 10% for U, 0.7% $^{234}U/^{238}U$and 0.005% $^{87}Sr/^{86}Sr$ (n=4). Measurements of the certified USGS rock standard QLO-1 previously analysed in the literature were also performed and results indicate that the standard measurement of U and Th within error of the recommended value (1.92, 1.9 ± 0.12 and 4.74, 4.5 ± 0.5, respectively) (USGS 2012). Additionally results indicate that $^{234}U/^{238}U$ accuracy is within error, however, $^{230}Th/^{238}U$ is slightly lower (in secular equilibrium ratio is 1, measured value 0.973 ± 0.009). The Th, U and Sr mass from total procedure blanks in shown in Table 1.

Table 4: Total procedure blanks for U-series and Sr isotopic analysis.

Lab No.	Th (pg)	U (pg)	Sr (ng)
180	6	3	12
210	15	295	65

4.9 Geospatial Analysis

Geospatial analysis was performed using the ArcGIS software ArcMap version 10, at the School of Earth and Environmental Sciences, University of Wollongong.

4.9.1 Defining Sample Catchment Areas

Drainage boundaries of sampled catchments were based on a 50 m Digital Elevation Model (DEM) of the South Island of New Zealand, which was obtained from LINZ (Land Information New Zealand) data service. Using ArcMap, the Hydrology Fill Tool was run over the DEM surface to remove small imperfections in the data associated with cells, which have an undefined drainage direction. A raster file of flow direction was subsequently created from the filled DEM, using the Flow Direction Tool, which highlights the direction of flow from each cell to its steepest down slope neighbour. The Hydrology Flow Accumulation Tool was then applied to the flow direction data, which created a raster of accumulated flow to each cell, as determined by accumulating the weight for all cells that flow into each down slope cell.

In order to obtain the drainage boundary for each sample point, the GPS location of each sample site was imported into GoogleEarth™ as a kml file and subsequently converted to point shape files using the ArcMap conversion tool. Sample points were then exported as individual shape files, before running the Hydrology Snap Pour Point Tool on each sample point. This tool moved the pour point to the cell that had the highest accumulated flow, within a 500 m radius of the sample point. The Snap Pour Point Tool was used to ensure that the sample point was not located in a small depression within the DEM, in which case the drainage boundary identified would be smaller than the actual catchment area. The Hydrology Watershed Tool was subsequently used to identify the catchment drainage area of the sample, represented by the pour point. This produced a drainage boundary catchment area for each sample point in raster format, which was then converted to a polygon boundary.

A preliminary assessment of the accuracy of the determined drainage boundary for each sample was performed using 3D satellite images of each river in GoogleEarth™ in conjunction with the original 50 m DEM. In some instances, it was clear that the analysis of a sample's drainage boundary was inaccurate as the boundary was either very localized or did not continue to follow the river up to the headwaters (as visually observed using GoogleEarth™). Primarily this was due to the sample point being located in an area with little elevation variation whereby an accurate flow direction was not able to be determined. In such circumstances, additional points were added upstream along the path of the river ensure drainage from the headwaters was captured. The drainage boundary was then obtained for these additional points by following the same GIS analysis steps that were outlined above. The output drainage boundary was then re-analysed and compared to the river profile in GoogleEarth™, to ensure its accuracy. In some instances, whereby multiple pore points were included, the catchment boundaries, for individual points, were not joined. In such instances the catchment boundary was manually digitized to connect these segmented catchment boundaries. The drainage catchment area for each sample was determined using the statistics function in ArcMap and is displayed in Table 1 (Chapter 3).

4.9.2 Distance from Headwaters

The distance between the headwaters of each river and the sample location was calculated using the Measure Tool in ArcMap, using the flow path of the river shown in the low depression areas in the 50 m DEM (LINZ). The major tributaries for each river were measured from sample point to drainage boundary and then averaged to obtain the distance of the sample from the headwaters. The distance of each sample from the headwaters is recorded in Table 1 (Chapter 3).

4.9.3 Average Annual Temperature and Rainfall

Median annual temperature and rainfall GIS raster grids, covering the South Island of New Zealand, were provided by the New Zealand National Climate Centre, National Institute of Water and Atmospheric Research (NIWA). These data files were based on a thirty-year period from 1971 to 2000 and are characterized by a spatial resolution of 500 m. An average annual temperature and rainfall rate for each drainage catchment was extracted by using the ArcMap Zonal Statistics Tool and recorded in Table 1 (Chapter 3).

4.9.4 Average Uplift Rates

Average uplift rates for catchments were based on Wellman's uplift contour map for the South Island of New Zealand (1979). The average uplift rates for catchment boundaries for a number of sample locations over the South Island are reported in Robinson *et al.* (2004). This study derived average uplift rates, by digitizing the Wellman *et al.* (1979) contour map and comparing to topography to ensure that the decrease in uplift around the Alpine fault was located correctly. Furthermore, Robinson *et al.* (2004) used additional referenced data points, particularly in the North Canterbury and Kaikoura Mountain areas, before interpolating and extracting a mean uplift rate for the catchment area.

Average annual uplift rates for catchments were quoted from Robinson *et al.* (2004) for river sediments which were sampled within 15 km of those referenced. The samples NZR05, NZR07 and NZR10 were not within 15 km of the locations reported in Robinson *et al.* (2004). For these samples, the Wellman (1979) uplift contour map was digitized over the areas of interest. Interpolation was then performed to create a surface of annual uplift rates. An average annual uplift value for NZR05, NZR07 and NZR10 was obtained by extracting all annual uplift values, within the catchment boundary, from the interpolated surface and recording the mean value. Average annual uplift rates for the drainage catchments of the samples are recorded in Table 1 (Chapter 3).

4.9.4 Simplifying Regional Geological Map

A detailed geological map was provided as an ArcGIS map project, in vector data format, from GNS Science. Geological units were simplified using the Identify Tool and then manually reclassifying the data layer. The geological map was reclassified into greywacke and argillite (Torlesse Terrane), greywacke (Greenland Group), Chlorite zone 2 & 3 schist, Biotite zone schist, Garnet-Oligoclase zone schist, fluvial deposits, glacial deposits, hillslope deposits, loess deposits, limestone, volcanic deposits, harzburgite, granite, granodiorite and ice. Reclassification was only performed over the drainage boundaries of the sample locations.

4.10 Statistical Analysis

Statistical regression analysis was used to investigate the relationship between mobile element depletion and annual uplift and rainfall rates. Analysis was additionally performed between geochemistry, mineralogy and clast composition and significant relationships noted. Statistical analysis was performed with JMP version 9.0.0 using a Whole Model, One-Way ANOVA and Standard Least Squares as the fitting method and the F, P and R^2 values noted (Davis 2002).

Chapter Five: Results & Discussion

5.1 Mineralogical and Geochemical Analysis of Grain Size Fractions

As discussed in Section 2.1, the mineralogy and geochemistry of bulk fluvial sediments can be influenced by grain size distribution. Such grain size effects have primarily been attributed to mechanical breakdown and chemical weathering of lithic fragments, whereby minerals are preferentially concentrated in particular fractions (Johnsson & Basu 1993). This section presents and discusses the effect of grain size on mineralogy and geochemistry of three representative river sediments, NZR15 (Haast), NZR02 (Rakaia) and NZR25 (Wairau), that cover a range of average rainfall and uplift rates [(2043 mm/yr & 2.1 mm/yr), (6676 mm/yr & 4.8 mm/yr) and (1129 mm/yr & 1.8 mm/yr), respectively].

5.1.1 Mineralogy

Mineralogical X-ray diffraction results for the grain size fractions of NZR15 (Haast), NZR02 (lower Rakaia) and NZR25 (Wairau) are displayed in Figure 19. Greywacke-derived sediments, NZR02 and NZR25, show a slight concentration of quartz in the coarser grain fractions. However, in the Haast Schist-derived NZR15, quartz is largely concentrated in the > 500 μm grain size fraction. Figure 19 highlights that plagioclase dominates the feldspar content in all sediments, with K-feldspar being minor. The plagioclase content is shown to be fairly evenly distributed throughout the grain size fractions of the greywacke-derived sediments, whereas K-feldspar is randomly scattered throughout the grain size fractions. In contrast to the greywacke-derived sediments, the schist-derived NZR15, shows a general increase in plagioclase concentration with decreasing grain size and K-feldspar is concentrated (16.3 wt%) in the 63 – 125 μm grain size fraction. Similarly Kautz and Martin (2007) reported that river sediments from the Haast River were dominated by quartz, in the coarser grain fractions, and plagioclase, in the finer grain fractions.

There is a stark contrast of titanite content between the greywacke and schist-derived sediments. In the schist-derived NZR15, the only presence of titanite is in the < 63 μm grain size fraction (2.1 wt%). In comparison, titanate is well distributed throughout all grain size fractions of the greywacke-derived NZR02 and NZR25, and ranges from 1.9 to 4.4 wt%. Additionally chlorite is well distributed throughout all grain size fractions of both the greywacke- and schist-derived sediments. However, overall, NZR15 has a higher proportion of chlorite than the greywacke-derived sediments.

Similarly mica is more prominent in the schist-derived NZR15, as compared to the greywacke sediments. This can be attributed to catchment lithology, whereby NZR15 drains all metamorphic grades of the Haast Schist which are enriched in micas. Furthermore, there is no systematic variation of mica content in the grain size fractions of NZR15, however, in the greywacke-derived sediments it generally increases with decreasing grain size. Therefore there is an apparent removal of mica from sand to silt fractions in NZR25 and NZR02, suggesting a dominance of physical weathering. Mica includes minerals, such as muscovite and biotite, whose physical properties make it more prone to physical weathering and therefore more likely to be winnowed from bedload (Kautz & Martin 2007). Therefore during mechanical attrition of sand sized grains, mica is more likely to be removed from bedload sediments, leaving sands enriched in quartz and plagioclase. This pattern is not observed in NZR15, whereby there is no preferential enrichment of mica in the silt fractions over sand. Although the processes of mechanical weathering are additionally likely to be evident in the Haast, the sediment residence times are expected to be shorter, as compared to the Wairau and Rakaia Rivers. The shorter residence time for NZR15 is inferred from the higher annual rainfall and steeper gradient of the Haast River, as compared to the Wairau and Rakaia, that drain through a series of ranges and basins (Hicks *et al.* 2011).

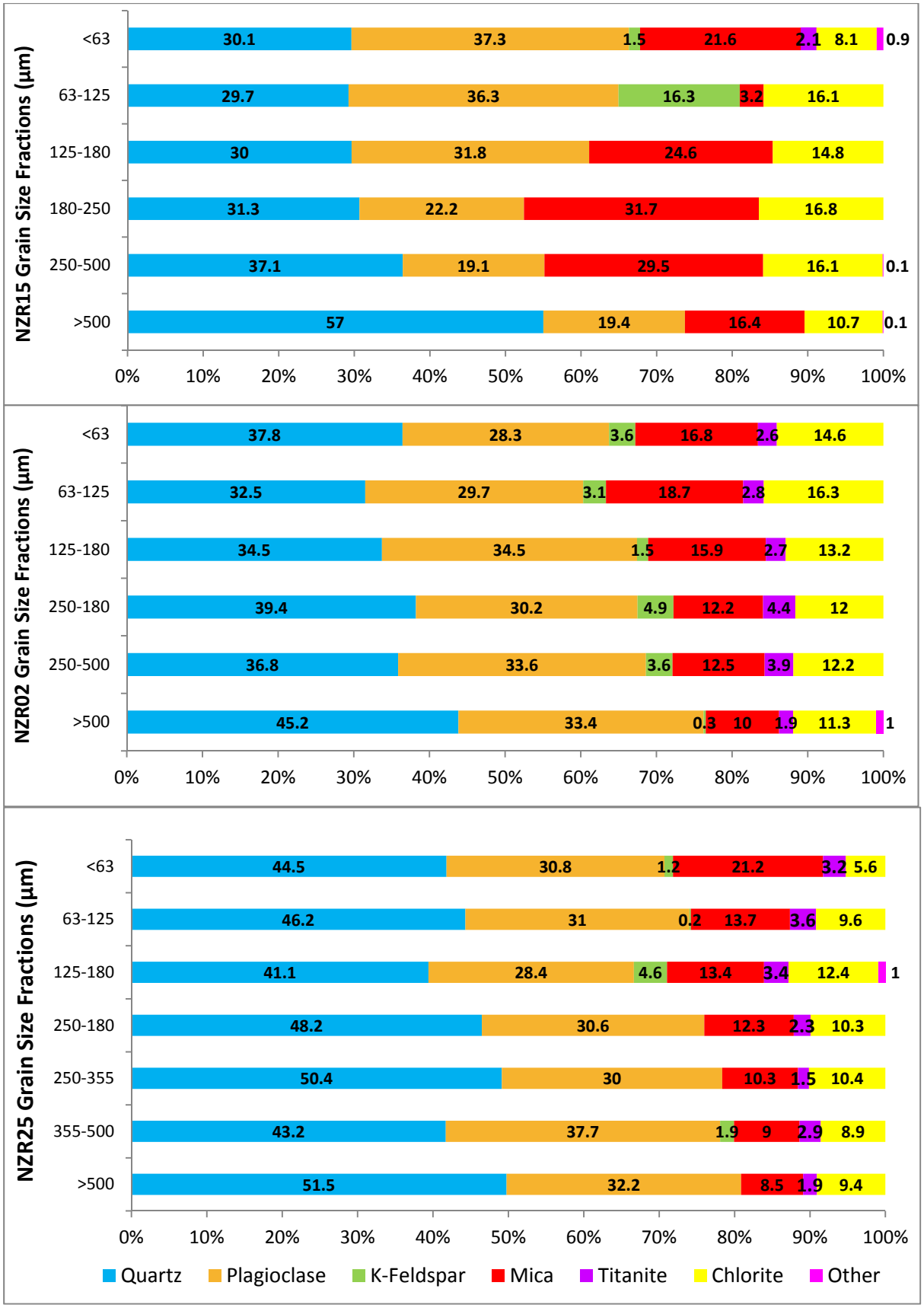

Figure 19: XRD mineralogy of grain size fractions of river sediments for (A) Haast Schist-derived NZR25 (Haast; rainfall = 6676 mm/yr, uplift = 4.8 mm/yr), (B) Rakaia Torlesse Terrane-derived NZR02 (Rakaia; rainfall = 2043 mm/yr, uplift = 2.1 mm/yr) and (C) Pahau Torlesse Terrane-derived NZR25 (Wairau; rainfall = 1129 mm/yr, uplift = 1.8 mm/yr).

Overall the grain size fractions of the Wariau, Rakaia and Haast sediment do not appear highly differentiated as the concentration of minerals is fairly consistent throughout all grain size fractions. This could be potentially attributed to relatively short residence times in the fluvial system, whereby the sediment may not be subjected to intense physical or chemical weathering. Furthermore, the greywacke sediments, NZR02 and NZR25, have different annual rainfall rates and show similar major mineralogy patterns. Therefore rainfall is not thought to induce mineralogy differentiated grain size fractions.

5.1.2 Geochemistry

Trace element data for the grain size fractions of NZR15, NZR02 and NZR25 are presented in Appendix A. No trace elemental data is provided for the silt (< 63 µm) fraction of NZR02 as there was insufficient mass obtained.

As can be observed in Figure 20, the three river sediments, NZR15, NZR02and NZR25 for Zr, show similar behaviour and are concentrated in the smaller grain size fraction. Specifically in the Haast Schist-derived NZR15, Zr is concentrated in the coarse silt fraction (< 125 µm), whereas in the Torlesse Terrane-derived sediment, NZR02 and NZR25, Zr is predominantly in a narrower range of < 63 µm. This suggests that the minerals which contain Zr are concentrated in the silt size fraction, which is similarly reported in the literature (Zhang *et al.* 2002).

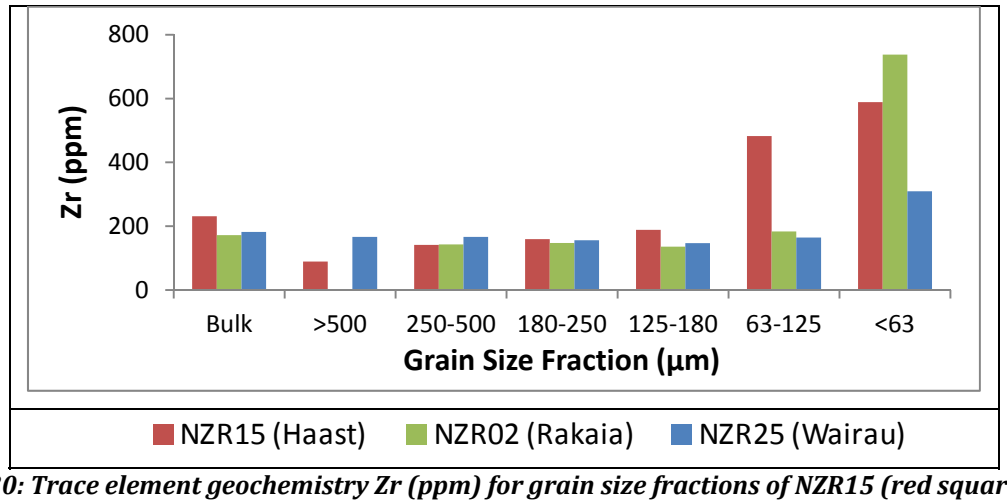

Figure 20: Trace element geochemistry Zr (ppm) for grain size fractions of NZR15 (red square; rainfall = 6676 mm/yr, uplift = 4.8 mm/yr), NZR02 (green triangle; rainfall = 2043 mm/yr, uplift = 2.1 mm/yr) and NZR25 (blue diamond; rainfall = 1129 mm/yr, uplift = 1.8 mm/yr). Note no data for >500 µm fraction of NZR02 was obtained.

Similarly to Zr, Figure 21 shows that the three rivers have the same grain size pattern of Ba and Zn concentrations. This suggests that the hydraulic sorting of minerals that contain Zr, Ba and Zn are consistent throughout the three rivers and therefore sorting is not sensitive to lithology, rainfall or uplift rates. In contrast to Zr, the concentration of Zn shows an overall systematic increase in concentration with decreasing grain size. Furthermore, Ba is relatively consistent throughout the grain size fractions of NZR25, NZR15 and NZR02. The exception for this is the >500 µm fraction of NZR15 that shows a dramatic decrease in Ba. This suggests that the minerals concentrating Ba, in the schist lithology, are depleted in the coarse sand. Additionally in NZR25, it can be seen that there is a slight increase of Ba concentration with decreasing grain size. In summary, for the greywacke-derived sediments, minerals that concentrate Ba are uniformly distributed across the grain size fractions, and for the schist-derived sediment, the mineral containing Ba is depleted in the coarse sand fraction. Consequently, it is suggested that Ba bearing minerals in the sediments, are not sensitive to hydraulic sorting, regardless of lithology, rainfall and uplift for grain size fractions < 500 µm.

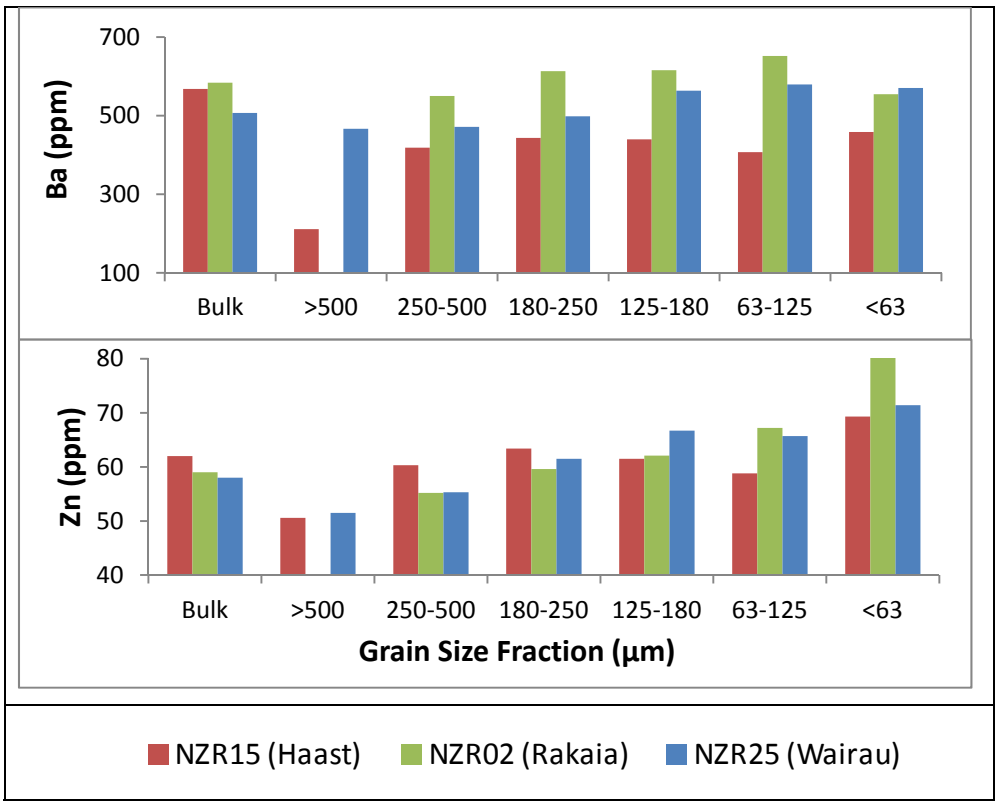

Figure 21: Trace element geochemistry (ppm) (A) Ba and (B) Zn for grain size fractions of NZR15 (red square; rainfall = 6676 mm/yr, uplift = 4.8 mm/yr), NZR02 (green triangle; rainfall = 2043 mm/yr, uplift = 2.1 mm/yr) and NZR25 (blue diamond; rainfall = 1129 mm/yr, uplift = 1.8 mm/yr) Note no data for >500 µm fraction of NZR02 was obtained.

As shown in Figure 22, the three river sediments show varying grain size patterns in relation to Rb and Ni (Figure 22). This figure indicates that is systematic variation of the relative concentrations of Rb and Ni in NZR25, whereby the concentration of the element generally increases with decreasing grain size. However, there is a slight decrease in Ni in the silt (< 63 µm) fraction of NZR25, and Rb concentration appears to peak between 125 and 250 µm, before slightly decreasing into the silt (< 63 µm) fraction for NZR15 and NZR02. Furthermore, the concentration of Rb in the < 500 µm fraction in the schist-derived NZR15, is relatively low. As the concentration of Ni is shown in Figure 22 to be most variable in NZR25, it appears that hydraulic sorting has a stronger influence in the Wairau River for the minerals which host Ni. This could be attributed to the lower annual rainfall of NZR25 as compared to higher rainfall regions of NZR02 and NZR15.

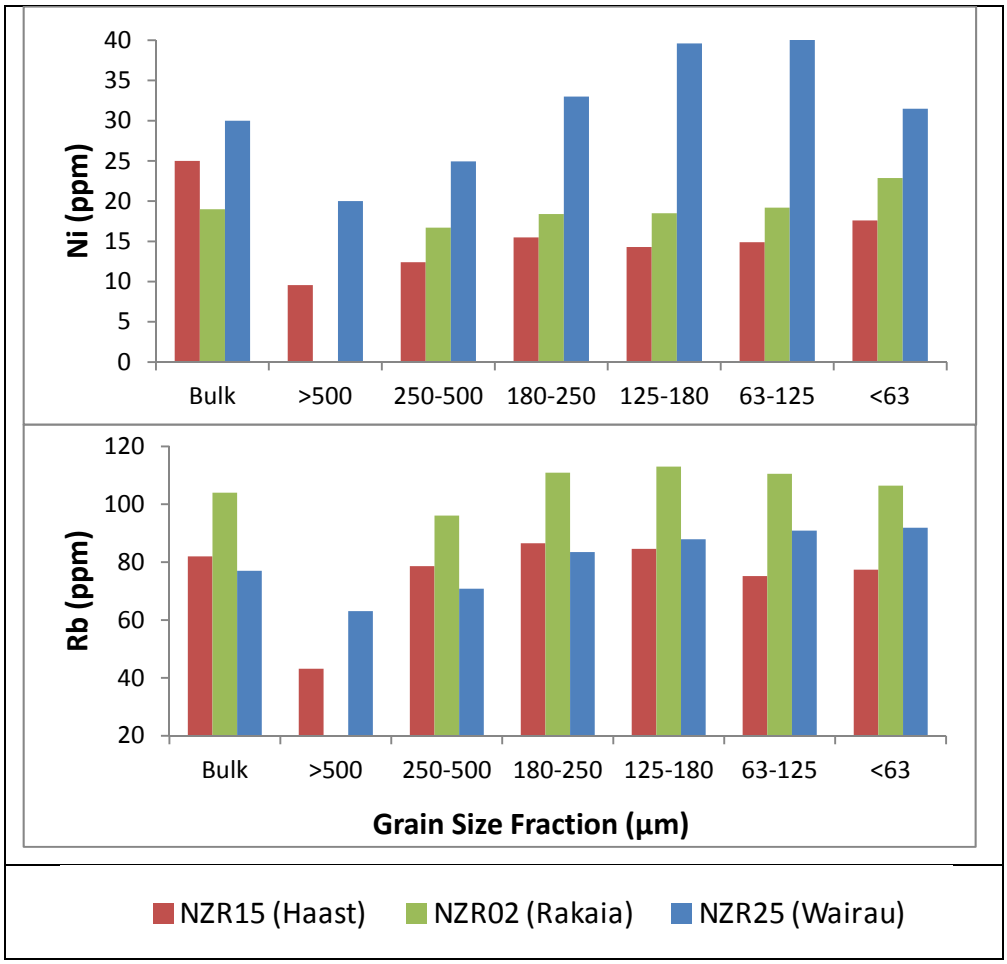

Figure 22: Trace element geochemistry (ppm) (A) Niand (B) Rb. for grain size fractions of NZR15 (red square; rainfall = 6676 mm/yr, uplift = 4.8 mm/yr), NZR02 (green triangle; rainfall = 2043 mm/yr, uplift = 2.1 mm/yr) and NZR25 (blue diamond; rainfall = 1129 mm/yr, uplift = 1.8 mm/yr). Note no data for >500 µm fraction of NZR02 was obtained.

The trace elements, Sr, Nb, Th and U, follow a similar pattern of distribution throughout grain size fractions of NZR25, NZR15 and NZR02. Figure 23 shows that the element concentrations are most variable between grain size fractions of NZR15, where increased concentration occurs with decreased grain size. This is in contrast to NZR02 and NZR25 where the element concentrations are fairly consistent across the grain size fractions. More specifically there is a slight decrease of Sr and increase of Rb with decreasing grain size for NZR25, whereas Th and U show only slight variations between grain sizes. However, the sediment, NZR02, has consistent Sr and Pb concentration over the grain size fractions. Th shows slight increase with increasing grain size but has a decreased concentration in the silt fraction and U shows no systematic variation. Overall there is a trend for Sr, Nb, Th and U to be more concentrated in the smaller grain size fractions with concentrations being more variable with grain size in NZR15, which experiences high annual rainfall and uplift rates. There in no marked differences in the elemental patterns of NZR25 and NZR02 which have similar uplift rates but differing annual rainfall rates. It therefore appears that hydraulic sorting for minerals containing Sr, Nb, Th and U tend to be sensitive with higher uplift and rainfall rates and therefore a lower residence time. Alternatively hydraulic sorting, in this case, could additionally be attributed to lithology, whereby NZR25 and NZR02 are derived from Torlesse Terrane, whereas NZR15 is sourced from Haast Schist.

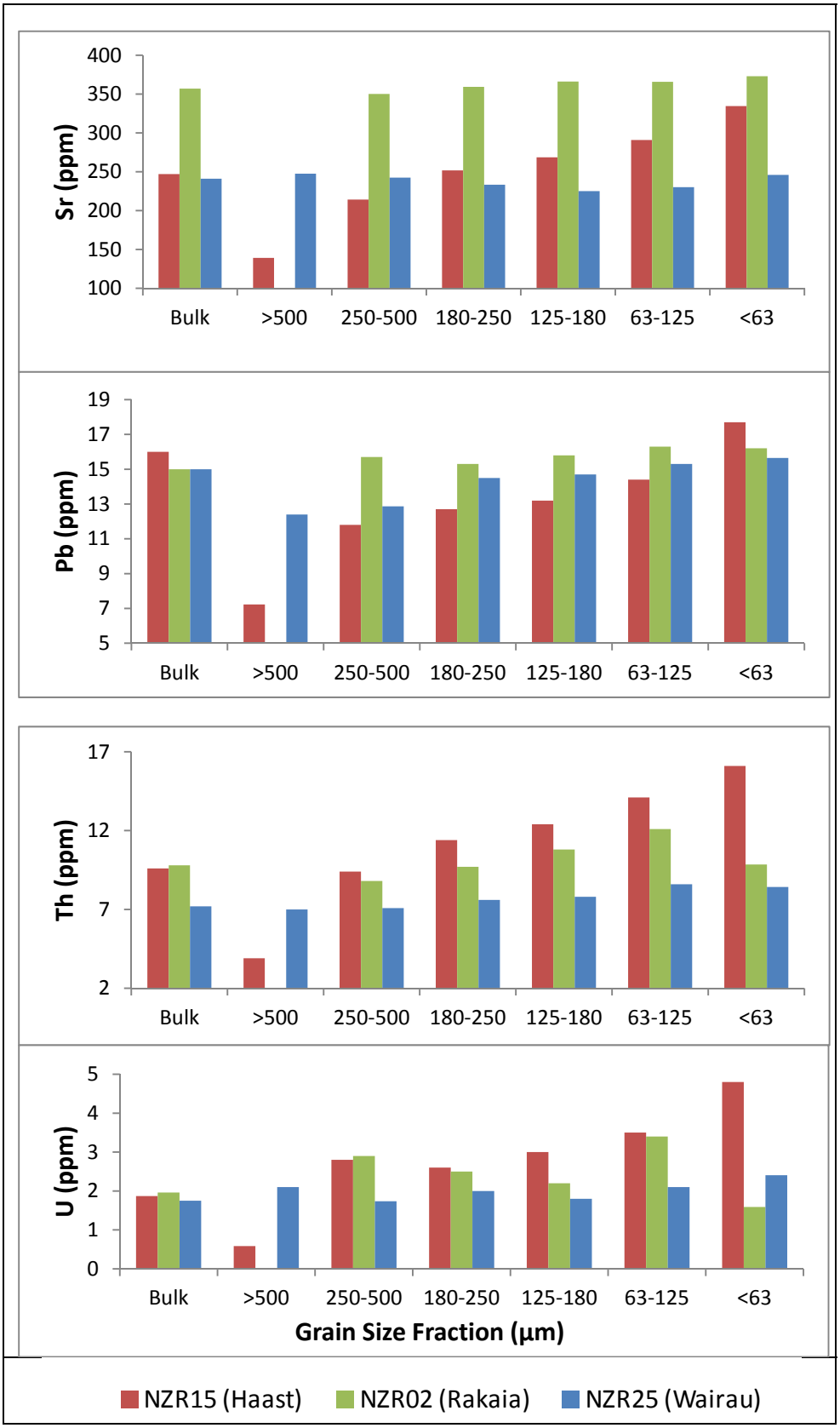

Figure 23: Trace element geochemistry (ppm) (A) Sr, (B) Pb, (C) Th and (D) U. for grain size fractions of NZR15 (red square; rainfall = 6676 mm/yr, uplift = 4.8 mm/yr), NZR02 (green triangle; rainfall = 2043 mm/yr, uplift = 2.1 mm/yr) and NZR25 (blue diamond; rainfall = 1129 mm/yr, uplift = 1.8 mm/yr). Note no data for >500 µm fraction of NZR02 was obtained.

The concentration of the trace elements Nb and Y, shown in Figure 24, tend to increase with decreasing grain size in all three rivers. However, the variation of the Nb and Y concentrations over the grain size fractions is much more pronounced in NZR02 and NZR15, as compared to NZR25. As NZR02 and NZR15 show the same grain size patterns, it is suggested that hydraulic sorting of minerals, bearing Nb and Y, are not sensitive to lithological, rainfall and uplift effects.

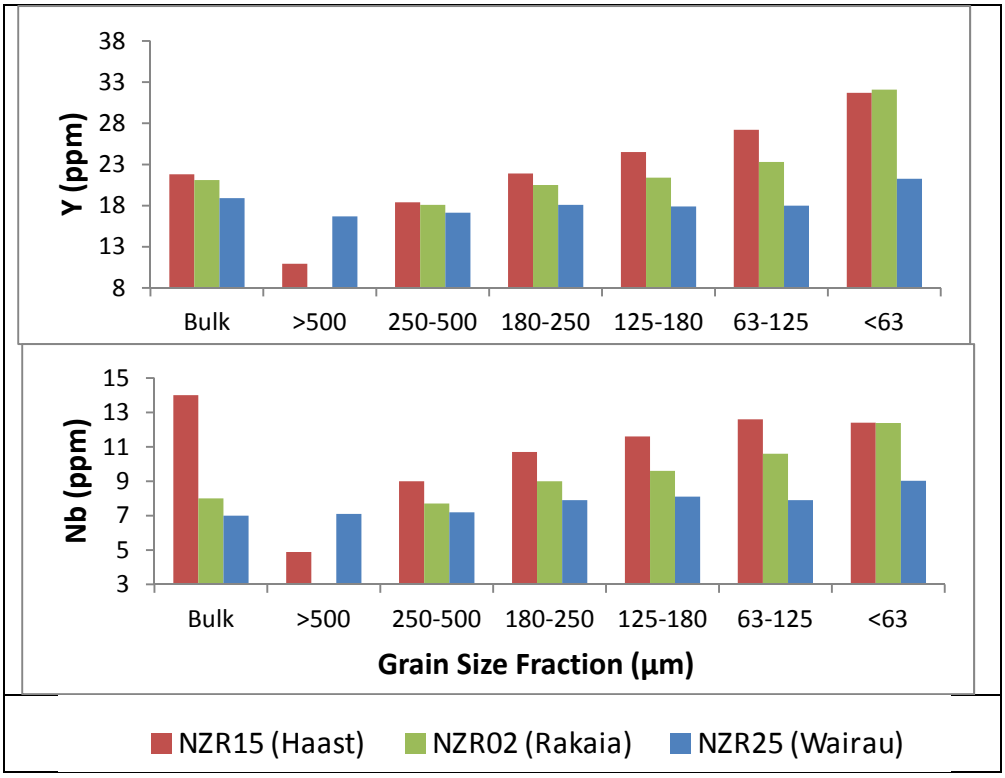

Figure 24: Trace element geochemistry (ppm) (A) Y and (B) Nb, for grain size fractions of NZR15 (red square; rainfall = 6676 mm/yr, uplift = 4.8 mm/yr), NZR02 (green triangle; rainfall = 2043 mm/yr, uplift = 2.1 mm/yr) and NZR25 (blue diamond; rainfall = 1129 mm/yr, uplift = 1.8 mm/yr). Note no data for >500 µm fraction of NZR02 was obtained.

In summary, analysis of grain size fractions for NZR15, NZR02 and NZR25 over a range of lithological, rainfall and uplift conditions suggests that there is little systematic variation of major mineralogy. However, geochemical analysis has highlighted that some trace elements vary with grain size fractions. Therefore such trace element variability, across grain size fractions, is likely to be attributed to variations in accessory mineralogy rather than major minerals. Therefore grain size analysis suggests that some accessory minerals, that concentrate particular trace elements, are sensitive to hydraulic sorting effects and may respond differently to rainfall and uplift conditions.

5.2 Grain Size Analysis

Mineralogical and geochemical analysis of grain size fractions in Section 5.1 highlighted that there is some differentiation between the grain size fractions of the river sediments. Therefore, in order to assess the geochemistry and mineralogy of bulk sediments, grain size considerations are necessary. Grain size analysis of the bulk sediment samples are summarised in Appendix B and are presented in a ternary diagram of sand, silt and clay fractions in Figure 25. Figure 25 shows that the majority of sediments plot in the greater than 75% sand portion of the triangle and therefore, according to Shepard (1954), are classified as sand whereas NZR24 (Awatere) is classified as silty sand. Overall there is a relatively low percentage of clay in the river sediments (< 1.85%) and a slightly higher amount in the terrace sediment, NZR19T, (2.10%). The proportion of clay in the sediment samples is likely to be attributed to their low density, which separates it the coarse fraction by particle sorting of minerals during transport. Therefore the clay is predominantly part of the suspended sediment load of the river and is transported to the ocean (Hicks *et al.* 2011).

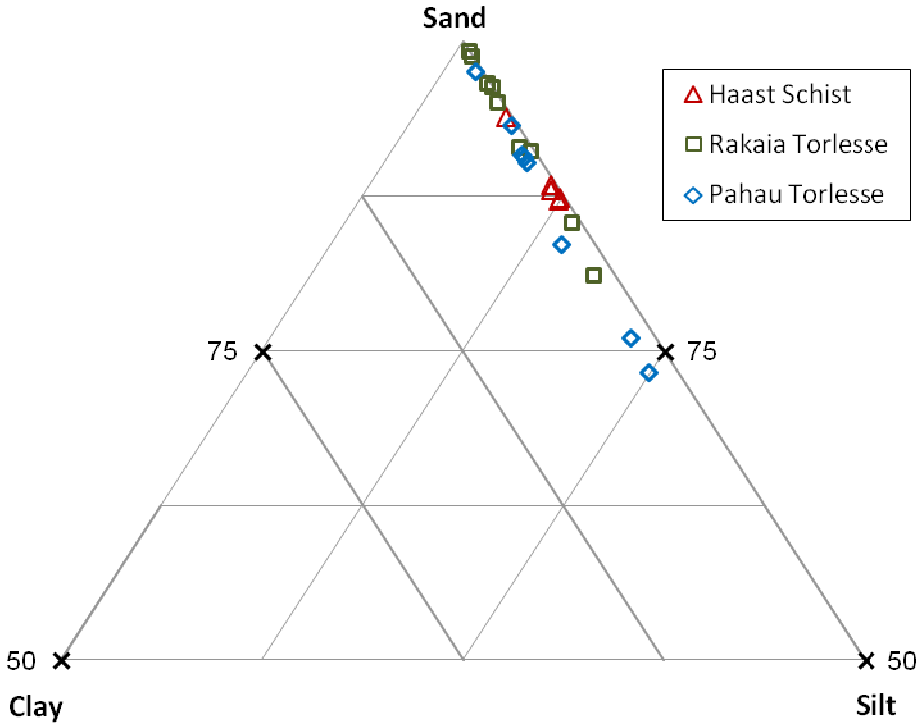

Figure 25: Sand, silt and clay ternary diagram of sediments derived from Haast Schist (red triangle), Rakaia Torlesse Terrane (green square) and Pahau Torlesse Terrane (blue diamond).

There was no systematic relationship identified between the sediment samples and the distance from their respective headwaters. However, within individual fluvial systems downstream fining was present, whereby volume weighted mean grain size decreased with increasing distance from the headwaters in the Rakaia, Waimakariri and Clarence Rivers (Figure 26). Downstream fining can be attributed to hydraulic sorting and abrasion of sediment particles (Gasparini *et al.* 1999). This trend is further evident in Figure 27, which shows the percentage sand fraction decreases, while the silt and clay fractions increases with distance from the headwaters. However, there was no relationship evident between the distance from the headwaters and the statistical sorting parameters of standard deviation, skewness and kurtosis.

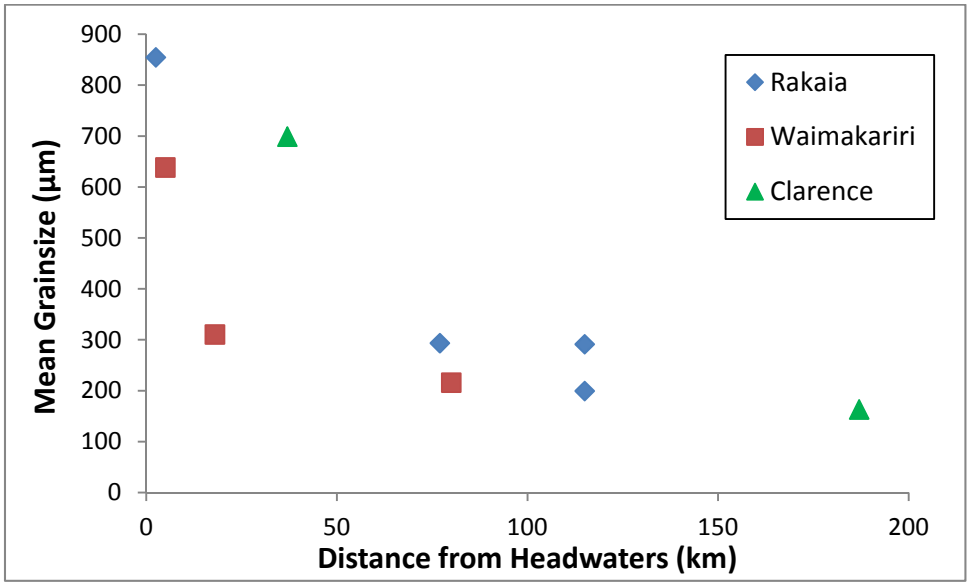

Figure 26: Mean grain size versus distance of from headwaters of Torlesse Terrane-derived river sediments from Rakaia (blue diamond), Waimakariri (red square) and Clarence (green triangle). Plot shows that the mean grain size of the sediment decreases with increasing distance from the headwaters.

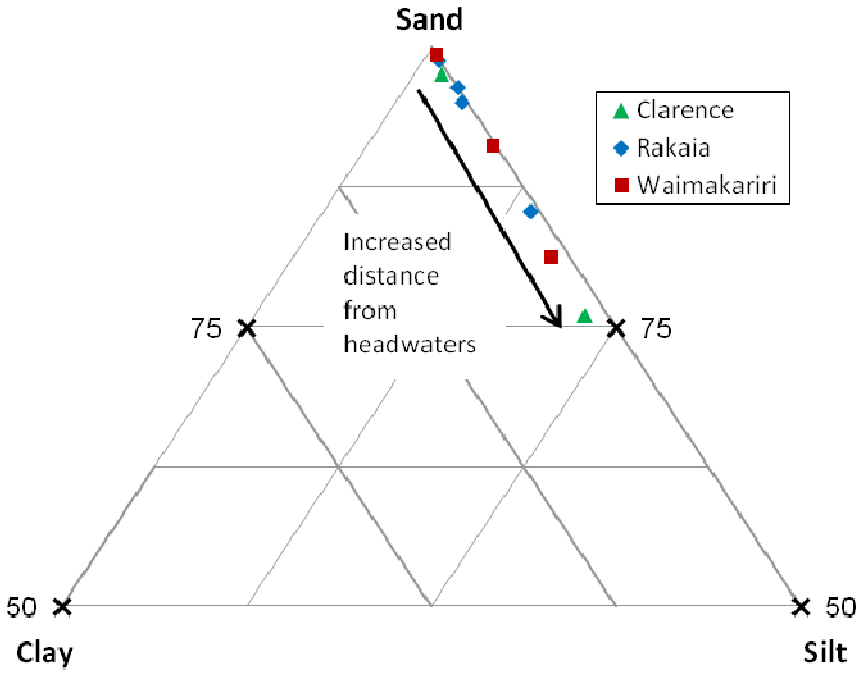

Figure 27: Sand, silt and clay ternary diagram of sediments from Clarence (green triangle), Rakaia (blue diamond) and Waimakariri (red square). Arrow shows that with increased distance downstream the sediments decrease their proportion of sand and increase in silt and clay.

In contrast, downstream fining was not observed in the Taramakau River where the upstream sediment sample NZR08 has a smaller average grain size (292 μm) and a greater > 2 mm grain size fraction (22.2 wt%) than the downstream NZR11 (533 μm and 0.7 wt%). This grain size variation can be attributed to sampling location, whereby there was an artificially placed bank revetment at the sample site of NZR08 (Figure 28). This rock revetment reduces hydraulic flow velocity by creating greater surface roughness and eddying (Schumm *et al.* 1984). This reduction in flow velocity would result in the deposition of suspended sediments between the rock revetments, therefore decreasing the overall mean grain size of the river braid bar. In comparison, NZR11 was collected from an unobstructed river braid bar with a likely higher hydraulic flow velocity, whereby the finer grained sediments would remain in suspension. Therefore this difference in flow velocity of the sample locations explains why the upstream sediment NZR08 has an overall smaller grain size and a lower proportion of coarse sand (> 2 mm), as compared to the downstream NZR11.

Figure 28: Photograph of bank revetment at sample location site NZR08, upper Taramakau River. Sample was collected from accumulated sediment between boulders. Water flows from left to right of photograph. Photograph taken by Dr. A Dosseto (2011).

Figure 29: Photograph of river bar at sample location site NZR11, lower Taramakau River. Sample was collected between larger cobbles. Water flows from left to right of photograph. Photograph taken by Dr. A Dosseto (2011).

5.3 Mineralogy

The sediments are derived from the lithological source regions of the Torlesse Terrane greywacke and the Haast Schist. Mineralogically the Torlesse Terrane is derived from volcanic detritus and predominantly consists of undifferentiated quartz, albite, muscovite and biotite (Grapes & Otsuki 1983). The Haast Schist is the metamorphic equivalent of the Torlesse Terrane has a fine grained foliated matrix mainly consisting of quartz, muscovite and small porphyroblasts, typically of plagioclase ± ilmenite ± titanate ± chlorite ± epidote and biotite ± tourmaline ± oligoclase ± garnet at higher grades (Mackinnon 1983; Roser & Cooper 1990; Vry *et al.* 2008). Hydrothermal activity, associated with the Alpine Fault, has deposited decimetre sized quartz-calcite veins, particularly in the higher grade zones of the Haast Schist (Jacobson *et al.* 2003).

5.3.1 X-ray Diffraction Analysis

Figure 30 shows the mineralogical variation in the Haast Schist-, Pahau and Rakaia Torlesse Terrane -derived sediments. Overall the percentage of quartz is fairly consistent between the greywacke and schist sediments. The sediments derived from schist have a quartz content that ranges from 35.9 wt% (NZR12: Peorua) to 47.5 wt% (NZR14; Haast), whereas those derived from greywacke range from 35.2 wt% (NZR24; Awatere) to 51 wt% (NZR25; Wairau). In all sediment samples the feldspar content is dominated by plagioclase as compared to K-feldspar. This is supported by MacKinnon's (1983) analysis of the Torlesse Terrane bedrock where he reports that ratio of plagioclase to K-feldspar is approximately 5:1. However, the greywacke-derived sediments appear to have slightly higher relative plagioclase content (23.4 to 38.5 wt%) as compared to the schist-derived sediments (19.4 to 28.5 wt%). Additionally K-feldspar is more prominent in the greywacke-derived sediments, whereas it is absent from all the schist-derived sediments, except for NZR11 (lower Taramakau). Similarly the presence of titanite is only detected in the greywacke-derived sediments (1.8 to 5.1 wt%), with the exception of NZR11 (lower Taramakau; 2.7 wt%). In contrast to K-feldspar and titanite, the schist-derived sediments tend to have higher mica contents (21 to 44.4 wt% vs. 12 to 22 wt%), with the exception of NZR09 (lower Waimakariri; 48.4 wt%). Additionally there is no systematic variation of chlorite between the greywacke (5.7 to 13.8 wt%) and schist (6.5 to 14.5 wt%) derived sediments.

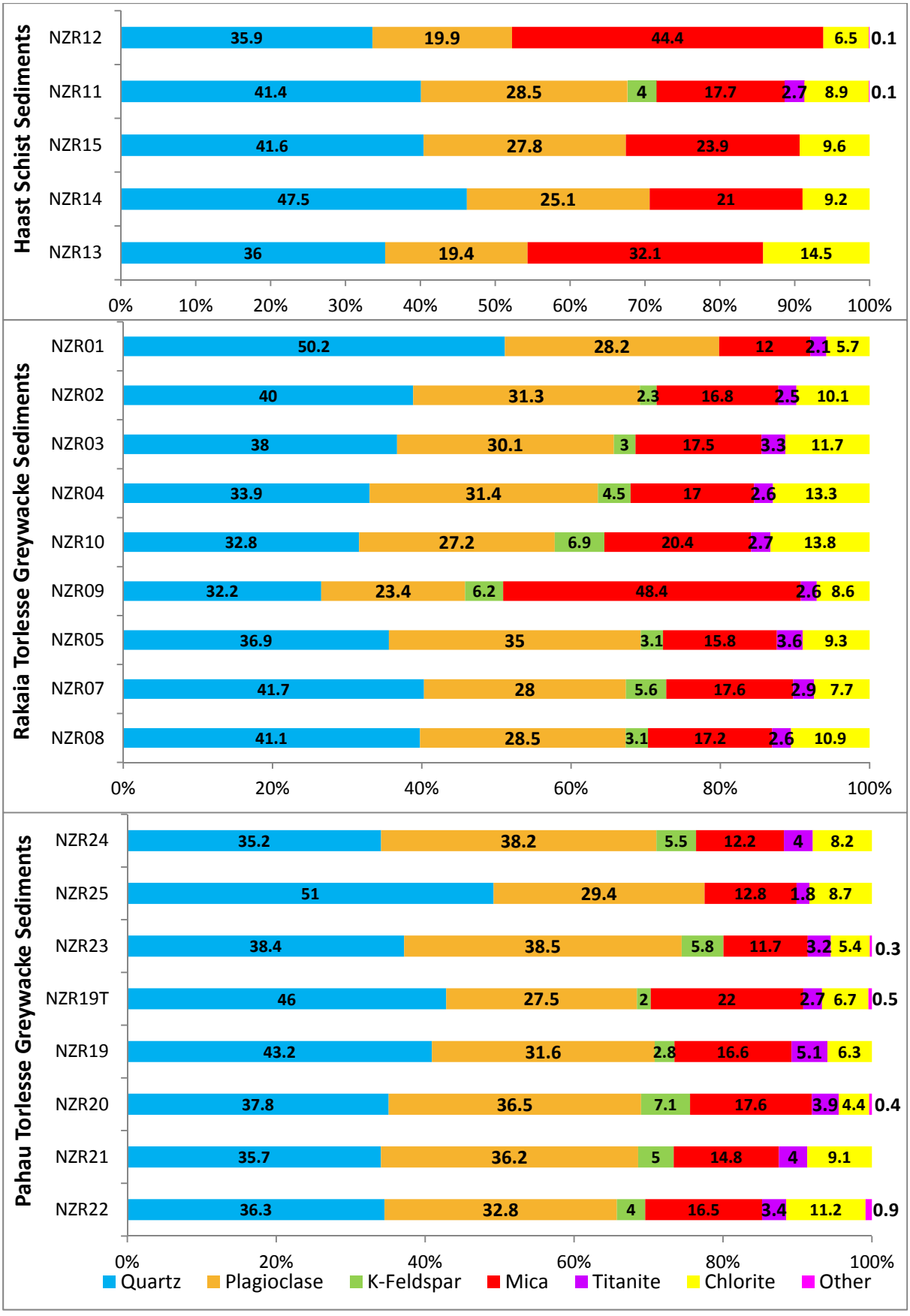

Figure 30: XRD Mineralogy of bulk river sediments derived from the (A) Haast Schist, (B) Pahau Torlesse and (C) Rakaia Torlesse.

Haast Schist-Derived Sediments

Mineralogical analysis indicates that the composition of Haast Schist sediments is relatively uniform. However, NZR12 (Peorua) and NZR13 (Whataroa) have considerably higher mica concentration (44.4 and 32.1 wt%, respectively), as compared to the other Haast Schist-derived sediments (17.47 to 23.9 wt%). Furthermore NZR13 additionally has a noticeably higher chlorite component (14.5 wt%), whereas in NZR12 it is slightly lower (6.5 wt%). The greater presence of mica in NZR12 can be attributed to its catchment only draining high grade Haast Schist of the Garnet-Oligoclase and Biotite zones. Consequently, it is expected that biotite contributes to a greater proportion of mica in the sediment. Both the Haast (NZR14 and NZR15) and Whataroa (NZR13) Rives drain all metamorphic grades of the Haast Schist and therefore their mineralogy compositions are expected to be similar. However, the chlorite and mica components appear more concentrated in NZR13. This could be attributed to quartz dilution in NZR14 and NZR15, which are 80 and 73 km from their headwaters, as compared to NZR13 that is 26 km. As previously stated, NZR11 (lower Taramakau) is the only schist-derived sediment which contains K-feldspar and titanite. In comparison, Taramakau is the only river sampled on the western coast that additionally drains Torlesse Terrane greywacke in the upper proportion of the catchment and granodiorite in the lower (Section 3.7.3, Figure 17).

Torlesse Terrane-Derived Sediment

Overall there is not substantial mineralogical differentiation between the Torlesse Terrane-derived sediments. Notable differences include the absence of K-feldspar in NZR01 (Pareora) and in NZR25 (Wairau). Furthermore these two sediments have comparatively higher quartz contents of 50.2 and 51.0 wt%, respectively. The relatively high quartz content of NZR01 could be explained by the presence of Late Pleistocene to Holocene alluvial deposits in the lower and middle proportions of the Parora catchment (Section 3.7.3; Figure 15). These alluvial deposits primarily consist of weathered greywacke which then are recycled and redeposited as modern river sediments. Consequently this increases the effect of quartz dilution, due to residual quartz being recycled from the Late Pleistocene to Holocene alluvial deposits. Similarly, the Wairau catchment overlies Early Pleistocene to Holocene alluvial and fan deposits, which could

increase the proportion of quartz within the sediment. Furthermore, NZR25 was collected 118 km from the headwaters and therefore hydraulic sorting of quartz could additionally contribute to the high quartz concentration.

It is interesting to note that neither quartz nor feldspar content of the sediments systematically correlate with distance downstream for all sediment samples. For example, this is the case with the sediments from the Clarence River where NZR23 is 187 km from the headwaters, has 38.4 wt% quartz, 38.5 wt% plagioclase and 5.8 wt% K-feldspar, while the upstream sediment NZR19 which is 37 km away from the headwaters, has 43.2 wt% quartz, 31.6 wt% plagioclase and 2.8 wt% K-feldspar. This is the opposite of what is expected when chemical weathering occurs, as quartz is more resistant to physical and chemical abrasion as compared to feldspar (Nesbitt & Young 1989). Furthermore the concentration of titanite and mica are lower in the downstream sediment NZR23, as compared to the upstream NZR19 (3.2 and 11.7 wt% versus 5.1 and 16.6 wt%, respectively). The lack of downstream trend within the Clarence can be explained by the shape and geography of the catchment. The Clarence is located between the Kaikoura mountain range, with the Inland Range to the north-west and the Seaward Range to the south east (Section 3.7.1, Figure 12). Consequently, the lower Clarence sediment is likely to be predominantly derived from this fault active mountain range. In comparison, sediment derived from the upper Clarence (NZR19) is sourced from the northern most extent of the Southern Alps. This hypothesis is supported by the similarity of the mineralogical content of NZR23 with NZR24 (Awatere), the northern adjacent catchment whose sediment is partly derived from the Inland Kaikoura Range.

The lower Rakaia sediments, NZR02 and NZR03, have a compatible mineralogy to NZR04, sampled approximately 40 km upstream. However, there are a few notable differences, where the upstream sediment has slightly lower quartz, higher K-feldspar and increased chlorite content. This suggests that the downstream sediments, NZR02 and NZR03, are subjected to slight quartz dilution. In contrast to these Rakaia River sediments, NZR10 was sampled at a tributary valley stream, approximately 2.5 km to its headwaters. NZR10 has similar mineralogical components to NZR04, However, has

slightly higher mica, less plagioclase and higher K-feldspar content. Consequently, it is suggested that the NZR10 tributary headwaters has a bedrock composition with a lower plagioclase to K-feldspar ratio, as compared to the whole Rakaia catchment.

The sediments sampled from the Waimakariri include NZR07, NZR05 and NZR09, located 5, 18 and 80 km from the headwaters, respectively. The upstream sediments have similar mineralogy to the other Torlesse Terrane-derived sediments. In comparison to NZR05, NZR07 has a higher relative quartz (41.7 vs. 36.9 wt%), mica (17.6 vs. 15.8 wt%) and K-feldspar (5.6 vs. 3.1 wt%) content and less plagioclase (28 vs. 35 wt%) and chlorite (7.7 vs. 9.3 wt%) content. However, the mineralogy of NZR09 is quite different to the upper Waimakariri and other Torlesse Terrane sediments. Similarly to the Clarence River, the downstream sediment of the Waimakariri, NZR09, has a notably lower quartz concentration (32.2 wt%) as compared to the upstream sediments. Furthermore NZR09 has a substantially larger mica concentration (48.4 wt%).

River vs. Terrace Sediment

The mineralogy between the river sediment (NZR19) and its adjacent terrace sample (NZR29T), of the upper Clarence, are highly comparable. However, there are some slight differences in the mineral contents. For instance, there is a greater quartz content in the terrace sediment (46 vs. 43.2 wt%), while its total feldspar (29.5 vs. 34.4 wt%) and mica (2.7 vs. 5.1 wt%) is lower. This can be explained by the resistance of quartz to chemical weathering as compared to feldspar, resulting in a concentration of quartz. Furthermore the mica content is higher in the terrace sediment (22.0 vs. 16.6 wt%). It is also interesting to note that the titanite concentration is higher in NZR19 at 5.1 wt% as compared to 2.7 wt% for NZR19T.

Overall there is no systematic trend of the weight percentage major minerals with distance from headwaters, catchment area, or annual average catchment uplift rate for the Torlesse Terrane or Haast Schist-derived sediments.

5.3.2 Petrology - Thin Section Analysis

Petrologic studies involve the description and systematic classification of rocks with the aid of optical microscopy and are often undertaken in conjunction with mineralogical and geochemical analyses (Nelson, 2011). Petrologic analysis, through thin section microscopy, was employed to gain a greater understanding of the clast composition of the sediments. Qualitative descriptions of the thin section analyses are listed in Appendix J and representative petrologic photos are presented in Appendix K. The results from point counting are summarised in Figure 33, Figure 32 and Figure 35. It should be noted that point counting results are presented as percentage of clast type, therefore do not take into consideration grain size of individual clasts. Consequently, these results should not be taken as a percentage of the sediment content but rather a percentage of clast type.

Torlesse Terrane-Derived Sediments

The Torlese Terrane greywacke-derived sediments are compositionally similar, whereby clasts are predominantly identified as greywacke, mudstone, quartz and feldspar. The sediments derived from the Rakaia Torlesse Terrane contain a lower percentage of phylite clasts (1.0 to 5.5%). However, NZR08 (upper Taramakau) is an exception as the sediment contains 11% schist. This can be attributed to the lower part of the upper Taramakau catchment being underlain by low grade Haast Schist (Section 3.7.3, Figure 17). The river sediments NZR02 and NZR03, sampled from south and northern bars of downstream Rakaia, have an overall similar clast percentage. Therefore it is interesting to note that NZR03 has a slightly higher mudstone content and a lower percentage of greywacke clasts (42% and 12%, respectively), as compared to NZR02 (35% and 18.5%, respectively). Furthermore, the mean grain size fraction of NZR03 (200 μm) is smaller than that of NZR02 (291 μm).

Qualitative analysis of the thin sections found that mudstone clasts were generally smaller and more rounded as compared to the greywacke clasts within the sediment (eg. Figure 31). This suggests that mudstones in the South Island of New Zealand are more prone to physical abrasion as compared to greywacke. The greater resistance of sandstones to physical weathering is documented in literature. For instance, a study conducted on the physical and mechanical properties of rocks from weathering profiles of mudstones and sandstones in Japan showed that once oxidised sandstones were strengthened while mudstones were weakened (Chigira & Oyama 2000). This was explained by the process of cementation by iron oxide or hydroxide which strengthened sandstones, whereas mudstone was weakened because it has greater clay fractions and larger specific surface areas than sandstone.

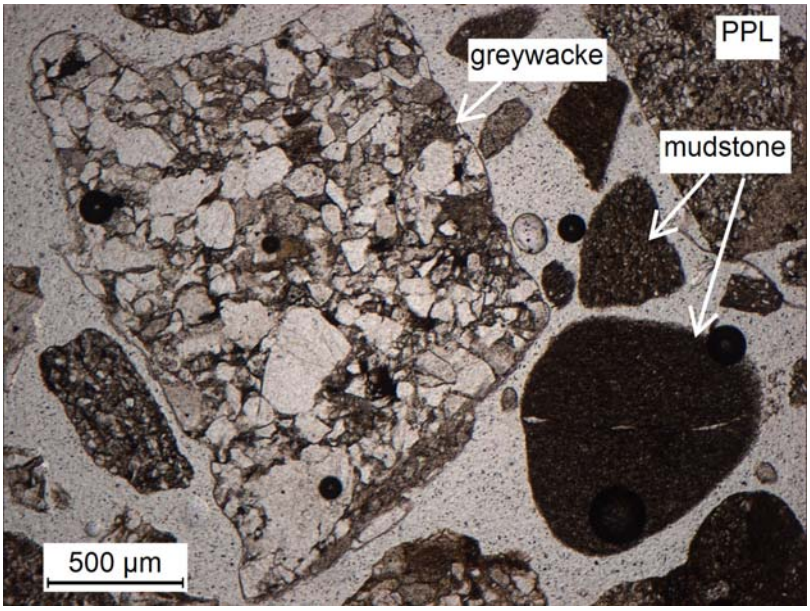

Figure 31: Thin section photo of NZR19, mudstone clast which is smaller and generally more rounded.

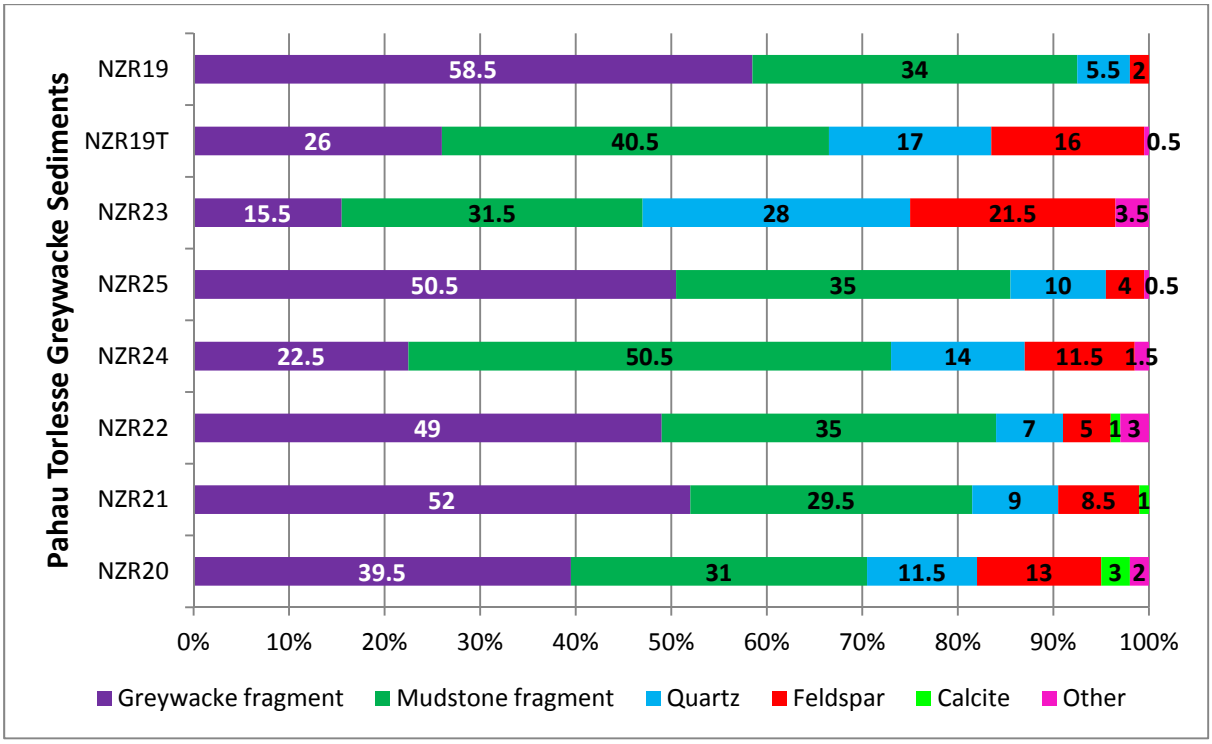

Figure 32: Bar graph showing percentage (%) composition from point counting for Rakaia Torlesse Terrane-derived sediments

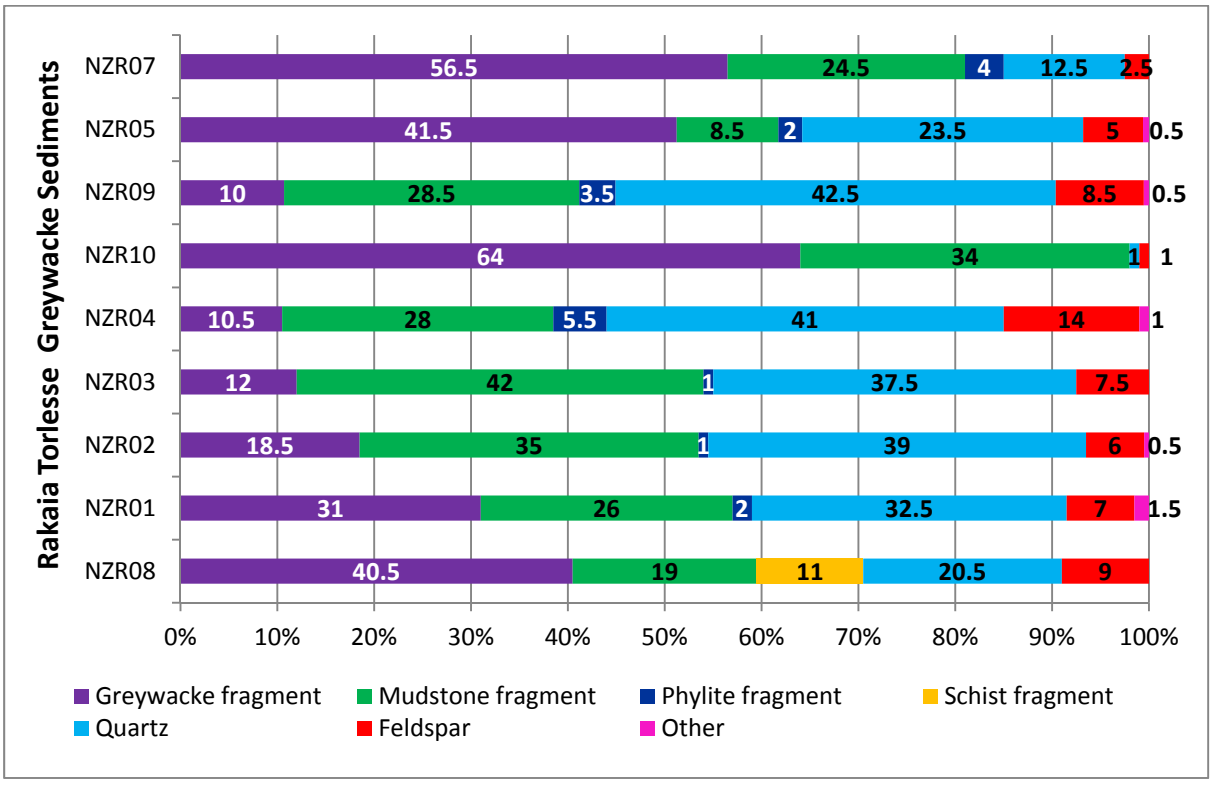

Figure 33: Bar graph showing percentage (%) composition from point counting for Pahau Torlesse Terrane-derived sediments and terrace sample

Haast Schist-Derived Sediments

Point counting identified that sediments from catchments underlain by the Haast Schist have a dominance of schist and quartz clasts. However, minor clast composition is inherited from lithological differences between the catchments. NZR13 (Whatroa) and NZR15 (Haast), show the most alike compositions, containing 68% and 58.5% schist, 25.5% and 37% quartz, 1.5% and 2.5% feldspar and 2.5% and 0.5% biotite fragments, respectively. NZR13 additionally has minor amphibole (1%) and muscovite (1.5%) fragments, while NZR15 has accessory chlorite (1.5%) fragments. Their compositional similarity can be attributed to the both the Whataroa and Haast Rivers draining all metamorphic grades of the Haast Schist (Section 3.7.3, Figure 16 and Figure 18).

In comparison to NZR13 and NZR15, NZR12 (Peorua) contains a greater proportion of quartz (46.5%), feldspar (6%), biotite (13%), muscovite (10%) and amphibole (7%) clasts and a smaller proportion of schist (17%) fragments. The negative correlation between the mineral and schist fragments in NZR12 suggests that the schist fragments are fracturing into their composite minerals to a higher degree than NZR13 and NZR15. This can be attributed to the Peorua draining only high metamorphic grades of the Haast Schist, whereby the relatively large metamorphic crystals break cleanly along highly schistose mineral boundaries and cleavage planes. As can be seen from Figure 34, biotite remains highly tabular and fibrous, therefore suggesting the sediment has been subjected to minimal physical weathering.

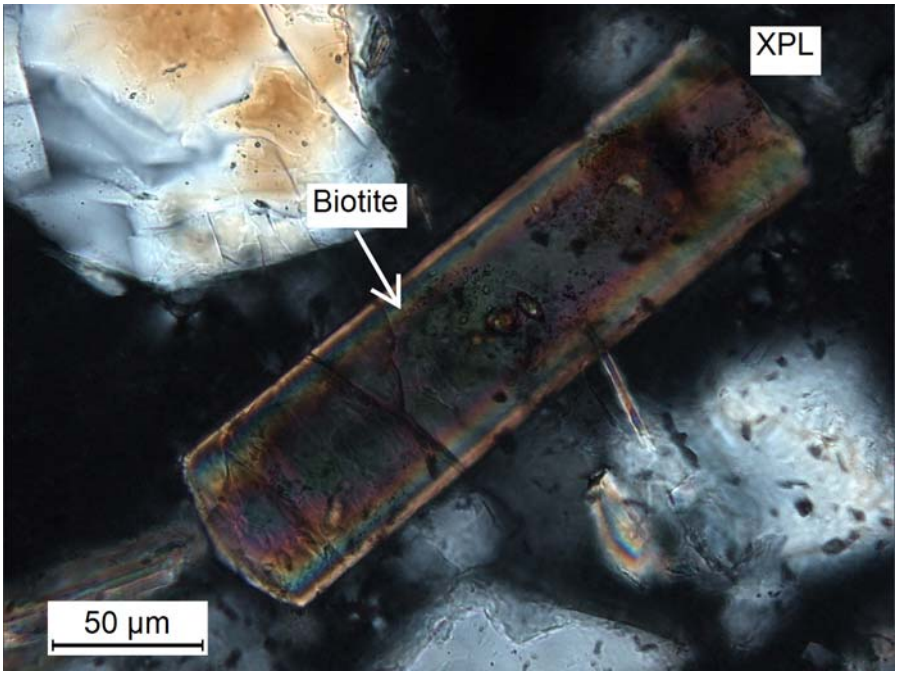

Figure 34: Thin section photo of NZR12 showing tabular biotite fragment that shows minimal physical abrasion (XPL).

NZR11 is compositionally the most diverse of the Haast Schist-derived sediments. As discussed in Section 3.7.3 (Figure 17), the upper proportion of the Taramakau catchment is predominantly Torlesse Terrane greywacke, which grades into its metamorphic equivalent Haast Schist in the middle catchment. This accounts for the presence of both schist (17%) and greywacke/mudstone (12.5%) fragments. Additionally, NZR11 has a higher content of feldspar fragments (7.5%), as compared to other schist-derived sediments. The additional feldspar fragments could be sourced from the greywacke proportion of the catchment, as the Torlesse Terrane-derived sediments have a greater proportion of feldspars (1 to 21.5%) as compared to those derived from the Haast Schist (1.5 to 7.5%). Furthermore, the lower proportion of the Taramakau flows between two plutonic intrusions which have been identified as predominantly granodiorite in nature (Section 3.7.3, Figure 17) (Waight *et al.* 1998). This lithological feature in the drainage boundary is reflected by NZR11 uniquely containing plutonic fragments (12%) and could additionally account for the higher feldspar content.

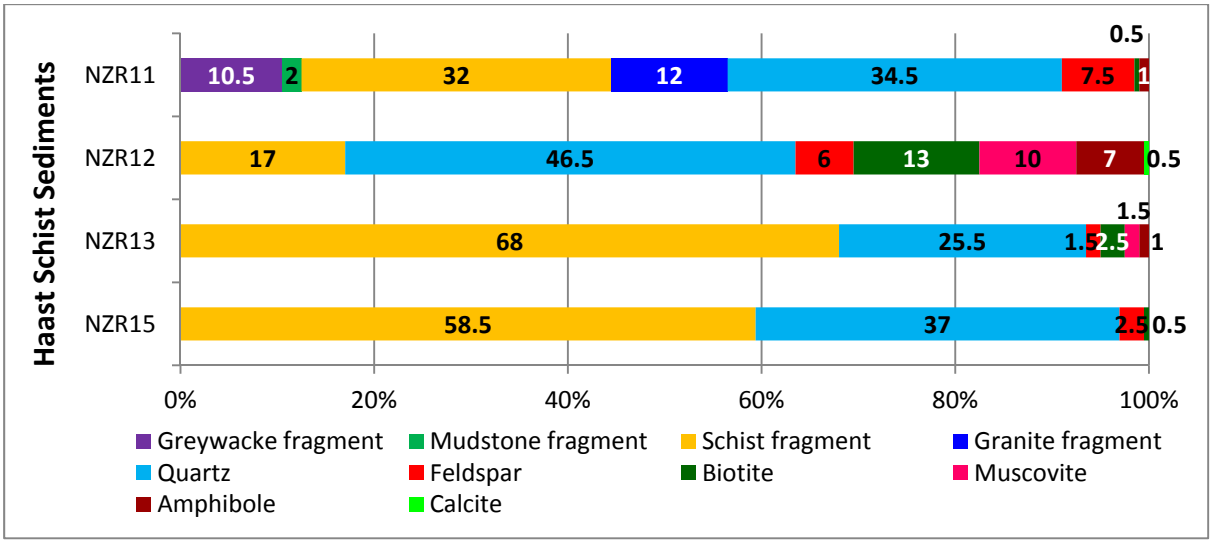

Figure 35: Bar graph showing percentage (%) composition from point counting for Haast Schist-derived sediments

Downstream Trends

Downstream trends, with respect to clast composition, are effectively displayed in the QFL (quartz – feldspar – lithic fragments) ternary diagram of Dickinson *et al.* (1983) (Figure 36). This diagram plots sediment samples, from Clarence, Rakaia, Waimakariri and Taramakau that were located varying distances from their headwaters. Figure 37 highlights that there is a shift in clast percentage with increasing distance from the headwaters in individual fluvial systems, whereby the sediment becomes more dominated by quartz and feldspar fragments, while the proportion of lithic fragments decreases. This relationship is additionally evident through the Torlesse Terrene-derived sediments, whereby Figure 37 shows that there is a positive correlation between the percentage of quartz fragments and distance from the headwaters. The converse relationship is evident with the percentage of lithic fragments and is shown in Figure 38. These relationships between quartz and lithic fragments, and distance from the headwaters, additionally correlates with the Haast Schist-derived sediments when NZR12 (Peorua) is disregarded. Unlike the other sediments derived from the Haast Schist, NZR12 primarily drains from high metamorphic grade Haast Schist (biotite and garnet-oligoclase zone), which is highly schistose and foliated. Consequently the schist fragments, within NZR12, break along cleavage and schistose planes into component minerals, leading to the sediment having higher quartz fragment content. However, there was no systematic relationship found between percentage of quartz, feldspar, or lithic fragments and annual average catchment uplift or rainfall. This suggests that the

distance the sediments are being transported, rather than uplift and rainfall rates, has the primary influence on physical abrasion of lithic fragments into their composite mineral grains.

Additionally, Figure 37 shows that the relationship between percentage of quartz fragments and distance is enhanced for the Haast Schist and Rakaia Torlesse Terrane-derived sediments. This could be due to the higher elevation of the central Southern Alps headwaters (2200 to 3000 m), that the Haast Schist and Rakaia Torlesse Terrane-derived sediments drain from (expect for NZR01 and NZR10), as compared to the Pahau Torlesse rivers that drain the northern Southern Alps and Kaikoura Range (1500 to 2100 m). The higher elevations could infer steeper gradients of the river at the headwaters, particularly for the western coast rivers, which dramatically drop in elevation over relatively short distances. Therefore, this could lead to greater physical abrasion of the sediments derived from rivers draining from the central Southern Alps, as compared to those draining the northern Southern Alps. The greater physical abrasion of sediments in rivers, with increased gradients, is further demonstrated from the Pahau Torlesse-derived sediments presented in Figure 37. The Conway, Kowhai and Hapuku Rivers, from where the sediments were collected, have apparent gradients of 100, 95 and 152 respectively and are circled in Figure 37. In comparison, the other sediments collected in this region from the Clarence, Awatere and Wairau, have apparent gradients that range from 9 to 24. The steeper relative gradients of Conway, Kowhai and Hapuku could increase the physical abrasion that the sediments are subjected to and therefore explain their greater proportion of quartz fragments, given their close proximity to their headwaters.

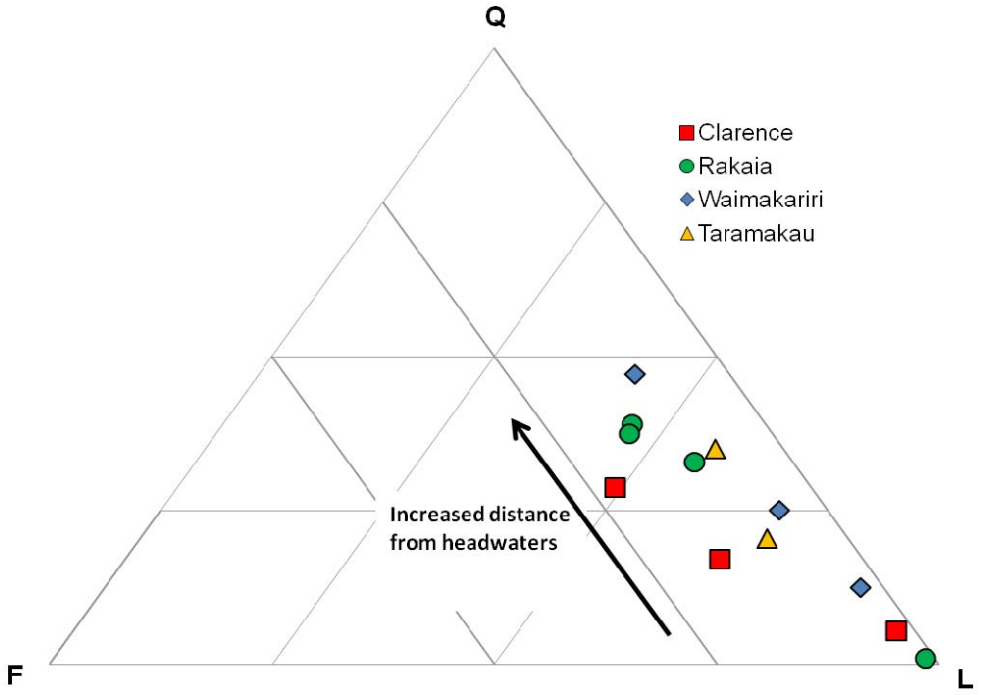

Figure 36: Ternary plot of total quartz-feldspar-lithic fragments (QFL) data from the river sediments from Clarence, Rakaia, Waimakaririand Taramakau Rivers, based on Dickinson et al., (1983).

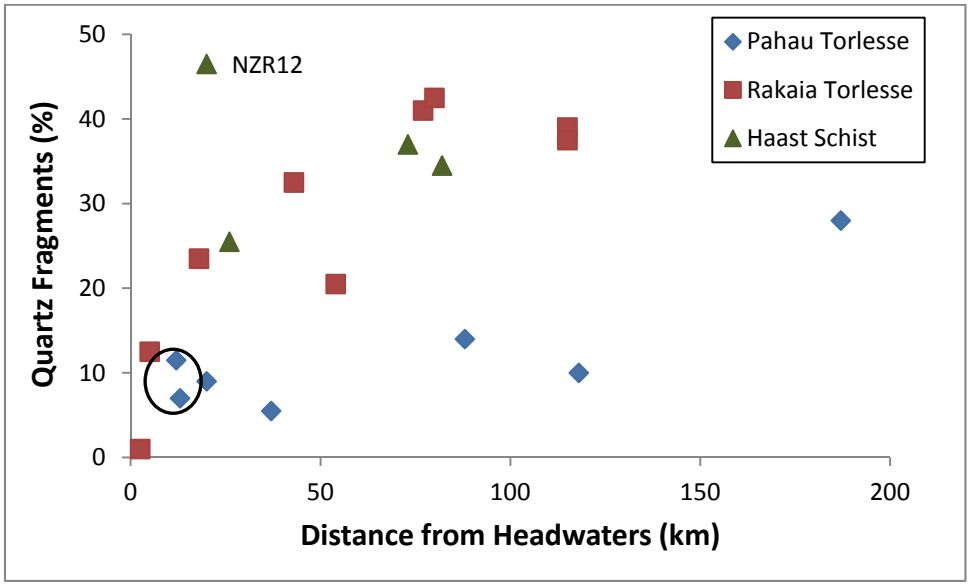

Figure 37: Percentage of quartz fragments versus distance from headwaters of sediments derived from Pahau Torlesse Terrane (blue diamond), Rakaia Torlesse Terrane (red square) and Haast Schist (green triangle). Black circle encompasses Conway, Kowhaiand Hapuku Rivers, which have relatively high gradients.

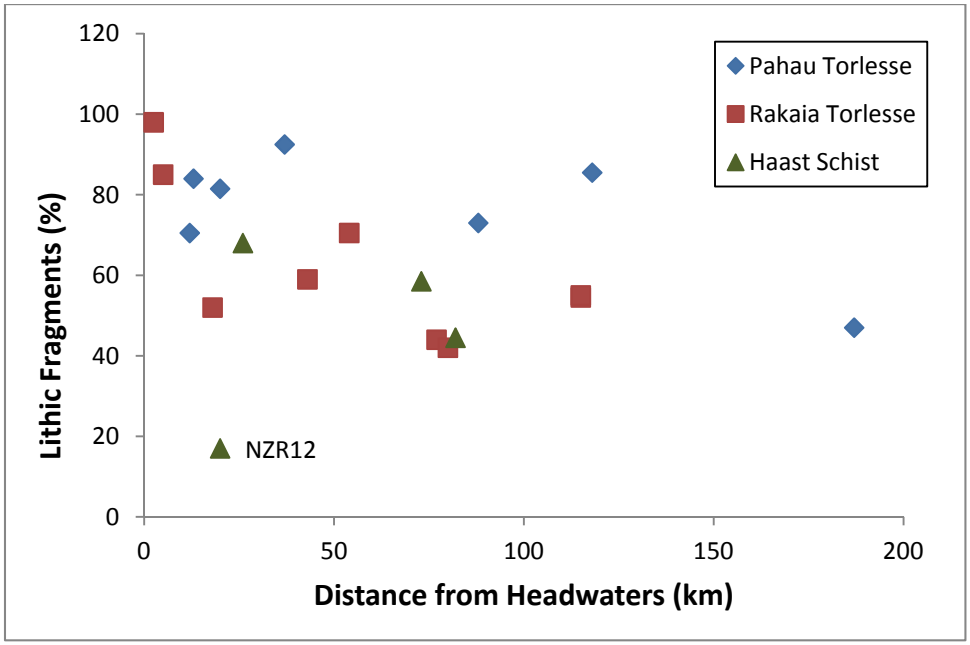

Figure 38: Percentage of lithic fragments versus distance from headwaters of sediments derived from Pahau Torlesse Terrane (blue diamond), Rakaia Torlesse Terrane (red square) and Haast Schist (green triangle).

River vs. Terrace Sediment

Compositionally the Clarence terrace sample, NZR19T, is similar to that of the adjacent river bar sample, NZR19, which both contain greywacke, mudstone, quartz and feldspar fragments. However, there are marked differences in the percentage of clasts between these two samples. For instance, NZR19T contains a greater percentage of mudstone, quartz and feldspar and less greywacke (40.5, 17, 16 and 26%, respectively) as compared to NZR19 (34, 5.5, 25 and 58.5%, respectively). This suggests that the terrace sample has been subjected to greater weathering, whereby the greywacke is broken up into its component minerals, increasing the feldspar and quartz components. More extensive abrasion of NZR19T is supported by grain size data, where NZR19T is composed of a smaller average clast size of 210 µm as compared to 700 µm of NZR19. Therefore, it is likely that the terrace sediment was deposited at a lower flow regime. Furthermore, the terrace sample visually appeared to have experienced greater chemical weathering due to the greater iron oxide staining surrounding and within the mudstone grain boundaries.

5.4 Major and Trace Geochemical Analysis

5.4.1 Source Rock Composition

Elemental bulk compositions of sediments were determined with the aim of quantifying the extent of chemical weathering. In order to gauge how the sediments differentiate from the bedrock, elemental compositions were compared to an average source rock composition. Four average source rock compositions were utilised in this study and were based on geographical location (Appendix E, Table 14). The average Torlesse Terrane source composition was referenced from Roser and Korsch (1999), where three source rock petrofacies were specified. PF5 represents the average composition of the Pahau sub-Terrane, in the north-east portion of the South Island, PF3 the Rakaia sub-Terrane in the central portion and PF1 in the south-eastern Rakaia (Section 3.2.1, Figure 7). Based on these defined locations, PF5 was used for the average source composition for the Wairau, Awatere, Clarence, Conway, Kowhai and Hapuku Rivers, PF3 for the Rakaia and Waimakariri Rivers and PF1 for the headwaters the Pareora River. The Taramakau drains both Rakaia Torlesse and Haast Schist lithologies as shown in Figure 17 (Section 3.7.3). Mineralogical analysis demonstrated that NZR08 (upper Taramakau) was predominantly derived from the Rakaia Torlesse and NZR11 (lower Taramakau) from the Haast Schist, due to the dominance of greywacke and schist fragments, respectively (Section 5.3.2, Figure 33 and Figure 35). Consequently PF3, quoted from Roser and Korsch's (1999), was used as the average source composition for NZR08.

The average source rock composition for the Haast Schist was derived from Grapes *et al.* (1982), who analysed 32 quartzofeldspathic schists from the Franz Josef and Fox Glacier Area of the Southern Alps. The bedrock samples were taken across the Chlorite to Garnet-Oligoclase zone of the Haast Schist (Grapes *et al.* 1982) and the average geochemistry was utilised as the source composition for the rivers draining predominantly Haast Schist (lower Taramakau, Whatroa, Peorua and Haast Rivers).

The Haast Schist is geochemically quite varied as it grades from Chlorite to Biotite and Garnet-Ogioclase zone schist. Bivarient plots of trace element ratios, shown in Figure 39, for the Haast Schist bedrock, as reported by Grapes *et al.* (1982), demonstrate the geochemical variability. Figure 39 shows that even though the geochemical composition of the bedrock is quite diverse, the Haast Schist-derived sediment samples plot in a small narrow range amongst the scatter. Therefore these plots suggest that the western rivers sampled effectively average out the variability in source rock composition. Consequently the geochemistry of sediment samples can be analysed and compared within geographical source regions.

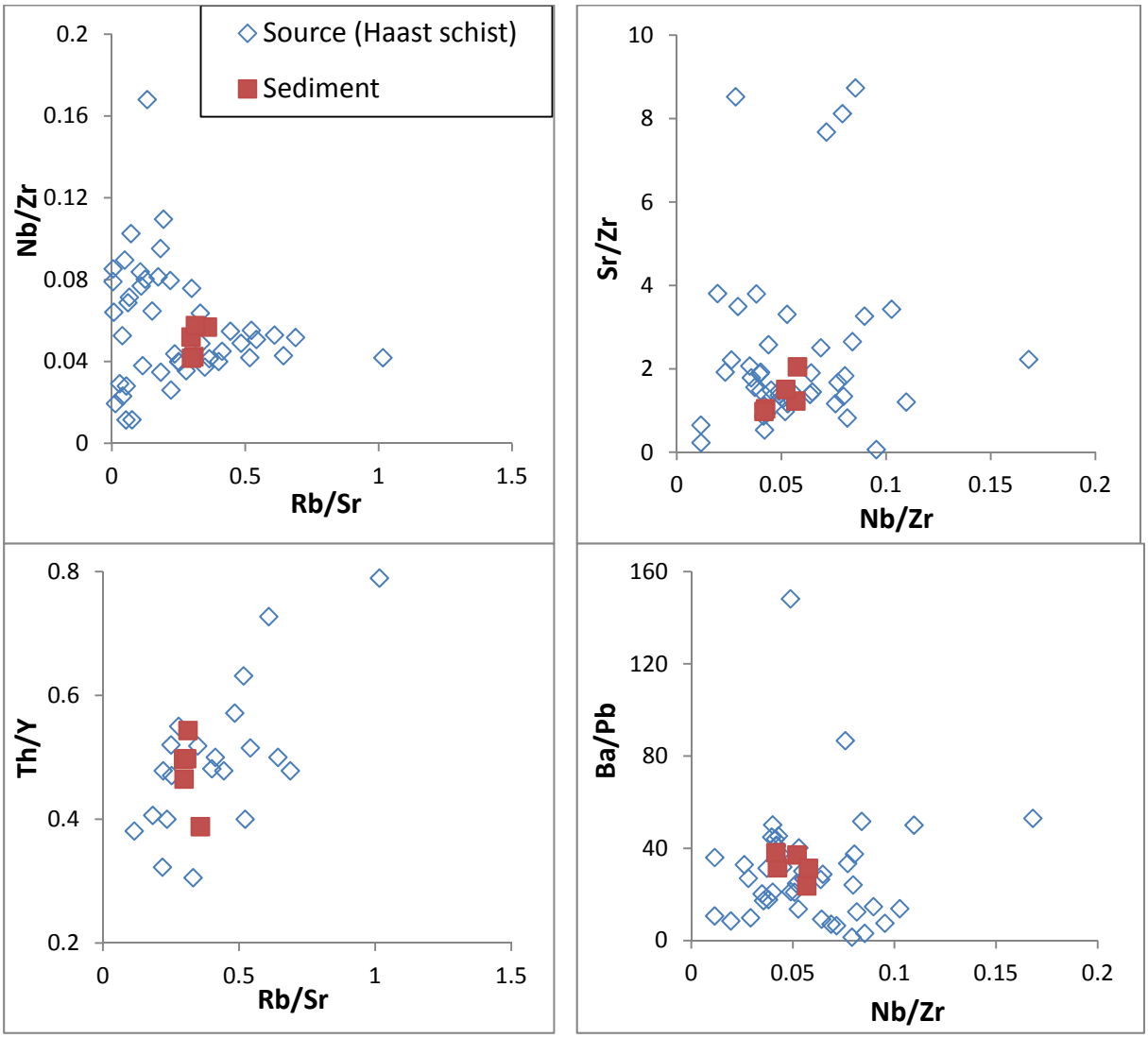

Figure 39: Elemental ratios (A) Nb/Zr versus Rb/Sr, (B) Sr/Zr versus Nb/Zr, (C) Th/Y versus Rb/Sr, & (D) Ba/Pb versus Nb/Zr. Source (open blue diamond) reported from Grapes et al., (1982) and Haast Schist-sediment (red closed square).

5.4.2 Elemental Ratios

Elemental ratios were calculated to identify whether sediments were enriched or depleted in certain elements, as compared to their source. As discussed in Section 2.3, elemental ratios use an immobile reference phase to eliminate geochemical concentration variability due to dilution effects produced by quartz enrichment in weathered sediments. Zr is often used as a reference element as it is often considered the most conservative element and therefore believed to stay in the weathered sediment (Green *et al.,* 2006).

As previously noted in Section 5.1.2, it was observed that Zr is concentrated in the < 63 μm fraction in NZR25 and NZR02 and in the < 125 μm fraction in NZR15. Zr is present in the heavy mineral zircon and for instance Zhang (2002) showed that in the silt fraction, zircon is concentrated in the coarse silt. To assess if grain size has a predominant control on the concentration of Zr in the bulk sediment and thus greatly influence the elemental ratios the relationship between grain size and Zr concentration was investigated. As Zr was observed to be concentrated in the silt fraction, a positive relationship is expected between Zr concentration and percentage silt, if grain size and hydraulic sorting have primary controls. However, Figure 40 shows there is no correlation between the coarse silt and fine sand fractions and Zr concentration for the Haast Schist-, Rakaia Torlesse- or Pahau Torlesse-derived sediments. Furthermore One-Way ANOVA statistical analysis demonstrated that the relationship was not considered significant (Appendix E, Table 18). The lack of systematic relationship suggests that grain size is not a predominant control on bulk Zr concentration and therefore Zr content corrections for grain size would be gratuitous.

Additionally, the source rock compositions of the Torlesse Terrane and Haast Schist have a relatively variable Zr concentration which range from 140 to 239 ppm and 132 to 234 ppm respectively. As the Zr concentration for the majority of the sediments is within the source composition range, it appears that the variation in source lithology has an influence on the Zr conent of the bulk sediment. Consequently, it is acknowledged that grain size does influence the Zr content, However, as source lithology has a more predominant control, its effect cannot be quantified.

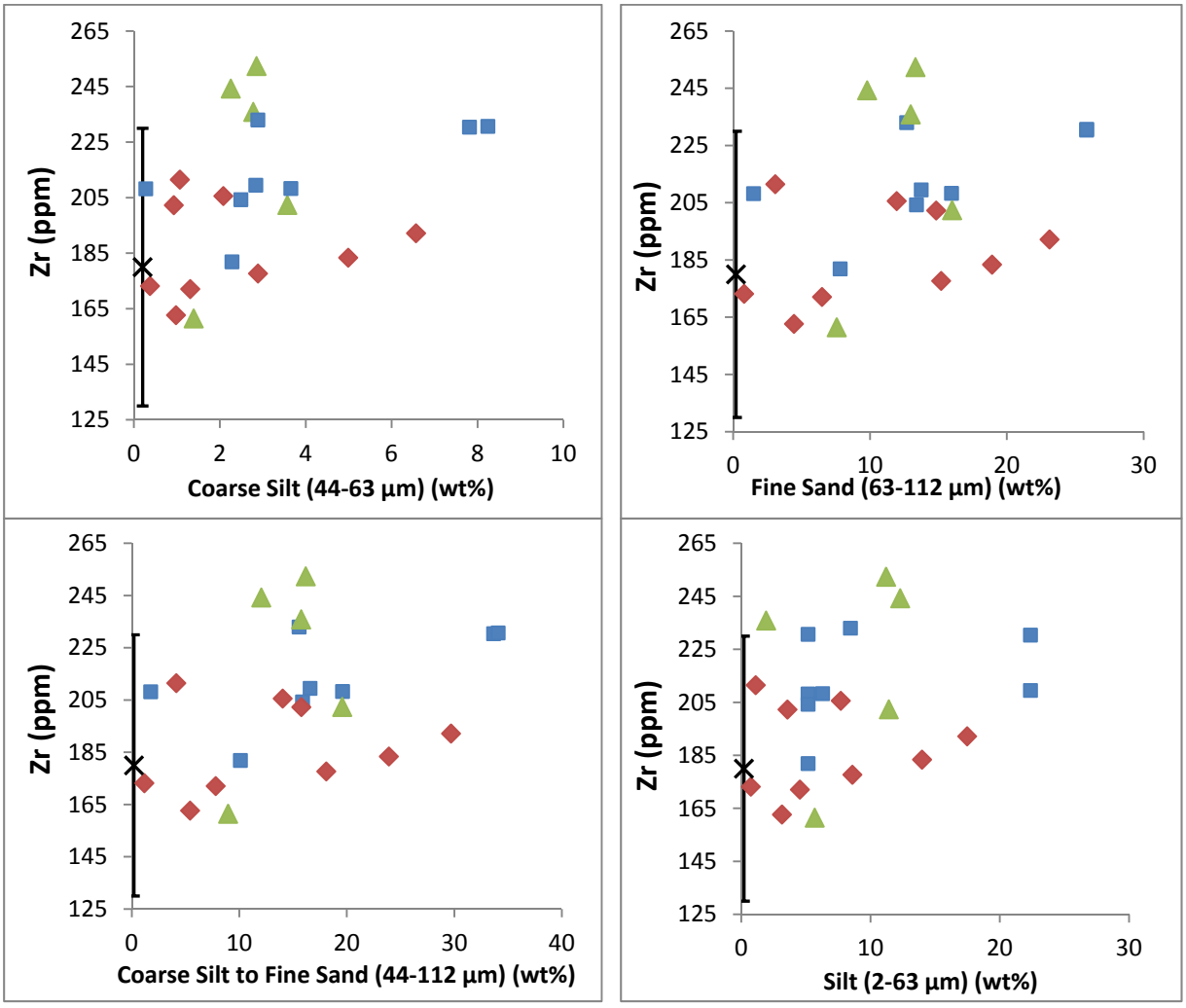

Figure 40: Scatter plots of grain size fractions (A) 44-63 µm, (B) 63-112 µm, (C) 44-112 µm and (D) 2-63 µm versus Zr concentration (ppm) in the Pahau Torlesse Terrane sediments (blue square), Rakaia Torlesse Terrane sediments (red diamond) and Haast Schist sediments (green triangle). Black cross is average Haast Schist and Torlesse Terrane Zr concentration and error bars indicate standard deviation (Grapes et al. 1982; Roser & Korsch 1999).

5.4.3 Major Elements

Phosphorus

As seen in Figure 41, P_2O_5/Zr ratios show that the Torlesse Terrane sediments, except for NZR08, are enriched with P as compared to the average source composition, whereas the Haast Schist sediments are within the range of source composition. Similarly to the Haast Schist-derived sediments, NZR08 is sampled from the western coast of the South Island. Therefore this pattern shows a geographical relationship whereby sediments sampled from the east coast are enriched in P and those sampled from the west show no marked change from the average source composition range. This geographically correlates with the presence of agricultural industry on the east coast, and is likely related to anthropogenic addition of P to waterways through fertilisers (Section 3.6, Figure 9). In contrast, the steep slopes of the Southern Alps on the west coast prevent agricultural industries and therefore are not affected by such addition of P. Consequently it is suggested that enrichment of P in the sediments is attributed to the agricultural industry on the eastern coast.

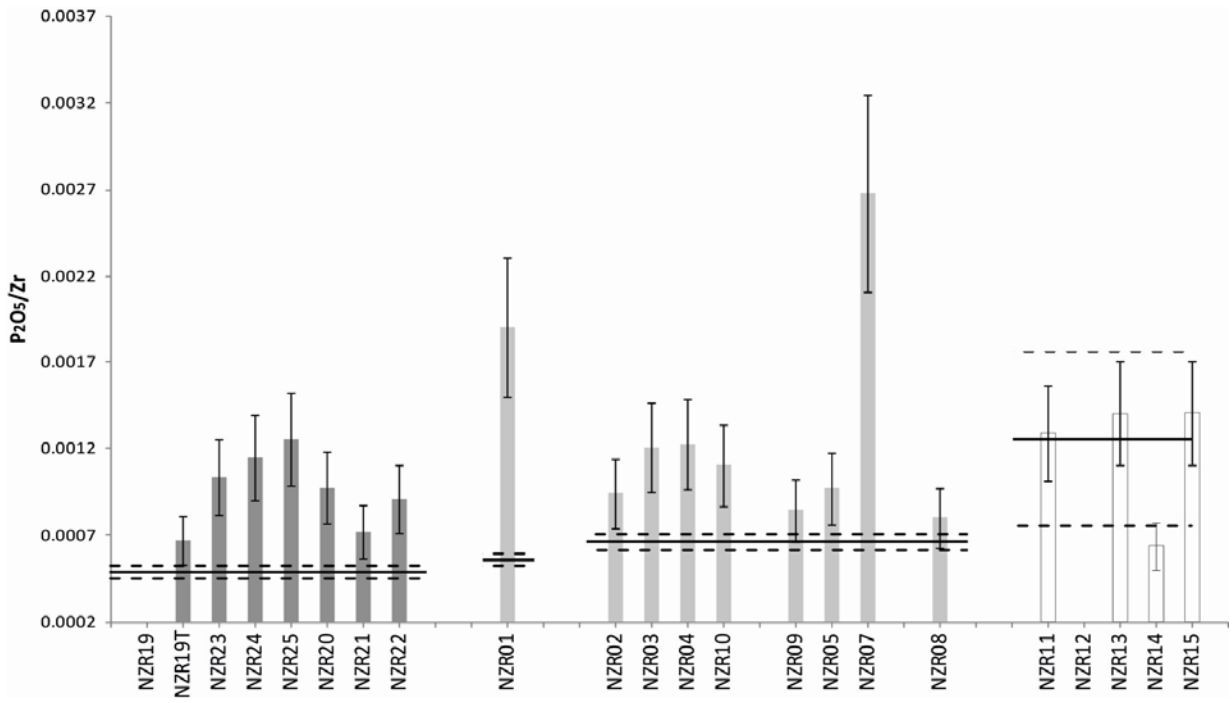

Figure 41: P_2O_5/Zr ratios for the sediments derived from the Pahau Torlesse Terrane (dark grey), Rakaia Torlesse Terrane (light grey) and Haast Schist (white) Solid black line indicates average source composition (Roser & Korsch, 1999; Grapes et al., 1982). Dotted lines above and below represent 2σ from average source.

Torlesse Terrane-Derived Sediments – Si, Fe, Ti & Al

As shown in Figure 42, the elemental ratios SiO_2/Zr, Fe_2O_3/Zr, TiO_2/Zr and Al_2O_3/Zr, for

Grain size Fractions (wt%)	Mean	Standard	Skewne

Torlesse-derived sediments predominantly plot within their source rock variability, when considering measurement error. However, there are a few anomalies, whereby the elemental ratio of the sediment either plots above or below the range of source composition, indicating enrichment or depletion, respectively. Ti and Al are considered to be immobile elements (Roy *et al.* 2008) and therefore, as expected, the majority of sediments plot within the compositional range of their average source rock. However, TiO_2/Zr for NZR24 and NZR25 plots well above the range of their average source composition, whereby their TiO_2 content (0.92 and 0.73 wt%, respectively) is slightly higher than the average of Pahau Torlesse-derived sediments (0.66 wt%). The high concentration of Ti in NZR24 can be explained by the presence of high Ti basaltic deposits within the Awatere catchment (Section 3.7.1, Figure 11) (Baker *et al.* 1994), which could increase Ti content in the sediment. The TiO_2/Zr anomaly in NZR25 could be similarly attributed to lithology, where there is an additional influence of a harzburgite, mafic extrusion in the northern part of the Wairau catchment (Section 3.7.2, Figure 11). Alternatively hydrological sorting may have additionally influenced low zircon content in NZR25.

Al_2O_3/Zr ratios for NZR23 and NZR24 plot just below the Pahau Torlesse composition range. The apparent lower elemental ratio for these sediments is suggested to be due to a higher Zr concentration. This higher concentration could be caused by hydraulic sorting of zircon, which concentrates in the coarse silt and fine sand fractions. Grain size data supports this suggestion, as NZR23 and NZR24 have a greater percentage of coarse silt and fine sand, which could mean a higher content of Zr (Appendix B,

River	*Sample*	coarse (> 2 mm)	sand (63 µm - 2mm)	silt (2 - 63 µm)	clay (< 2 µm)			
Awatere	**NZR24**	0.43	72.88	24.83	1.85	206	1.6	0
Upper Clarence	**NZR19**	12.89	84.73	1.92	0.46	699	1.03	0.2
Clarence (terrace)	**NZR19T**	0.00	83.66	14.24	2.10	208	1.44	0.31
Clarence	**NZR23**	0.68	75.39	22.37	1.57	163	1.36	0.12
Conway	**NZR20**	17.48	75.84	6.29	0.40	324	1.29	0.08
Haast	**NZR14**	0.00	87.21	12.29	0.51	221	1.25	0.29
Haast	**NZR15**	0.00	88.39	11.20	0.41	290	1.41	0.2
Hapuku	**NZR22**	7.34	83.35	8.44	0.86	286	1.3	0.14
Kowhai	**NZR21**	9.62	81.34	8.13	0.91	313	1.34	0.18
Pareora	**NZR01**	13.03	83.67	3.14	0.17	521	1.19	0.11
Poerua	**NZR12**	1.10	86.30	12.32	0.28	237	1.28	0.18
Rakaia Tributary (Andre Creek)	**NZR10**	74.69	24.15	1.11	0.05	855	1.15	0.42
Rakaia	**NZR04**	0.00	85.39	13.98	0.63	293	1.49	0.06
Rakaia	**NZR02**	0.00	95.16	4.53	0.31	291	0.91	0.2
Rakaia	**NZR03**	0.00	96.43	3.57	0.00	200	0.73	0.09
Upper Taramakau	**NZR08**	0.74	90.78	7.69	0.78	292	1.23	0.13
Taramakau	**NZR11**	22.24	71.68	5.68	0.41	533	1.63	0.15
Upper Waimakariri	**NZR07**	8.65	90.62	0.73	0.00	638	0.89	0.02
Upper Waimakariri	**NZR05**	8.53	72.66	17.47	1.34	311	1.81	-0.12
Waimakariri	**NZR09**	0.00	91.19	8.59	0.22	216	1	0.2
Wairau	**NZR25**	0.44	89.87	8.73	0.96	355	1.36	0.3
Whataroa	**NZR13**	0.00	88.01	11.41	0.58	272	1.37	0.31

Table 8). Alternatively, source lithology could explain the lower Al_2O_3/Zr, as NZR23 and NZR24 are sourced from the Inland Kaikoura Range, whose bedrock may have lower Zr content than the average Pahau Torlesse (Section 3.7.1, Figure 12).

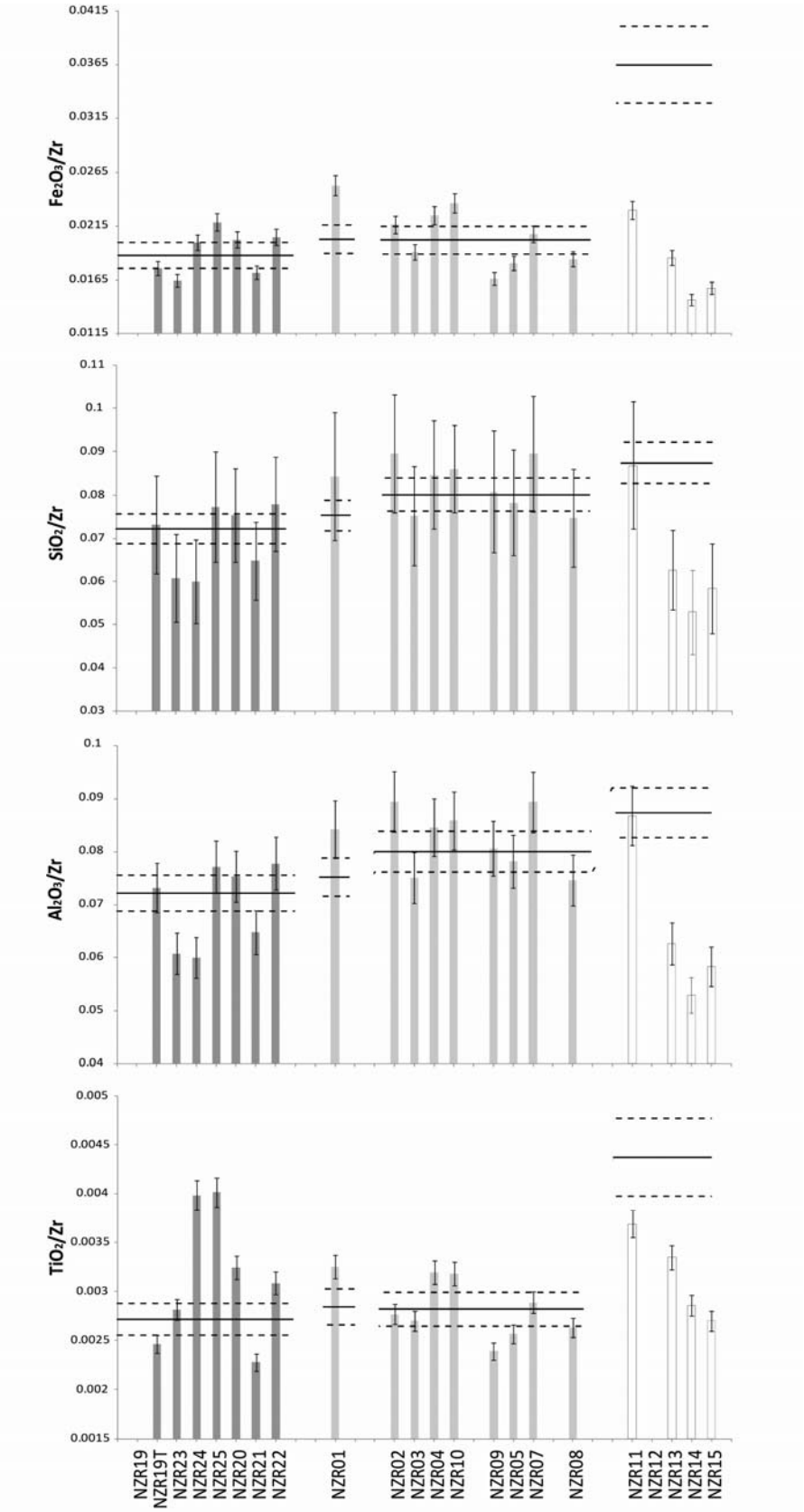

Figure 42: (A) Fe_2O_3/Zr, (B) SiO_2/Zr, (C) Al_2O_3/Zr and (D) TiO_2/Zr for the sediments derived from the Pahau Torlesse Terrane (dark grey), Rakaia Torlesse Terrane (light grey) and Haast Schist (white). No data was obtained for NZR12 or NZR19. Solid black line indicates average source composition (Roser & Korsch, 1999; Grapes et al., 1982). Dotted lines above and below represent standard error from average source. Error bars are 2σ.

Haast Schist-Derived Sediments – Si, Fe, Ti & Al

In contrast to the sediments derived from the Torlesse Terrane, those from the Haast Schist plot below their average compositional source range for the elemental ratios SiO_2/Zr, Fe_2O_3/Zr, TiO_2/Zr and Al_2O_3/Zr (Figure 42). Excepting NZR11 (lower Taramakau), the depletion of these elements could be attributed the geochemical diversity of the Haast Schist, whereby its standard deviation is 2 to 18 times greater than the Torlesse Terrane (Appendix E, Table 14). Even though some of the sediments plot outside their source compositional range defined by the standard error, they still plot within the standard deviation (Figure 43). Therefore the elemental ratios for the Haast Schist sediments could reflect variations in lithology between catchments.

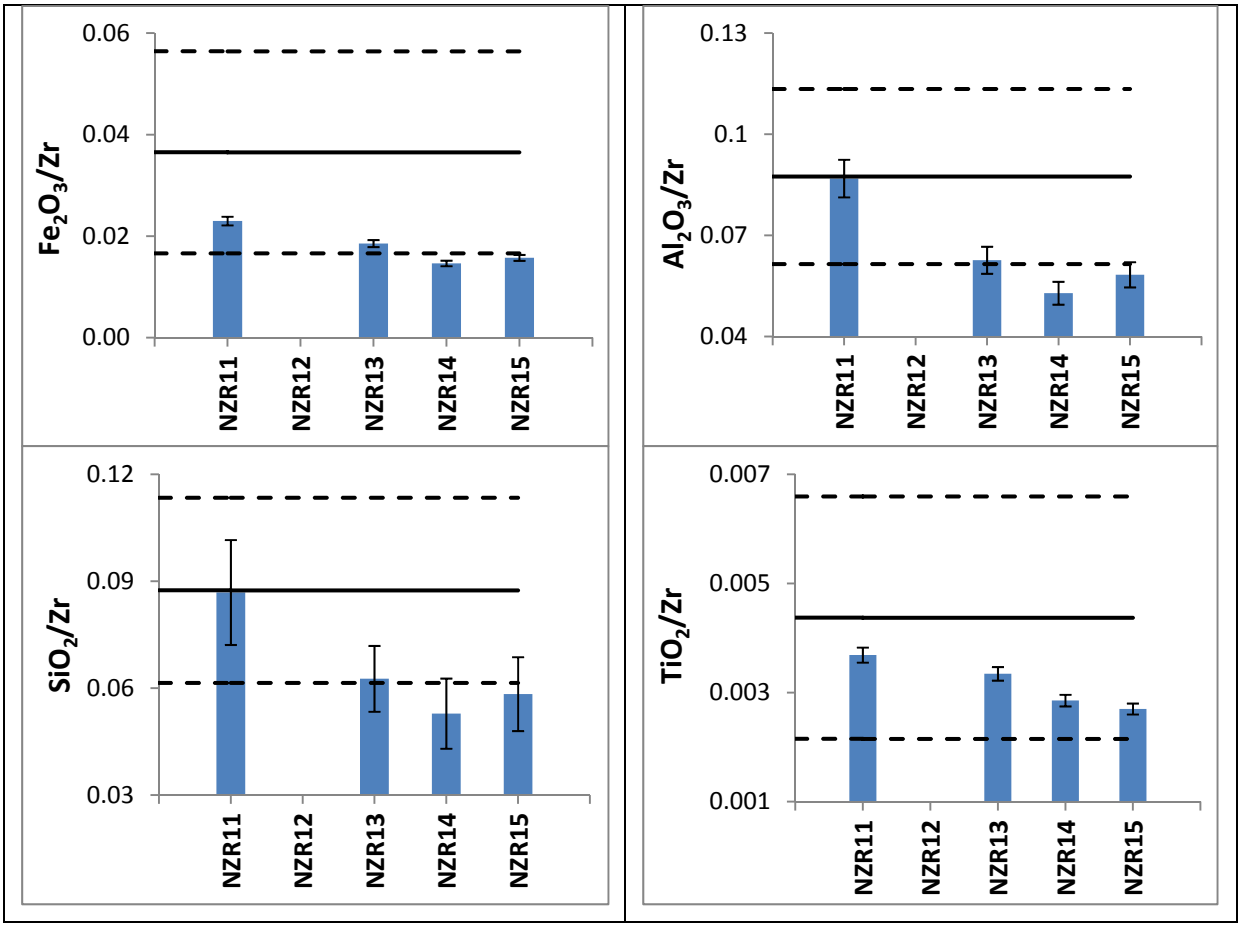

Figure 43: (A) Fe_2O_3/Zr, (B) SiO_2/Zr, (C) Al_2O_3/Zr and (D) TiO_2/Zr for the Haast Schist-derived sediments. No data was obtained for NZR12. Solid black line indicates average source composition (Grapes et al., 1982). Dotted lines above and below represent standard deviation from average source. Error bars are 2σ.

Mobile Oxides – Na, K, Mg & Ca

As previously discussed in Section 2.3, the four most mobile elements in the regolith environment in order of decreasing solubility, are Na, K, Ca and Mg (Taylor & Eggleton 2001). Figure 44 shows that there is a depletion of Na in all the Torlesse Terrane-derived sediments. Furthermore, the Haast Schist-derived sediments plot below the standard deviation of their source composition (Figure 45) suggesting that these sediments are additionally experiencing removal of Na. It is suggested that the depletion of Na could be attributed to the dissolution of plagioclase as Na_2O content is highly significantly and positively correlated with plagioclase content ($F=17.48$, $P> 0.0006$) (Figure 46).

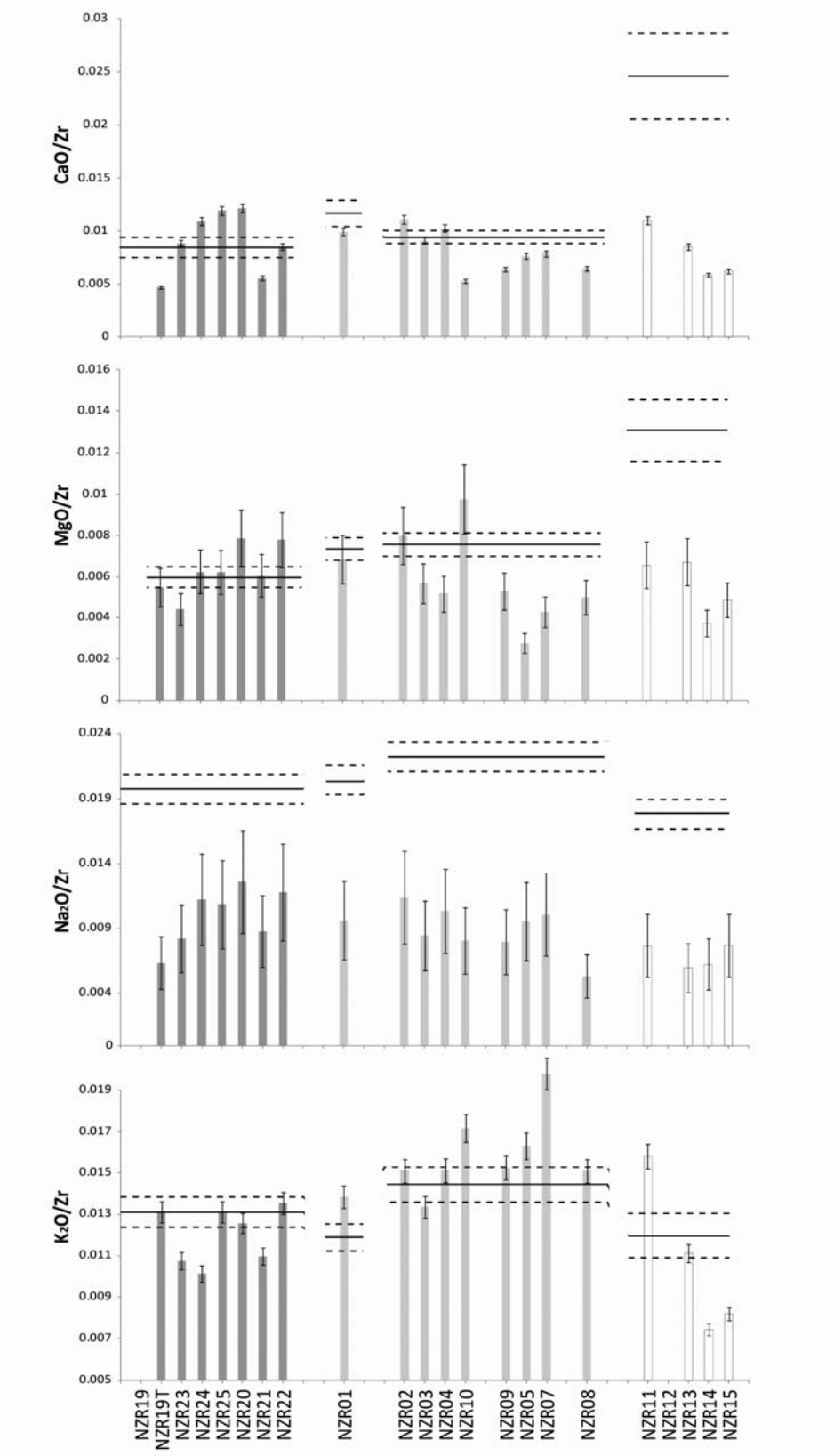

Figure 44: (A) CaO/Zr, (B) MgO/Zr, (C) Na_2O/Zr and (D) K_2O/Zr for the sediments derived from the Pahau Torlesse Terrane (dark grey), Rakaia Torlesse Terrane (light grey) and Haast Schist (white). No data was obtained for NZR12 or NZR19. Solid black line indicates average source composition (Roser & Korsch, 1999; Grapes et al., 1982). Dotted lines above and below represent standard error from average source. Error bars are 2σ.

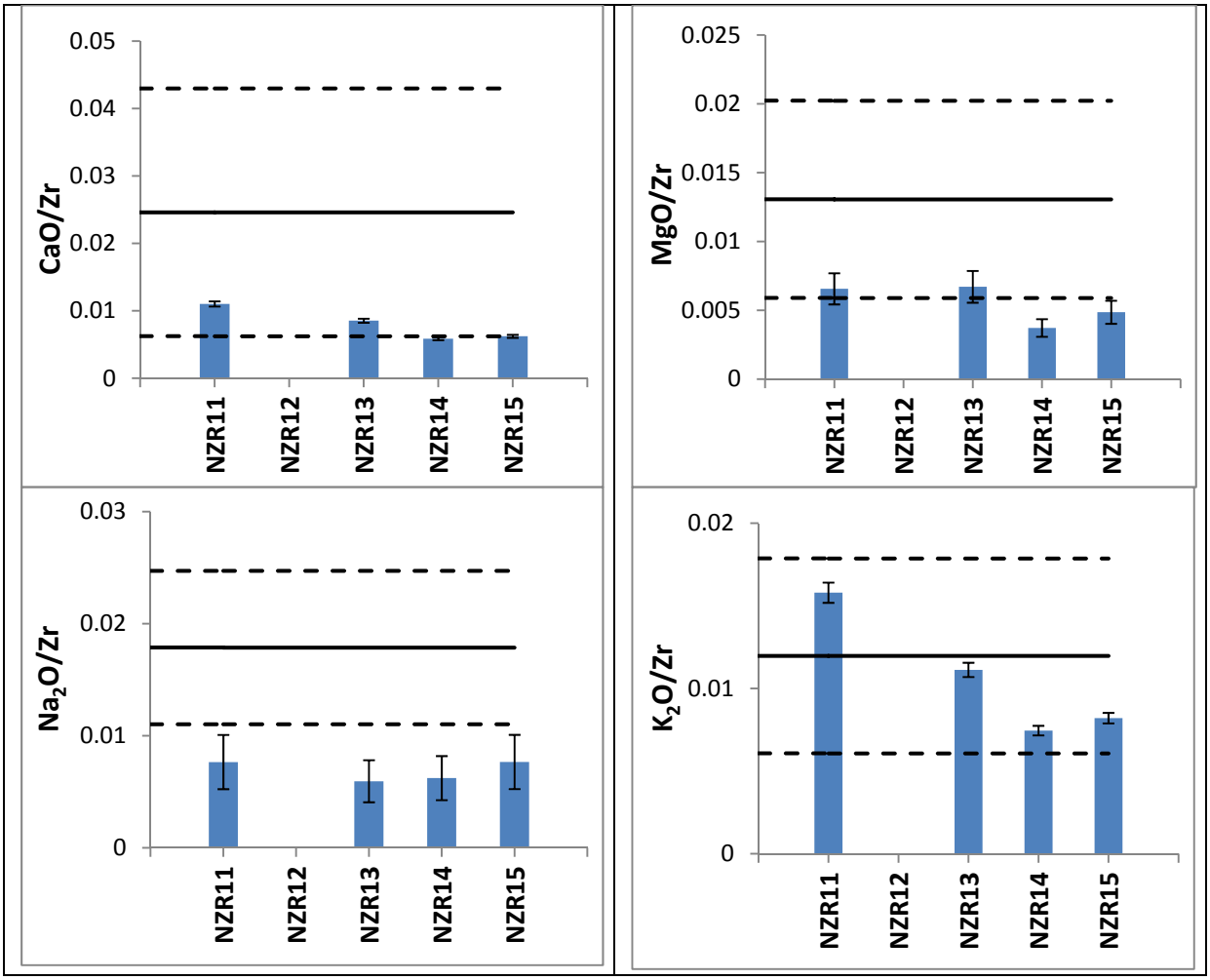

Figure 45: (A) CaO/Zr, (B) MgO/Zr, (C) Na_2O/Zr and (D) K_2O/Zr for the Haast Schist-derived sediments No data was obtained for NZR12. Solid black line indicates average source composition (Grapes et al., 1982). Dotted lines above and below represent standard deviation from average source. Error bars are 2σ.

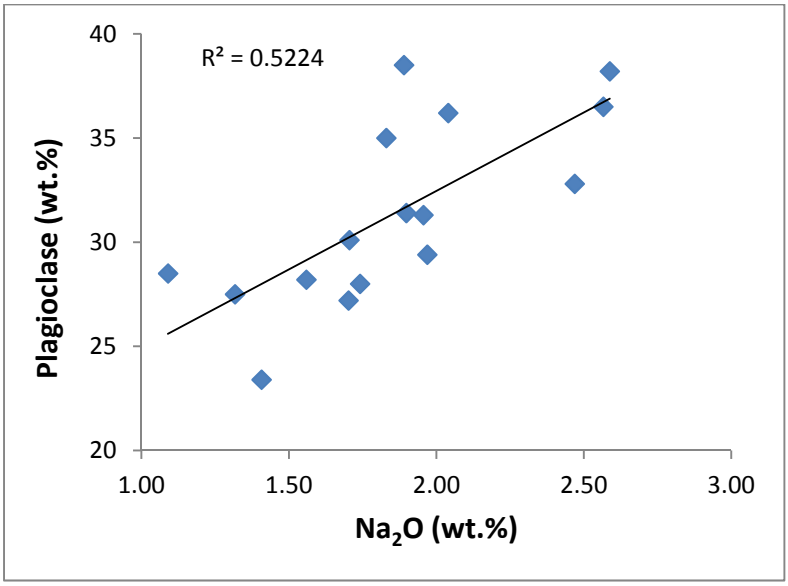

Figure 46: Weight percent of plagioclase versus weight percent of Na_2O in the river sediments.

In contrast, K does not show the same extent of depletion as compared to Na. The majority of the Torlesse Terrane- and Haast Schist-derived sediments plot within standard error of average source rock composition for K, with the exception of NZR21, NZR23, NZR24, NZR14 and NZR15 that plot just below (Figure 44). As previously discussed, NZR23 and NZR24 appear to be enriched in Zr due to hydraulic sorting. NZR21 may also be influenced by an equivalent process, as the concentration of zircon by hydraulic sorting, due to the sample site only contains some pockets of fine sand and silt amongst boulders and cobbles (Figure 47). The dominance of boulders and cobbles could suggest winnowing of the finer grain size fractions, which therefore concentrates zircon as it is a heavy mineral. Furthermore, the K content for NZR21, NZR23 and NZR24 are within standard deviation of the source rock composition, and as such there is no apparent depletion of K in the Torlesse Terrane-derived sediments. The Haast River sediments, NZR14 and NZR15, show depletion in K, however, as previously discussed, this could just be a reflection of lithology variability within the Haast catchment. This is shown in Figure 45, as the K content in the sediments is within standard deviation of the source rock composition. Similarly to Na, K is concentrated in feldspars, namely orthoclase and microcline and is also present in muscovite and biotite (Jacobson 2001). This could explain the apparent enrichment of K in NZR11 due to the higher concentration of orthoclase in the granodiorite intrusions present in the lower proportion of the Taramakau catchment (Section 3.7.3, Figure 17).

Figure 47: Photograph of river bar at sample location site NZR21, Kowhai River. Sample was collected from pockets of sand/silt between boulders and cobbles. Photograph taken by Dr. A Dosseto (2011).

The MgO/Zr ratio for the Pahau Torlesse-derived sediments plot within their source rock composition, whereas the Rakaia Torlesse Terrane and Haast Schist-derived sediments predominantly lower, with the exception of NZR10 and NZR02. Figure 45 additionally highlights that the MgO/Zr ratios for the Haast Schist-derived sediments plot near the lower standard deviation for the source rock composition. This suggests that there is Mg depletion is occurring in the Haast Schist sediments.

The Haast Schist bedrocks contains a relatively high concentration of ferro-magnesian minerals in the (Grapes & Otsuki 1983), which is reflected by a greater average source concentration of Mg as compared to the Torlesse Terrane. Furthermore, the western proportion of the Rakaia sub-Terrane grades into lower grade chlorite schist and therefore additionally has a greater amount of ferro-magnesian minerals contained in phylite fragments. The apparent decrease of Mg in the Rakaia Torlesse Terrane and Haast Schist could possibly be due to weathering of these ferro-magnesian minerals such as amphiboles and biotite.

The Torlesse Terrane-derived sediments do not show marked depletion of Ca, whereby NZR23, NZR24 and NZR25 appear to be enriched in Ca (Figure 44). NZR24 and NZR25 drain from the fault angle depression of the Awatere and Wairau Faults, respectively (Grapes & Wellman 1986; Eden 1989; Grapes *et al.* 1992). The presence of these faults could increase hydrothermal deposits of calcite within the Wairau and Awatere catchments, therefore increasing the Ca concentration of the bedrock. The high Ca content in NZR20 (Conway) is likely to be due to a concentration of calcite, whereby mineralogical analysis identified 3% of clasts as calcite fragments. The regional geological map shows that the lower Conway drainage basin is affected by hillslope deposits (Section 3.7.1, Figure 10), and a landslide upstream from the sampled location was confirmed by fieldwork observation (Figure 48). The landslide results in the erosion of material deep in the weathering profile, providing fresh, primarily unweathered sediment to the river (Corcoran 2005). Therefore the presence of a landslide upstream could explain the presence of highly weatherable calcite fragments within the sediment.

Figure 48: Photograph of a major landslide upstream from sample site NZR21, Conway River. Photograph taken by Dr. A Dosseto (2011).

In contrast to the Torlesse Terrane-derived sediments, those derived from the Haast Schist show a marked depletion of Ca from their average source rock composition (Figure 44). The average CaO content of the Haast Schist (4.50 wt%) is greater than Torlesse Terrane (1.86 wt%) and can be attributed to the presence of hydrothermal calcite veins, associated with the Alpine Fault (Jacobson *et al.* 2003). Even though the CaO content of Haast Schist source rock has a large standard deviation, as compared to the average (4.50 ± 3.12 wt%), the elemental ratios of the sediments are just within the lower standard deviation (Figure 45). Consequently, it can be concluded that there is a greater loss of Ca from the Haast Schist sediments as compared to those derived from the Torlesse Terrane. This supports Jacobson's (2001) study on solute chemistry of streams draining the Southern Alps, which reported that streams draining schist lithology had higher dissolves Ca contents than those draining greywacke.

In summary, Na is the only mobile major element which shows significant depletion within the sediments across all catchments. In comparison, Ca and Mg are markedly depleted in the sediments from the Haast Schist and are slightly depleted in those derived from the Rakaia Torlesse. In contrast, the Pahau Torlesse-derived sediments do

not show a marked depletion of Ca or Mg. However, there was no removal of K observed in any of the catchments. This can be attributed to the greater resistance of K-feldspars to weathering as compared to plagioclase (Nesbitt & Young 1989). The apparent immobility of K suggests that chemical weathering in the South Island is not intense enough to result in the dissolution of K-feldspar. These results are supported by the study conducted by Jacobson *et al.* (2003) who found that the average relative molar abundance of major dissolved cations in rivers draining the Southern Alps, follows the order Ca>Na>Mg>K.

5.4.4 Trace Elements – Sr, Ba, Rb & U

Marx and Kamber (2010) reported that the trace elements Sr, Ba, Rb and U are amongst those that are most sensitive to weathering. Consequently these trace elements are most likely to highlight the extent of weathering the sediment has been subjected to. This section will present preliminary trace element analysis, whereas downstream trends will be discussed in Chapter 6.

Torlesse Terrane-Derived Sediments

Figure 49 highlights that overall the Pahau Torlesse-derived sediments have lower Sr/Zr, Ba/Zr, Rb/Zr and U/Zr ratios as compared to those derived from the Rakaia Torlesse. This can be explained by the depositional history of the Torlesse Terrane whereby the Pahau sub-Terrane was deposited through erosion of the Rakaia sub-Terrane along with the Haast Schist (Roser & Korsch 1999; Wandres *et al.* 2004). Consequently the Pahau Torlesse- derived sediments are more depleted in the mobile U, Rb, Ba and Sr as compared to those derived from the Rakaia Torlesse.

The Sr/Zr and Rb/Zr ratios of the Pahau Torlesse-derived sediments do not appear to deviate from their compositional source range. However, NZR20 appears enriched in Sr and NZR23 and NZR24, Rb. As previously discussed, mineralogical analysis identified 3% of the clasts in NZR20 as calcite fragments. As Sr is chemically similar to Ca, Sr is enriched into calcite by diffusion during water-sediment interaction. This therefore

explains the apparent enrichment of Sr in NZR20 as compared to the average Pahau Torlesse composition. As previously discussed, it is suggested that NZR23 and NZR24 have higher Zr contents due to hydraulic sorting, which could explain their apparent Rb and Ba depletion. Overall the Pahau Torlesse-derived sediments appear to have been subjected to minimal Ba loss. However, due to measurement errors and the compositional range of Ba in bedrock, this observation is not conclusive. In contrast, for the Pahau Torlesse-derived sediments, U is the only trace element that shows marked depletion from the source. Furthermore, Figure 49 shows that U depletion is apparent in NZR19T as compared to NZR19, whereas there appears to be no depletion of Sr, Ba or Rb in the terrace sample compared to the adjacent river sediment. This suggests that further weathering in the terrace deposit leaches U and is not intense enough to remove Sr, Ba or Rb.

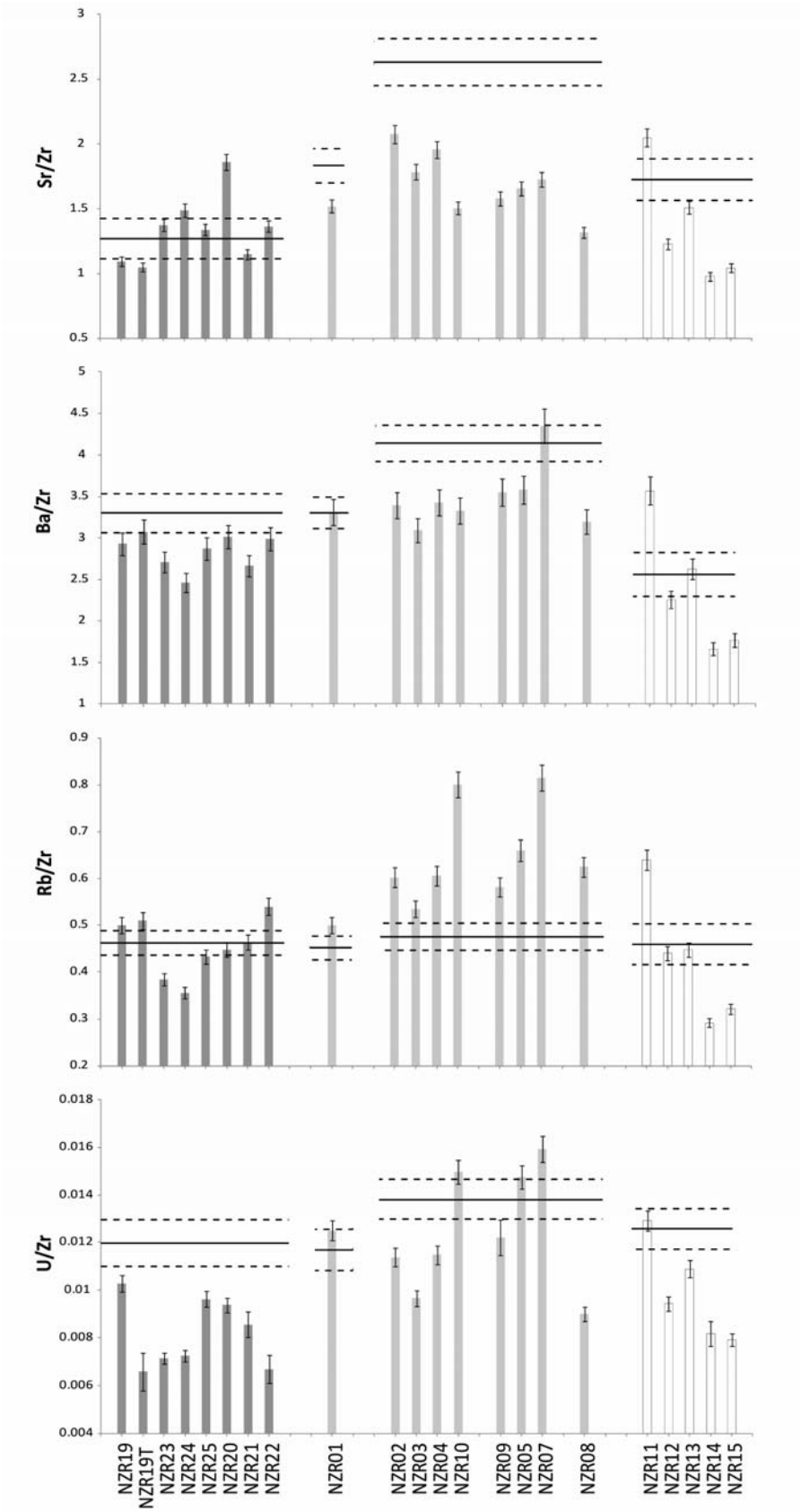

Figure 49: (A) Sr/Zr, (B) Ba/Zr, (C) Rb/Zr and (D) U/Zr for the sediments derived from the Pahau Torlesse Terrane (dark grey), Rakaia Torlesse Terrane (light grey) and Haast Schist (white). Solid black line indicates average source composition (Roser & Korsch, 1999; Grapes et al., 1982). Dotted lines above and below represent standard error from average source. Error bars are 2σ.

In contrast to the Pahau Torlesse-derived sediments, those derived from the Rakaia Torlesse show depletions in Sr, Ba and U. However, the Rb/Zr ratio for all Rakaia Torlesse-derived sediments plots above their compositional source range, indicating that the sediments are enriched in Rb. This could be explained by the Rb concentration of the source rock being underestimated or an external source of Rb.

NZR02 and NZR03 were sampled from the lower Rakaia River, from the southern and northern banks, respectively. Therefore it is interesting to note that the Sr/Zr, Ba/Zr, Rb/Zr and U/Zr ratios, shown in Figure 49, are lower for NZR03 as compared to NZR02. Sections 5.3.1 and 5.3.2 highlighted that the major mineralogy and clast composition between NZR02 and NZR03 is very similar. Additionally these two sediments are geochemically comparable, except for the Zr and Ba contents, whereby NZR02 has a lower Zr and Ba content (NZR02 = 172 and 548 ppm, NZR03 = 202 and 626 ppm). As discussed in Section 4.1, NZR02 and NZR03 were only able to be collected from a relatively small area and therefore are less spatially representative and could be subjected to heterogeneity.

Alternatively, the higher Zr content in NZR03 could be attributed to hydrologic sorting of zircon, which concentrates in the coarse silt fraction. Figure 50 shows that there are cobbles present at the sample site of NZR03, suggesting that winnowing is removing the less dense finer fractions, while zircon (as a heavy mineral) becomes concentrated. The higher hydraulic flow regime of the NZR03 sample site is observed in Figure 51, whereas Figure 52 shows a lower hydraulic flow regime for the sample location of NZR02. This is coupled with NZR02 being collected from behind a vegetated bar, which provides and barrier and further reduces the hydraulic flow. Consequently it is suggested that silt is deposited at this location and therefore the Zr content of NZR02 could be diluted as compared to NZR03. This is supported by grain size analysis where the coarse silt fraction (44 – 63 μm) accounts for 1.3% and 0.9% of NZR02 and NZR03, respectively.

Figure 50: Site location for NZR03. River flow is running right to left on the photograph. The presence of cobbles suggest that the site is experiencing winnowing.

Figure 51: Site location for NZR03. Photo taken to the right of Figure 50. Shows the higher hydraulic flow regime as compared to NZR02.

Figure 52: NZR02 sample site. River flow is running from left to right across photo. The lack of cobbles as compared to NZR03 suggests winnowing is not occurring.

Haast Schist-Derived Sediments

Figure 49 shows that the Haast River sediments NZR14 and NZR15 appear more depleted in Sr, Ba, Rb and U as compared to the average source rock concentration. In contrast NZR11, sampled from the lower Taramakau, appeared enriched in Sr, Ba and Rb, as compared to the average source rock composition. As discussed in Section 3.7.3 (Figure 17), the lower Taramakau hosts a granodiorite pluton, which could explain the higher Sr, Ba and Rb contents in NZR11. Furthermore, the differences in trace elemental ratios could be attributed to the geochemical variation across the metamorphic grades of Haast Schist. Figure 53 highlights that the Haast Schist-derived sediments are within standard deviation of the source composition range. Consequently, this study can not conclusively state whether these sediments show depletions in Sr, Ba, Rb and U, as the ratios could reflect lithology differences, particularly with accessory minerals.

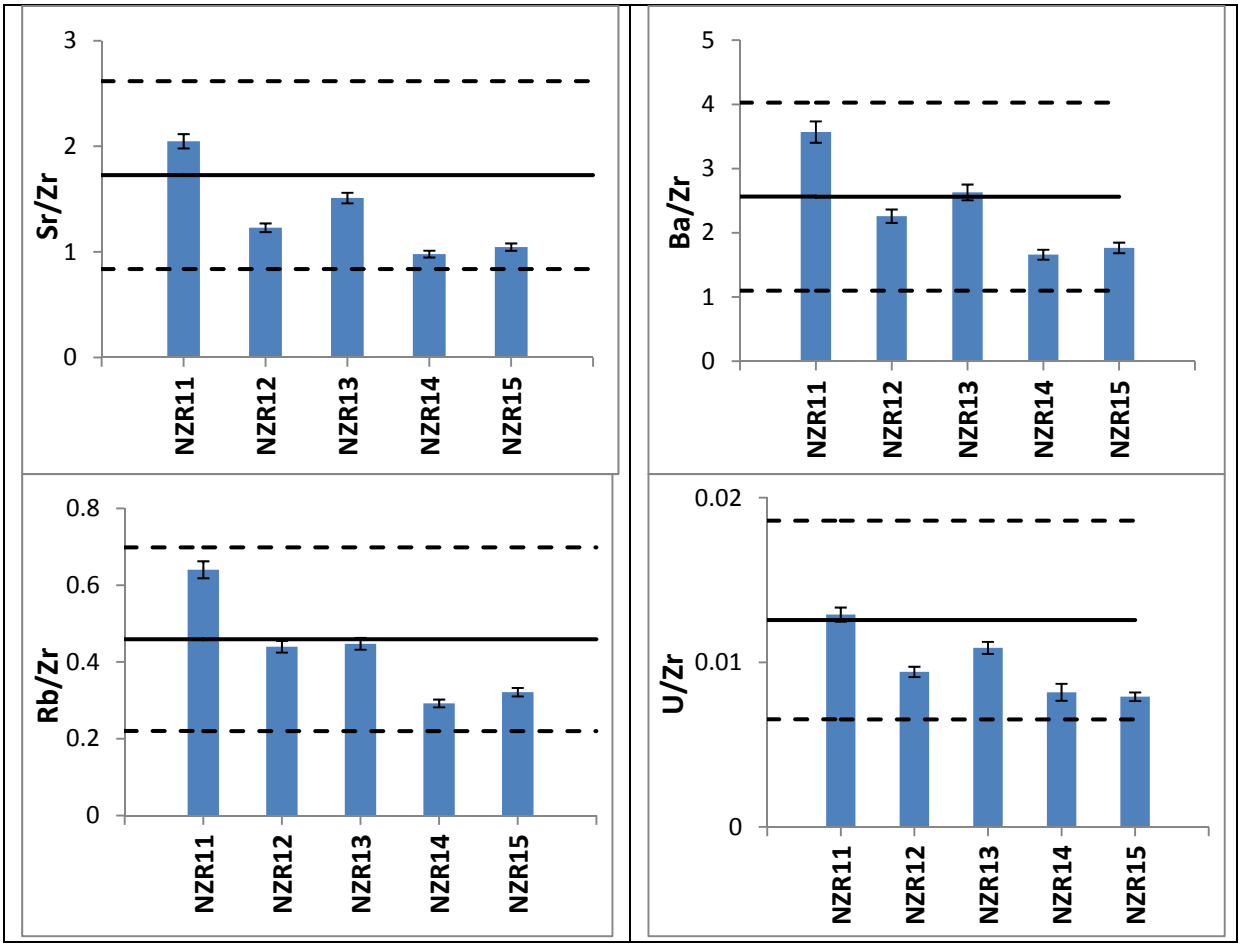

Figure 53: (A) Sr/Zr, (B) Ba/Zr, (C) Rb/Zr and (D) U/Zr for the Haast Schist-derived sediments. Solid black line indicates average source composition (Grapes et al., 1982). Dotted lines above and below represent standard deviation from average source. Error bars are 2σ.

5.4.5 Weathering Indicies – CIA & WIP

As discussed in Section 2.4, a large portion of studies quantify the degree of chemical weathering of sediments by using Nesbitt & Young's (1982) Chemical Index of Alteration (CIA) (Chapter 2, Equation 4), or the Weathering Index of Parker (WIP) (Chapter 2, Equation 5) (Parker 1970). In the calculation of CIA the CaO* parameter is required to be corrected for all carbonate phases, particularly calcite and apatite. In the South Island of New Zealand, hydrothermal activity along the Alpine Fault and associated uplift of the Southern Alps has resulted in extensive quartz-calcite veins (Koons & Craw, 1991; Smith *et al.,* 1996; Templeton *et al.,* 1998). Jacobson *et al.* (2003) reported that Torlesse Terrane and Haast Schist, particularly the higher metamorphic grades, have up to 3% calcite. In addition, Jacobson *et al.* (2003), found that bulk bedload sediments from rivers draining both east and west of the Southern Alps, only had 0.15-0.36 wt% calcite. The low concentration of calcite in the sediments is in agreement with the mineralogy, which only detected calcite in NZR23 (0.1 wt%) and NZR20 (0.1 wt%). Additionally, individual calcite fragments were identified in NZR12 (0.5%), NZR20 (3%), NZR21 (1%) and NZR22 (1%). As the river sediments potentially have small amounts of calcite, in order to calculate CIA, the CaO content needs to be corrected to only include the contribution from silicate minerals.

In this study CaO* was calculated for the river sediments after Honda and Shimizu (1998), assuming the Ca:Na ratio in plagioclase to be 1:3. Plagioclase compositions of Torlesse Terrane greywacke and its metamorphic equivalent, were assumed to be similar to those of average UCC, about a 1:3 ratio of Ca:Na on a molar basis (Taylor & McLennan, 1985). It was assumed that only albite contributed to the Na content of the sediments. Therefore, the number of moles of CaO associated with plagioclase can be calculated using Equation 8 (Honda & Shimizu 1998). Furthermore, the only two major minerals of the sediments to contain Ca are plagioclase and calcite (Roser & Korsch 1999). Consequently the CaO calculated in the above equation was employed in the formula of CIA of Nesbitt and Young (1982).

Equation 8:

$$CaO^{*} = 0.35 \text{ x } 2 \text{ (wt\% } Na_2O)/62$$

Figure 54 shows that the WIP and CIA values for the sediments are within the range of source rock composition, due to the large propagated error associated with measurement of geochemistry within the samples. Even though the sediment WIP values (and CIA values to a lesser extent), seem to indicate that they are more weathered than the source rock, this study cannot conclude on the significance of these results.

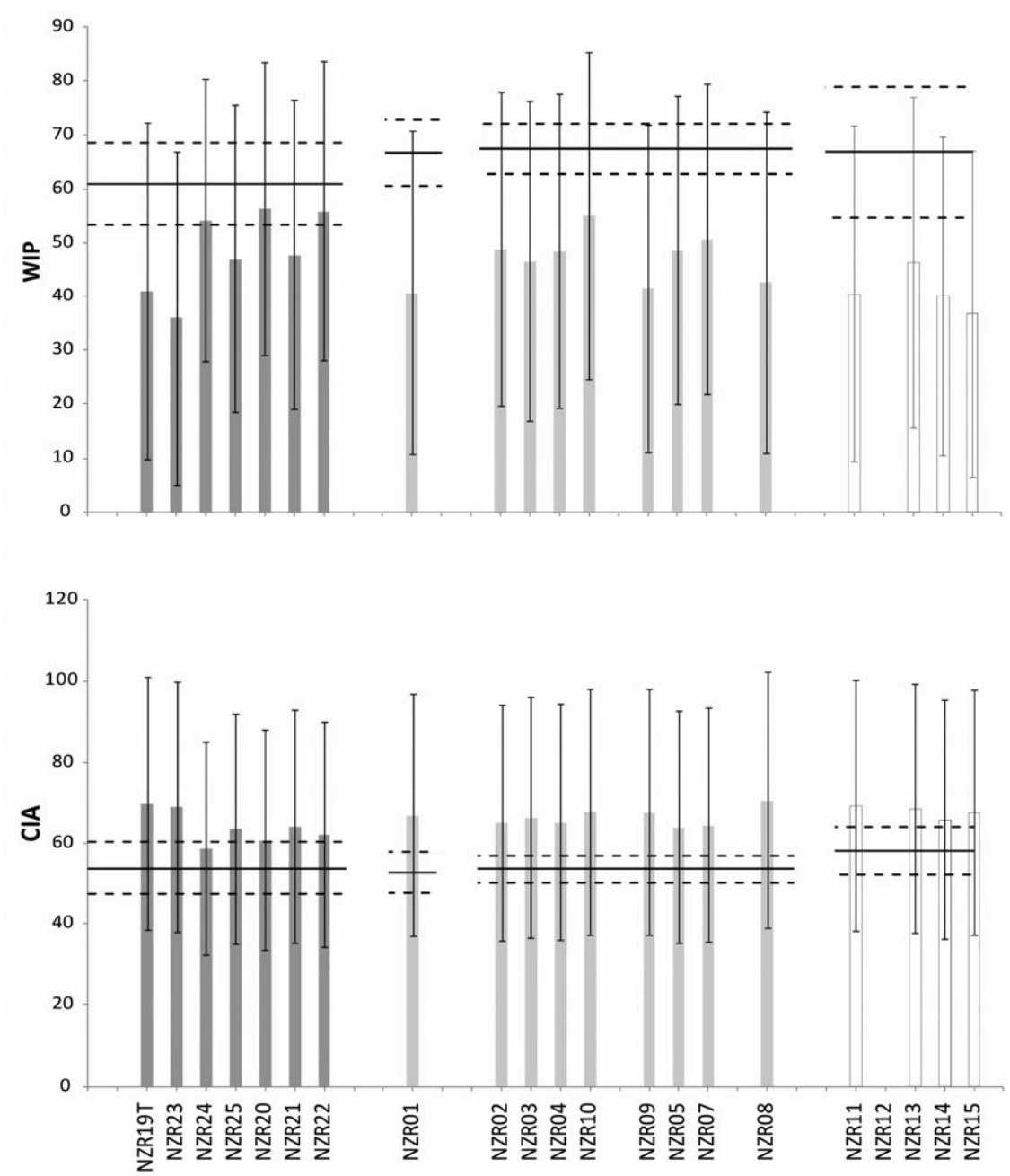

Figure 54: WIP and CIA weathering index values for the sediments derived from the Pahau Torlesse Terrane (dark grey), Rakaia Torlesse Terrane (light grey) and Haast Schist (white) Solid black line indicates average source composition (Roser & Korsch, 1999; Grapes et al., 1982). Dotted lines above and below represent standard error from average source. Error bars are 2σ.

5.4.6 Elemental Ternary Diagrams

A – CN – K Diagram

The bulk composition of river sediments are plotted along with average source rock compositions as molar proportions in Al_2O_3 – CaO* (silicate only) + Na_2O – K_2O (A-CN-K) space (Nesbitt & Young, 1984; Nesbitt *et al.* 1997) in Figure 55. Theoretical weathering trend is indicated by the arrow, which sub parallel to the A-CN axes in Figure 55 (Fedo *et al.* 1995). Roser & Korsch (1999) report that CIA values are similar throughout the Torlesse Terrane, in the range of 52 to 54, which ratios are comparable with those of feldspar (50) and unweathered felsic plutonic and volcanic rocks (45-55). As can be seen from Figure 55, the river sediment compositions somewhat follow the theoretical weathering trend, whereby the Rakaia Torlesse-derived sediments appear to be more weathered as compared to those derived Pahau Torlesse. Furthermore, the Haast Schist-derived sediments follow a similar weathering trend. All bulk river sediments and source rock compositions plot in A-CN-K space on a mixing line between plagioclase (albite) and muscovite. As seen in the A-CN-K diagram (Figure 55), river sediments show a marked loss in Na and Ca and a slight decrease in K, when compared to average source rock composition of the Torlesse Terrane and Haast Schist. This reflects the dominance of chemical weathering of plagioclase and a slight dissolution of K-feldspars.

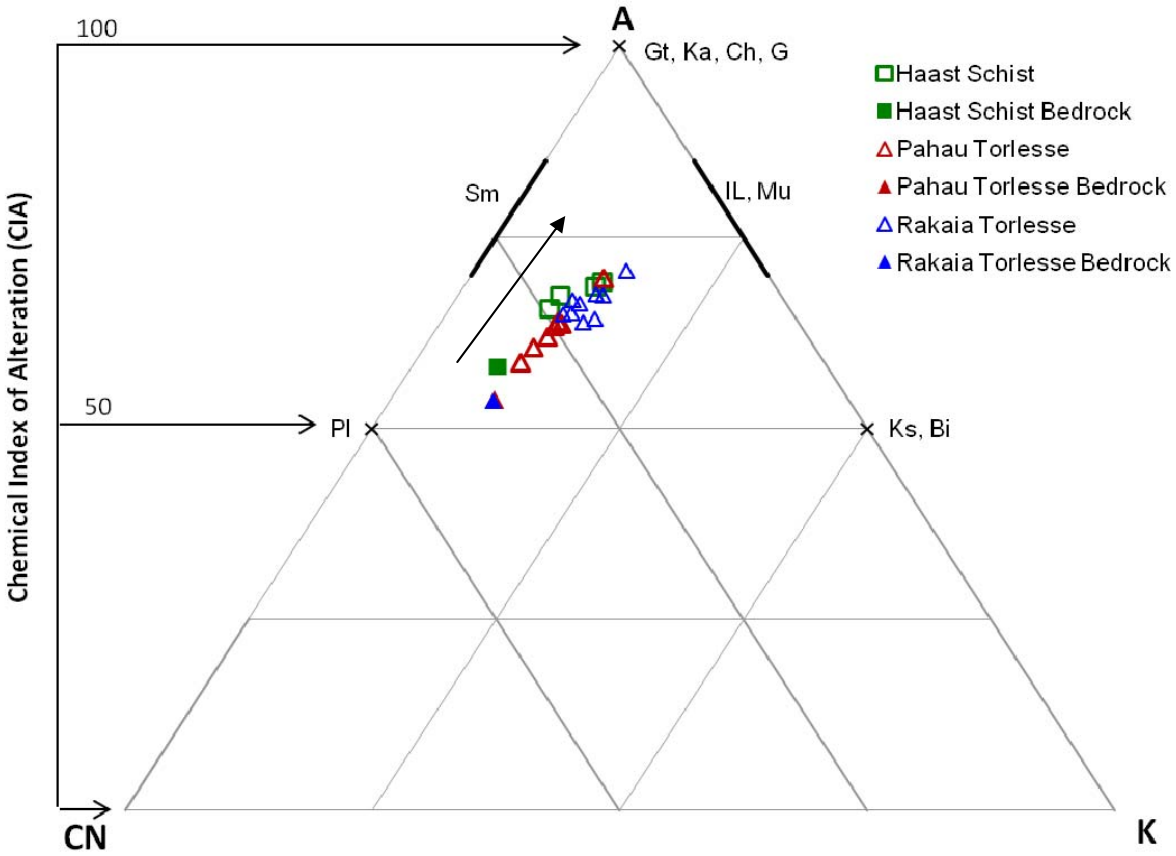

Figure 55: Al_2O_3 – (CaO^* + Na_2O) – K_2O (molar proportions)(A-CN-K) ternary diagram (Nesbitt & Young, 1982). The relationship between the CIA scale and the ternary diagram is shown on the left side of the diagram. The bulk composition of the sediments derived from the Pahau Torlesse Terrane (red open triangle), Rakaia Torlesse Terrane (blue open triangle) and Haast Schist (green open square) are plotted. The closed green square represents the average bedrock composition of the Haast Schist (Grapes et al., 1982) and the closed triangles represent the average bedrock composition of the Rakaia (closed blue triangle) and Pahau (closed red triangle) Torlesse Terrane (Roser & Korsch, 1999). The arrow represents the chemical weathering trend. Abbreviations: Gt = garnet; Ka = kaolinite; Ch = chlorite ; G = gibbsite; IL = illite; Mu = muscovite; Sm = smectite; Pl = plagioclase; Ks = alkali feldspar; Bi = biotite.

A – CNK – FM Diagram

Additionally to the A-CN-K ternary diagram, A-CNK-FM can be used to show weathering trends associated with Fe-Mg bearing mineral assemblages. Figure 56 portrays the molar proportions of Al_2O_3 (A of Figure 56), CaO* + Na_2O (CNK of Figure 56) and FeO (total) + MgO (FM of Figure 56), where CaO represents CaO associated with silicate minerals (Nesbitt & Young, 1989). All sediment samples plot close to the feldspar tie line, which links plagioclase and K-feldspar. This is in agreement with the XRF mineralogy results, reflecting the dominance of feldspars, particularly plagioclase in the sediment composition. The green line indicates the chemical weathering trend of the Haast Schist, which shows that the sediments experience a differential enrichment of Al and therefore move towards the A apex with increased chemical weathering. The lack of deviation from this vertical line suggests that chemical weathering of ferro-magnesian minerals is occurring at a similar rate to feldspars. This can be attributed to the presence of amphiboles in the Haast Schist, which are susceptible to weathering (Grapes *et al.* 1982). The sediments derived from the Torlesse Terrane show two weathering trends, which correspond to their geographical location either in the Pahau or Rakaia sub-Terrane. The red line represents the chemical weathering trend of the sediments from the Pahau Torlesse region and shows a greater depletion of feldspar elements and minimal to no ferro-magnesian change. Furthermore the blue arrow represents the weathering trend of the Rakaia Torlesse Terrane, whereby sediments are being depleted in Ca, Na and K more rapidly than dissolution of ferro-magnesian minerals. This marked difference between the two Torlesse sub-Terranes, reflects the small presence of amphiboles in phylite greywacke, which are located in the western most region of the Rakaia sub terrain and are susceptible to weathering.

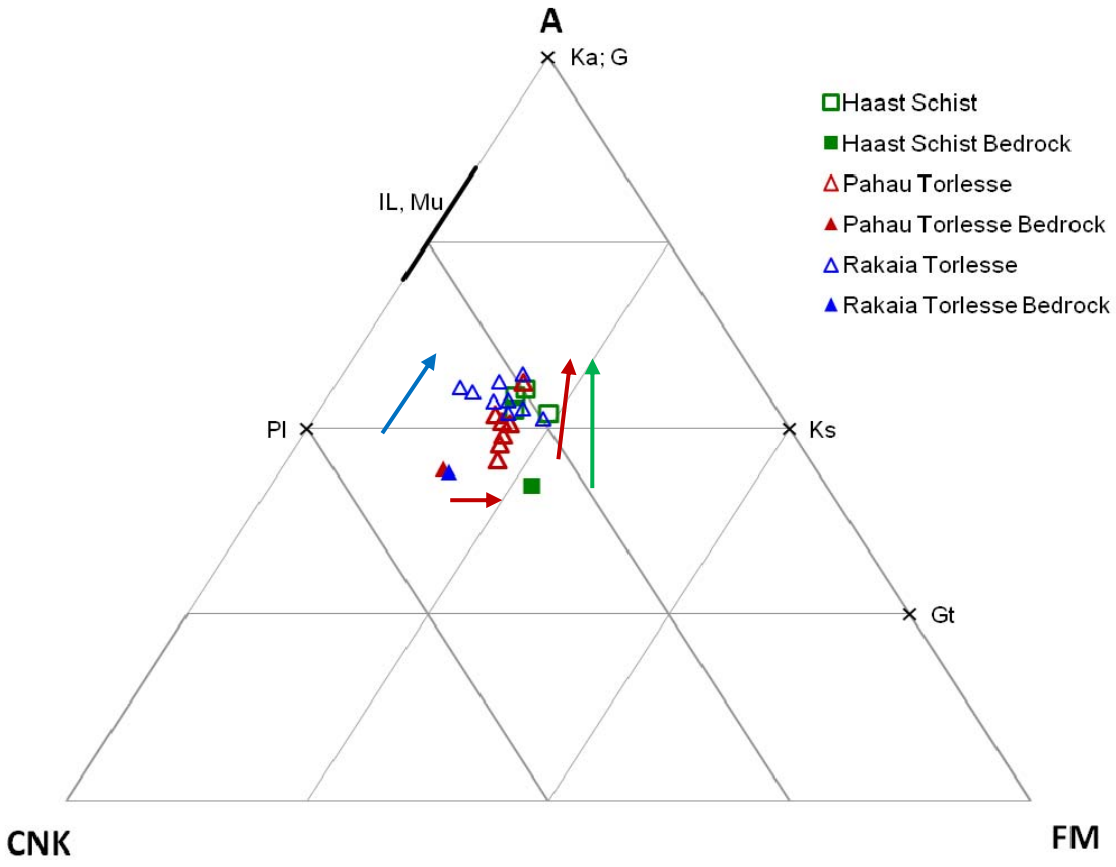

Figure 56: Al_2O_3 – (CaO^* + Na_2O + K_2O) – (FeO_T + MgO) (molar proportions) (A-CNK-FM) ternary diagram (Nesbitt & Young, 1982) for the bulk composition of the river sediments derived from the Pahau Torlesse Terrane (red open triangle), Rakaia Torlesse Terrane (blue open triangle) and Haast Schist (green open square) are plotted. The closed green square represents the average bedrock composition of the Haast Schist (Grapes et al., 1982) and the closed triangles represent the average bedrock composition of the Rakaia (closed blue triangle) and Pahau (closed red triangle) Torlesse Terrane (Roser & Korsch, 1999). Arrows indicate chemical weathering trend for Rakaia Torlesse (blue), Pahau Torlesse (red) and Haast Schist (green). Abbreviations: Gt = garnet; Ka = kaolinite; G = gibbsite; IL = illite; Mu = muscovite; Pl = plagioclase; Ks = alkali feldspar.

S/10-CM-NK Diagram

The sediment samples are plotted into Vital & Stattegger's (2000) $SiO_2/10$ – CaO + MgO – Na_2O + K_2O (S/10-CM-NK) ternary diagram to assist in the investigation of the effects of quartz dilution (Figure 57). The green arrow in this diagram represents the weathering trend of the Haast Schist. Similarly to Figure 56, these sediments are shown to be depleting in both Ca and Mg and Na and K and subsequently becoming enriched in silica. There are two weathering trends of the Torlesse Terrane. The red arrow represents chemical weathering of the Pahau Torlesse, where silicate weathering is dominated by the removal of Na and K and there is no depletion of Ca and Mg silicates. The blue arrow shows the weathering pattern of the Rakaia Torlesse Terrane, showing a similar trend to that observed in Figure 56, whereby there is a greater reduction rate of Na and K as compared to Ca and Mg with is additionally depleting.

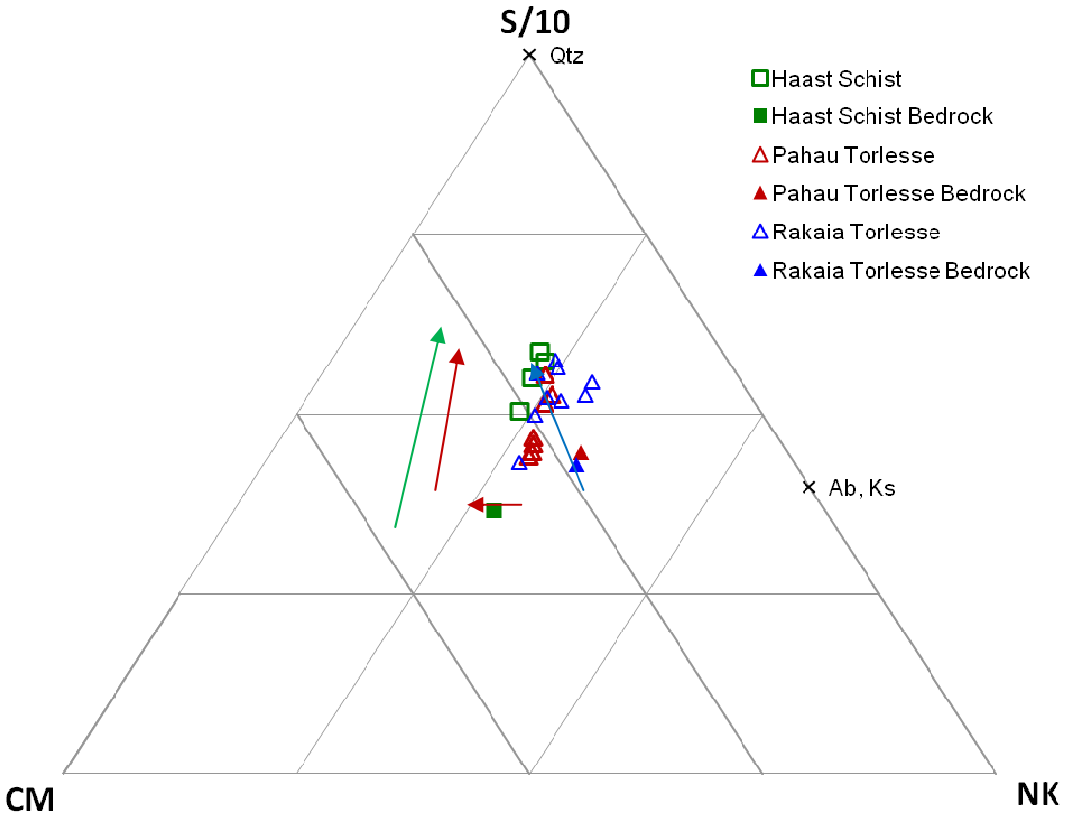

Figure 57: $SiO_2/10$ – (CaO* + MgO) – (Na_2O + K_2O) (molar proportions) (S/10 – CM – NK) ternary diagram (Vital & Stattegger, 2000) for bulk composition of the sediments derived from the Pahau Torlesse Terrane (red open triangle), Rakaia Torlesse Terrane (blue open triangle) and Haast Schist (green open square) are plotted. The closed green square represents the average bedrock composition of the Haast Schist (Grapes et al., 1982) and the closed triangles represent the average bedrock composition of the Rakaia (closed blue triangle) and Pahau (closed red triangle) Torlesse Terrane (Roser & Korsch, 1999). Arrows indicate chemical weathering trend for Rakaia Torlesse (blue), Pahau Torlesse (red) and Haast Schist (green). Abbreviations: Qtz = quartz; Ks = alkali feldspar; Ab = albite.

5.5 Sr-Series Isotopes

As discussed in Section 4.8, an additional leaching step with sodium acetate was performed on two aliquots of NZR03 and NZR23 before undergoing acid digestion, to remove carbonate minerals. This was performed as carbonates could have a different $^{87}Sr/^{86}Sr$ signature than the primary silicate minerals. Analysis showed that the additional leaching of sodium acetate removed 254 and 106 ppm of Sr from NZR03 and NZR23, respectively. The non-leached aliquots carbonates were found to have a higher concentration of $^{87}Sr/^{86}Sr$, as compared to the primary minerals (Appendix F, Table 19). Due to the low relative standard deviation of between leached and non-leached aliquots (NZR03 = 0.018% s.d., NZR23 = 0.013% s.d.), for the purposes of this study, carbonate content did not have a major effect on use of $^{87}Sr/^{86}Sr$ as a provenience tracer for the sediments.

$^{87}Sr/^{86}Sr$ ratios for sediments derived from the Torlesse Terrane and Haast Schist are graphically displayed in Figure 59, while those derived from the Grey River are shown in Figure 58, for comparison. It can be observed from Figure 58, that the three samples from the Grey River tributaries show relatively variable $^{87}Sr/^{86}Sr$ ratios, which range from 0.714265 (NZR16) to 0.728370 (NZR18). In contrast, $^{87}Sr/^{86}Sr$ ratios from the river sediments from catchments underlain by Torlesse Terrane and Haast Schist are less variable, ranging from 0.707080 (Awatere; NZR24) to 0.711994 (Andre Creek; NZR10). The relative high variation of the $^{87}Sr/^{86}Sr$ values for Grey River can be attributed to the complex geological setting of the Buller Terrane, consisting of Green Group greywacke, fluvial deposits and an extensive series of granitic intrusions (Mew 1980; Mason & Taylor 1987; Jongens 2006). In comparison the narrow range of $^{87}Sr/^{86}Sr$ values for rivers draining the Torlesse Terrene and Haast Schist, can be explained by their single origin, whereby the Haast Schist is the metamorphic equivalent of the Torlesse Terrane (Roser & Cooper 1990).

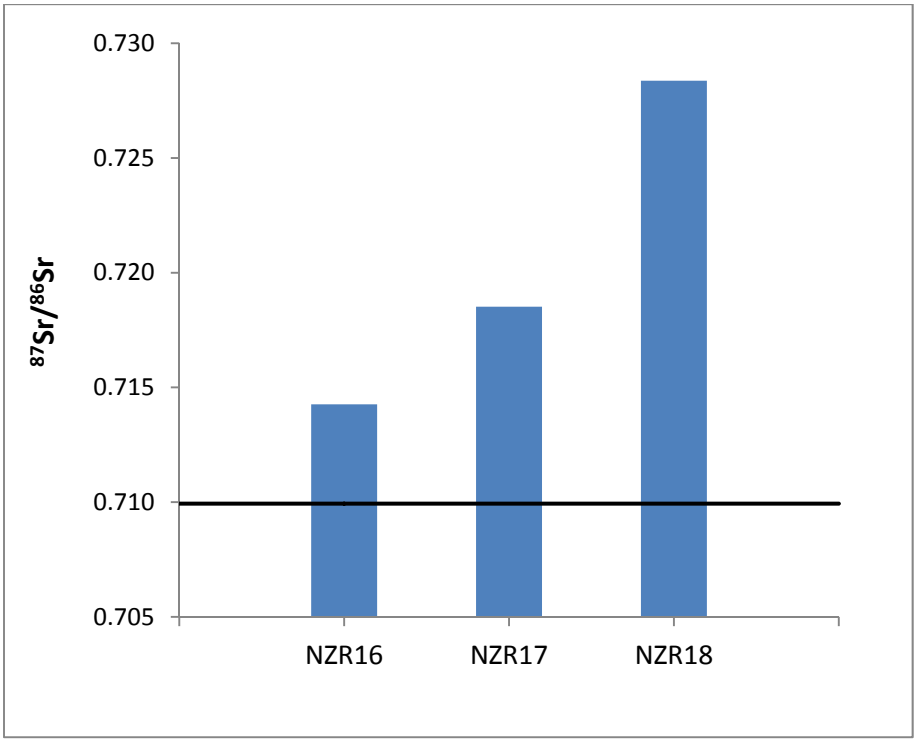

Figure 58: $^{87}Sr/^{86}Sr$ ratio of river sediments from tributaries of the Grey River. Solid black line represents the average $^{87}Sr/^{86}Sr$ ratio of Terrane greywacke and Haast Schist sediments.

The river sediments sampled from the Rakaia Torlesse have a very narrow range of $^{87}Sr/^{86}Sr$ ratios from 0.710062 (Pareora; NZR01) to 0.711994 (Andre Creek; NZR10). Figure 59 visually displays that the $^{87}Sr/^{86}Sr$ ratio is very similar between the Rakaia River sediments (NZR02, NZR03, & NZR04; varying from 0.710271 to 0.710562), however, the sediment sample from the headwaters of a Rakaia tributary (Andre Creek) is relatively different (0.711994; NZR10). This could be explained by the small drainage catchment area of NZR10 (1.8 km^2), which therefore drains from a small locality, whereby the $^{87}Sr/^{86}Sr$ ratio could be relatively high on a catchment scale. This is compared to the relatively large drainage catchment areas NZR02, NZR03and NZR04 (2833, 2833, & 2590 km^2, respectively) that average the $^{87}Sr/^{86}Sr$ bedrock signature throughout the catchment. Furthermore these markedly different $^{87}Sr/^{86}Sr$ ratios, suggest that Andre Creek is not the main sediment source for the Rakaia River.

Similarly, the Waimakariri River sediments (NZR09, NZR05, & NZR07) show a very narrow range of $^{87}Sr/^{86}Sr$ ratios (0.711105 to 0.711145). Furthermore these values are slightly lower than the sediment from upper Taramakau (NZR08; 0.711879). This confirms that the Waimakariri and upper Taramakau headwaters drain similar bedrock, whereby the Taramakau drains the opposite side of the Southern Alps to the Waimakariri. These $^{87}Sr/^{86}Sr$ values are in agreement with literature referenced ratios for the Rakaia Torlesse reported in Pickett and Wasserburg (1989) of 0.7115 ± 0.0125 (± 1 s.d.).

Likewise, rivers draining the Pahau Torlesse that have a similar geographical location, have analogous $^{87}Sr/^{86}Sr$ ratios. For instance Hapuku (NZR22) and Kowhai (NZR21) are geographically adjacent catchments and have $^{87}Sr/^{86}Sr$ values of 0.708463 and 0.708667, respectively. The upper Clarence River sediment has an $^{87}Sr/^{86}Sr$ ratio compatible with its adjacent terrace sediment (0.710595 and 0.710730, respectively). However, the river sediment sampled in the lower Clarence catchment has a lower $^{87}Sr/^{86}Sr$ ratio of 0.707819. This ratio is similar to the adjacent catchments of Awatere to the north (0.707080) and Conway to the south west (0.707160). It is therefore suggested that the greywacke in the upper proportion of the Clarence catchment has a higher $^{87}Sr/^{86}Sr$ ratio, than that in the middle and lower proportions of the drainage basin. Furthermore, the upper Clarence (NZR19) and Wairau (NZR25) headwaters drain adjacent bedrock and have similar $^{87}Sr/^{86}Sr$ ratios (0.710595 and 0.709196, respectively). This supports the hypothesis that western most proportion of the Pahau Terrane has a relatively higher $^{87}Sr/^{86}Sr$ signature than the Rakaia and eastern portion.

Despite slight differences in lithology, Peorua (NZR12), Whatroa (NZR13) and lower Taramakau (NZR11) have comparable $^{87}Sr/^{86}Sr$ ratios (0.710267, 0.710662 and 0.710716, respectively). Whereas the river sediments sampled from the Haast River, NZR14 and NZR15, have similar $^{87}Sr/^{86}Sr$ ratios (0.709016 & 0.709175, respectively). These values are slightly lower than those from the more northern sediments, suggesting the $^{87}Sr/^{86}Sr$ signature is slightly higher in the northern Haast Schist.

Overall the $^{87}Sr/^{86}Sr$ values demonstrate a geographical relationship whereby sediments within similar regions are derived from bedrock that has equivalent $^{87}Sr/^{86}Sr$ ratios. Furthermore the $^{87}Sr/^{86}Sr$ values in this study is in agreement with those for the Haast Schist and Torlesse Terrane, reported by Jacobson (2001) (0.7043 to 0.7124).

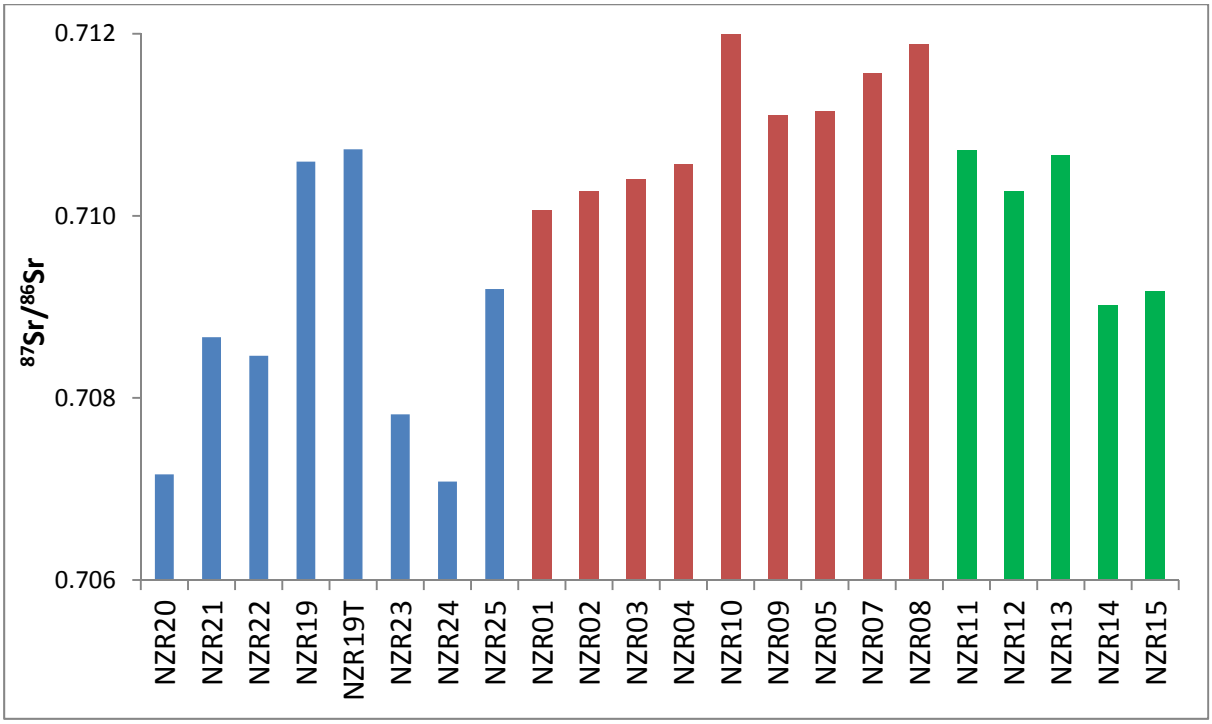

Figure 59: $^{87}Sr/^{86}Sr$ ratio of sediments derived from Pahau Torlesse (blue), Rakaia Torlesse (red) and Haast Schist (green).

5.6 U- Series Isotopes

As discussed in Section 4.8, an additional leaching step with sodium acetate was performed on two aliquots of NZR03 and NZR23 before undergoing acid digestion, to remove carbonates. This was performed to investigate the effect of carbonates on U-series analysis, in addition to their contribution to the $^{87}Sr/^{86}Sr$ ratio. Analysis showed the two samples that had carbonates leached had higher U and Th concentrations, than their respective non leached sample (Appendix G, Table 20). Furthermore, the activity ratios between the leached and non leached sample were within error. This suggests that U or Th is minimal or non-existent in the carbonates and consequently do not contribute to the activity ratio.

U concentrations in the suspended particles show a relatively narrow range of values, ranging from 1.40 (Hapuku; NZR22) to 3.17 ppm (Rakaia tributary headwaters; NZR10). The top range of these values is equivalent to the average upper crust (2.8 ppm; Taylor & McLennan, 1985). The highest values are those which are sampled at the headwaters of the Waimakariri (NZR05 & NZR07) and Rakaia tributary (NZR10), whereas the lower values are those sampled from the rivers that drain Pahau Torlesse Terrane greywacke. The lower concentration of U in rivers draining the Pahau Torlesse Terrane could mean these sediments could have previously experience greater leaching of U as compared to the Rakaia Torlesse Terrane during an earlier weathering cycle. This is consistent with Roser & Korsch's (1999) theory that the Pahau Terrane is derived from erosion of exposed Rakaia sediments (see Chapter 3, Figure 6).

The Th concentrations range from 7.92 (Awatere; NZR24) to 14.97 ppm (Whataroa; NZR13). All the sediments, which were analysed for Th, apart from Rakaia tributary headwaters (NZR10) have Th/U ratios higher than an average upper continental crust composition (3.8; Taylor & McLennan, 1985). As U is a lot more mobile than Th, these results are in agreement with literature references which report that the Rakaia terrane was deposited as a turbidite succession (Roser & Korsch 1999; Wandres *et al.* 2004).

($^{234}U/^{238}U$) ratios in sediment particles are close to secular equilibrium, ranging from 0.838 (Haast; NZR 14) to 1.139 (Upper Clarence Terrace; NZR19T). Excluding NZR19T and NZR14, the ($^{234}U/^{238}U$) ratio of the river sediments are in a relatively narrow range of 0.959 (Upper Clarence; NZR19) to 1.064 (Upper Taramakau; NZR08). Note that all South Island river sediments sampled, except Waimakaimi (NZR05 & NZR09), Haast (NZR14), Conway (NZR20), Clarence (NZR19 & 23) and Wairau (NZR25) exhibit ($^{234}U/^{238}U$) > 1. This is unexpected as the ($^{234}U/^{238}U$) ratio for sediment particles is anticipated to be less than 1 (Vigier et al., 2001). As previously discussed (Section 2.5.2), this is because when ^{238}U decays to ^{234}Th it can be injected from the minerals grain by recoil, before rapidly decaying to ^{234}U (Dosseto *et al.* 2008). This therefore results in the solution having ($^{234}U/^{238}U$) > 1 and sediment < 1. Other studies have similarly reported ($^{234}U/^{238}U$) activity ratios greater than 1 (Porcelli *et al.* 2001; Dosseto *et al.* 2006), which have been explained by adsorption of U from solution with an ($^{234}U/^{238}U$) > 1, onto secondary phase Fe-oxides, which are precipitated onto sediment grains in the fluvial system (Dosseto *et al.* 2008). Fluvial systems in the South Island, have been reported to have ($^{234}U/^{238}U$) activity ratios greater than 1, which support this explanation for sediment ($^{234}U/^{238}U$) being less than 1 in this thesis (Robinson *et al.* 2004). This study reported ($^{234}U/^{238}U$) river water values that range from 1.1 (Taramakau) to 4.6 (Kowhai), for catchments covered in this thesis (Appendix G, Table 20). It is also interesting to note that the two lower Haast river sediment samples, NZR14 and NZR15, which were sampled approximately 10 km apart, have quite difference ($^{234}U/^{238}U$) ratios of 0.838 and 1.007, respectively.

($^{230}Th/^{238}U$) ratios in sediment particles are close to secular equilibrium, ranging from 0.936 (Rakaia tributary headwaters; NZR10) to 1.044 (Lower Clarence; NZR23). Rakaia tributary headwaters (NZR10) and lower Taramakau (NZR08) show ^{238}U enrichment relative to ^{230}Th. This is the opposite of what is usually expected for sediment particles due to the greater mobility of ^{238}U, as compared to the immobile ^{230}Th (Vigier et al., 2001). Similarly findings have been documented in other studies, such as Dosseto *et al.,* (2006), who reported ($^{230}Th/^{238}U$) < 1 in suspended sediments in the lowland rivers of the Amazon basin. This finding was attributed to the increased solubility of Th by high dissolved organic carbon in the water, whereby Th complexes to the organic colloid

molecules (Dosseto *et al.* 2006; Dosseto *et al.* 2008). NZR08 could be subjected to lower pH conditions due to the presence of dredge tailings and sluiced ground mining waste in close proximity to the sampling site (see Chapter 3, Figure 17) (Nathan 1993). Once mobilised, by the lower pH environment, the Th could complex to organic colloids which may be in the fluvial system. Mobilization of Th in Andre Creek (tributary of the Rakaia; NZR10) could have additionally occurred by the influence of vegetation and the longer residence time in the weathering profile. Vegetation in the catchment can increase the acidity soil water due to the production of organic acids, causing Th to mobile and complex with the organic matter (Kump *et al.* 2000). The longer residence time of NZR10 in the weathering profile can be inferred from the relatively low uplift (0.3 mm/yr) and rainfall rates (1048 mm/yr) of the drainage basin, resulting in minimal denudation of its catchment's headwaters. The longer residence time of NZR10 in the weathering profile means the vegetation microenvironment may have a more pronounced impact, as compared to the other sediments. Consequently, the (^{230}Th/^{234}U) activity ratio less than one for NZR08 and NZR10 can be explained by the mobilization of Th due to a low pH environment, whereby Th then is removed by complexing with organic matter or colloids.

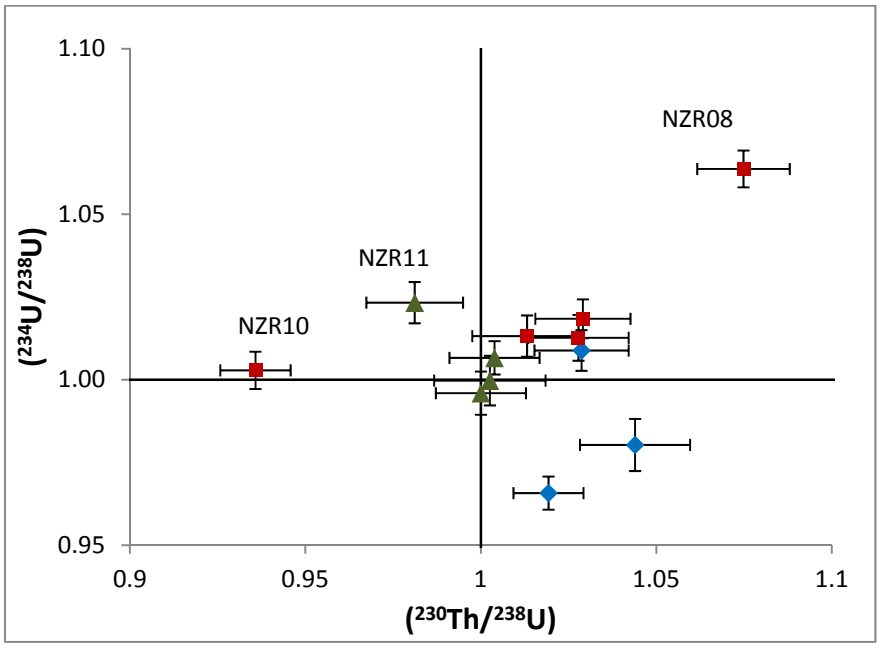

Figure 60: Daughter-parent activity ratios, (^{234}U/ ^{238}U) versus (^{230}Th/^{238}U) for sediments derived from Rakaia Torlesse (red square), Pahau Torlesse (blue diamond) and Haast Schist (green triangle). Error bars represent 2σ. Horizontal and vertical lines indicate secular equilibrium for (^{234}U/^{238}U) and (^{230}Th/^{238}U), respectively.

($^{230}Th/^{232}Th$) was plotted against ($^{238}U/^{232}Th$) in an ^{230}Th – ^{238}U isochron diagram shown in Figure 61. U loss due to weathering, or Th gain, is indicated by horizontal arrows to the left, whereas the horizontal arrows to the right indicate Th mobilization, or U gain, from the sediment. ^{234}U-^{238}U-^{230}Th disequilibria will then begin return to secular equilibrium by radioactive decay of the daughter and parent nuclides (Dosseto et al. 2008). This diagram shows that the river sediments plot in close proximity to the equiline, indicating that the sediments are close to secular equilibrium for ($^{230}Th/^{238}U$). Furthermore, the ($^{230}Th/^{232}Th$) and ($^{238}U/^{232}Th$) ratios in sediment particles sampled range from 0.503 and 0.513 (lower Taramakau; NZR11) to 0.749 and 0.801 (Rakaia tributary headwaters; NZR10). These values for all of the sediment samples analysed, except for NZR10, are substantially lower than the ratio for upper continental crust (0.81; Taylor & McLennan, 1985). This coupled with the modern river sediments being close to secular equilibrium, suggests that the bedrock must have lost part of its uranium in a previous weathering cycle. To return to secular equilibrium the geological system is closed for more than five to six half lives ($T_{1/2}$) of the daughter nuclei, in this case 300 ka, assuming a discrete fractionation between ^{238}U, ^{234}U ($T_{1/2}$ = 244 ka) and ^{230}Th ($T_{1/2}$ = 75 ka) (Dosseto et al. 2008). This suggestion is in agreement with Roser and Korsch's (1999) findings that the Permian to Late Triassic Rakaia Torlesse Terrane are first-cycle erosion products of an active continental margin arc system and that the Late Jurassic to Early Cretaceous Pahau Torlesse is derived in part from the same source, combined with material supplied from cannibalistic recycling of the Rakaia sediments (Wandres et al. 2004). Whereas the formation of the Early Jurassic Haast Schist has been attributed to metamorphism of the Rakaia Torlesse Terrane (Roser & Korsch 1999). Additionally Figure 61 shows that the ancient U loss was more intense in the Haast Schist as compared to the Torlesse Terrane greywacke. This could possibly be attributed to U mobilization during metamorphism, whereby breakdown and recrystallisation of minerals result in trace impurities being expelled (Frey 1987).

Modern fractionation of ^{234}U-^{238}U-^{230}Th is relatively low at approximately 5% deviation from secular equilibrium. The lack of vertical deviation of the sediments from the equiline suggests that modern chemical weathering is low, especially in comparison to the previous weathering cycle. The exception to this observation is NZR10, which

deviates from the equiline to a greater extent. Additionally, as previously discussed, NZR10 appears to have experienced mobilisation of Th, as indicated by the ($^{230}Th/^{234}U$) being less than one. This explains NZR10 plotting on to the right of the equiline and radioactive decay therefore shifts NZR10 vertically, in an upwards direction, in an effort to achieve secular equilibrium (Figure 61). NZR10 is located in close proximity to the headwaters of a tributary from the Rakaia (Andre Creek), which has a relatively low average annual uplift (0.3 mm/yr) and annual rainfall (1048 mm/yr). As previously discussed, these conditions infer minimal physical erosion is occurring and therefore it is possible that NZR10 has a much greater residence time in the weathering profile. Such fractionation is not observed in the sediments from the middle or lower Rakaia River (NZR04 and NZR03, respectively). This is because the headwaters of NZR04 and NZR03 are located at the Southern Alps, which is more likely to contribute a greater sediment load, as compared to the tributary. This is supported by the Sr-isotopic data as the $^{87}Sr/^{86}Sr$ ratio for NZR03 and NZR04 is similar (0.71040 and 0.710562, respectively), whereas NZR10 has a relatively distinct ratio (0.711994) (Figure 59). This suggests that the headwaters of NZR10 are geochemically different to that of NZR03 and NZR04.

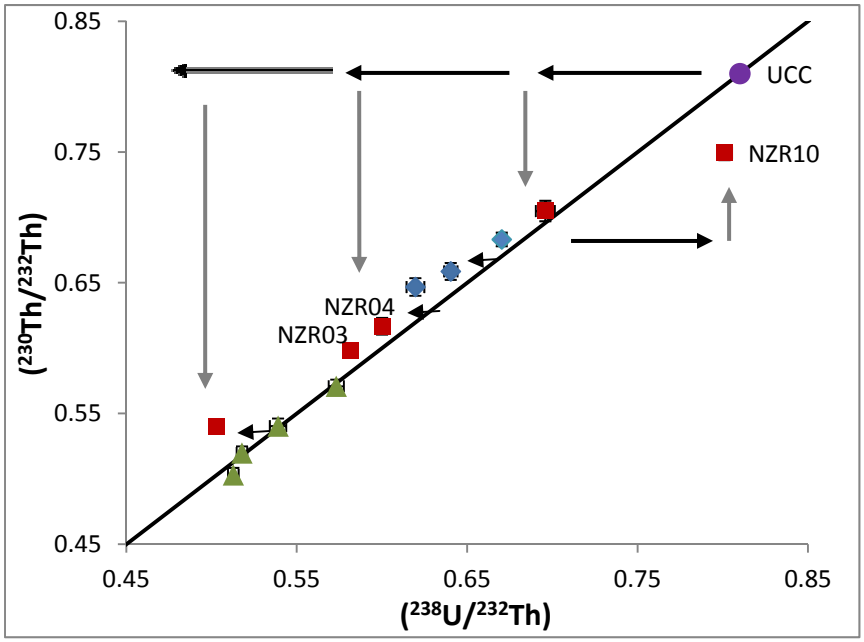

Figure 61:^{230}Th – ^{238}U isochron diagram for the river sediments. The average upper continental crust (UCC) is indicated by purple circle (McLennan 2001). The red squares represent Rakaia Torlesse Terrane, blue diamond the Pahau Torlesse and green triangle indicate the Haast Schist-derived sediments. Error bars indicate 2σ. Equiline represents secular equilibrium for ($^{230}Th/^{238}U$). The black arrows indicate weathering-induced fractionation. Arrows to the left indicate preferential ^{238}U removal or ^{232}Th gain in sediment grains. The arrows to the right indicate ^{232}Th mobilisation or ^{238}U gain. The grey arrows show the effect of radioactive decay (return to secular equilibrium), assuming that the sediments behave as a closed system after fractionation.

Chapter Six: Weathering in the South Island and the Role of Climate and Tectonics

6.1 Where is Weathering Occurring?

The compositions of sedimentary material are primarily modified from the bedrock by chemical and physical weathering. The degree of alteration is largely dependent upon the intensity and duration of weathering, which occurs in the pedogenic weathering profile, during fluvial transport and temporary storage in alluvial sequences (Robinson & Johnsson 1997).

6.1.1 Chemical Weathering Trends

Chemical weathering is primarily reflected by the loss of mobile elements in sediments. As discussed in Section 5.4.3, Na is the only element to show significant depletion in all river sediments. Figure 62 displays the Na/Zr range of the source rock in comparison to the sediments in relation to the distance from their respective headwaters. This figure highlights that there is a marked depletion of Na from source rock composition to the sediment composition. Furthermore, Figure 62 shows that the Na elemental ratio does not vary greatly, or systematically, with increasing distance from the headwaters. This suggests that Na loss predominantly occurs within the weathering profile before being eroded and transported in the fluvial system.

Mineralogical analysis highlighted that Na rich feldspars are major primary mineral phases in the sediments derived from both the Torlesse Terrane and Haast Schist. As discussed in Section 5.4.3, the Na_2O content in the bulk sediments were positively and significantly correlated with the plagioclase content (Figure 46, $F=17.48$, $P > 0.0006$). Therefore this suggests that the depletion of Na, from source to sediment, is attributed to the dissolution of plagioclase.

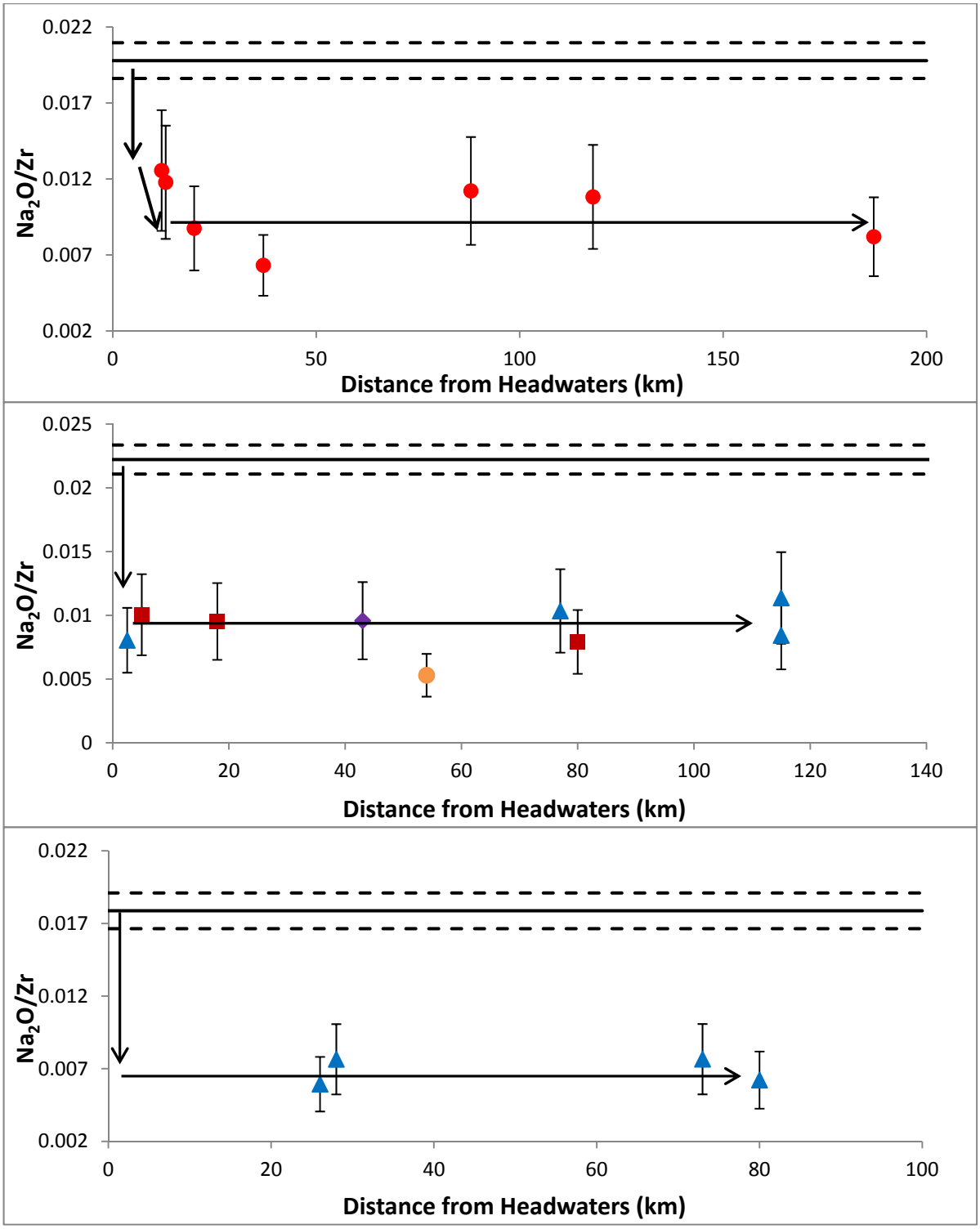

Figure 62: Na_2O/Zr versus distance from headwaters for (A) Pahau Torlesse river sediments, (B) Rakaia Torlesse river sediments [Waimakariri (red square), Rakaia (blue triangle), Pareora (purple diamond) and upper Taramakau (yellow circle)] and (C) Haast Schist river sediments. Solid black line represents average source composition and dotted lines above and below represent standard error. Torlesse Terrane source composition quoted from Roser & Korsch (1999) and Haast Schist quoted from Grapes et al. (1982). Error bars represent 2σ. Black arrows indicate possible weathering path.

Similarly to Na, Mg and Ca showed marked depletion in the Haast Schist-derived sediment (Section 5.3.3). Figure 63 highlights that MgO/Zr and CaO/Zr ratios show minimal variation with increased distance from the headwaters. This suggests that the majority of leaching of Ca and Mg in the Haast Schist-derived sediments occurs in the weathering profile, whereby further, more minor, depletion may occur in the fluvial system (as shown by the slight decrease of elemental ratio with increased distance from headwaters). As the primary phase of plagioclase, in the Haast Schist and Torlesse Terrane, is albite while labradorite is subordinate, (Jacobson 2001), the depletion of Ca is primarily thought to occur due to the dissolution of calcite rather than plagioclase.

The higher metamorphic zones of the Haast Schist host up to 3% calcite, due to hydrothermal activity associated with the Alpine Fault (Jacobson *et al.* 2003). Consequently Haast Schist-derived sediments are expected to drain a more calcite rich lithology, as compared those derived from the Torlesse Terrane. As the Torlesse Terrane-derived sediments show moderate depletion of Ca, it is suggested that dissolution of calcite is more prominent in the west coast region of the South Island. This is supported by Jacobson *et al.* (2003), who estimated that calcite weathers approximately 350 times faster than plagioclase in an environment of tectonic exhumation and mechanical denudation, such as on the western coast of the South Island.

Nesbitt and Young's (1984) A-CNK-FM ternary diagram indicates that the depletion of Mg in the Haast Schist sediments is attributed to the dissolution of ferro-magnesian minerals, such as amphiboles, which are susceptible to weathering (Grapes *et al.* 1982) (see Section 5.4.6, Figure 56). Furthermore, this ternary diagram suggests that the rate of dissolution of amphibole is occurring at a similar rate to plagioclase in the Haast Schist-derived sediments.

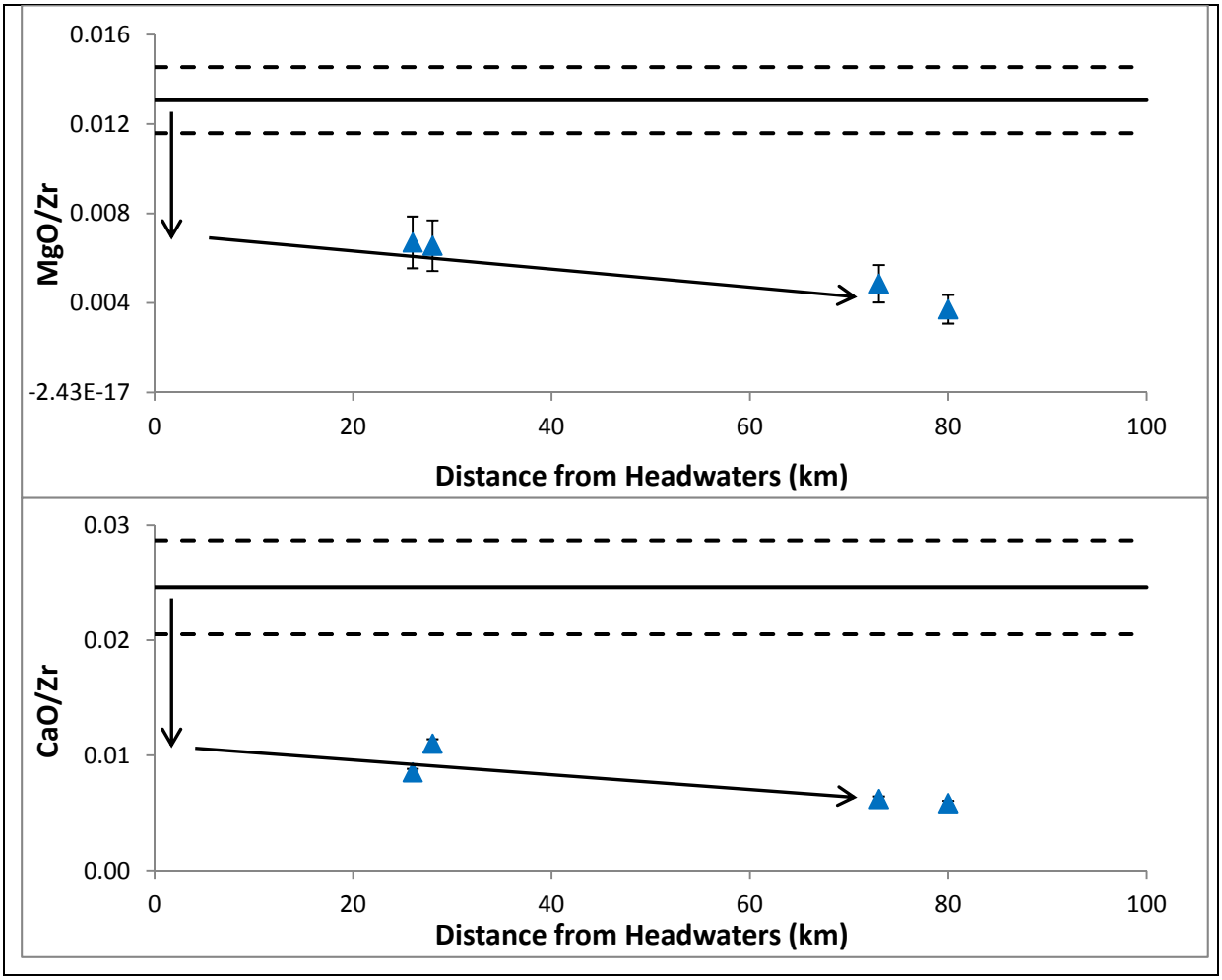

Figure 63: (A) MgO/Zr and (B) CaO/Zr for Haast Schist sediments. Solid black line represents average source composition and dotted lines above and below represent standard error (Grapes et al., 1982). Error bars represent 2σ. Black arrows indicate possible weathering path.

Of the trace elements, Sr and Ba have been reported in literature to be the most mobile during chemical weathering (Marx & Kamber 2010). Geochemical analysis showed that Sr only appeared to be depleted in the Rakaia Torlesse-derived sediments, whereas Ba showed depletions in both the Pahau and Rakaia Torlesse-derived sediments (Section 5.3.4). Even though the Haast Schist-derived sediments were shown in Figure 44 (Section 5.3.4) to be depleted in Ba and Sr, as compared to the average Haast Schist, the sediments are within standard deviation of their source compositional range. Consequently, this study could not conclude on the significance of Ba and Sr loss in the Haast Schist-derived sediments. Figure 64 demonstrates that the Sr/Zr ratio (for the sediments derived from the Rakaia Toresse) and Figure 65 the Ba/Zr ratio (for those derived from both Torlesse sub-Terranes) show similar downstream trends as Na/Zr. These figures highlight there is significant depletion of Ba and Sr, however there appears to be no further elemental loss with increased distance from the headwaters. This further supports the finding that chemical weathering is predominantly occurring on the hillslope in the weathering profile before being transported in the fluvial system.

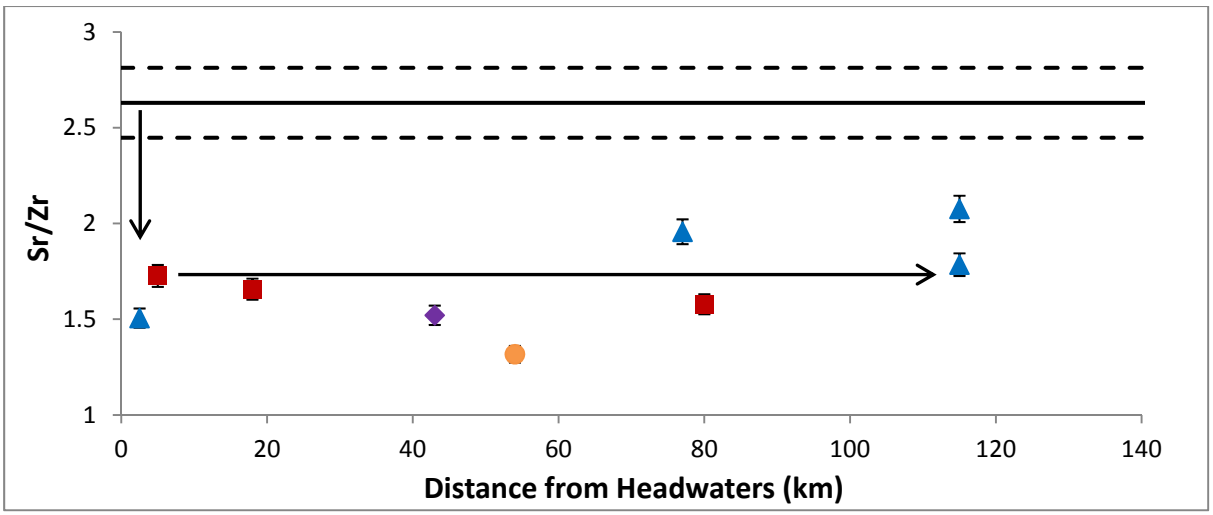

Figure 64: Sr/Zr versus distance from headwaters for Rakaia Torlesse sediments – Waimakariri (red square), Rakaia (blue triangle), Pareora (purple diamond) and upper Taramakau (yellow circle). Solid black line represents average source composition and dotted lines above and below represent standard error (Roser & Korsch, 1999). Error bars represent 2σ. Black arrows indicate possible weathering path.

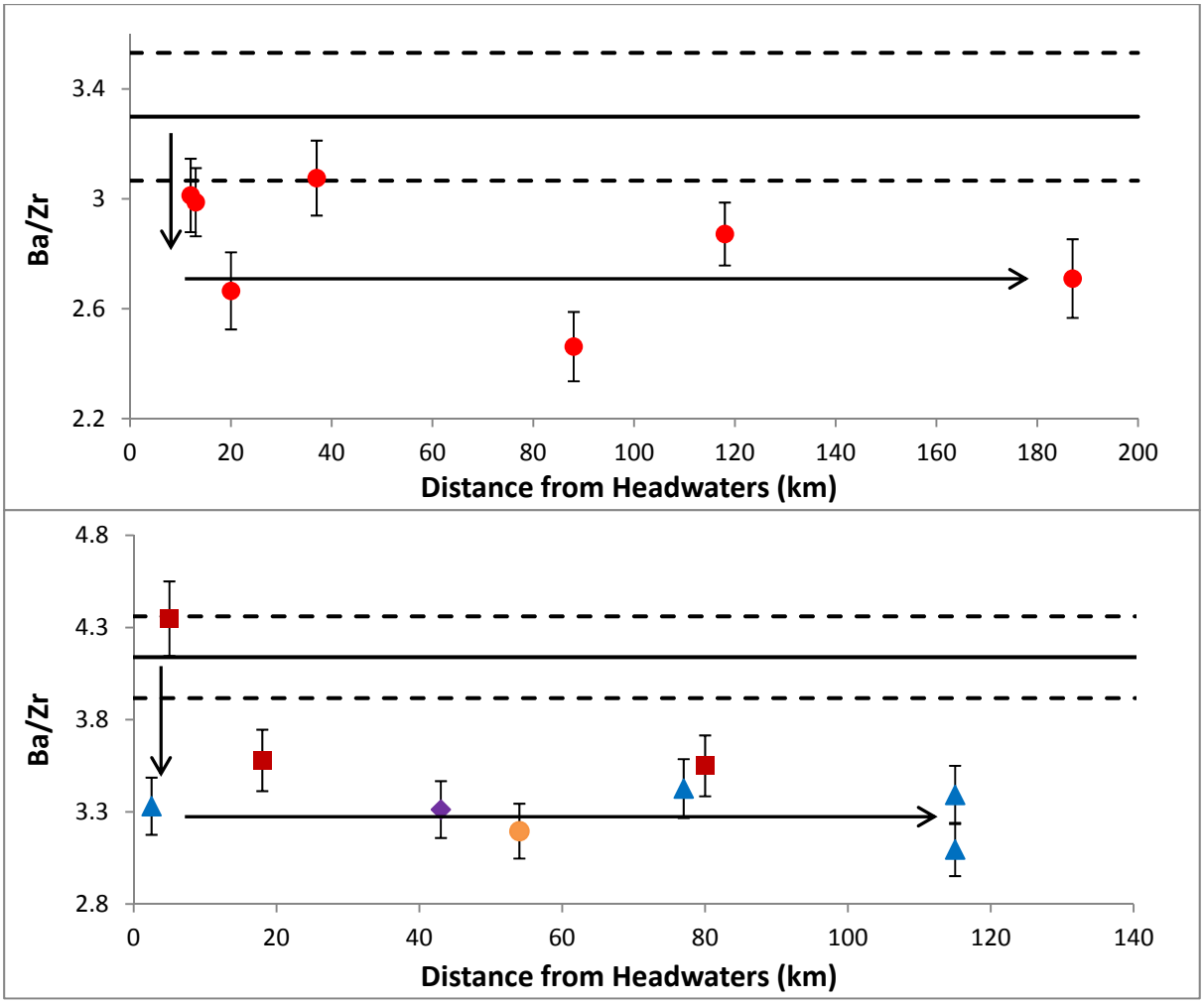

Figure 65: Ba/Zr versus distance from headwaters for (A) Pahau Torlesse Terrane river sediments, (B) Rakaia Torlesse Terrane river sediments [Waimakariri (red square), Rakaia (blue triangle), Pareora (purple diamond) and upper Taramakau (yellow circle)]. Solid black line represents average source composition and dotted lines above and below represent standard error, quoted from Roser & Korsch (1999). Error bars represent 2σ. Black arrows indicate possible weathering path.

However, U/Zr ratios do not appear to follow the same weathering trend as the mobile elements discussed above. Figure 66 highlights that in addition to U loss on the hillslope, the U/Zr ratio decreases with increasing distance from the headwaters. As Zr is considered immobile, this figure suggests that U is leached during transport within the fluvial system.

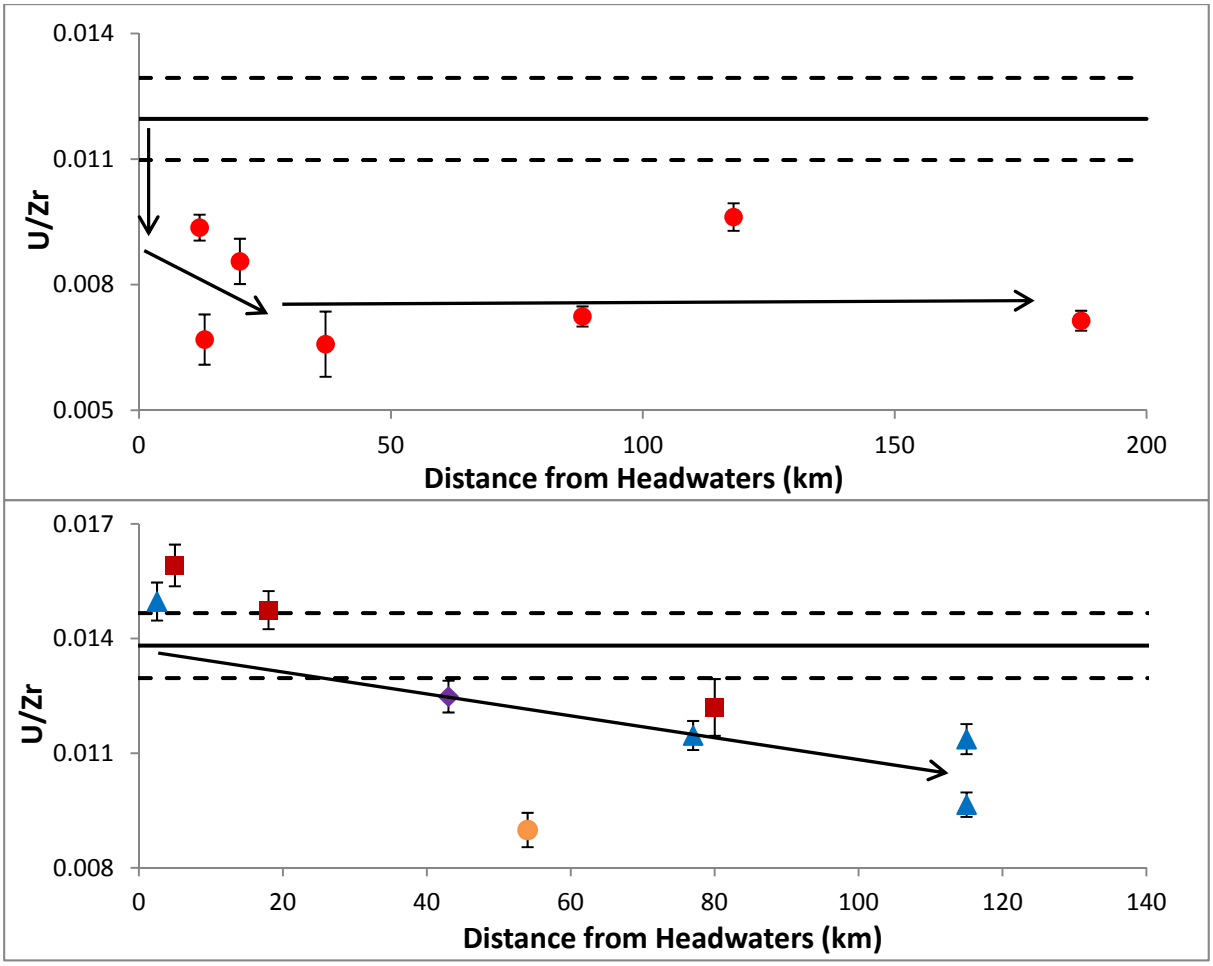

Figure 66: U/Zr elemental ratios for (A) Pahau Torlesse Terrane sediments and (B) for Rakaia Torlesse Terrane sediments [Waimakariri (red square), Rakaia (blue triangle), Pareora (purple diamond) and upper Taramakau (yellow circle)]. Solid black line represents average source composition and dotted lines above and below represent standard error (Roser & Korsch, 1999). Error bars represent 2σ. Black arrows indicate possible weathering path.

The (^{230}Th/^{238}U) activity ratio can be used to further investigate the apparent leaching of U during transport in the fluvial system. As discussed in Section 2.5.1, bedrock is assumed to be in secular equilibrium if closed for a period of time greater than five half lives of the daughter nuclei (in this case ^{230}Th, with a half-life of 75 ka) (Dosseto *et al.* 2008). Therefore for (^{230}Th/^{238}U) to be in secular equilibrium (i.e. equal to unity) the geological system is required to be closed for more than 1Ma. As the Rakaia and Pahau sub-Terranes were deposited during the Permian to Late Triassic and Late Jurassic to Early Cretaceous, respectively, the (^{230}Th/^{238}U) ratio is considered to be equal to one, before the onset of weathering. In oxidising conditions, ^{238}U is soluble and ^{230}Th immobile, therefore the (^{230}Th/^{238}U) ratio of sediments is expected to increase with continued weathering.

Figure 67 shows the ($^{230}Th/^{238}U$) ratio for the sediments, in relation to the distance from their respective headwaters, for the three lithological regions. It can be seen that the sediments derived from the Rakaia and Pahau sub-Terranes, exhibit ($^{230}Th/^{238}U$) fractionation with increased distance from the headwaters, indicating that ^{230}U is being leached during transport in the fluvial system. Additionally, Figure 67 highlights that the NZR08 ($^{230}Th/^{238}U$) ratio does not show the same fractionation trend as the other Torlesse Terrane-derived sediments. This is investigated in Figure 68, which demonstrates that a positive relationship exists between the degree of ($^{230}Th/^{238}U$) fractionation and mean annual rainfall. Therefore, this suggests that NZR08 is experiencing greater ^{238}U loss and is subjected to more intense chemical weathering due to a higher annual rainfall.

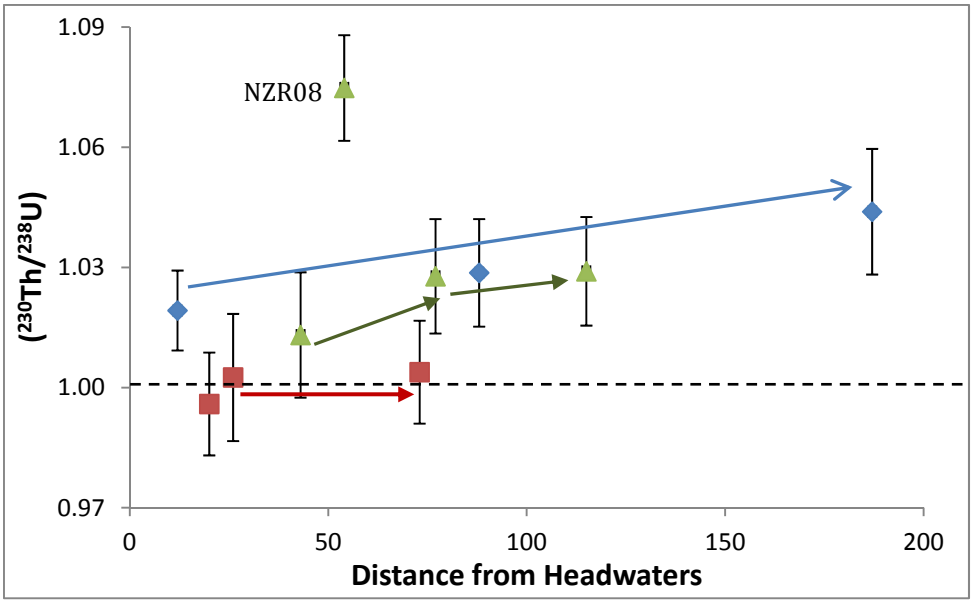

Figure 67: ($^{230}Th/^{238}U$) ratio versus distance downstream for the sediments derived from the Rakaia Torlesse Terrane (green triangles), Pahau Torlesse Terrane (blue diamond) and Haast Schist (red squares). The arrows show the path of ($^{230}Th/^{238}U$) fractionation with distance from the headwaters (red = Haast Schist sediments, green = Rakaia Torlesse sediments and blue = Pahau Torlesse sediments). Dashed line represents secular equilibrium of the bedrock. Error bars indicate 2σ.

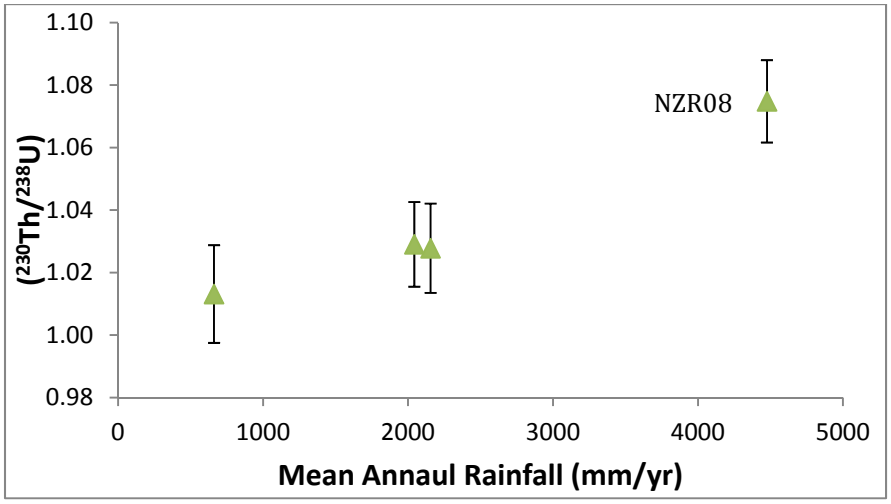

Figure 68: $^{230}Th/^{238}U$ ratio versus mean annual rainfall of the Pahau Torlesse Terrane-derived sediments. Error bars indicate 2σ.

In contrast to the Torlesse Terrane-derived sediments, Figure 67 shows that the ($^{230}Th/^{238}U$) ratios of the Haast Schist-derived sediments do not appear to deviate from secular equilibrium, with increased distance from the headwaters. An explanation for the differing trends of ($^{230}Th/^{238}U$) fractionation could be the contrasting residence time of the sediments in the weathering profile and fluvial system. For instance, the western coast is characterised by high denudation rates, due to the rapid uplift and high rainfall rates, resulting in sediment being readily lost from the hillslope (Hicks *et al.* 2011). Furthermore, the schistose and friable nature of the bedrock results in high landslide frequencies (Korup 2005a; b). The reduction of residence time in the weathering profile is coupled with steep gradients of rivers on the west coast, resulting in rapid hydraulic flow which acts to transport the sediments through the fluvial system at a faster rate (Hicks *et al.* 2011).

In contrast, rivers on the eastern side of the Southern Alps drain from the Main Divide through a series of ranges and basins (Korup 2005b; Hicks *et al.* 2011). Consequently, the eastern flowing rivers have a gentler gradient, resulting in comparatively slower hydraulic flow, meaning the sediments are subjected to a relatively longer residence time in the fluvial system (Hicks *et al.* 2011). Furthermore, there is a greater proportion of alluvial deposits associated with rivers draining east of the Southern Alps (Section 3.7), suggesting that temporary storage of fluvial sediments occurs, which increases the

residence time of the sediments. The lower residence time of rivers draining the Haast Schist on the western coast, reflects the lack of fractionation of ($^{230}Th/^{238}U$) and could infer that these sediments are experiencing less chemical weathering during fluvial transport.

In summary, mineralogical analysis has shown that neither percentage of quartz or feldspar content of the sediments correlate with distance from the headwaters. This is the opposite of what is expected when chemical weathering is occurring in the fluvial system, as quartz is a more resistant to physical and chemical abrasion as compared to feldspar (Nesbitt & Young 1989). Furthermore, U is the only mobile element to show significant systematic depletion during transport in the fluvial systems draining Torlesse Terrane. These results suggest that chemical weathering is predominantly occurring within weathering profiles rather than during transport in the fluvial system. Similarly, Jacobson *et al.* (2003) and Kautz and Martin (2007) reported that dissolution of calcite was occurring in the weathering profile prior to the entry of sediments into the fluvial system. Furthermore, Nesbitt *et al.* (1997) and Tonkin and Basher (2001) have found that the bulk of chemical weathering of feldspars occurs in weathering profiles, as feldspar weathering rates in a fluvial system are one or two orders of magnitude greater than that in a weathering profile.

6.1.2 Intensity of Chemical Weathering

The geochemistry of river sediments that are eroded from a landscape provides important insights into the nature and intensity of the weathering processes taking place at a catchment scale. The alkali metals and the alkaline earths are the most easily solubilised during weathering of silicate minerals (Nesbitt *et al.* 1997; Gaillardet *et al.* 1999). The extent of fractionation of these elements depends on the intensity and the residence time of the sediments in the weathering profile and in the riverine floodplain.

Analysis of major and trace elemental composition of the river sediments indicates that depletion from average source rock composition is occurring for only the most mobile elements. Na is the only mobile major element to show depletion within the sediments across all catchments. In contrast, there was no marked depletion of K detected in the any of the river sediments. This suggests that chemical weathering was effective in dissolving plagioclase, but not intense enough to weather K-feldspar. This is expected in low intensity weathering environments, as plagioclase is weathered more rapidly than K-feldspar (Nesbitt & Young 1989). Furthermore there appears to be no systematic depletion of Sr, which is considered to be the most mobile trace element (Marx & Kamber 2010). However, dissolution of calcite seems to be apparent on the western coast, in sediments derived from the Haast Schist, due to lithology availability and rapid physical denudation.

As discussed in the Section 2.4, many sediment chemical weathering studies utilise the Chemical Index of Alteration (CIA) and the Weathering Index of Parker (WIP) to quantify the intensity of chemical weathering. Figure 54 (Section 5.4.5) highlights that these weathering index values, particularly WIP, appear to indicate that the sediments are more chemically weathered as compared to their source rock composition. However, the CIA and WIP values calculated for the river sediments are within propagated standard error of their source rock compositional range. Consequently this study cannot conclude on the significance of deviation of weathering index values from source to sediment.

Overall the elemental geochemistry of the sediments suggests that silicate weathering in the South Island is of a low to moderate intensity. This finding is further supported by the ^{230}Th-^{238}U isochron diagram (Section 5.6, Figure 61). As discussed in Section 5.6, the sediments plot in close proximity to the equiline, indicating the isotopic ratio ($^{230}Th/^{238}U$) is close to secular equilibrium. This observation highlights that modern fractionation of ^{234}U-^{238}U-^{230}Th is relatively low at approximately 5% deviation from secular equilibrium, suggesting that the sediments are being subjected to minimal chemical weathering. Furthermore the ($^{230}Th/^{232}Th$) and ($^{238}U/^{232}Th$) activity ratios of

the river sediments are substantially lower than the average upper continental crust, as reported by Taylor and McLennan (1985), indicating that the sediments have previously (>300 ka) been subjected to a more intense chemical weathering cycle. Additionally, Section 5.6 highlighted that ancient U depletion was more intense in the Haast Schist, as compared to the Torlesse Terrane, due to a lower ($^{230}Th/^{238}U$) ratio. This observation is supported by previous studies that have suggested the Rakaia and Pahua sub-Terranes are first and second order erosion products, respectively, and the Haast Schist is the metamorphic equivalent of the Rakaia sub-Terrane (Roser & Korsch 1999; Wandres *et al.* 2004).

The low degree of silicate weathering, reflected in the sediments, is in agreement with studies on solute chemistry of rivers draining the Southern Alps conducted by Jacobson *et al.* (2003) and Lyons *et al.* (2005). However, geochemical analysis of the sediments disagrees with Kautz and Martin (2007), who reported that the sediments from the Haast and Clutha Rivers, draining either side of the Southern Alps, displayed no greater intensity of silicate chemical weathering than the parent bedrock.

6.1.3 Physical Weathering Trends

Downstream trends of physical weathering were investigated through mineralogical, grain size and thin section analysis. In individual fluvial systems, downstream fining was observed with the mean grain size and the proportion of sand decreasing, while silt and clay increased with distance from the headwaters (Figure 26 & Figure 27). Downstream fining of clast size within fluvial systems has widely been recognised and reported in literature (Gomez *et al.* 2001). Furthermore, downstream fining in braided rivers of the Canterbury Plains has similarly been reported by Browne (2004). Downstream fining has been mainly attributed to the processes of hydraulic sorting and abrasion of sediment particles (Gasparini *et al.* 1999; Gomez *et al.* 2001).

Mineralogical analysis supported the notion that the river sediments were experiencing greater physical weathering and abrasion with increased distance from the headwaters. The Dickinson *et al.* (1970b) QFL ternary diagram of the sediments (Section 5.3.2, Figure 36) showed that the with increasing distance from the headwaters in individual fluvial systems, the sediment becomes more dominated by quartz and feldspar fragments, while the proportion of lithic fragments decreases. This observation appears to indicate that the lithic fragments are being mechanically weathered during transport, consequently breaking them down to their composite minerals. Figure 69 supports this hypothesis, whereby there is a positive relationship between the clast ratio of quartz to lithic fragments and distance from the headwaters for each litholoigcal region. Similarly Kautz and Martin (2007), reported a gradual increase of quartz downstream in the 355 µm – 2 mm grain size fraction within the Haast and Clutha Rivers, which drain opposing flanks of the Southern Alps.

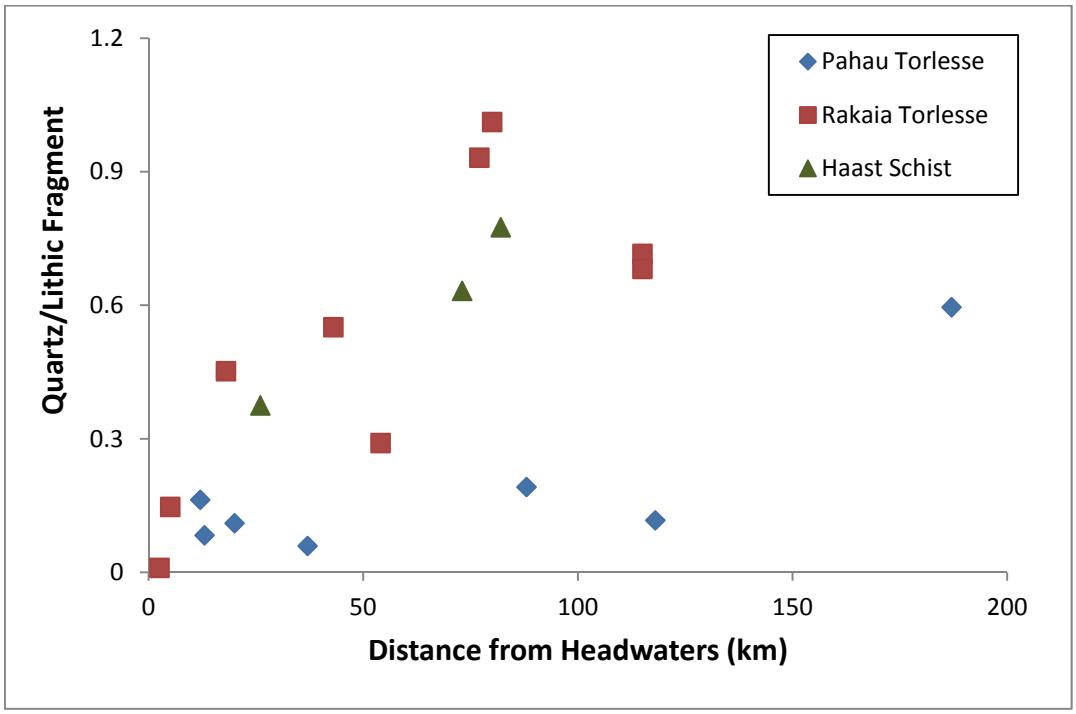

Figure 69: Clast ratio of quartz to lithic fragments versus distance from headwaters of sediments derived from Pahau Torlesse Terrane (blue diamond), Rakaia Torlesse Terrane (red square) and Haast Schist (green triangle).

These results suggest that physical weathering is occurring during transport within the fluvial system, whereby lithic fragments are fracturing into their composite mineral grains. The increased physical abrasion downstream is coupled with the presence of downstream fining within individual fluvial systems (Figure 27 & Figure 26). These observations could be attributed to lithic fragments being crushed between cobbles during periods of high discharge, whereby the fragment breaks along primary mineral cleavages or grain boundary imperfections. Furthermore, freeze-thaw action in grain micro-fractures may additionally be evident during the cooler months, particularly at higher altitude. These results suggest that downstream fining is attributed to a combined process of hydraulic sorting and physical weathering. Similarly Whitmore *et al.* (2004) reported downstream fining for modern river sediments in Papua New Guinea where, irrespective of provenance, sediments showed a marked decrease in the abundance of lithic fragments and an increase in mineral grains.

6.2 Climate, Tectonics & Weathering

The controls of chemical weathering are still highly debated in the literature, most notably involving the controls of tectonics and climate on physical erosion and its relationship to chemical weathering. This section discusses the influence of rainfall and uplift on weathering in the Southern Alps.

6.2.1 Rainfall & Physical Weathering

Petrological analysis suggests that the sediments derived from the Torlesse Terrane contained mudstone fragments that were generally smaller and more well-rounded, as compared to the sandstone fragments. As discussed in Section 5.3.2, this observation was attributed to the greater resistance of sandstone to physical abrasion due to the cementation by iron oxides, which strengthens the fragments (Chigira & Oyama 2000). However, mudstones are weakened due to a greater proportion of clay fractions and larger specific surface areas than sandstone fragments (Chigira & Oyama 2000). Figure 69 shows that the percentage of mudstone fragments in the Torlesse Terrane greywacke-derived sediments is negatively correlated with the catchment's mean annual rainfall ($R^2 = 0.48$). Least squares regression ANOVA analysis, statistically

determined the relationship as highly significant ($F_{1,19}$=9.46, P = 0.0069). However, no relationship was found between the percentage of mudstone fragments and the average uplift rate, or with distance downstream. Consequently, it is suggested that the breakdown of mudstone is enhanced with increasing rainfall, which reduces the overall percentage of mudstone fragments in the sediment. In contrast, the percentage of greywacke fragments showed no correlation with average annual rainfall.

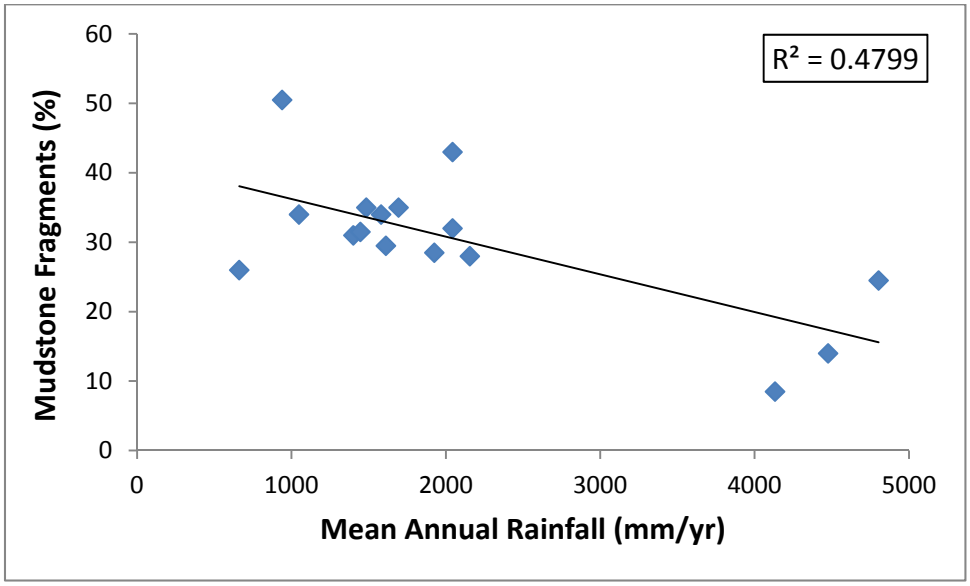

Figure 70: Proportion of mudstone fragments (%) in Torlesse Terrane-derived sediments, from pointing counting, versus mean rainfall of the catchment. Percentage of mudstone fragments are negatively correlated with mean rainfall (R^2 = 0.48, F=9.46, P = 0.0069).

6.2.2 Rainfall & Chemical Weathering

The enhancement of rainfall has been reported in the literature to both promote and inhibit the extent of chemical weathering of sediments. Nesbitt and Young (1984) have reported that the degree of chemical weathering is predominantly determined by the rate of precipitation, as it controls the amount of carbonate acid that comes into contact with the bedrock. However, rainfall has been shown to also increase physical erosion, therefore reducing the residence time of sediments within the weathering profile (Kump *et al.* 2000). Studies have demonstrated that chemical weathering predominantly occurs in the weathering profile (Tonkin & Basher 1990; Nesbitt *et al.* 1997), therefore it can be established that enhanced rainfall can inhibit the extent of chemical weathering on a sediment.

As previously discussed, the intensity of chemical weathering of river sediments can be inferred from the extent of depletion of mobile elements, as compared to the composition of the bedrock. Furthermore, the utilisation of an immobile reference element reduces the effects of quartz dilution. Figure 71 shows that there is a negative relationship of the normalised Mg/Zr and Ca/Zr ratios with mean annual rainfall. This suggests that with increased rainfall there is a greater dissolution of minerals bearing Ca and Mg. Least squares regression ANOVA analysis, statistically considers the negative relationship between depletion of Mg and Ca with rainfall as highly significant (R^2 =0.64, $F_{1,19}$ = 32, R > 0.00001 and R^2 =0.50, $F_{1,19}$ = 18, R = 0.00005, respectively). As previously discussed, the majority of Ca depletion, particularly on the western coast, is thought to be attributed by the dissolution of calcite. Therefore, Figure 71b suggests that there is an enhancement of carbonate weathering with increased rainfall. However, lithology appears to have an influence as the sediments derived from the Haast Schist are more depleted in Ca from their source composition, as compared to those derived from the Torlesse Terrane. This can be attributed to the greater presence of hydrothermal calcite veins associated with the Alpine Fault and deposited in the Haast Schist (Jacobson & Blum 2003). Furthermore, high physical denudation on the western coast results in exposure of calcite to the weathering environment (Hicks *et al.* 2011). Consequently, Figure 71 highlights the greater occurrence of carbonate weathering in the Haast Schist-derived sediments. This is in agreement with Jacobson (2001), who reported that streams draining Haast Schist typically had a higher Ca solute chemistry than streams draining greywacke.

In comparison to Ca, the correlation between the normalised elemental ratio of Mg and rainfall shows a uniform relationship with both the Haast Schist and Torlesse Terrane derived- sediments (Figure 71a). Lithology therefore does not appear to govern the relationship between Mg depletion and rainfall. Consequently, this suggests that with increased rainfall there is increased leaching of Mg.

Figure 71c displays the relationship between the depletion of Na in the river sediments and rainfall. Statistically there is no significant correlation of Na loss with increased rainfall. In comparison to Mg, the relationship between Na depletion and rainfall is not as prominent. This could be attributed to the higher mobility of Na (Nesbitt *et al.* 1997), meaning that it is preferentially removed with minimal rainfall. This therefore infers that Na leaching in the Southern Alps is not particularly sensitive to the control of rainfall and is mobilised, regardless of the intensity and duration of rainfall.

Furthermore, no correlation was found between rainfall and the normalised elemental ratios of the mobile trace elements Sr, Ba and U (Appendix I, Figure 77). The lack of systematic depletion of these mobile trace elements and rainfall suggest that this parameter does not significantly control the dissolution of Sr, Ba and U.

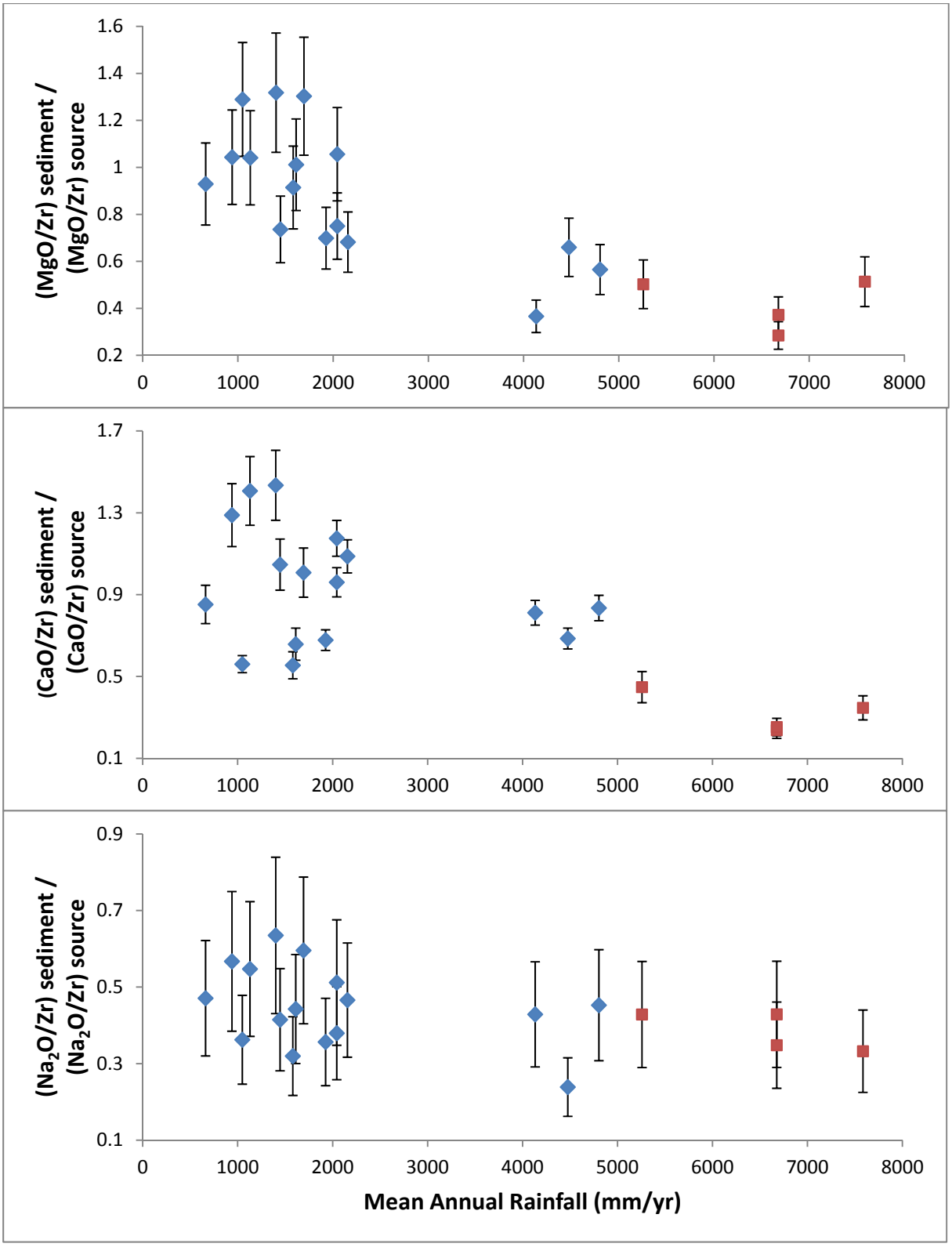

Figure 71: Normalised elemental ratios to Zr versus mean annual rainfall for mobile major elements (A) MgO (R^2 =0.64, $F_{1,19}$ = 32, R > 0.00001) (B) CaO (R^2 =0.50, $F_{1,19}$ = 18, R = 0.00005) and (C) Na_2O (R^2=0.19, $F_{1,19}$=4.29, P= 0.05) for sediments derived from the Torlesse Terrane (blue diamond) and Haast Schist (red square). Source composition for Torlesse Terrane quoted from Roser and Korsch (1999) and Haast Schist from Grapes et al. (1982). Error bars represent 2σ.

As discussed in Section 5.6, the U/Th ratio can be used to quantify weathering intensity, due to the high mobility of U and the immobile nature of Th. Figure 72 shows that with increased weathering the mobile elements U, Na and Ca will deplete with respect to Th and Zr. The advantage of using the U/Th ratio is U and Th were measured using the high precision technique of ICP-MS, as compared to the other elements which were quantified using X-ray fluorescence (see Section 4.6 and 4.8). Furthermore, as discussed in Section 5.6, carbonates were found to contain very minimal to no U and Th. Consequently, depletion of U, as compared to Th, can be attributed to silicate weathering rather than dissolution of calcite.

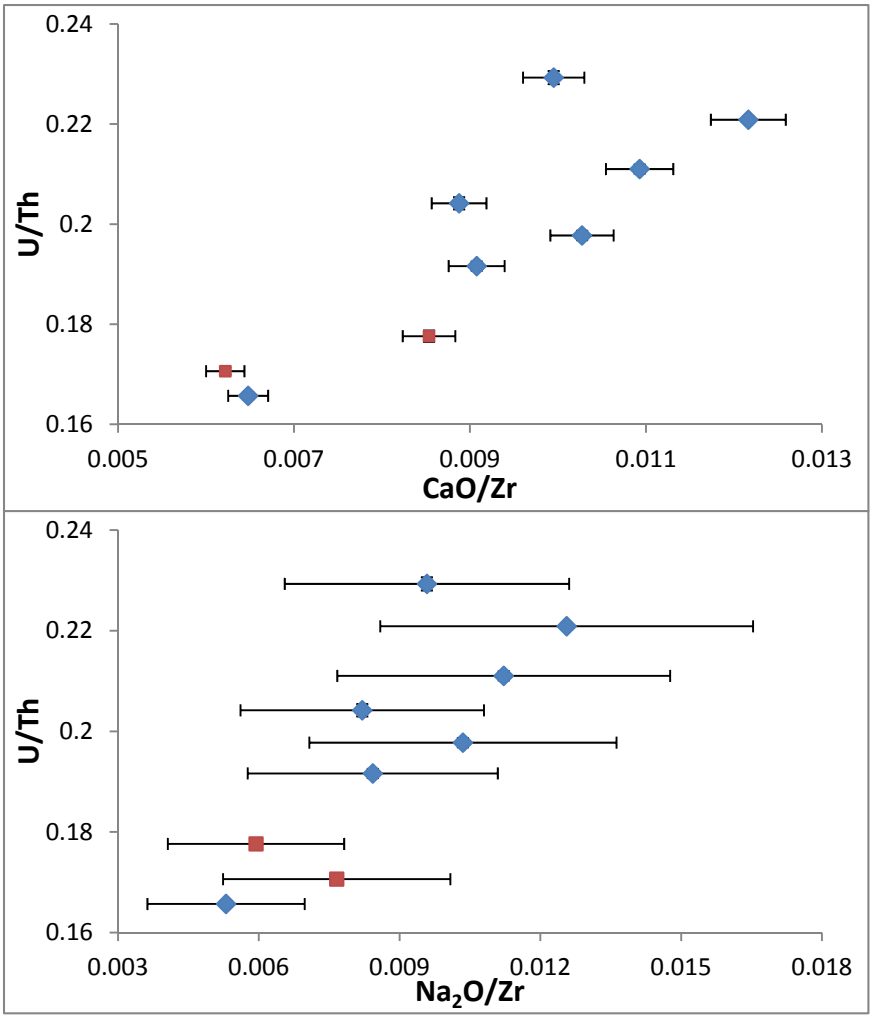

Figure 72: U/Th versus (A) CaO (R^2 = 0.73, $F_{1,9}$=18.7, F=0.0034) and (B) Na_2O (R^2 = 0.66, $F_{1,9}$=13.58, F=0.0078) for sediments derived from Torlesse Terrane (blue diamond) and Haast Schist (red square). Data excludes NZR10 and NZR11 due to Th mobilization. Error bars represent 2σ.

Figure 73a shows that for the Torlesse Terrane-derived sediments, U is increasingly preferentially lost to Th with increasing rainfall. This relationship is additionally evident with the ($^{230}Th/^{238}U$) ratio, which increases with amplified rainfall in the Torlesse Terrane sediments. As discussed in Section 5.6, the bedrock is considered to be in secular equilibrium before the onset of modern weathering, whereby the ($^{230}Th/^{238}U$) ratio is equal to unity. Figure 73b highlights that with increasing rainfall, fractionation is occurring between ^{230}Th and ^{238}U away from secular equilibrium (R^2= 0.77, $F_{1.7}$=16.8, P=0.0093). This suggests that silicate weathering is enhanced by increased rainfall in the Torlesse Terrane-derived sediments.

In contrast to the Torlesse Terrane-derived sediments, Figure 73 shows that the sediments derived from the Haast Schist do not show the same pattern of fractionation between ^{230}Th and ^{238}U or U/Th ratio with rainfall. The ($^{230}Th/^{238}U$) ratio plots the Haast Schist sediments within error of secular equilibrium, regardless of rainfall. This suggests that silicate weathering, as reflected by ($^{230}Th/^{238}U$) fractionation, is not sensitive to rainfall in the Haast Schist-derived sediments. Furthermore, the lack of deviation of ($^{230}Th/^{238}U$) from secular equilibrium in the Haast Schist-derived sediments, as discussed in Section 6.1.1, has been attributed to their short residence time in the weathering profile and fluvial system. Therefore, a relationship between rainfall and ($^{230}Th/^{238}U$) is not evident with the Haast Schist sediments because there is insufficient time for ^{230}Th and ^{238}U to fractionate.

In summary, these results suggest that chemical weathering increases with increasing rainfall. This relationship is evident in the depletion of Mg, in both the Torlesse Terrane and Haast Schist-derived sediments, and by the fractionation of ^{230}Th and ^{238}U in the Torlesse Terrane sediments. Furthermore, these results indicate that the South Island acts as a weathering limited setting, whereby the intensity of chemical weathering is limited by residence time of the sediments in the catchment. On the east coast the effect of rainfall enhances chemical weathering whereas on the western coast it inhibits the extent of chemical weathering, whereby only the most mobile elements are depleted. This contradicts Kautz and Martin's (2007) findings who reported that there was

minimal climatic control on weathering intensity of sediments from Haast and Clutha Rivers. Furthermore, these results highlight the interrelationship between physical erosion and chemical weathering and support Gaillardet *et al.*'s (1999) observation that regions with the highest rates of physical denudation produce the least weathered sediments.

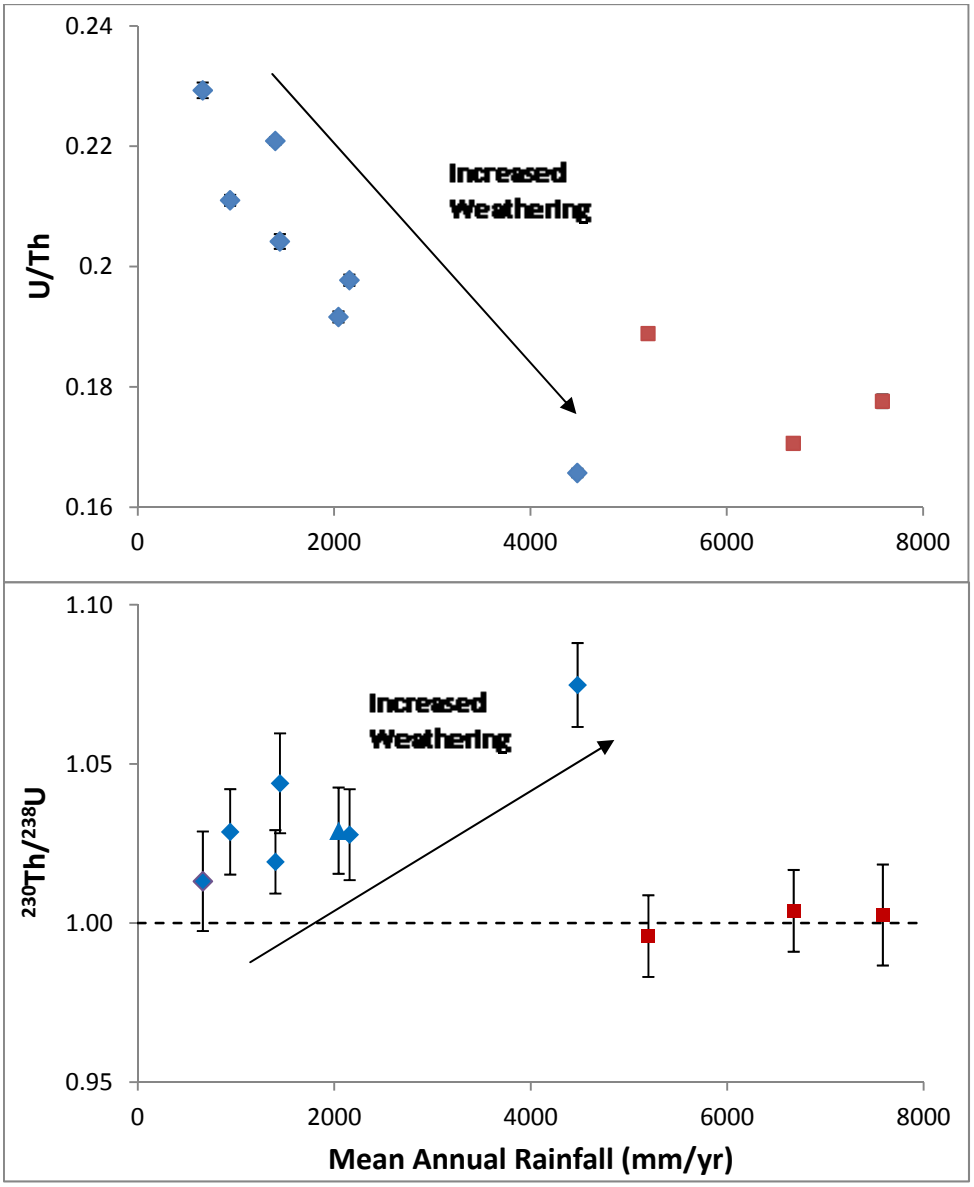

Figure 73: (A) U/Th versus mean annual rainfall (Torlesse Terrane R^2= 0.88, $F_{1,7}$=35.4, P=0.0019) and (B) $^{230}Th/^{238}U$ versus mean annual rainfall (Torlesse Terrane R^2= 0.77, $F_{1,7}$=16.8, P=0.0093). For sediments derived from Torlesse Terrane (blue diamond) and Haast Schist (red square). Arrows shows direction of increased weathering. Dotted line in (B) indicates secular equilibrium of bedrock. Data excludes NZR10 and NZR11 due to Th mobilization. Error bars represent 2σ.

6.2.3 Uplift & Chemical Weathering

Similarly to rainfall, uplift rates have been found to either enhance or inhibit the extent of chemical weathering of sediments. Tectonic uplift results in increased mechanical erosion, which continually exposes fresh bedrock to the atmosphere. The continual removal of unconsolidated material and increased reactive surface area of mineral has been suggested by Raymo and Ruddiman (1992) to enhance chemical weathering. They proposed that the tectonic collision and subsequent uplift of the Tibetan Plateau increased silicate weathering, thus leading to global cooling during the late Cenozoic. Alternatively, the rapid removal of unconsolidated material by uplift, leads to thin soil cover and short residence times of the sediment in the weathering profile. As chemical weathering is thought to predominantly occur in the weathering profile, as opposed to during transport within the fluvial system, low residence time could result in insufficient time for the dissolution of minerals before being eroded off the hillslope (Nesbitt *et al.* 1997).

Correlation between mean annual uplift and normalised Na/Zr, Ca/Zr, Mg/Zr, Sr/Zr, Ba/Zr and U/Zr, showed that there was no systematic relationship evident between uplift and the intensity of chemical weathering in either the Haast Schist or Torlesse Terrane-derived sediments (Appendix H, Figure 75 and Figure 76). The lack of systematic relationship suggests that, in the Southern Alps, uplift is not the predominant control on the intensity of chemical weathering.

Figure 74 highlights that uplift does not appear to influence the fractionation between ^{230}Th and ^{238}U in the Haast Schist sediments. The lack of fractionation of ($^{230}Th/^{238}U$), from secular equilibrium, can be attributed to their short residence time in the weathering profile and fluvial system (as discussed in Section 6.1.1). In contrast, however, fractionation between ^{230}Th and ^{238}U in the Torlesse Terrane-derived sediments, appears to be sensitive to increased uplift rates (R^2=0.60, $F_{1,7}$ = 7.52, P = 0.041). Therefore, this correlation suggests that uplift is enhancing silicate weathering, in the Torlesse Terrane, due to exposing fresh minerals to the weathering environment.

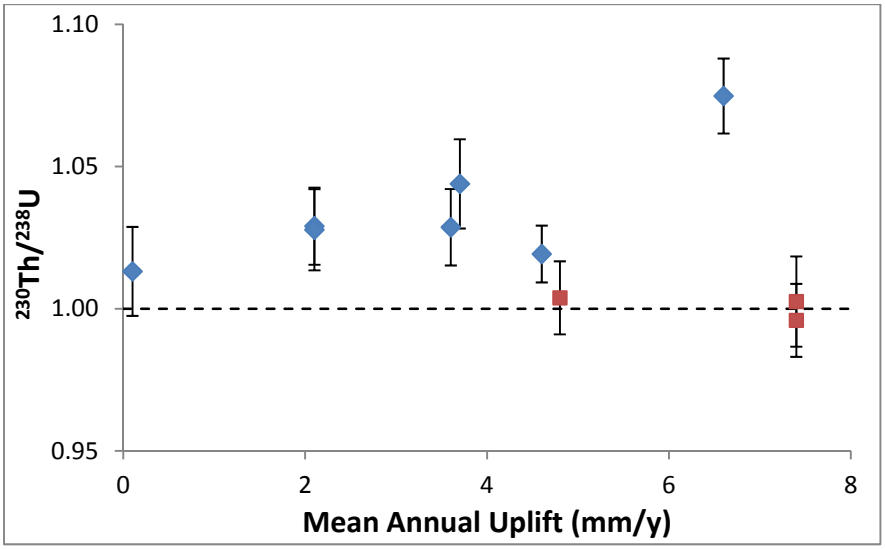

Figure 74: $^{230}Th/^{238}U$ versus mean annual rainfall (Torlesse Terrane R^2=0.60, $F_{1,7}$ = 7.52, P = 0.041). Dotted line in indicates secular equilibrium of bedrock. For sediments derived from Torlesse Terrane (blue diamond) and Haast Schist (red square). Data excludes NZR10 and NZR11 due to Th mobilization. Error bars represent 2σ.

However, Figure 67 and Figure 68 demonstrate that ($^{230}Th/^{238}U$) additionally correlates with rainfall and increased distance from the headwaters, respectively. There was no systematic relationship evident between uplift and the normalised elemental ratios for the mobile elements. It is therefore concluded that rainfall and residence time in the fluvial system primarily are the controlling factors of the observed fractionation pattern of ($^{230}Th/^{238}U$) in the Torlesse Terrane-derived sediments. However, high uplift rates on the western coast, promoting rapid physical denudation and reduce sediment residence time. Consequently the extent of chemical weathering of the Haast Schist-derived sediments is inhibited by high uplift rates, whereby only the most mobile elements are depleted.

Chapter Seven: Conclusions, Limitations & Perspectives

7.1 Conclusions

The aim of this study was to improve the understanding of how chemical weathering responds to uplift and precipitation in the Southern Alps, through the use of geochemistry and mineralogy of fluvial sediments. Through analysis of major mineralogy, major and trace chemistry, Sr isotopes and U-series for 25 river sediments, from varying rainfall and uplift regions, the following conclusions were drawn:

- Mineralogical analysis suggested that physical weathering is occurring within the fluvial system, whereby lithic fragments are fracturing into their composite minerals with increased distance from the headwaters. Consequently downstream fining was found to be attributed to combined processes of hydraulic sorting and physical weathering.
- Mineralogical analysis highlighted that rainfall enhanced the physical abrasion of mudstones fragments, suggesting physical weathering is overall amplified. The sensitivity of mudstone fragments to physical weathering was attributed to their greater proportion of clay and a larger composite mineral surface area.
- Through geochemical comparison of the sediments with their source, the lack of elemental mobility suggests that the Southern Alps are experiencing modest chemical weathering. Additionally U-series analysis highlighted that overall modern chemical weathering of South Island sediments is relatively moderate as compared to the previous weathering cycle.
- Furthermore, mobile elemental loss appears to be occurring within the weathering profile, suggesting that chemical weathering is occurring before erosion of the hillslope. Additionally geochemical analysis highlighted that U is the only mobile element, which appears to be significantly leached during transport within the fluvial system. Therefore, the intensity of U loss within the sediment has the potential to quantify the residence time within the fluvial system.
- The presence of hydrothermal calcite in the Haast Schist, combined by high uplift rates on the western coast result in rapid physical denudation, which continually

exposes highly weatherable calcite. Consequently, dissolution of calcite dominates chemical weathering in the Haast Schist-derived sediments.

- Geochemical analysis demonstrated that depletion of Mg is enhanced with increased annual rainfall in both Haast Schist- and Torlesse Terrane-derived sediments. In contrast Na was not found to be sensitive to rainfall and is significantly leached from sediments regardless of rainfall intensity. Consequently, when investigating climatic controls on silicate weathering using sediment geochemistry, it is suggested that Mg is a more appropriate silicate weathering tracer.
- This study found that carbonate minerals, in the Haast Schist and Torlesse Terrane, contained very minor, or no, U and Th. Consequently it is suggested that the ($^{230}Th/^{238}U$) activity ratio is an appropriate measure of silicate weathering intensity of sediments. Furthermore fractionation of ($^{230}Th/^{238}U$) for the Torlesse Terrane-derived sediments was found to occur with enhanced rainfall and increased distance from the headwaters. This suggests that silicate weathering on the east coast is amplified by rainfall and with increased residence time in the fluvial system, respectively.
- As the ($^{230}Th/^{238}U$) ratio for the Haast Schist-derived sediments did not deviate from secular equilibrium, it was suggested that residence time was not sufficient to fractionate ($^{230}Th/^{238}U$). It was concluded that the high uplift rates on the western coast, result in rapid erosion and short residence time of sediments in the weathering profile, acting to inhibit the extent of chemical weathering.

In summary, these results suggest that the South Island acts as a weathering limited setting, whereby the intensity of chemical weathering is limited by the residence time of the sediments in the catchment and rainfall. The east coast is characterised by more modest uplift and lower erosion rates, increasing the residence time of sediments in weathering profiles. Consequently, there is substantial time to allow the enhancement of chemical weathering by increased rainfall. In contrast, chemical weathering is inhibited on the western coast due to high uplift rates, resulting in the short residence time of sediments. Accordingly in such environments, only the most mobile elements are depleted and are sensitive to rainfall.

7.2 Limitations & Perspectives

Key limitations and perspectives for this study and for future geochemical and mineralogical fluvial sediment studies, investigating chemical weathering, in the Southern Alps are as follows:

- This study found that mineralogical and geochemical investigation of representative grain size fractions illustrated that some trace elements in accessory minerals are sensitive to hydraulic sorting. Consequently, the data in this study was potentially limited by hydraulic sorting effects. Therefore, future studies should analyse geochemistry and mineralogy of individual grain size fractions, to reduce hydrological sorting effects in analysis. Furthermore it is also recommended that sediment sampling be conducted in similar sedimentary and hydraulic settings.
- As the majority of catchments, covered in this study, had only one sample site, this study was limited in investigating chemical and physical weathering trends within individual fluvial systems. Therefore samples should be taken at a number of points along each river, in order to more accurately gauge and identify minor weathering trends and effects.
- As chemical weathering has found to be modest in the South Island geochemical analysis of major and trace element should be also undertaken using a more precise analytical technique, such as ICP-MS. This would reduce measurement errors, therefore enhancing the ability to compare the mobility of elements between localities.
- As the Haast Schist is quite variable, both mineralogically and geochemically, it is suggested that representative bedrock samples are collected from the headwaters of each catchment. This would ensure that the source rock composition is most representative of the actual catchment. As the Torlesse Terrane was deposited in a turbidic sedimentary setting, its geochemistry and mineralogy is thought to be more homogenous throughout the catchments. Consequently, sampling representative bedrock from each catchment would not be as necessary as the drainage basins underlain by Haast Schist.

References

Ahmad, T., P. P. Khanna, G. J. Chakrapani & S. Balakrishnan (1998). "Geochemical characteristics of water and sediment of the Indus river, Trans-Himalaya, India: constraints on weathering and erosion." Journal of Asian Earth Sciences **16**(2–3): 333-346.

Bahlburg, H. & N. Dobrzinski (2011). "Chapter 6 A review of the Chemical Index of Alteration (CIA) and its application to the study of Neoproterozoic glacial deposits and climate transitions." Geological Society, London, Memoirs **36**(1): 81-92.

Baker, J. A., J. A. Gamble & I. J. Graham (1994). "The age, geology and geochemistry of the Tapuaenuku Igneous Complex, Marlborough, New Zealand." New Zealand Journal of Geology and Geophysics **37**(3): 249-268.

Barthelmy, D. (2010). "Minerals Arranged by X-Ray Powder Diffraction." Retrieved 20/09/2012, from http://webmineral.com/MySQL/xray.php.

Bellingham, P. J., D. A. Peltzer & L. R. Walker (2005). "Contrasting impacts of a native and an invasive exotic shrub on flood-plain succession." Journal of Vegetation Science **16**(1): 135-142.

Bhuiyan, M. A. H., M. J. J. Rahman, S. B. Dampare & S. Suzuki (2011). "Provenance, tectonics and source weathering of modern fluvial sediments of the Brahmaputra–Jamuna River, Bangladesh: Inference from geochemistry." Journal of Geochemical Exploration **111**(3): 113-137.

Bhushan, R. & S. K. Singh (2008). "Sediment Provenance in the Bay of Bengal using Sr and Nd Isotopes." HIMALAYAN GEOLOGY **29**(3): 9-9.

Blake, K. (2012). "FAQ - XRD/XRF." Retrieved 20/09/2012, from http://www.jcu.edu.au/aac/servicesresources/resourcesextras/JCUPRD1_073680.html#_What_is_the.

Brown, L. J. (1981). "Late Quaternary geology of the Wairau Plain, Marlborough, New Zealand." New Zealand Journal of Geology & Geophysics **24**(4): 477-490.

Browne, G. (2004). "Downstream Fining and Sorting of Gravel Clasts in the Braided Rivers of mid-Canterbury, New Zealand." New Zealand Geographer **60**(2): 2-14.

Chabaux, F., J. Riotte & O. Dequincey (2003). U-Th-Ra fractionation during weathering and river transport. Chantilly, Mineralogical Society America. **52:** 533-576.

Chamberlain, C. P., J. R. Waldbauer & A. D. Jacobson (2005). "Strontium, hydrothermal systems and steady-state chemical weathering in active mountain belts." Earth and Planetary Science Letters **238**(3): 351-366.

Chigira, M. & T. Oyama (2000). "Mechanism and effect of chemical weathering of sedimentary rocks." Engineering Geology **55**(1-2): 3-14.

Christensen, K. & C. Doscher (2010). "The interaction of river engineering and geomorphology in the Lower Wairau River, Marlborough, New Zealand." Journal of Hydrology New Zealand **49**(2): 79-98.

Corcoran, P. L. (2005). "Recycling and chemical weathering in technically controlled mesozoic-cenozoic basins of New Zealand." Sedimentology **52**(4): 757-774.

Dalai, T. K., R. Rengarajan & P. P. Patel (2004). "Sediment geochemistry of the Yamuna River System in the Himalaya: Implications to weathering and transport." Geochemical Journal **38**(5): 441-453.

Davis, J. C. (2002). Statistics and data analysis in geology. New York, John Wiley & Sons.

DePaolo, D. J., K. Maher, J. N. Christensen & J. McManus (2006). "Sediment transport time measured with U-series isotopes: Results from ODP North Atlantic drift site 984." Earth and Planetary Science Letters **248**(1–2): 394-410.
Dickinson, W. R. (1970a). "Interpreting detrital modes of greywacke and arkose." Journal of Sedimentary Petrology **40**(2): 695-707.
Dickinson, W. R. (1970b). "Interpreting detrital modes of greywacke and arkose." Journal of Sedimentary Petrology **40**: 695-707.
Dickinson, W. R., L. S. Beard, G. R. Brakenridge, J. L. Erjavec, R. C. Ferguson, K. F. Inman, K. R.A, F. A. Lindberg & P. T. Ryberg (1983). "Proenance of North American Phanerozoic sandstones in relation to tectonic setting." Geological Society of America Bulletin **94**: 222-235.
Donkin, M. J. (1991). "Loss-on-Ignition as an estimator of soil organic-carbon in A-horizon forestery soils." Commuications in Soil Science and Plant Anlaysis **22**(3-4): 233-241.
Dosseto, A. (2012). Laboratory procedure for strontium, Wollongong Isotope Geochronology Lab, University of Wollongong.
Dosseto, A., B. Bourdon, J. Gaillardet, C. J. Allègre & N. Filizola (2006). "Time scale and conditions of weathering under tropical climate: Study of the Amazon basin with U-series." Geochimica et Cosmochimica Acta **70**(1): 71-89.
Dosseto, A., B. Bourdon & S. P. Turner (2008). "Uranium-series isotopes in river materials: Insights into the timescales of erosion and sediment transport." Earth and Planetary Science Letters **265**(1–2): 1-17.
Dutrow, B. L. & C. M. Clark. (2012). "X-ray Powder Diffraction (XRD)." Retrieved 20/09/2012, from http://serc.carleton.edu/research_education/geochemsheets/techniques/XRD.html.
Eden, D. N. (1989). "River terraces and their loessial cover beds, Awatere River valley, South Island, New Zealand." New Zealand Journal of Geology & Geophysics **32**(4): 487-497.
Eiriksdottir, E. S., S. R. Gislason & E. H. Oelkers (2011). "Does runoff or temperature control chemical weathering rates?" Applied Geochemistry **26**: S346-S349.
Fedo, C. M., H. Wayne Nesbitt & G. M. Young (1995). "Unraveling the effects of potassium metasomatism in sedimentary rocks and paleosols, with implications for paleoweathering conditions and provenance." Geology **23**(10): 921-924.
Frey, M. (1987). Low temperature metamorphism. Glasgow, Blackie.
Gabet, E. J., D. Wolff-Boenisch, H. Langner, D. W. Burbank & J. Putkonen (2010). "Geomorphic and climatic controls on chemical weathering in the High Himalayas of Nepal." Geomorphology **122**(1–2): 205-210.
Gaillardet, J., B. Dupré & C. J. Allègre (1999). "Geochemistry of large river suspended sediments: silicate weathering or recycling tracer?" Geochimica et Cosmochimica Acta **63**(23–24): 4037-4051.
Gasparini, N. M., G. E. Tucker & R. L. Bras (1999). "Downstream fining through selective particle sorting in an equilibrium drainage network." Geology **27**(12): 1079-1082.
Goldich, S. S. (1938). "A Study in Rock-Weathering." The Journal of Geology **46**(1): 17-58.
Goldstein, S. J. & S. B. Jacobson (1988). "The Nd and Sr isotopic systematics of river-water dissolved material: implications for the sources of Nd and Sr in seawater." Deep-Sea Research Part B. Oceanographic Literature Review **35**(6): 534-534.

Gomez, B., B. J. Rosser, D. H. Peacock, D. M. Hicks & J. A. Palmer (2001). "Downstream fining in a rapidly aggrading gravel bed river." Water Resour. Res. **37**(6): 1813-1823.

Grapes, R. & M. Otsuki (1983). "Peristerite compositions in quartzofeldspathic schists, Franz Josef-Fox Glacier Area, New Zealand." Journal of Metamorphic Geology **1**(1): 47-61.

Grapes, R. H., S. H. Lamb & C. J. Adams (1992). "K-Ar ages of basanitic dikes, Awatere Valley, Marlborough, New Zealand." New Zealand Journal of Geology & Geophysics **35**(4): 415-419.

Grapes, R. H., T. Watanabe & K. Palmer (1982). XRF Analyses of Quartzofeldspathic Schists and Metacherts, Franz Josef-Fox Glacier Area, Southern Alps of New Zealand. Victoria University of Wellington, Department of Geology; Publication No. 25.

Grapes, R. H. & H. W. Wellman (1986). "The north-east end of the Wairau Fault, Marlborough, New Zealand." Journal - Royal Society of New Zealand **16**(3): 245-250.

Griffiths, G. A. (1979). "Recent sedimentation history of the Waimakariri river, New Zealand." Journal of Hydrology (New Zealand) **18**(1): 6-28.

Harris, S. E. & A. C. Mix (2002). "Climate and tectonic influences on continental erosion of tropical South America, 0–13 Ma." Geology **30**(5): 447-450.

Hicks, D. M., J. Hill & U. Shankar (1996). "Variation of suspended sediment yields around New Zealand: The relative importance of rainfall and geology." IAHS-AISH Publication **236**: 149-156.

Hicks, D. M., U. Shankar, A. I. McKerchar, L. Basher, I. Lynn, M. Page & M. Jessen (2011). "Suspended Sediment Yields from New Zealand Rivers." Journal of Hydrology (New Zealand) **50**(1): 81-142.

Honda, M. & H. Shimizu (1998). "Geochemical, mineralogical and sedimentological studies on the Taklimakan Desert sands." Sedimentology **45**(6): 1125-1143.

Hren, M. T. (2007). The role of tectonics, climate, and biology in chemical weathering and carbon dioxide consumption. United States -- California, Stanford University. **Ph.D.**

Jacobson, A. D. (2001). Silicate versus carbonate weathering in the Himalaya Mountains and the New Zealand Southern Alps. United States -- Michigan, University of Michigan. **Ph.D.:** 273 p.

Jacobson, A. D. & J. D. Blum (2003). "Relationship between mechanical erosion and atmospheric CO2 consumption in the New Zealand Southern Alps." Geology **31**(10): 865-868.

Jacobson, A. D., J. D. Blum, C. P. Chamberlain, D. Craw & P. O. Koons (2003). "Climatic and tectonic controls on chemical weathering in the New Zealand Southern Alps." Geochimica et Cosmochimica Acta **67**(1): 29-46.

Johnsson, M. J. (1990). "Tectonic versus chemical-weathering controls on the composition of fluvial sands in tropical environments." Sedimentology **37**(4): 713-726.

Johnsson, M. J. & A. Basu (1993). Processes controlling the composition of clastic sediments. Boulder, Colo, Geological Society of America.

Jongens, R. (2006). "Structure of the Buller and Takaka Terrane rocks adjacent to the Anatoki Fault, northwest Nelson, New Zealand." New Zealand Journal of Geology and Geophysics **49**(4): 443-461.

Kamber, B. S., A. Greig & K. D. Collerson (2005). "A new estimate for the composition of weathered young upper continental crust from alluvial sediments, Queensland, Australia." Geochimica et Cosmochimica Acta **69**(4): 1041-1058.
Kautz, C. Q. & C. E. Martin (2007). "Chemical and physical weathering in New Zealand's Southern Alps monitored by bedload sediment major element composition." Applied Geochemistry **22**(8): 1715-1735.
Koons, P. O. (1990). "Two-sided orogen: Collision and erosion from the sandbox to the Southern Alps, New Zealand." Geology **18**(8): 679-682.
Korup, O. (2005a). "Distribution of landslides in southwest New Zealand." Landslides **2**(1): 43-51.
Korup, O. (2005b). "Geomorphic imprint of landslides on alpine river systems, southwest New Zealand." Earth Surface Processes and Landforms **30**(7): 783-800.
Kump, L. R., S. L. Brantley & M. A. Arthur (2000). "Chemical Weathering, Atmospheric CO2, and Climate." Annual Review of Earth and Planetary Sciences **28**(1): 611-667.
Li, C. & S. Y. Yang (2010). "Is the Chemical Index of Alteration (CIA) a reliable proxy for chemical weathering in global drainage basins?" American Journal of Science **310**(2): 111-127.
Limmer, D. R., P. Böning, L. Giosan, C. Ponton, C. M. Köhler, M. J. Cooper, A. R. Tabrez & P. D. Clift (2012). "Geochemical record of Holocene to Recent sedimentation on the Western Indus continental shelf, Arabian Sea." Geochemisty, Geophysics & Geosystems **13**: Q01008.
Liu, H.-C., C.-F. You, C.-H. Chung, K.-F. Huang & Z.-F. Liu (2011). "Source variability of sediments in the Shihmen Reservoir, Northern Taiwan: Sr isotopic evidence." Journal of Asian Earth Sciences **41**(3): 297-306.
Lowson, R. T., S. A. Short, B. G. Davey & D. J. Gray (1986). "234U 238U and 230Th 234U activity ratios in mineral phases of a lateritic weathered zone." Geochimica et Cosmochimica Acta **50**(8): 1697-1702.
LWNZ. (2010). "Pareora River." Retrieved 20/09/2012, from http://landandwater.co.nz/councils-involved/environment-canterbury/pareora-river/.
Lyons, W. B., A. E. Carey, D. M. Hicks & C. A. Nezat (2005). "Chemical weathering in high-sediment-yielding watersheds, New Zealand." Journal of Geophysical Research **110**(F1): F01008.
Mackinnon, T. C. (1983). "Origin of the Torlesse terrane and coeval rocks, South Island, New Zealand." GSA Bulletin **94**(8): 967.
Marx, S. K. & B. S. Kamber (2010). "Trace-element systematics of sediments in the Murray–Darling Basin, Australia: Sediment provenance and palaeoclimate implications of fine scale chemical heterogeneity." Applied Geochemistry **25**(8): 1221-1237.
Mason, B. & S. R. Taylor (1987). "High-grade basement gneisses and granitoids in Westland, New Zealand." Journal of the Royal Society of New Zealand **17**(2): 115-138.
McCalpin, J. P. (1992). "Glavial and postglacial geology near Lake Tennyson, Clarence River, New Zealand." New Zealand Journal of Geology and Geophysics **35**(2): 201-210.

McLennan, S. M. (2001). "Relationships between the trace element composition of sedimentary rocks and upper continental crust." Geochem. Geophys. Geosyst. **2**(4).
McWethy, D. B., C. Whitlock, J. M. Wilmshurst, M. S. McGlone & X. Li (2009). "Rapid deforestation of South Island, New Zealand, by early Polynesian fires." The Holocene **19**(6): 883-897.
Mew, G. (1980). Soils, Forestry, and Agriculture of the Grey Valley, South Island, New Zealand, New Zealand Soil Bureau, Department of Scientific and Industrial Research.
Mortatti, J. & J.-L. Probst (2003). "Silicate rock weathering and atmospheric/soil CO2 uptake in the Amazon basin estimated from river water geochemistry: seasonal and spatial variations." Chemical Geology **197**(1–4): 177-196.
Mortimer, N. (2004). "New Zealand's Geological Foundations." Gondwana Research **7**(1): 261-272.
Nathan, S. (1993). Revising the 1:250,000 Geological Map of New Zealand. Institute of Geological & Nuclear Sciences Science Report **93/26**.
Nesbitt, H. W., C. M. Fedo & G. M. Young (1997). "Quartz and feldspar stability, steady and non steady state state weathering, and petrogenesis of siliciclastic sands and muds." The Journal of Geology **105**(2): 173-192.
Nesbitt, H. W. & G. M. Young (1984). "Prediction of some weathering trends of plutonic and volcanic rocks based on thermodynamic and kinetic considerations." Geochimica et Cosmochimica Acta **48**(7): 1523-1534.
Nesbitt, H. W. & G. M. Young (1989). "Formation and Diagenesis of Weathering Profiles." The Journal of Geology **97**(2): 129-147.
Nesbitt, H. W. & G. M. Young (1996). "Petrogenesis of sediments in the absence of chemical weathering: effects of abrasion and sorting on bulk composition and mineralogy." Sedimentology **43**(2): 341-358.
Padoan, M., E. Garzanti, Y. Harlavan & I. M. Villa (2011). "Tracing Nile sediment sources by Sr and Nd isotope signatures (Uganda, Ethiopia, Sudan)." Geochimica et Cosmochimica Acta **75**(12): 3627-3644.
Parker, A. (1970). "An index of weathering for silicate rocks." Geological Magazine **107**(6): 501-504.
Pickett, D. A. & G. J. Wasserburg (1989). "Neodymium and strontium isotopic characteristics of New Zealand granitoids and related rocks." Contributions to Mineralogy and Petrology **103**(2): 131-142.
Porcelli, D., P. S. Andersson, M. Baskaran & G. J. Wasserburg (2001). "Transport of U- and Th-series nuclides in a Baltic shield watershed and the Baltic sea." Geochimica et Cosmochimica Acta **65**(15): 2439-2459.
Price, J. R. & M. A. Velbel (2003). "Chemical weathering indices applied to weathering profiles developed on heterogeneous felsic metamorphic parent rocks." Chemical Geology **202**(3,Äì4): 397-416.
Rajamani, V., J. K. Tripathi & V. P. Malviya (2009). "Weathering of lower crustal rocks in the Kaveri river catchment, southern India: Implications to sediment geochemistry." Chemical Geology **265**(3–4): 410-419.
Raymo, M. E. & W. F. Ruddiman (1992). "Tectonic Forcing of Late Cenozoic Climate." Nature **359**(6391): 117-117.
Riebe, C. S., J. W. Kirchner, D. E. Granger & R. C. Finkel (2001). "Strong tectonic and weak climatic control of long-term chemical weathering rates." Geology **29**(6): 511-514.

Robinson, L. F., G. M. Henderson, L. Hall & I. Matthews (2004). "Climatic Control of Riverine and Seawater Uranium-Isotope Ratios." Science **305**(5685): 851-854.
Robinson, R. S. & M. J. Johnsson (1997). "Chemical and physical weathering of fluvial sands in an Arctic environment; sands of the Sagavanirktok River, North Slope, Alaska." Journal of Sedimentary Research **67**(3): 560-570.
Rollinson, H. R., - (1993). Using geochemical data : evaluation, presentation, interpretation / Hugh R. Rollinson. Harlow, Essex, England : New York :, Longman Scientific & Technical ; Copublished in the U.S. with J. Wiley & Sons.
Roser, B. P. & A. F. Cooper (1990). "Geochemistry and terrane affiliation of Haast Schist from the western Southern Alps, New Zealand." New Zealand Journal of Geology and Geophysics **33**(1): 1-10.
Roser, B. P., R. A. Cooper, S. Nathan & A. J. Tulloch (1996). "Reconnaissance sandstone geochemistry, provenance, and tectonic setting of the lower Paleozoic terranes of the West Coast and Nelson, New Zealand." New Zealand Journal of Geology and Geophysics **39**(1): 1-16.
Roser, B. P. & R. J. Korsch (1999). "Geochemical characterization, evolution and source of a Mesozoic accretionary wedge: the Torlesse terrane, New Zealand." Geological Magazine **136**(05): 493-512.
Roy, P. D., M. Caballero, R. Lozano & W. Smykatz-Kloss (2008). "Geochemistry of late quaternary sediments from Tecocomulco lake, central Mexico: Implication to chemical weathering and provenance." Chemie der Erde - Geochemistry **68**(4): 383-393.
Savage, K. M. & P. E. Potter (1991). "Petrology of Modern Sands of the Rios Guaviare and Inirida, Southern Colombia: Tropical Climate and Sand Composition." The Journal of Geology **99**(2): 289-298.
Schumm, S. A., C. C. Watson & M. D. Harvey (1984). Incised channels: morphology, dynamics and control. Littleton, Colo, Water Resources Publications.
Shepard, F. P. (1954). "Nomenclature based on sand-silt-clay ratios." Journal of Sedimentary Research **24**(3): 151.
Shulmeister, J., D. Fink, O. M. Hyatt, G. D. Thackray & H. Rother (2010). "Cosmogenic 10Be and 26Al exposure ages of moraines in the Rakaia Valley, New Zealand and the nature of the last termination in New Zealand glacial systems." Earth and Planetary Science Letters **297**(3-4): 558-566.
Singh, M., M. Sharma & H. J. Tobschall (2005). "Weathering of the Ganga alluvial plain, northern India: implications from fluvial geochemistry of the Gomati River." Applied Geochemistry **20**(1): 1-21.
Suggate, R. P. (1978). The Geology of New Zealand. Wellington, NZ, Government Printer.
Suttner, L. J. & A. Basu (1985). "The effect of grain size on detrital modes: A test of the Gazzi-Dickinson point-counting method-discussion." Journal of Sedimentary Petrology **55**(4): 616-617.
Taylor, G. & R. A. Eggleton (2001). Regolith Geology & Geomorphology, J. Wiley, New York.
Tippett, J. M. & P. J. J. Kamp (1993). "Fission Track Analysis of the Late Cenozoic Vertical Kinematics of Continental Pacific Crust, South Island, New Zealand." Journal of Geophysical Research **98**(B9): 16119-16148.
Tonkin, P. J. & L. R. Basher (1990). "Soil-stratigraphic techniques in the study of soil and landform evolution across the Southern Alps, New Zealand." Geomorphology **3**(3–4): 547-575.
UCSB. (2012).

USGS. (2012). "U.S. Geological Survey Geochemical Reference Materials and Certificates." from http://crustal.usgs.gov/geochemical_reference_standards/quartz.html.
Vital, H. & K. Stattegger (2000). "Major and trace elements of stream sediments from the lowermost Amazon River." Chemical Geology **168**(1–2): 151-168.
von Gunten, H. R., E. Roessler, R. T. Lowson, P. D. Reid & S. A. Short (1999). "Distribution of uranium- and thorium series radionuclides in mineral phases of a weathered lateritic transect of a uranium ore body." Chemical Geology **160**(3): 225-240.
Vry, J. K., R. Powell & J. Williams (2008). "Establishing the P–T path for Alpine Schist, Southern Alps near Hokitika, New Zealand." Journal of Metamorphic Geology **26**(1): 81-97.
Waight, T. E., S. D. Weaver, R. J. Muir, R. Maas & G. N. Eby (1998). "The Hohonu Batholith of North Westland, New Zealand: Granitoid compositions controlled by source H2O contents and generated during tectonic transition." Contributions to Mineralogy and Petrology **130**(3-4): 225-239.
Wandres, A. M., J. D. Bradshaw, S. Weaver, R. Maas, T. Ireland & N. Eby (2004). "Provenance of the sedimentary Rakaia sub-terrane, Torlesse Terrane, South Island, New Zealand: the use of igneous clast compositions to define the source." Sedimentary Geology **168**(3–4): 193-226.
Wang, H., Z. Liu, E. Sathiamurthy, C. Colin, J. Li & Y. Zhao (2011). "Chemical weathering in Malay Peninsula and North Borneo: Clay mineralogy and element geochemistry of river surface sediments." Science China. Earth Sciences **54**(2): 272-282.
Wellman, H. W. (1979). "An Uplift Map for the South Island of New Zealand, and a Model for Uplift of the Southern Alps." The Royal Society of New Zealand **Bulletin 18**: 13-20.
Whitmore, G. P., K. A. W. Crook & D. P. Johnson (2004). "Grain size control of mineralogy and geochemistry in modern river sediment, New Guinea collision, Papua New Guinea." Sedimentary Geology **171**(1–4): 129-157.
Willenbring, J. K. & F. von Blanckenburg (2010). "Long-term stability of global erosion rates and weathering during late-Cenozoic cooling." Nature **465**(7295): 211-214.
Williams, P. W. (1991). "Tectonic geomorphology, uplift rates and geomorphic response in New Zealand." CATENA **18**(5): 439-452.
Wilson, D. D. (1985). "Erosional and depositional trends in rivers of the Canterbury Plains, New Zealand." Journal of Hydrology (New Zealand) **24**(1): 32-44.
Zhang, C., L. Wang, G. Li, S. Dong, J. Yang & X. Wang (2002). "Grain size effect on multi-element concentrations in sediments from the intertidal flats of Bohai Bay, China." Applied Geochemistry **17**(1): 59-68.

Appendices

Appendix A: Grain size Fraction Data

Table 5: Weight percentage (wt%) of grain size fractions for NZR25, NZR02 and NZR15

	Pahau Torlesse	Rakaia Torlesse	Haast Schist
Grain Size (μm)	NZR25 (Wairau)	NZR02 (Rakaia)	NZR15 (Haast)
0-63	10.4	3.5	10.2
63-125	8.2	14.1	18.0
125-180	8.6	16.6	15.3
180-250	15.5	29.8	15.1
250-355	21.5	-	-
355-500	19.7	-	-
250-500	-	34.4	21.8
>500	16.1	1.5	19.5

Table 6: Mineral abundances (wt%) for grain size fractions of NZR25, NZR02 and NZR15

	Pahau Torlesse Terrane							Rakaia Torlesse Terrane						Haast Schist					
Sample & River	**NZR25 (Wairau)**							**NZR02 (Rakaia)**						**NZR15 (Haast)**					
Grain Size Fraction (μm)	**>500**	**355-500**	**250-355**	**250-180**	**125-180**	**63-125**	**<63**	**>500**	**250-500**	**250-180**	**125-180**	**63-125**	**<63**	**>500**	**250-500**	**180-250**	**125-180**	**63-125**	**<63**
ϕ^2	3.84	4.58	3.75	3.88	4.21	4.13	3.45	3.79	5.01	4.82	4.97	4.63	3.83	5.4	8.14	8.64	9.8	8.81	5.48
Quartz	51.5	43.2	50.4	48.2	41.1	46.2	44.5	45.2	36.8	39.4	34.5	32.5	37.8	57	37.1	31.3	30	29.7	30.1
Albite	31.6	37.7	28.8	29.6	28.4	31	27.9	30.7	33.6	30.2	34.5	29.7	28.3	19.4	19.1	22.2	31.8	26.9	29.6
Labradorite	0.6	-	1.2	1	-	-	2.9	2.7	-	-	-	-	-	-	-	-	-	9.4	7.7
Orthoclase	-	-	-	-	0.8	-	0.5	-	0.5	2.7	0.7		2.3	-	-	-	-	9.5	-
Microcline	-	1.9	-	-	3.8	0.2	0.7	0.3	3.1	2.2	0.8	3.1	1.3	-	-	-	-	6.8	1.5
Chlorite	9.4	8.9	10.4	10.3	12.4	9.6	5.6	11.3	12.2	12	13.2	16.3	14.6	10.7	16.1	16.8	14.8	16.1	8.1
Titanite	1.9	2.9	1.5	2.3	3.4	3.6	3.2	1.9	3.9	4.4	2.7	2.8	2.6	-	-	-	-	-	2.1
Mica	8.5	9	10.3	12.3	13.4	13.7	21.2	10	12.5	12.2	15.9	18.7	16.8	16.4	29.5	31.7	24.6	3.2	21.6
Calcite	-	-	-	-	-	-	-	-	-	-	-	-	-	-	-	-	-	-	-
Tourmaline	-	-	-	-	1	-	-	1	-	-	-	-	-	-	-	-	-	-	0.9
Garnet	-	-	-	-	-	-	-	-	-	-	-	-	-	0.1	0.1	-	-	-	-

Table 7: Trace element geochemistry (ppm) of grain size fractions of NZR25, NZR15and NZR02

	NZR25 (µm)						NZR15 (µm)						NZR02 (µm)				
(ppm)	***>500***	***250-500***	***180-250***	***125-180***	***63-125***	***<63***	***>500***	***250-500***	***180-250***	***125-180***	***63-125***	***<63***	***250-500***	***180-250***	***125-180***	***63-125***	***<63***
Ba	467	472	498	563	580	571	211	419	443	440	407	458	550	613	616	652	555
Cl	< 2.0	< 2.0	< 2.0	< 2.0	< 2.0	29	4	< 2.0	< 2.0	< 2.0	< 2.0	39	< 2.0	< 2.0	< 2.0	< 2.0	8
Cr	35	49	60	74	70	72	21	37	34	33	33	39	42	44	46	46	58
Cu	22	22	23	20	30	58	37	23	24	18	33	59	18	15	17	34	68
Nb	7	7	8	8	8	9	5	9	11	12	13	12	8	9	10	11	12
Ni	20	25	33	40	40	31	10	12	16	14	15	18	17	18	19	19	23
Pb	12	13	15	15	15	16	7	12	13	13	14	18	16	15	16	16	16
Rb	63	71	84	88	91	92	43	79	87	85	75	77	96	111	113	111	106
S	14	19	29	35	54	90	33	29	43	78	97	116	36	33	33	82	161
Sr	248	242	233	225	230	246	139	214	252	269	291	335	350	359	366	366	373
Th	7	7	7.6	7.8	8.6	8	4	9.4	11.4	12.4	14.1	16.1	8.8	9.7	10.8	12.1	10
U	2.1	2	2	1.8	2.1	2	1	2.8	2.6	3	3.5	4.8	2.9	2.5	2.2	3.4	2
V	69	81	93	97	97	89	31	79	91	91	80	86	83	94	93	91	78
Y	17	17	18	18	18	21	11	18	22	25	27	32	18	21	21	23	32
Zn	52	55	62	67	66	71	51	60	63	62	59	69	55	60	62	67	81
Zr	166	166	156	147	165	310	89	142	160	189	483	589	143	148	136	184	738

Appendix B: Grain Size Data

Table 8: Table of grain size data of bulk sediments

		Grain size Fractions (wt%)				Mean Grain Size (µm)	Standard Deviation (σ)	Skewness	Kurtosis
River	*Sample*	coarse (> 2 mm)	sand (63 µm - 2mm)	silt (2 - 63 µm)	clay (< 2 µm)				
Awatere	**NZR24**	0.43	72.88	24.83	1.85	206	1.6	0	1.23
Upper Clarence	**NZR19**	12.89	84.73	1.92	0.46	699	1.03	0.2	1.06
Clarence (terrace)	**NZR19T**	0.00	83.66	14.24	2.10	208	1.44	0.31	1.35
Clarence	**NZR23**	0.68	75.39	22.37	1.57	163	1.36	0.12	1.08
Conway	**NZR20**	17.48	75.84	6.29	0.40	324	1.29	0.08	1.02
Haast	**NZR14**	0.00	87.21	12.29	0.51	221	1.25	0.29	1.31
Haast	**NZR15**	0.00	88.39	11.20	0.41	290	1.41	0.2	1.18
Hapuku	**NZR22**	7.34	83.35	8.44	0.86	286	1.3	0.14	1.13
Kowhai	**NZR21**	9.62	81.34	8.13	0.91	313	1.34	0.18	1.09
Pareora	**NZR01**	13.03	83.67	3.14	0.17	521	1.19	0.11	1.07
Poerua	**NZR12**	1.10	86.30	12.32	0.28	237	1.28	0.18	1.14
Rakaia Tributary (Andre Creek)	**NZR10**	74.69	24.15	1.11	0.05	855	1.15	0.42	1.63
Rakaia	**NZR04**	0.00	85.39	13.98	0.63	293	1.49	0.06	0.98
Rakaia	**NZR02**	0.00	95.16	4.53	0.31	291	0.91	0.2	1.15
Rakaia	**NZR03**	0.00	96.43	3.57	0.00	200	0.73	0.09	0.99
Upper Taramakau	**NZR08**	0.74	90.78	7.69	0.78	292	1.23	0.13	1.21
Taramakau	**NZR11**	22.24	71.68	5.68	0.41	533	1.63	0.15	0.99
Upper Waimakariri	**NZR07**	8.65	90.62	0.73	0.00	638	0.89	0.02	0.95
Upper Waimakariri	**NZR05**	8.53	72.66	17.47	1.34	311	1.81	-0.12	1
Waimakariri	**NZR09**	0.00	91.19	8.59	0.22	216	1	0.2	1.1
Wairau	**NZR25**	0.44	89.87	8.73	0.96	355	1.36	0.3	1.27
Whataroa	**NZR13**	0.00	88.01	11.41	0.58	272	1.37	0.31	1.38

Appendix C: Mineralogical Data – X-ray Diffraction

Table 9: Mineral abundances (wt%) for Rakaia Torlesse Terrane-derived sediments

Rakaia Torlesse Terrane									
River	**Pareora**	**Rakaia**				**Upper Taramakau**	**Waimakariri**		
Sample	**NZR01**	**NZR10**	**NZR04**	**NZR03**	**NZR02**	**NZR08**	**NZR07**	**NZR05**	**NZR09**
ϕ2	3.78	4.28	4.42	4.18	4.37	4.39	4.35	4.26	3.99
Quartz	50.2	32.8	33.9	38	40	41.1	41.7	36.9	32.2
Albite	28.2	25.4	31.4	29.4	28.8	26.1	28	35	20.2
Labradorite	-	1.8	-	0.7	2.5	2.4	-	-	3.2
Orthoclase	-	3.1	2.3	0.5	0.9	0.5	2.5	0.7	2.3
Microcline	-	3.8	2.2	2.5	1.4	2.6	3.1	2.4	3.9
Chlorite	5.7	13.8	13.3	11.7	10.1	10.9	7.7	9.3	8.6
Titanite	2.1	2.7	2.6	3.3	2.5	2.6	2.9	3.6	2.6
Mica	12	20.4	17	17.5	16.8	17.2	17.6	15.8	48.4
Calcite	-	-	-	-	-	-	-	-	-
Tourmaline	4.2	-	-	-	-	-	-	-	-
Garnet	0.5	-	-	-	-	-	-	-	-

Table 10: Mineral abundances (wt%) for Pahau Torlesse Terrane and Haast Schist-derived sediments

	Pahau Torlesse Terrane								Haast Schist				
River	**Awatere**	**Clarence**			**Conway**	**Hapuku**	**Kowhai**	**Wairau**	**Haast**		**Peorua**	**Lower Taramakau**	**Whataroa**
Sample	**NZR24**	**NZR19**	**NZR19T**	**NZR23**	**NZR20**	**NZR22**	**NZR21**	**NZR25**	**NZR14**	**NZR15**	**NZR12**	**NZR11**	**NZR13**
ϕ2	3.97	4.8	3.77	3.88	3.91	3.69	4.96	6.62	4.62	5.67	15.23	5.06	6.86
Quartz	35.2	43.2	46	38.4	37.8	36.3	35.7	51	47.5	41.6	35.9	41.4	36
Albite	32.9	26.2	24.7	34.1	27.9	31.1	32.7	29.4	23.9	26.5	16	26.7	19.4
Labradorite	5.3	5.4	2.8	4.4	8.6	1.7	3.5	-	1.2	1.3	3.9	1.8	-
Orthoclase	3.1	0.8	0.5	2.4	3.5	1.4	1.6	-	-	-	-	1.2	-
Microcline	2.4	2	1.5	3.4	3.6	2.6	3.4	-	-	-	-	2.8	-
Chlorite	8.2	6.3	6.7	5.4	4.4	11.2	9.1	8.7	9.2	9.6	6.5	8.9	14.5
Titanite	4	5.1	2.7	3.2	3.9	3.4	4	1.8	-	-	-	2.7	-
Mica	12.2	16.6	22	11.7	17.6	16.5	14.8	12.8	21	23.9	44.4	17.7	32.1
Calcite	-	-	-	0.1	0.2	-	-	-	-	-	-	-	-
Tourmaline	-	-	0.4	0.1	0.1	0.9	-	-	-	-	-	-	-
Garnet	-	-	0.1	0.1	0.1	-	-	-	-	-	0.1	0.1	-

Appendix D: Mineralogical Data – Thin Section Point Count

Table 11: Clast type percentage (%) of river bar and terrace sediments from the Pahau Torlesse Terrane

	Pahau Torlesse Terrane							
River	**Awatere**	**Clarence**			**Conway**	**Hapuku**	**Kowhai**	**Wairau**
Sample	**NZR24**	**NZR19**	**NZR19T**	**NZR23**	**NZR20**	**NZR22**	**NZR21**	**NZR25**
Qtz monocrystalline	12	3.5	14	24.5	10.5	5.5	6	5.5
Qtz metamorphic	2	2	3	3.5	1	1.5	3	3.5
Qtz polycrystalline	-	-	-	-	-	-	-	1
feldspar	11.5	2	16	21.5	13	5	8.5	4
mudstone	43.5	31	37	28.5	25	31	23	30
chert	7	3	3.5	3	6	4	6.5	5
siltstone	10	25.5	22	7.5	11.5	19.5	17	22
sandstone	12.5	33	4	8	28	29.5	35	28.5
basalt	1	-	-	1	1.5	-	-	-
biotite	-	-	0.5	1.5	-	0.5	-	-
chlorite	-	-	-	-	-		-	-
amphibole	0.5	-	-	0.5	0.5	2.5	-	-
calcite	-	-	-	-	3	1	1	-
glauconite	-	-	-	-	-	-	-	-
radiolarian chert	-	-	-	0.5	-	-	-	0.5

Table 12: Clast type percentage (%) of river sediments from the Rakaia Torlesse Terrane

	Rakaia Torlesse Terrane								
River	**Pareora**	**Rakaia**				**Upper Taramakau**	**Waimakariri**		
Sample	**NZR01**	**NZR10**	**NZR04**	**NZR03**	**NZR02**	**NZR08**	**NZR07**	**NZR05**	**NZR09**
Qtz monocrystalline	21	-	28	31	23	7.5	5.5	19.5	40
Qtz metamorphic	5	-	1.5	-	4	13	2	0.5	0.5
Qtz polycrystalline	6.5	1	3.5	6.5	12	-	5	3.5	6.5
feldspar	7	1	11	16	15	9	2.5	5	10.5
mudstone	21.5	33	27	25	24.5	14	22.5	15.5	28.5
chert	4.5	1	4	2.5	3	-	2	4.5	-
siltstone	22	24	10.5	8	8	3.5	11.5	4	4.5
sandstone	9	40	8	4	1	8	45	39	5.5
phylite	2	-	6.5	7	9	-	4	2	3.5
schist	-	-	-	-	-	45	-	-	-
plutonic	-	-	-	-	0.5	-	-	-	-
igneous	-	-	-	-	-	-	-	-	-
biotite	0.5	-	1	-	-	-	-	0.5	0.5
amphibole	-	-	-	-	-	-	-	1	-
muscovite	-	-	-	-	-	-	-	5	-
glauconite	1	-	-	-	-	-	-	-	-

Table 13: Clast type percentage (%) of river sediments from the Haast Schist

	Haast Schist			
River	**Haast**	**Peorua**	**Lower Taramakau**	**Whataroa**
Sample	**NZR15**	**NZR12**	**NZR11**	**NZR13**
Qtz monocrystalline	12	30	3.5	6
Qtz metamorphic	25	16.5	31	19.5
feldspar	2.5	6	7.5	1.5
mudstone	-	-	2	-
siltstone	-	-	2.5	-
sandstone	-	-	8	-
schist	58.5	17	32	68
basalt	-	-	-	-
plutonic	-	-	12	-
biotite	0.5	13	0.5	2.5
chlorite	1.5	-	-	-
amphibole	-	7	1	1
muscovite	-	10	-	1.5
calcite	-	0.5	-	-

Appendix E: Major and Trace Geochemical Data

Table 14: Average source rock composition with standard deviations

	Torlesse Terrane (Roser & Korsch, 1999)			Haast Schist (Grapes *et al.*, 1982)
(%)	**PF5**	**PF3**	**PF1**	
SiO2	73.91 ± 2.69	71.45 ± 2.59	70.03 ± 2.17	60.00 ± 9.62
TiO2	0.50 ± 0.08	0.51 ± 0.10	0.56 ± 0.11	0.80 ± 0.34
Al2O3	13.29 ± 1.16	14.50 ± 0.98	14.83 ± 0.68	16.00 ± 1.65
Fe2O3	3.46 ± 0.65	3.66 ± 0.79	4.00 ± 0.86	6.68 ± 3.13
MnO	0.06 ± 0.01	0.06 ± 0.02	0.07 ± 0.02	0.11 ± 0.06
MgO	1.10 ± 0.32	1.37 ± 0.40	1.45 ± 0.39	2.39 ± 1.35
CaO	1.56 ± 0.64	1.71 ± 0.39	2.30 ± 0.98	4.50 ± 3.12
Na2O	3.64 ± 0.59	4.02 ± 0.43	4.01 ± 0.37	3.27 ± 0.86
K2O	2.41 ± 0.34	2.61 ± 0.45	2.34 ± 0.29	2.19 ± 0.89
P2O5	0.09 ± 0.02	0.12 ± 0.03	0.11 ± 0.02	0.23 ± 0.20
(ppm)				
Ba	607 ± 133	749 ± 100	650 ± 100	469 ± 234
Nb	7 ± 1	8 ± 2	8 ± 1	10 ± 7
Ni	10 ± 4	11 ± 4	6 ± 3	24 ± 17
Pb	18 ± 2	22 ± 3	19 ± 3	18 ± 8
Rb	85 ± 12	86 ± 16	89 ± 13	84 ± 37
Sr	234 ± 103	476 ± 121	361 ± 91	316 ± 137
Th	9.4 ± 1.7	10.4 ± 1.8	10.9 ± 1.5	12.2 ± 2.4
U	2.2 ± 0.6	2.5 ± 0.5	2.3 ± 0.6	2.3 ± 0.6
Y	19 ± 3	20 ± 4	20 ± 3	29 ± 8
Zn	55 ± 11	56 ± 15	57 ± 11	95 ± 37
Zr	184 ± 30	181 ± 41	197 ± 42	183 ± 51

Table 15: Major and trace element concentrations for Torlesse Terrane-derived river sediments and terrace sediment from the Pahau region, South Island, NZ.

	Pahau Torlesse Terrane								
River	**Awatere**		**Clarence**			**Conway**	**Hapuku**	**Kowhai**	**Wairau**
Sample	**NZR24**	**NZR24 (duplicate)**	**NZR23**	**NZR19**	**NZR19T**	**NZR20**	**NZR22**	**NZR21**	**NZR25**
(%)									
Na2O	2.59	3.47	1.89	-	1.32	2.57	2.47	2.04	1.97
MgO	1.44	1.62	1.01	-	1.14	1.61	1.63	1.41	1.13
Al2O3	13.84	14.07	14.00	-	15.25	15.40	16.31	15.09	14.05
SiO2	67.11	67.50	69.66	-	70.19	65.54	67.58	62.73	68.78
P2O5	0.27	0.27	0.24	-	0.14	0.20	0.19	0.17	0.23
SO3	0.07	0.13	0.06	-	0.00	0.09	0.07	0.05	0.06
K2O	2.34	2.38	2.47	-	2.73	2.57	2.83	2.56	2.38
CaO	2.52	2.56	2.05	-	0.98	2.49	1.79	1.30	2.17
TiO2	0.92	0.94	0.65	-	0.51	0.66	0.65	0.53	0.73
MnO	0.06	0.06	0.05	-	0.04	0.05	0.06	0.04	0.05
Fe2O3	4.61	4.67	3.79	-	3.66	4.14	4.29	4.00	3.98
LOI	2.57	2.56	2.96	3.10	3.94	3.79	2.84	1.97	2.69
Total	98.33	100.23	98.83	-	99.90	99.09	100.71	91.88	98.21
(ppm)									
Ba	568	576	624	610	641	616	626	621	507
Nb	14	14	10	8	8	9	10	9	7
Ni	25	24	18	15	14	22	20	17	30
Pb	16	13	15	15	17	16	17	18	15
Rb	82	83	88	104	106	92	113	108	77
Sr	343	343	317	228	219	380	286	268	241
Th	9.6	9.2	9.1	9.5	8.6	9.0	11.3	10.7	7.2
U	4.5	3.8	4.0	3.3	4.7	3.8	4.4	4.0	3.6
Y	21.8	21.8	20.6	20.6	19.7	21.1	24.1	23	18.9
Zn	62	66	57	67	66	66	68	67	58
Zr	231	233	230	208	208	204	210	233	182

Table 16: Major and trace element concentrations for Torlesse Terrane-derived river sediments from the Rakaia region, South Island, NZ.

	Rakaia Torlesse Terrane									
River	**Pareora**	**Rakaia**				**Taramakau**	**Waimakariri**			
Sample	**NZR01**	**NZR02**	**NZR03**	**NZR04**	**NZR10**	**NZR08**	**NZR05**	**NZR05 (duplicate)**	**NZR07**	**NZR09**
(%)										
Na2O	1.56	1.96	1.71	1.90	1.70	1.09	1.83	1.57	1.74	1.41
MgO	1.11	1.38	1.15	0.95	2.06	1.03	0.53	1.24	0.74	0.94
Al2O3	13.72	15.41	15.21	15.52	18.18	15.36	15.04	15.99	15.49	14.35
SiO2	71.54	69.23	68.66	68.13	63.22	69.20	69.67	69.47	68.65	74.04
P2O5	0.31	0.16	0.24	0.23	0.23	0.16	0.19	0.14	0.46	0.15
SO3	0.03	< 0.01	< 0.01	< 0.01	0.01	< 0.01	0.01	0.01	0.09	0.00
K2O	2.25	2.60	2.70	2.77	3.63	3.10	3.13	3.10	3.42	2.71
CaO	1.62	1.91	1.84	1.88	1.12	1.33	1.47	1.48	1.37	1.14
TiO2	0.53	0.48	0.55	0.59	0.67	0.54	0.49	0.49	0.50	0.42
MnO	0.05	0.05	0.05	0.05	0.07	0.05	0.05	0.05	0.04	0.04
Fe2O3	4.12	3.73	3.86	4.13	5.01	3.79	3.47	3.43	3.60	2.95
LOI	2.92	2.52	2.80		4.47	2.87	2.66	2.65	2.75	2.21
Total	99.76	99.41	98.76	96.14	100.37	98.52	98.54	99.63	98.86	100.36
(ppm)										
Ba	539	584	626	628	704	657	688	710	753	631
Nb	7	8	9	9	12	10	9	9	9	7
Ni	13	19	19	16	25	16	13	14	15	14
Pb	14	15	16	17	20	20	20	20	20	16
Rb	81	104	108	111	169	129	127	127	141	104
Sr	247	357	361	359	319	271	319	318	299	281
Th	8.0	9.8	10.5	11.7	12.2	11.7	11.5	12.4	11.4	8.2
U	3.0	4.6	5.0	4.8	< 1.5	5.1	5.5	3.8	5.3	3.8
Y	19.7	21.1	22.7	24.3	22.8	23.1	21.7	21.9	22.5	17.7
Zn	58	59	61	64	91	65	59	58	64	47
Zr	163	172	202	183	212	206	192	185	173	178

Table 17: Major and trace element concentrations for Haast Schist & Buller Granite derived river sediments and standards.

	Haast Schist-derived					Buller Granite		
River	**Haast**		**Peorua**	**Taramakau**	**Whatroa**	**Grey**		
Sample	**NZR15**	**NZR14a**	**NZR12**	**NZR11**	**NZR13**	**NZR17**	**NZR18**	**NZR16**
(%)								
Na2O	1.81	1.57	-	1.24	1.45	0.77	0.62	0.72
MgO	1.15	0.94	-	1.06	1.64	1.17	0.89	0.93
Al2O3	13.76	13.34	-	14.03	15.30	13.92	13.10	13.05
SiO2	72.82	74.04	-	70.79	67.23	74.14	75.80	75.33
P2O5	0.33	0.16	-	0.21	0.34	0.13	0.13	0.16
SO3	0.02	< 0.01	-	< 0.01	0.04	< 0.01	< 0.01	< 0.01
K2O	1.94	1.88	-	2.55	2.72	3.26	3.35	2.65
CaO	1.47	1.48	-	1.78	2.09	0.95	1.24	0.96
TiO2	0.64	0.72	-	0.60	0.82	0.37	0.19	0.42
MnO	0.06	0.06	-	0.08	0.07	0.03	0.06	0.04
Fe2O3	3.71	3.70	-	3.71	4.53	2.93	2.39	2.81
LOI	1.77	1.95	1.73	1.96	2.28	1.72	0.90	2.01
Total	99.46	99.84	-	98.01	98.50	99.38	98.66	99.07
(ppm)								
Ba	416	419	457	577	642	552	415	545
Nb	10	11	12	9	13	8	6	7
Ni	14	12	24	18	23	20	19	15
Pb	13	11	19	18	17	23	33	18
Rb	76	74	89	103	109	129	139	102
Sr	247	247	249	331	369	184	152	227
Th	11.2	10.6	10.4	11.9	15.7	7.6	7.7	7.6
U	4.1	4.9	4.1	4.5	4.9	3.4	6.5	2.8
Y	22.5	22.8	26.8	21.9	31.6	16.6	24.4	20.9
Zn	56	54	72	54	76	55	38	44
Zr	236	252	202	162	244	142	99	167

Table 18: Statistical One-Way ANOVA analysis between bulk Zr concentration and grain size fractions. Significant correlation considered if P<0.05 (95% CI).

Grain Size Fraction (µm)	Source Rock	R^2 =	$F_{1,x}$ =[1]	P =
44-63	***Pahau Torlesse***	0.39	3.77	0.10
	Rakaia Torlesse	0.007	0.46	0.84
	Haast Schist	0.21	0.80	0.44
63-112	***Pahau Torlesse***	0.40	4.03	0.09
	Rakaia Torlesse	0.051	0.37	0.56
	Haast Schist	0.15	0.53	0.52
44-112	***Pahau Torlesse***	0.40	4.05	0.09
	Rakaia Torlesse	0.039	0.29	0.61
	Haast Schist	0.16	0.58	0.50
2-63	***Pahau Torlesse***	0.096	0.64	0.45
	Rakaia Torlesse	0.003	0.02	0.89
	Haast Schist	0.07	0.24	0.66

[1] x = 8 (PahauTorlesse), 9 (Rakaia Torlesse) and 5 (Haast Schist)

Appendix F: Sr Isotopic Data

Table 19: Sr isotopic data for the bulk river sediments and the terrace sediment of South Island, NZ rivers

River	Sample Name	87Sr/86Sr
Greywacke-derived sediments		
Awatere	NZR24	0.707080 ± 0.000006
Awatere (duplicate)	NZR24 #2	0.707141 ± 0.000008
Upper Clarence	NZR19	0.710595 ± 0.000008
Upper Clarence (Terrace)	NZR19T	0.710703 ± 0.000007
Clarence	NZR23	0.707819 ± 0.000036
Clarence (leach with NaOAc)	NZR23L	0.707894 ± 0.000008
Conway	NZR20	0.707160 ± 0.000010
Hapuku	NZR22	0.708463 ± 0.000008
Kowhai	NZR21	0.708667 ± 0.000009
Pareora	NZR01	0.710062 ± 0.000007
Rakaia	NZR02	0.710271 ± 0.000009
Rakaia	NZR03	0.710405 ± 0.000008
Rakaia (leach with NaOAc)	NZR03L	0.710586 ± 0.000007
Rakaia	NZR04	0.710562 ± 0.000009
Rakaia (tributary)	NZR10	0.711994 ± 0.000008
Upper Taramakau	NZR08	0.711879 ± 0.000008
Upper Waimakariri	NZR05	0.711145 ± 0.000010
Upper Waimakrariri (duplicate)	NZR05 #2	0.711103 ± 0.000009
Upper Waimakariri	NZR07	0.711564 ± 0.000009
Waimakariri	NZR09	0.711105 ± 0.000008
Wariau	NZR25	0.709196 ± 0.000009
Schsit derived sediments		
Haast	NZR14	0.709016 ± 0.000008
Haast	NZR15	0.709175 ± 0.000008
Peorua	NZR12	0.710267 ± 0.000008
Taramakau	NZR11	0.710716 ± 0.000007
Whatroa	NZR13	0.710662 ± 0.000009
Granite derived sediments		
Grey	NZR16	0.714265 ± 0.000009
Grey	NZR17	0.718519 ± 0.000009
Grey	NZR18	0.728370 ± 0.000009

Appendix G: U-series Data

Table 20: U-series data for the bulk river sediments and the terrace sediment of South Island, NZ rivers

River	Sample name	Th (ppm)	U (ppm)	($^{234}U/^{238}U$)	($^{230}Th/^{238}U$)	($^{238}U/^{232}Th$)	($^{230}Th/^{232}Th$)	Riverine ($^{234}U/^{238}U$)[1]
Greywacke Draining Rivers								
Awatere	NZR24	7.92 ± 0.02	1.67 ± 0.01	1.009 ± 0.006	1.029 ± 0.013	0.640 ± 0.004	0.659 ± 0.006	2.078 ± 0.007
Upper Clarence	NZR19	-	2.13 ± 0.01	0.959 ± 0.009	-	-	-	2.548 ± 0.445
Upper Clarence (Terrace)	NZR19T	-	1.37 ± 0.16	1.139 ± 0.183	-	-	-	-
Clarence	NZR23	8.06 ± 0.03	1.64 ± 0.01	0.980 ± 0.008	1.044 ± 0.016	0.620 ± 0.005	0.647 ± 0.007	2.861 ± 0.037
Clarence (leach with NaOAc)	NZR23L	9.04 ± 0.02	1.82 ± 0.01	0.976 ± 0.006	1.034 ± 0.011	0.612 ± 0.004	0.633 ± 0.005	-
Conway	NZR20	8.66 ± 0.02	1.913 ± 0.004	0.966 ± 0.005	1.019 ± 0.010	0.670 ± 0.003	0.683 ± 0.005	2.277 ± 0.008
Hapuku	NZR22	-	1.40 ± 0.12	1.043 ± 0.115	-	-	-	3.843 ± 0.011
Kowhai	NZR21	-	1.99 ± 0.11	1.127 ± 0.126	-	-	-	4.614 ± 0.011
Peorua	NZR01	8.86 ± 0.03	2.03 ± 0.01	1.013 ± 0.006	1.013 ± 0.016	0.696 ± 0.006	0.705 ± 0.008	-
Rakaia	NZR02	-	1.96 ± 0.02	0.996 ± 0.017	-	-	-	1.411 ± 0.025
Rakaia	NZR03	10.19 ± 0.03	1.95 ± 0.01	1.018 ± 0.006	1.029 ± 0.014	0.581 ± 0.004	0.598 ± 0.006	1.411 ± 0.025
Rakaia (leach with NaOAc)	NZR03L	10.45 ± 0.03	1.98 ± 0.01	1.008 ± 0.006	1.043 ± 0.015	0.575 ± 0.004	0.600 ± 0.006	-
Rakaia	NZR04	10.63 ± 0.03	2.10 ± 0.01	1.013 ± 0.007	1.028 ± 0.014	0.600 ± 0.004	0.617 ± 0.006	1.411 ± 0.025
Rakaia (tributary)	NZR10	11.99 ± 0.03	3.17 ± 0.01	1.003 ± 0.006	0.936 ± 0.010	0.801 ± 0.004	0.749 ± 0.006	-
Upper Taramakau	NZR08	11.16 ± 0.03	1.85 ± 0.01	1.064 ± 0.006	1.075 ± 0.013	0.503 ± 0.003	0.540 ± 0.005	1.928 ± 0.025
Upper Waimakariri	NZR05	-	2.83 ± 0.02	0.981 ± 0.011	-	-	-	2.589 ± 0.009
Upper Waimakariri	NZR07	-	2.76 ± 0.03	1.002 ± 0.014	-	-	-	2.589 ± 0.009
Waimakariri	NZR09	-	2.17 ± 0.11	0.965 ± 0.078	-	-	-	1.735 ± 0.010
Wairau	NZR25	-	1.75 ± 0.02	0.977 ± 0.013	-	-	-	1.946 ± 0.187
Schist Draining Rivers								
Haast	NZR14	-	2.06 ± 0.11	0.838 ± 0.118	-	-	-	-
Haast	NZR15	10.94 ± 0.03	1.87 ± 0.01	1.007 ± 0.005	1.004 ± 0.013	0.518 ± 0.003	0.520 ± 0.005	1.185 ± 0.026
Peorua	NZR12	10.09 ± 0.04	1.91 ± 0.01	1.000 ± 0.007	0.996 ± 0.013	0.573 ± 0.004	0.571 ± 0.005	1.232 ± 0.015
Taramakau	NZR11	12.33 ± 0.03	2.08 ± 0.01	1.023 ± 0.006	0.981 ± 0.014	0.513 ± 0.003	0.503 ± 0.005	1.092 ± 0.016
Whataroa	NZR13	14.97 ± 0.06	2.66 ± 0.01	1.000 ± 0.007	1.003 ± 0.016	0.539 ± 0.005	0.540 ± 0.006	1.158 ± 0.007
Granite Draining Rivers								
Grey	NZR16	-	1.87 ± 0.10	1.021 ± 0.075	-	-	-	-
Grey	NZR17	9.66 ± 0.03	2.31 ± 0.01	1.006 ± 0.005	1.017 ± 0.012	0.725 ± 0.005	0.737 ± 0.007	-
Grey	NZR18	10.30 ± 0.03	2.54 ± 0.01	1.002 ± 0.006	0.982 ± 0.012	0.748 ± 0.005	0.735 ± 0.007	-

[1.](Robinson *et al.* 2004)

Appendix H: Normalised Mobile Elemental Ratios versus Uplift

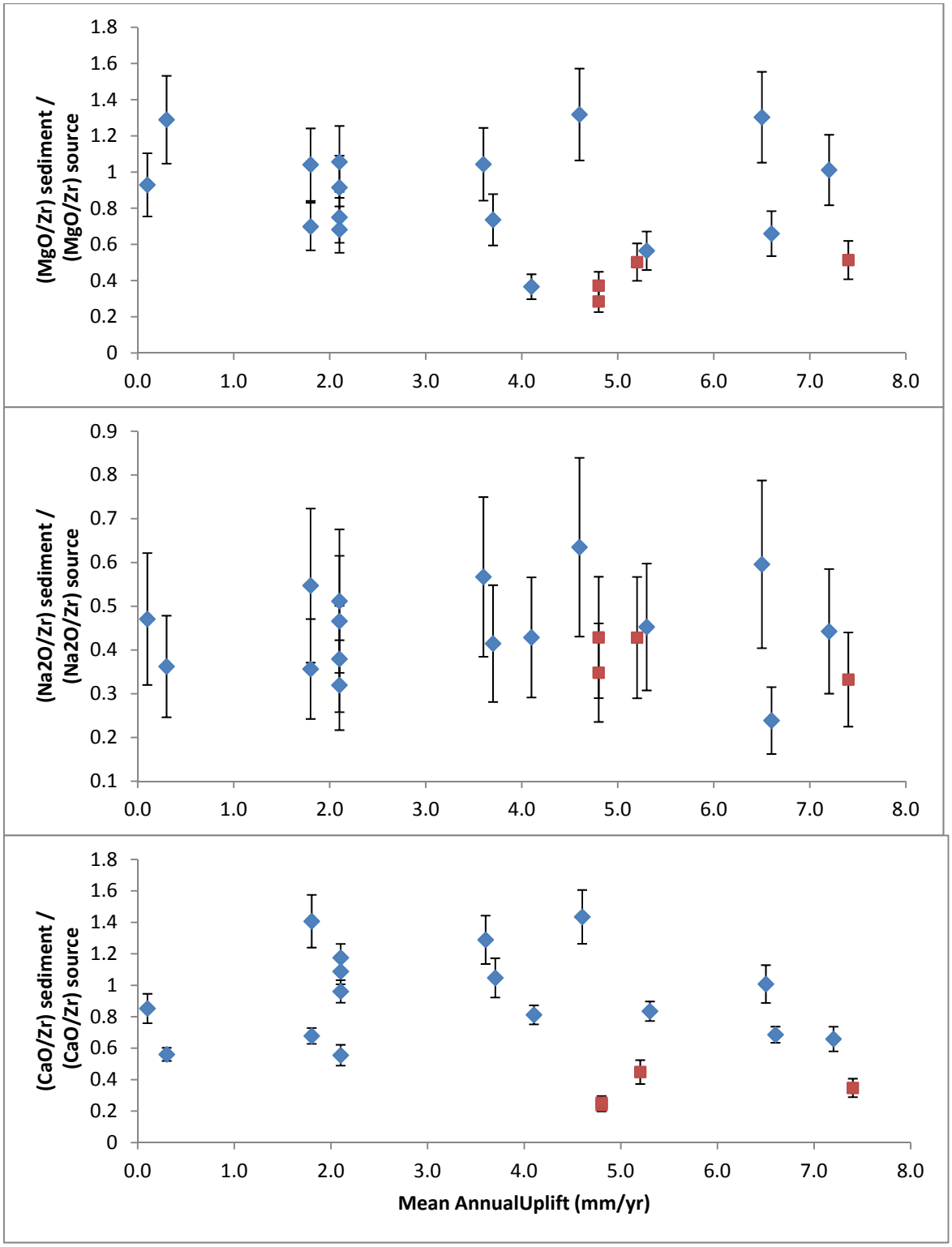

Figure 75: Normalised elemental ratios to Zr versus mean annual uplift for mobile major elements (A) MgO, (B) CaO and (C) Na_2O for sediments derived from the Torlesse Terrane (blue diamond) and Haast Schist (red square). Source composition for Torlesse Terrane sediments quoted from Roser and Korsch (1999) and Haast Schist from Grapes et al. (1982). Error bars represent 2σ.

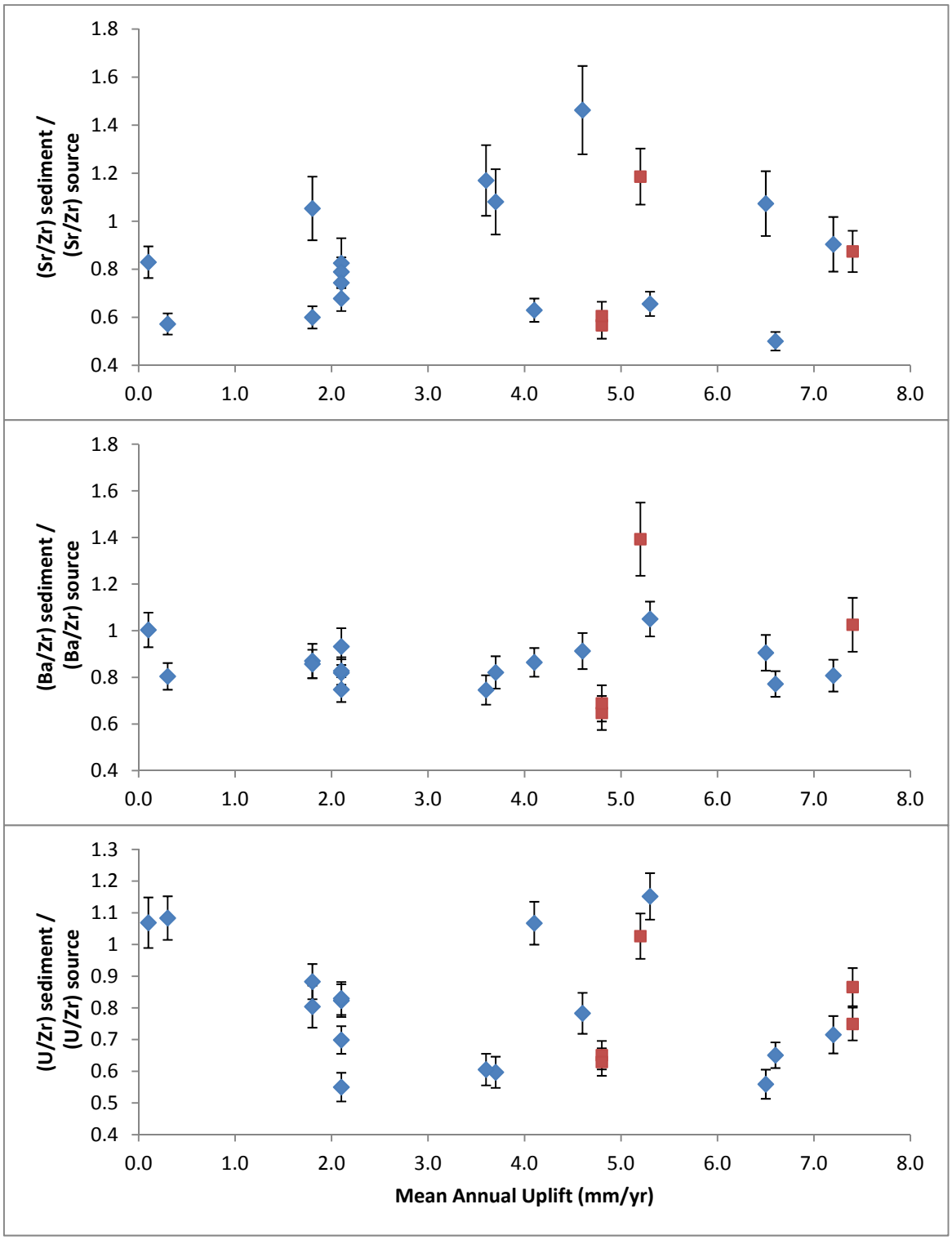

Figure 76: Normalised elemental ratios to Zr versus mean annual uplift for mobile trace elements (A) Sr, (B) Ba and (C) for sediments derived from the Torlesse Terrane (blue diamond) and Haast Schist (red square). Source composition for Torlesse Terrane sediments quoted from Roser and Korsch (1999) and Haast Schist from Grapes et al. (1982). Error bars represent 2σ.

Appendix I: Normalised Mobile Elemental Ratios versus Rainfall

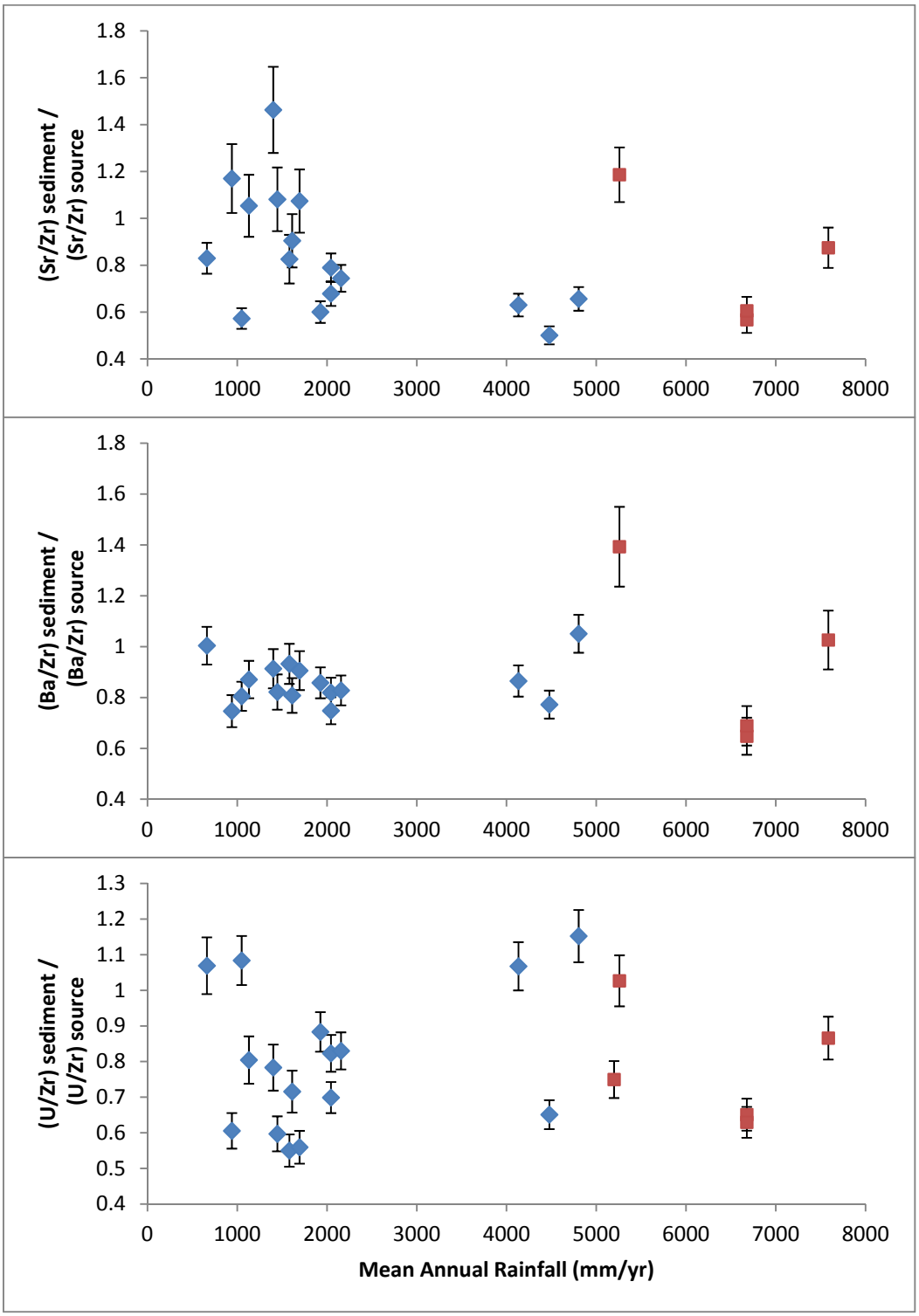

Figure 77: Normalised elemental ratios to Zr versus mean annual rainfall for mobile trace elements (A) Sr, (B) Ba and (C) U for sediments derived from the Torlesse Terrane (blue diamond) and Haast Schist (red square). Source composition for Torlesse Terrane sediments quoted from Roser and Korsch (1999) and Haast Schist from Grapes et al. (1982). Error bars represent 2σ.

Appendix J: Thin Section Descriptions

River	Wairau	Awatere
Sample	NZR25	NZR24
Grain Size	1 mm – 100 µm	500 µm – 100 µm
Sorting	Moderately sorted	Well sorted
Composition	- Quartzofeldspathic greywacke lithic clasts with varying degrees of iron oxide staining along grain boundaries, however, generally with a high degree of staining. Individual grain size within clasts ranges from silty to coarse sandstone. - Mudstone lithic clasts - Metamorphic quartz - Radiolarian chert - Feldspar clasts including plagioclase and weathered K-feldspars	- Quartzofeldspathic greywacke lithic clasts with varying degrees of iron oxide staining along grain boundaries. The degree of iron oxide staining is generally high, however, not as severe as NZR25. Individual grain size within clasts ranges from silty to coarse sandstone. - Mudstone lithic clasts - Metamorphic quartz - Basaltic lithic clasts - Feldspar clasts including plagioclase and weathered K-feldspars
Grain Description	- Clast shape ranges from sub-discoidal to spherical in shape, whereby larger grain clasts are generally more spherical, while smaller grain clasts are generally sub-discoidal in shape. - Clasts range from sub-rounded to rounded, whereby overall mudstone clasts are more rounded than sandstone clasts.	- Clast shape ranges from sub-discoidal to spherical in shape, whereby larger grain clasts are generally more spherical, while smaller grain clasts are generally sub-discoidal in shape. - Clasts range from sub-rounded to rounded, whereby overall mudstone clasts are more rounded than sandstone clasts and generally more spherical.

River	Clarence (upstream)	Clarence (upstream terrace sample)
Sample	NZR19	NZR19T
Grain Size	2 mm – 100μm	500 μm – 100 μm
Sorting	Poorly sorted	Moderately sorted
Composition	- Quartzofeldspathic greywacke lithic clasts with varying degrees of iron oxide staining along grain boundaries. Individual grain size within clasts ranges from silty to coarse sandstone. - Mudstone lithic clasts - Quartz clasts - Basalt clasts - Feldspar clasts including plagioclase and weathered K-feldspars	- Quartzofeldspathic greywacke lithic clasts with varying degrees of iron oxide staining along grain boundaries. The degree of iron oxide staining is generally higher than NZR19. Individual grain size within clasts ranges from silty to coarse sandstone. - Mudstone lithic clasts - Metamorphic quartz - Feldspar clasts including plagioclase and weathered K-feldspars
Grain Description	- Clast shape ranges from sub-discoidal to spherical in shape and from sub-rounded to rounded. - mudstone clasts are generally well rounded and spherical, whereas greywacke is sub-rounded and sub-discoidal.	- Clasts are sub-angualar to sub-rounded, whereby smaller clasts being more angular than larger clasts. - Shape of clasts is generally sub-discoidal to spherical

River	Clarence (downstream)	Hapuku
Sample	NZR23	NZR22
Grain Size	500 μm – 25 μm	2 mm – 100 μm
Sorting	Well sorted	Very poorly sorted
Composition	- Quartzofeldspathic greywacke lithic clasts with varying degrees of iron oxide staining along grain boundaries, however, generally with a high degree of staining. Individual grain size within clasts ranges from silty to coarse sandstone. - Mudstone lithic clasts - Quartz clasts - Feldspar clasts including plagioclase and weathered K-feldspars	- Quartzofeldspathic greywacke lithic clasts with varying degrees of iron oxide staining along grain boundaries. The degree of iron oxide staining is generally lower than NZR25 and NZR24. Individual grain size within clasts ranges from silty to coarse sandstone. - Mudstone lithic clasts - Quartz clasts - Granite clasts - Feldspar clasts including plagioclase and weathered K-feldspars - Biotite - Amphibole
Grain Description	- Clast shape ranges from sub-discoidal to spherical in shape. Some smaller grain size clasts are sub-prismodal in shape. - Clasts are predominantly sub-rounded to rounded, whereby overall mudstone clasts are more rounded than sandstone clasts. - Clasts have an appearance of higher degree of physical weathering than upstream sample of NZR19.	- Clast shape is generally sub-discoidal in shapeand varies from rounded to sub-angular. Mudstone clast edges are predominantly sub to well rounded. Small fragments are generally more angular than larger clasts.

River	Kowhai	Conway
Sample	NZR21	NZR20
Grain Size	1mm – 100 μm	3 mm – 50 μm
Sorting	Moderately to poorly sorted	Very poorly sorted
Composition	- Quartzofeldspathic greywacke lithic clasts with varying degrees of iron oxide staining along grain boundaries. The degree of iron oxide staining is generally lower than NZR25 and NZR24. Individual grain size within clasts ranges from silty to coarse sandstone. - Mudstone lithic clasts - Quartz clasts - Feldspar clasts including plagioclase and weathered K-feldspars	- Quartzofeldspathic greywacke lithic clasts with varying degrees of iron oxide staining along grain boundaries. The degree of iron oxide staining is generally lower than NZR25 and NZR24. Individual grain size within clasts ranges from silty to coarse sandstone. - Mudstone lithic clasts - Quartz clasts - Basalt clasts (showing beginnings of distrification of glass) - Feldspar clasts including plagioclase and weathered K-feldspars - Calcite
Grain Description	- Clast shape is generally sub-discoidal or sub-prismoidal in shape whose edges are sub-rounded. In general mudstone clasts are more rounded than sandstone fragments.	- Mudstone clast shape ranges from sub-discoidal to spherical to sub-prismoidal in shapeand varies from rounded to sub-angular. - Sandstone fragments are generally sub-rounded and sub-discoidal.

River	Rakaia (downsteam)	Rakaia (downstream)
Sample	NZR02	NZR03
Grain Size	500 μm – 50 μm	500 μm – 50 μm
Sorting	Well to very well sorted	Very well sorted
Composition	- Quartzofeldspathic greywacke lithic clasts with varying degrees of iron oxide staining along grain boundaries. Individual grain size within clasts ranges from silty to coarse sandstone. - Mudstone lithic clasts - Quartz clasts - Fine grained phylite clasts - Feldspar clasts including plagioclase and weathered K-feldspars. Feldspars appear comparatively well weathered.	- Quartzofeldspathic greywacke lithic clasts with varying degrees of iron oxide staining along grain boundaries. Individual grain size within clasts ranges from silty to coarse sandstone. - Mudstone lithic clasts - Quartz clasts - Fine grained phylite clasts - Feldspar clasts including plagioclase and weathered K-feldspars. Feldspars appear comparatively well weathered.
Grain Description	- Quartz edges are sub-angular to rounded and greywacke clasts are rounded. - Phylite is generally present as small fragments, which are fibrous and elongate. - Mudstone is sub-rounded to well rounded and has a shape described as sub – discoidal to spherical. - Sandstone is present as rounded clasts which are sub-discoidal to spherical in shape.	- Quartz edges are sub-angular to rounded and greywacke clasts are rounded. - Phylite is generally present as small fragments, which are fibrous and elongate. - Mudstone is sub-rounded to well rounded and has a shape described as sub – discoidal to spherical. - Sandstone is present as rounded clasts which are sub-discoidal to spherical in shape.

River	Rakaia (upstream)	Rakaia (upstream, localized catchment of stream)
Sample	NZR04	NZR10
Grain Size	500 µm – 50 µm	4 mm – 300 µm
Sorting	Well sorted	Very poorly sorted
Composition	- Quartzofeldspathic greywacke lithic clasts with varying degrees of iron oxide staining along grain boundaries. Individual grain size within clasts ranges from silty to coarse sandstone. - Mudstone lithic clasts - Quartz clasts - Fine grained phylite clasts - Feldspar clasts including plagioclase and weathered K-feldspars. Feldspars appear comparatively well weathered.	- Quartzofeldspathic greywacke lithic clasts. Minimal iron oxide staining present along grain boundaries. Individual grain size within clasts ranges from silty to coarse sandstone. - Mudstone lithic clasts - Vein quartz clasts - Fine grained phylite clasts - Feldspar clasts including plagioclase and weathered K-feldspars. Feldspars appear comparatively well weathered.
Grain Description	- Quartz edges are sub-angular to rounded and greywacke clasts are rounded. - Phylite is generally present as small fragments, which are fibrous and elongate. - Mudstone is sub-rounded to rounded and has a shape described as sub – discoidal to spherical. - Sandstone is present as sub-rounded to angular clasts which are sub-discoidal to spherical in shape.	- Quartz edges are sub-angular to rounded and greywacke clasts are rounded. - Phylite is generally present as small fragments, which are fibrous and elongate. - Mudstone is sub-rounded to well rounded and has a shape described as sub – discoidal to spherical. - Sandstone is present as rounded clasts which are sub-discoidal to spherical in shape.

River	Pareora	Haast
Sample	NZR01	NZR15
Grain Size	100 μm – 50 μm	50 μm – 1 mm
Sorting	Very poorly sorted	Well sorted
Composition	- Quartzofeldspathic greywacke lithic clasts with varying degrees of iron oxide staining along grain boundaries. Individual grain size within clasts ranges from silty to coarse sandstone. Feldspars appear weathered within sandstone clasts. - Mudstone lithic clasts - Quartz clasts - Fine grained phylite clasts - Feldspar clasts including plagioclase and weathered K-feldspars. Feldspars appear comparatively well weathered. - minor presence of glauconite, ore fragment	- metamorphic and quartz clasts - chlorite intergrown with quartz - biotite and muscovite fragments - biotite and chlorite schist lithic fragments - Plagioclase and sadine - minor calcite fragments present
Grain Description	- Quartz edges are rounded - Phylite is generally present as small fragments, which are fibrous and elongate. - Mudstone is sub-rounded to well-rounded and has a shape described as sub – discoidal to spherical. - Sandstone is present as angular to sub-rounded to angular clasts which are sub-discoidal to sub-prismodial	- biotite fragments are elongate and tabular - metamorphic quartz fragments are sub-angular to sub-rounded and have a sub-disconcoidal shape. - Small schist fragments are elongate and fibrous

River	Taramakau (upstream)	Taramakau (downstream)
Sample	NZR08	NZR11
Grain Size	50 μm – 2mm	50 μm – 4 mm
Sorting	Moderate to well sorted	Very poorly sorted
Composition	- Quartzofeldspathic greywacke lithic clasts with minor iron oxide staining along grain boundaries. Individual grain size within clasts ranges from silty to coarse sandstone. - Mudstone lithic clasts - metamorphic and quartz clasts with fused quartz boundaries. - minor biotite schist fragments - Feldspar clasts including plagioclase and weathered K-feldspars. Feldspars appear comparatively well weathered.	- minor quartzofeldspathic greywacke and brown mudstone lithic clasts - metamorphic quartz clasts and plagioclase intergrown in quartz - biotite fragments - biotite and chlorite schist lithic fragments - Feldspar clasts including microcline, sadine and plagioclase. -plutonic granodiorite fragments (>65% feldspars, biotite, hornblende)
Grain Description	- Quartz edges are sub-angular to sub-rounded and has a sub-disconcoidal shape. - Schist generally is generally present as sub-angular to angular and are elongate. - Mudstone is sub-rounded and has a shape described as sub – disconcoidal - Sandstone is present as sub-rounded to angular clasts which are sub-discoidal to spherical in shape. - Plagioclase is commonly tabular.	- larger greywacke, metamorphic quartz and granodiorite fragments - Quartz edges are sub-angular to rounded - Schist has comparatively smaller fragments, which are fibrous, angular and elongate. - biotite fragments are tabular - Mudstone is sub-rounded to well rounded and has a shape described as sub – discoidal to spherical. - Sandstone is present as rounded clasts which are sub-discoidal to spherical in shape.

River	Peorua	Whataroa
Sample	NZR12	NZR13
Grain Size	50 – 500 μm	50 - 500 μm
Sorting	very well sorted	Well sorted
Composition	- minor biotite schist fragments - dominated by metamorphic mineral fragments, including amphibole, biotite, muscovite - metamorphic quartz fragments	- metamorphic and polycrystalline quartz clasts - quartz veining - biotite and amphibole fragments - biotite and chlorite schist lithic fragments - Plagioclase - minor calcite fragments present
Grain Description	- biotite fragments are highly fibrous and needle-like, indicating they have experienced minimal physical weathering. - metamorphic minerals are very angular - quartz fragments are sub-angular to angular and have a sub-disconcoidal shape. - Schist fragments are elongate and fibrous	- biotite fragments are elongate and tabular - quartz fragments are sub-angular to angular and have a sub-disconcoidal shape. - Schist fragments are elongate and fibrous

Appendix K: Petrology Photos

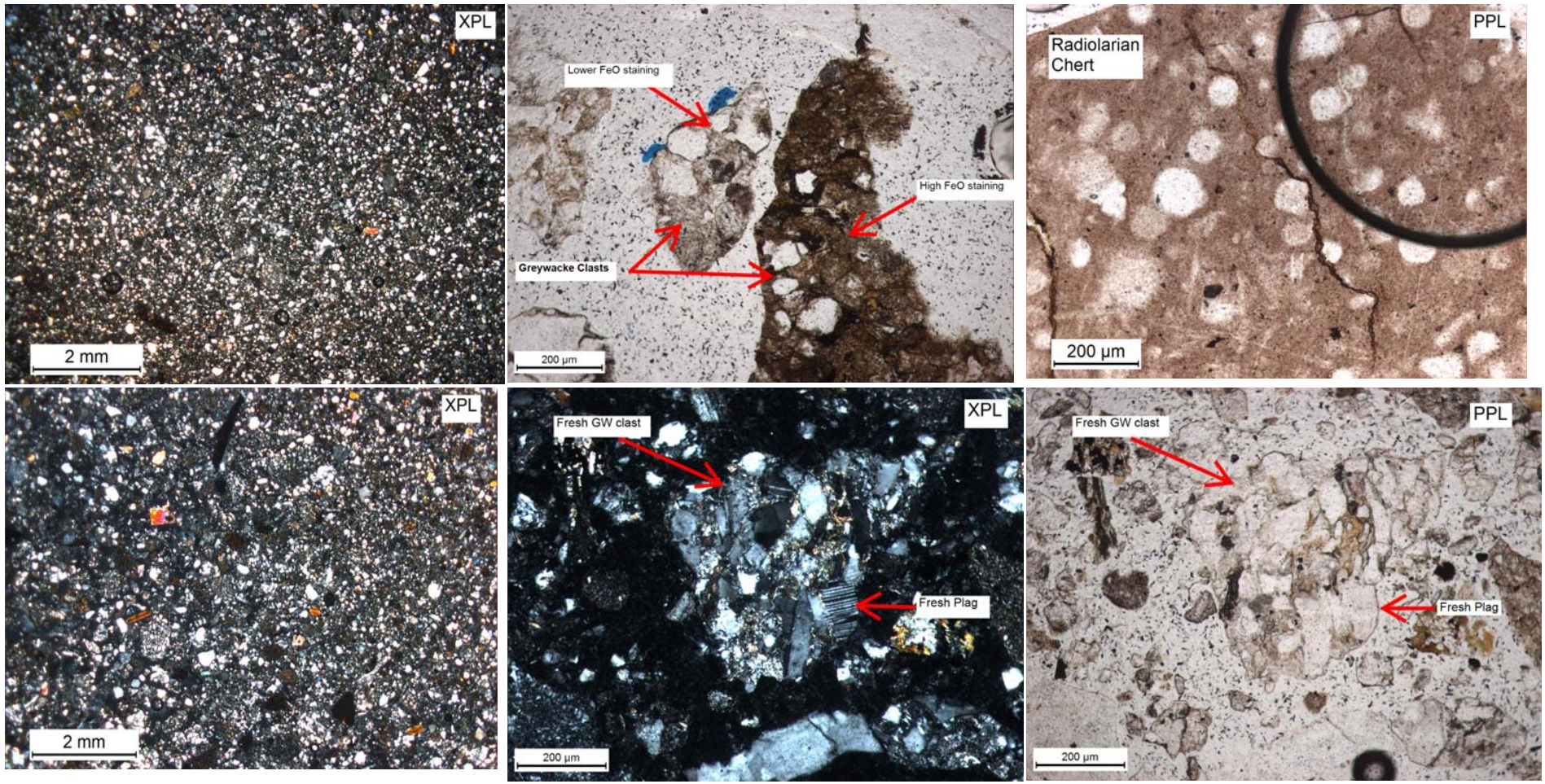

Figure 78: (A) NZR25 (B) NZR25 – greywacke clasts showing varying degrees of Fe-oxide staining, (C) NZR25 – Radiolarian chert, (D) NZR24, (E) NZR24 – unweathered greywacke fragment in XPL and (F) NZR24 – unweathered greywacke fragment in PPL

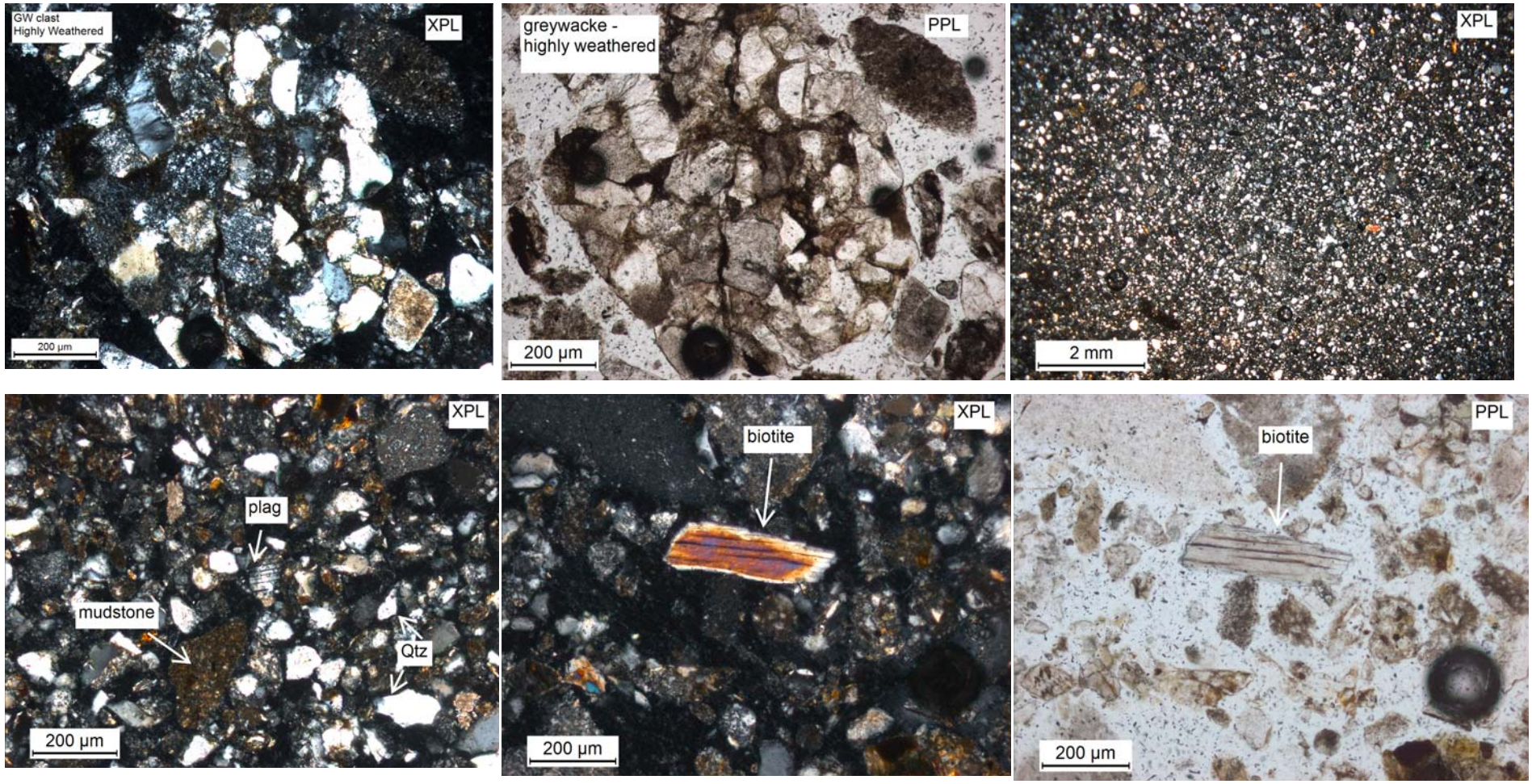

Figure 79: (A) NZR24 – Highly weathered greywacke fragment showing Fe-oxide staining in XPL, (B) NZR24 – Highly weathered greywacke fragment showing Fe-oxide staining in PPL, (C) NZR23, (D) NZR23 – mudstone, plagioclase and quartz fragments. Mudstone appears more rounded than quartz., (E) NZR23 – tabular biotite fragment in XPL and (F) NZR23 – tabular biotite fragment in PPL.

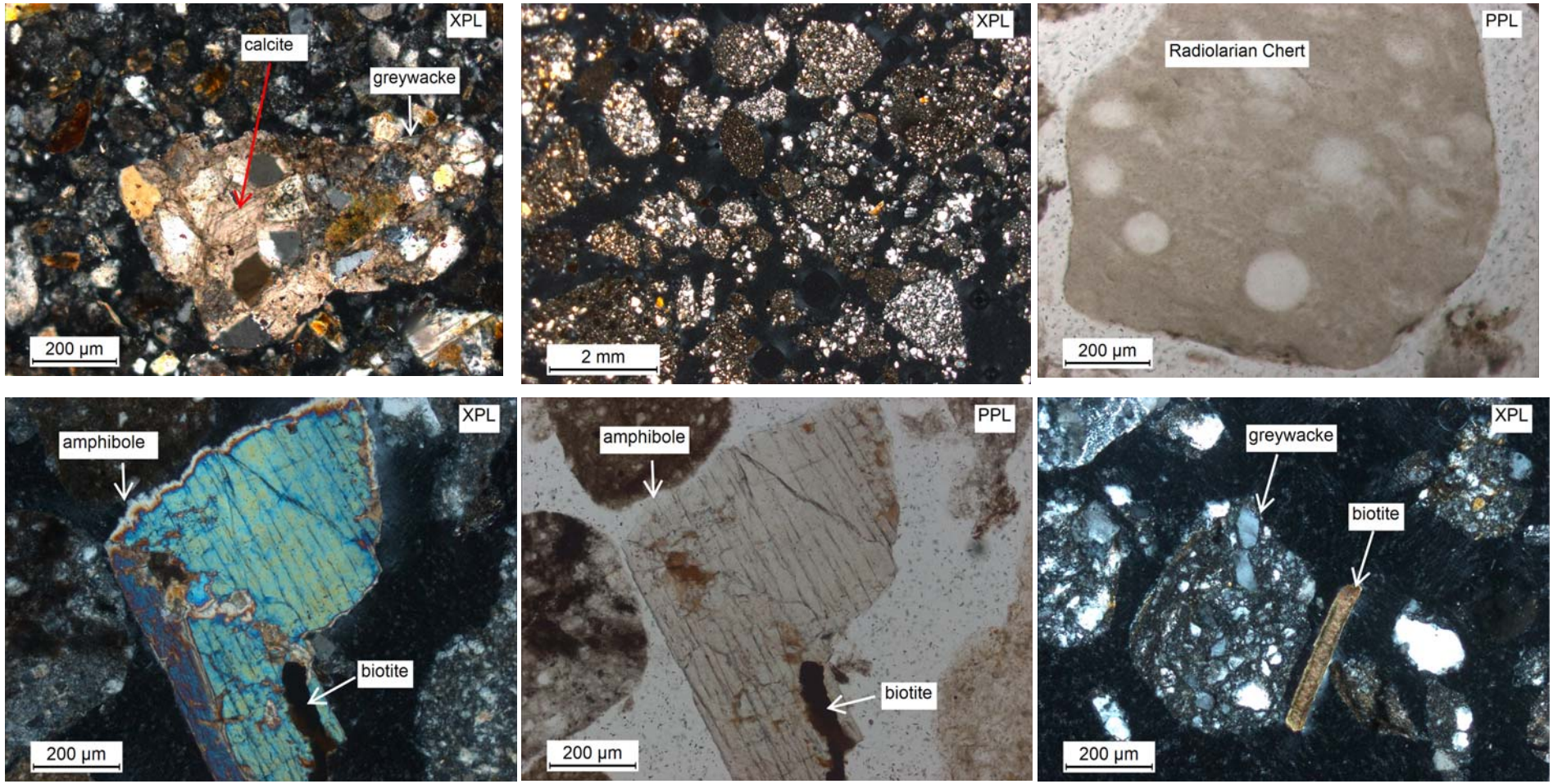

Figure 80; (A) NZR23 – Greywacke fragment showing Fe-oxide staining and calcite composition, (B) NZR22, (C) NZR22 – Radiolarian chert fragment, (D) NZR22 – Amphibole with biotite intergrown fragment in XPL, (E) NZR22 – Amphibole with biotite intergrown fragment in PPL and (F) NZR22 – greywacke and tabular biotite fragment.

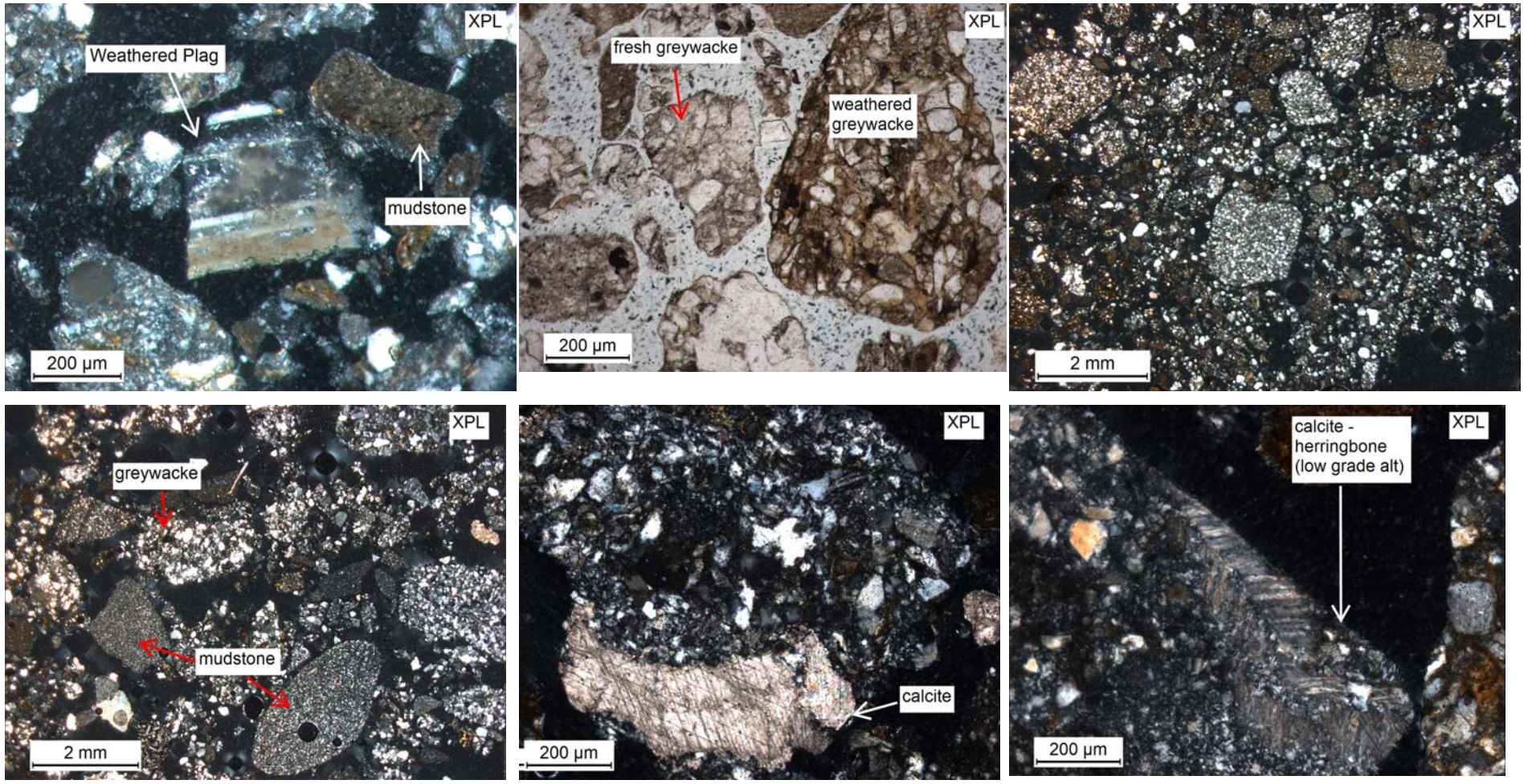

Figure 81: (A) NZR22 – plagioclase weathering to clay and mudstone fragment in XPL, (B) NZR20 – greywacke fragments showing varying degrees of weathering reflected by the intensity of Fe-oxide staining, (C) NZR21, (D) NZR20 – greywacke and mudstone fragments. Mudstone is more rounded than greywacke, (E) NZR20 - Lithic fragment with calcite, (F) NZR20 – Calcite fragment with herringbone texture indicating low grade alteration.

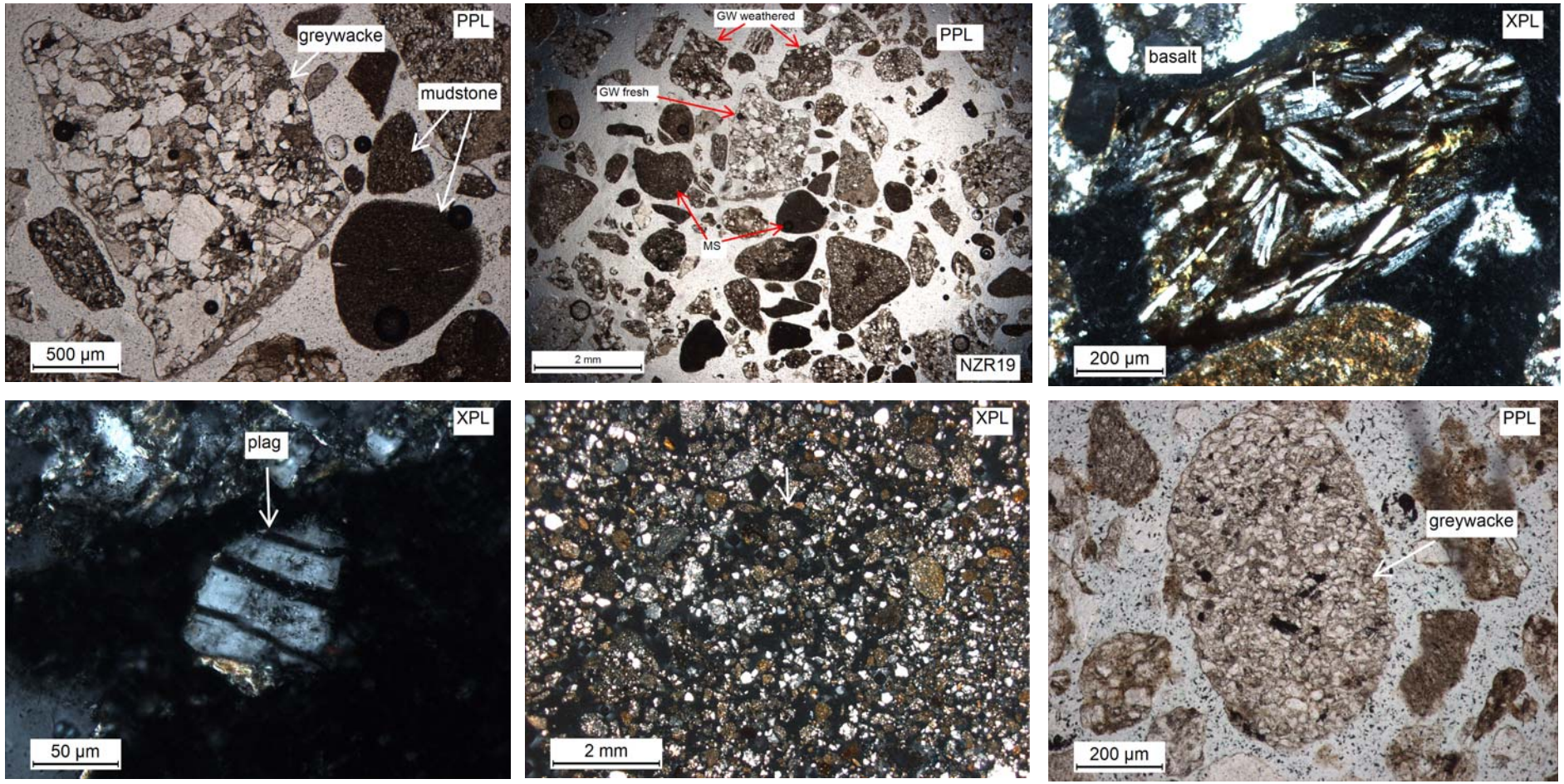

Figure 82: (A) NZR19 – well rounded mudstone and sub-rounded greywacke fragment, (B) NZR19 – well rounded mudstone and greywacke showing varying degrees of weathering intensity, (C) NZR19 – basalt fragment, (D) NZR19 – Plagioclase fragment, (E) NZR19T and (F) NZR19T – rounded greywacke fragment,

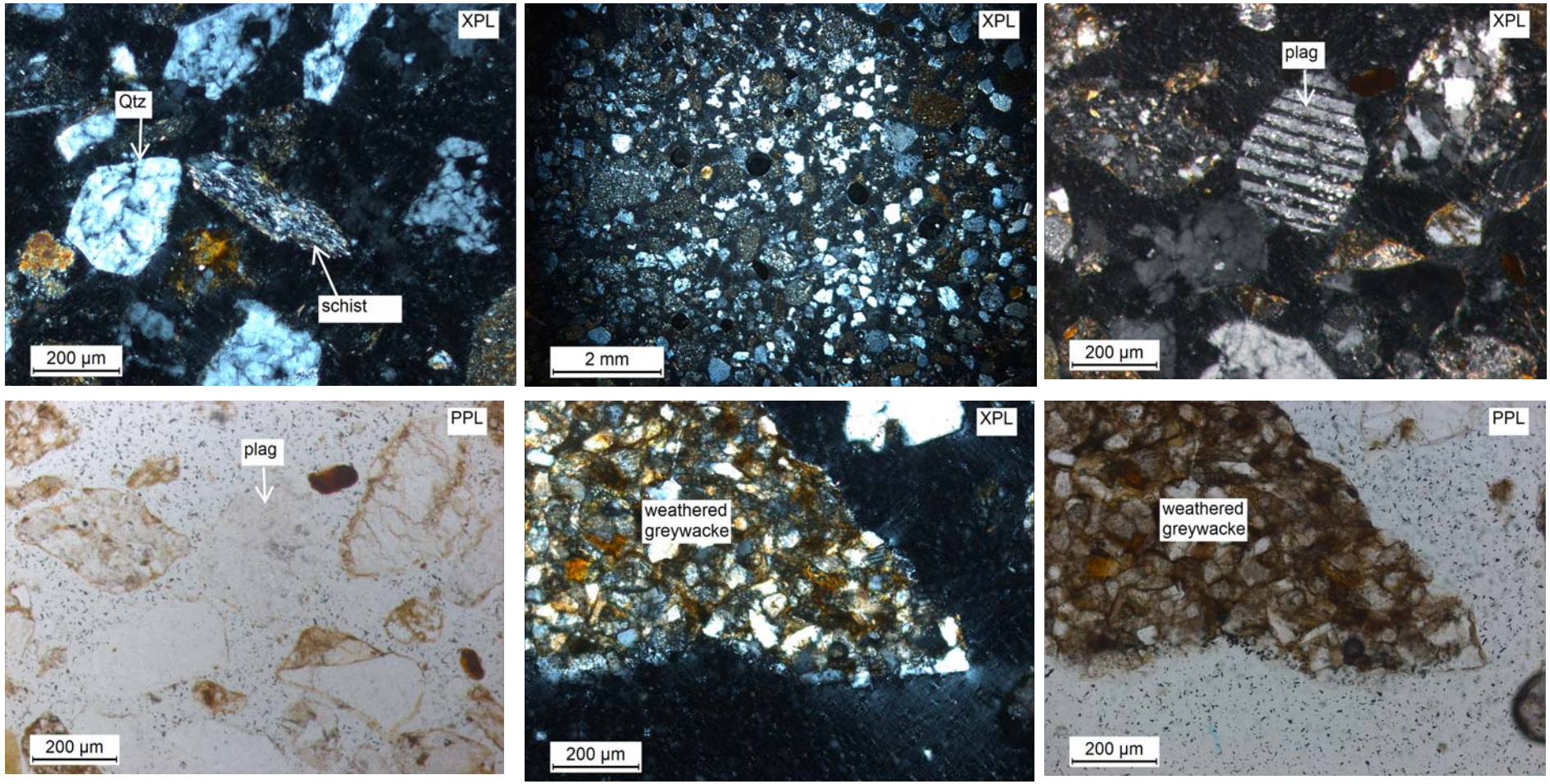

Figure 83: (A) NZR01 – Schist and quartz fragment (B) NZR01, (C) NZR01 – plagioclase fragment showing dissolution and greywacke fragment in XPL, (D) NZR01 – plagioclase fragment showing dissolution and greywacke fragment in PPL, (E) NZR01 – highly chemically weathered greywacke fragment showing severe Fe-oxide straining in XPL and (F) NZR01 – highly chemically weathered greywacke fragment showing severe Fe-oxide straining in PPL.

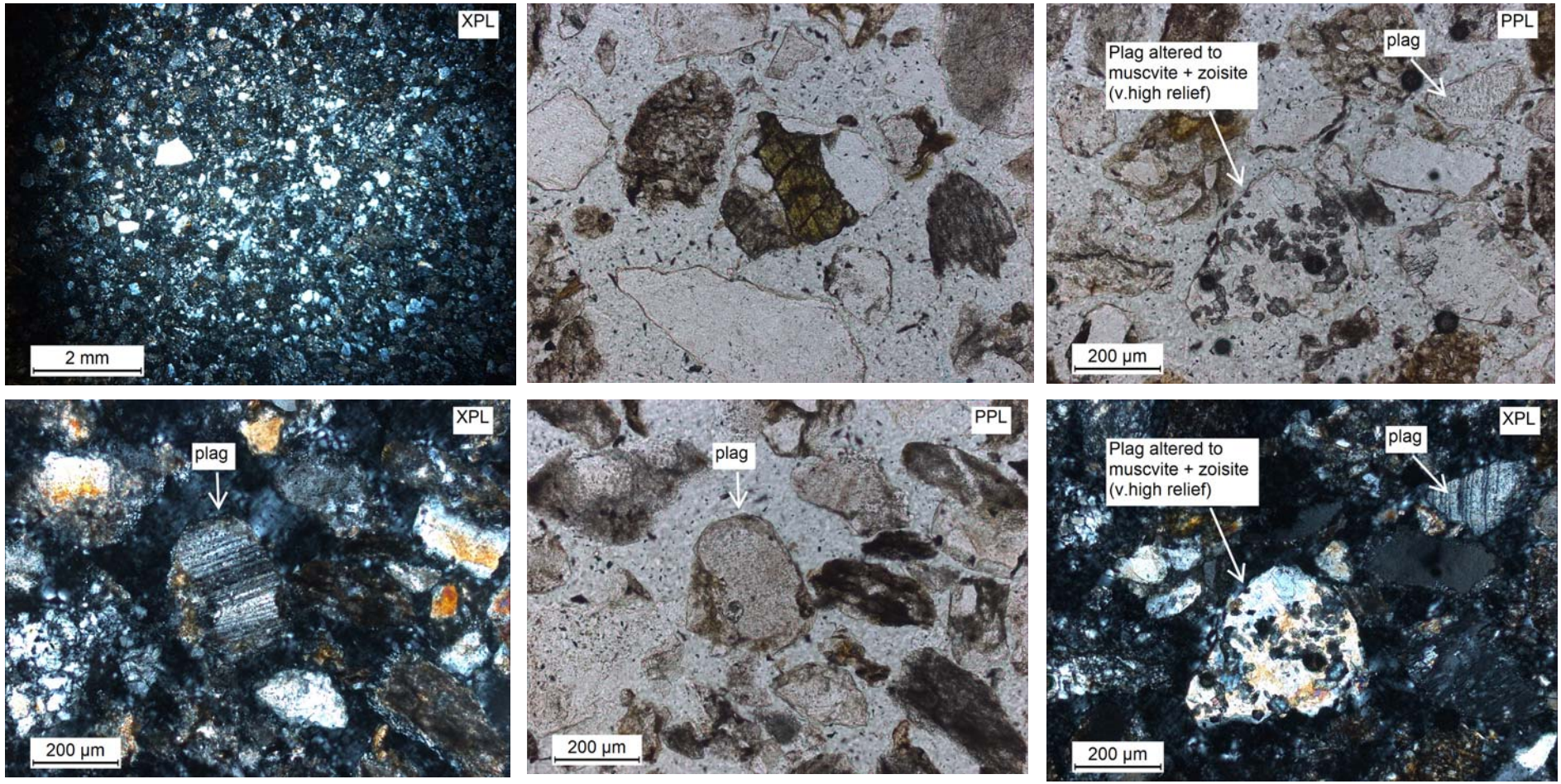

Figure 84: (A) NZR02, (B) NZR02 – amphibole fragment, (C) NZR02 – Plagioclase breaking down to muscovite and zoisite and weathered plagioclase fragment in PPL, (D) NZR02 – weathered plagioclase fragment in XPL, (E) NZR02 – weathered plagioclase fragment in PPL and (F) NZR02 – Plagioclase breaking down to muscovite and zoisite and weathered plagioclase fragment in XPL.

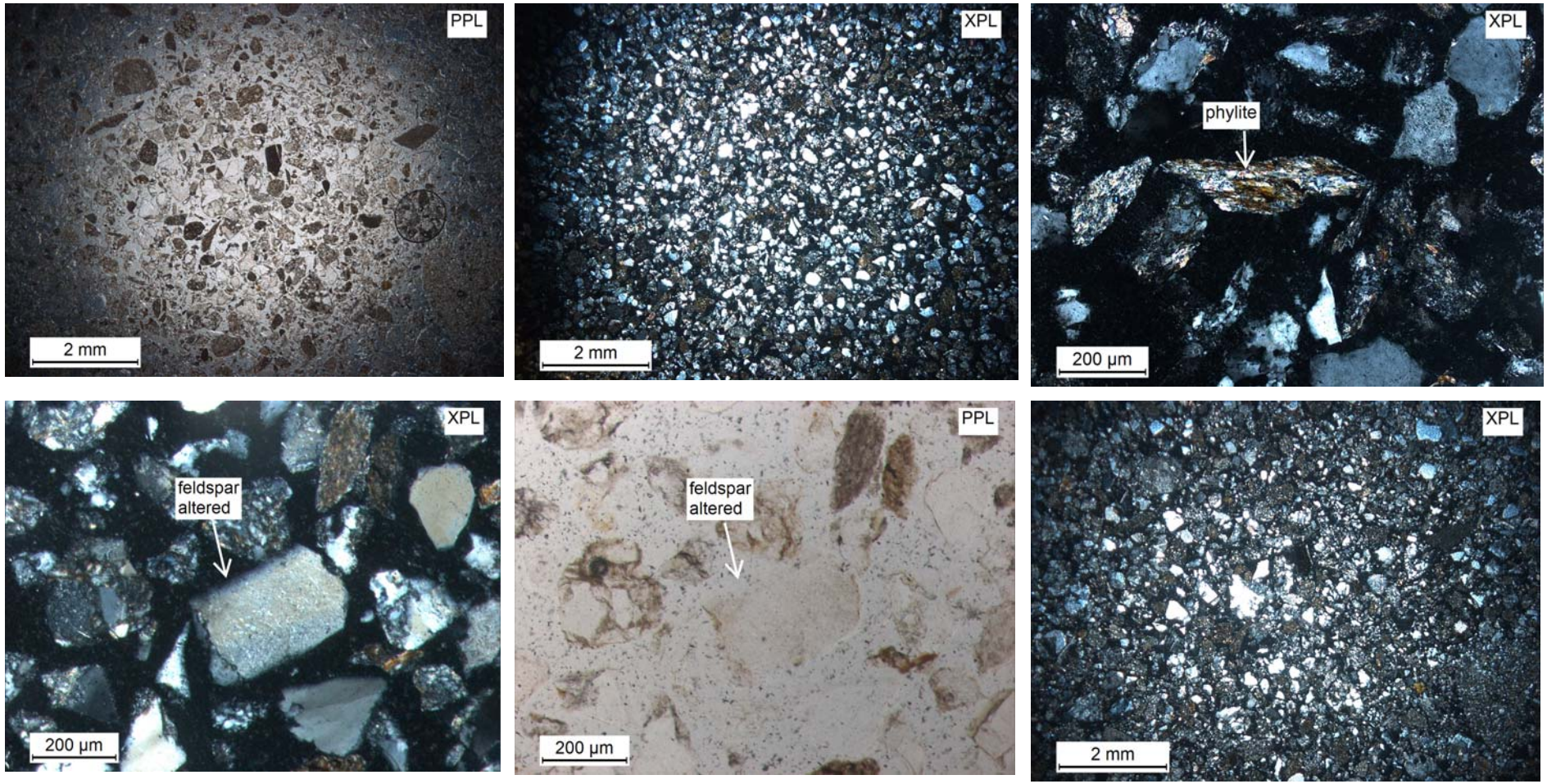

Figure 85: (A) NZR04 in PPL, (B) NZR03, (C) NZR03 – Phylite fragment, (D) NZR03 – weathered feldspar fragment in XPL, (E) NZR03 – weathered feldspar fragment in PPL and (F) NZR04 in XPL

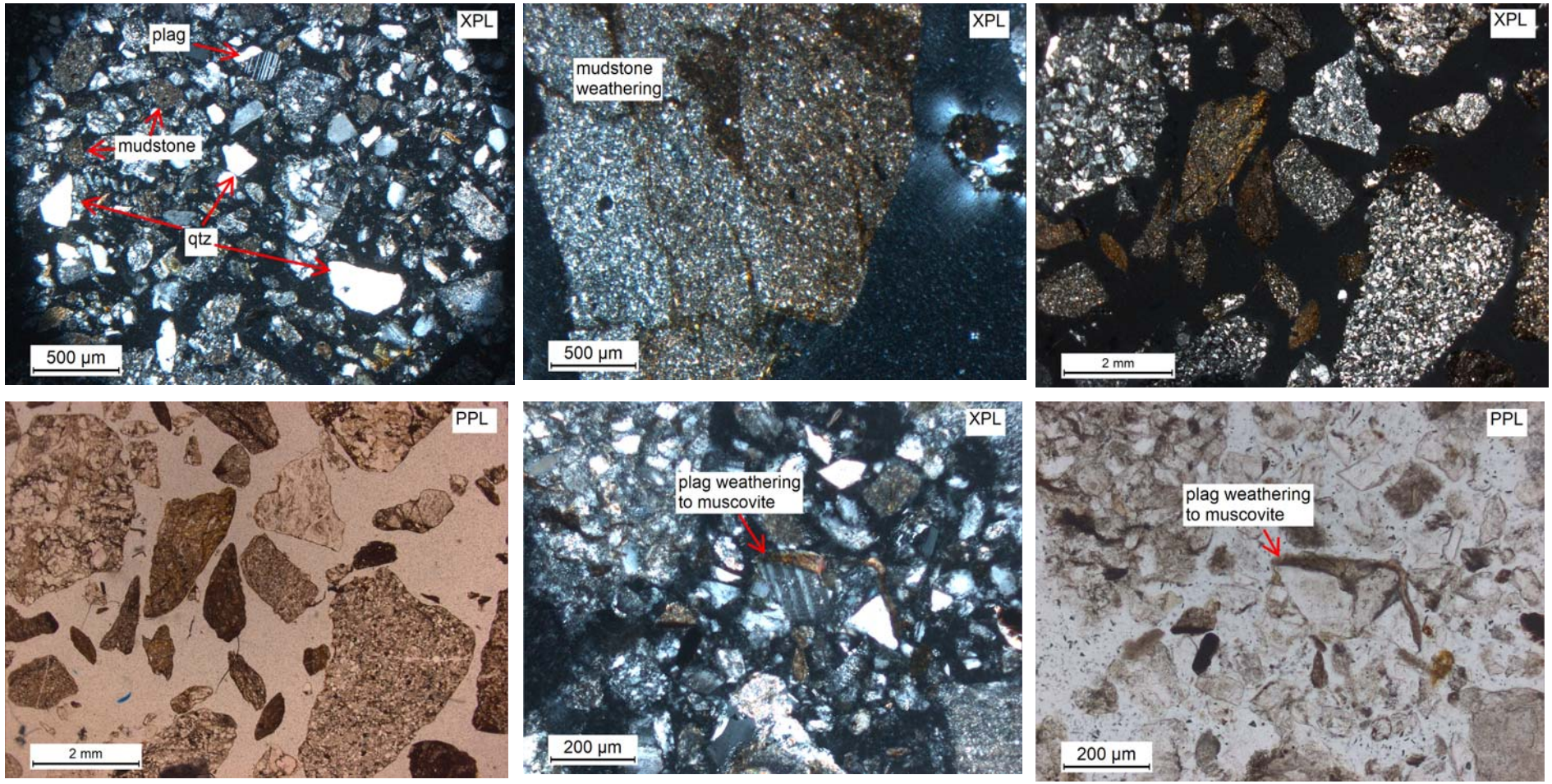

Figure 86: (A) NZR04 – mudstone, plagioclase and quartz fragments, (B) NZR10 – mudstone fragment showing Fe-oxide staining and weathering, (C) NZR10 – greywacke and mudstone fragments sub-rounded to sub-angular in XPL, (D) NZR10 – greywacke and mudstone fragments sub-rounded to sub-angular in PPL, (E) NZR05 – Plagioclase fragment weathering to muscovite in XPL and (F) NZR05 – Plagioclase fragment weathering to muscovite in PPL.

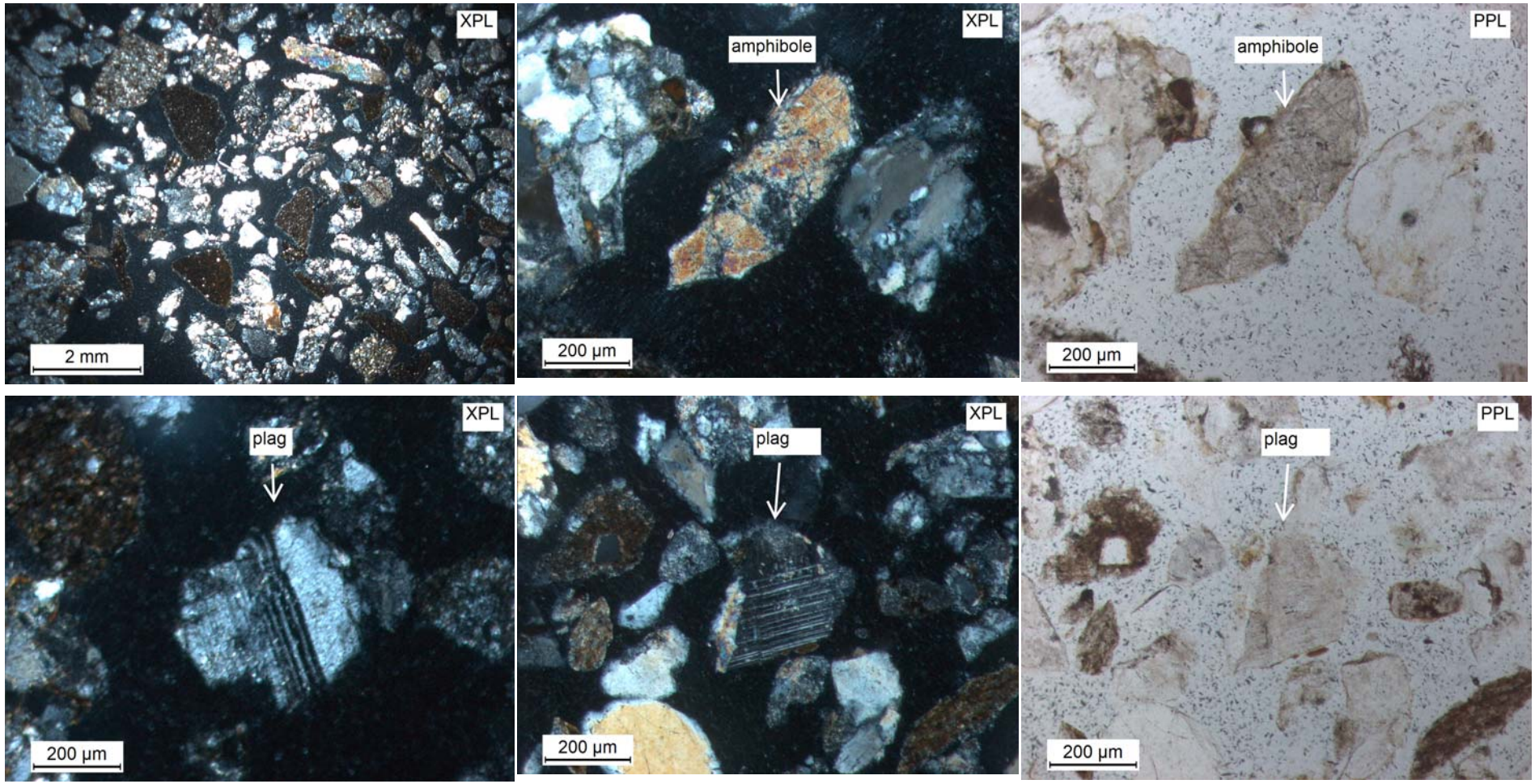

Figure 87: (A) NZR07 in XPL, (B) NZR07 – amphibole fragment in XPL, (C) NZR07 – amphibole fragment in PPL, (D) NZR07 – plagioclase fragment, (E) NZR09 – plagioclase fragment in XPL and (F) NZR09 – plagioclase fragment in PPL

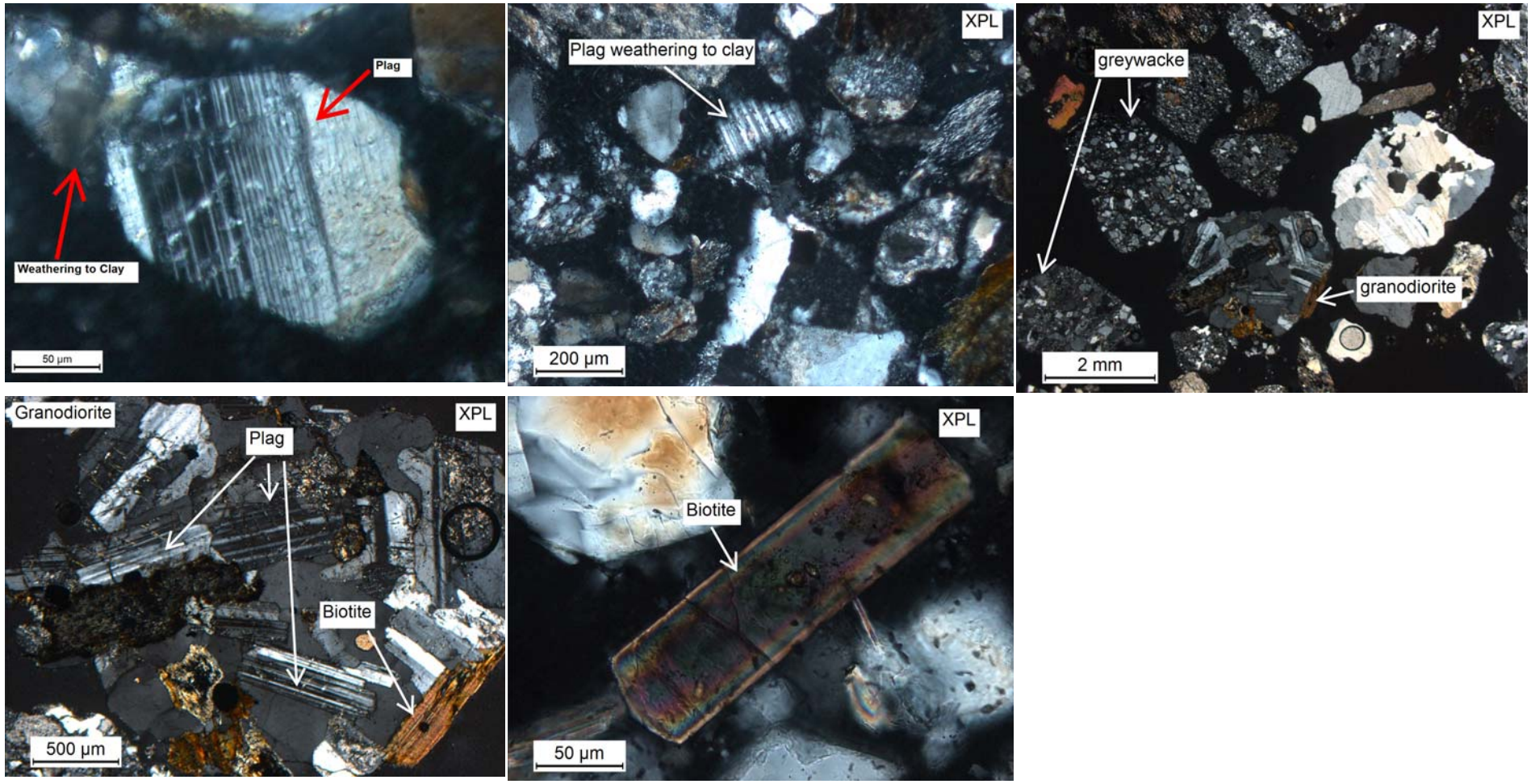

Figure 88: (A) NZR09 – plagioclase weathering to clay in XPL, (B) NZR08 – plagioclase fragment weathering to clay, (C) NZR11 – greywacke, granodiorite and metamorphic quartz fragments, (D) NZR11 – granodiorite fragment hosting plagioclase and biotite and (E) NZR12 – tabular biotite fragment

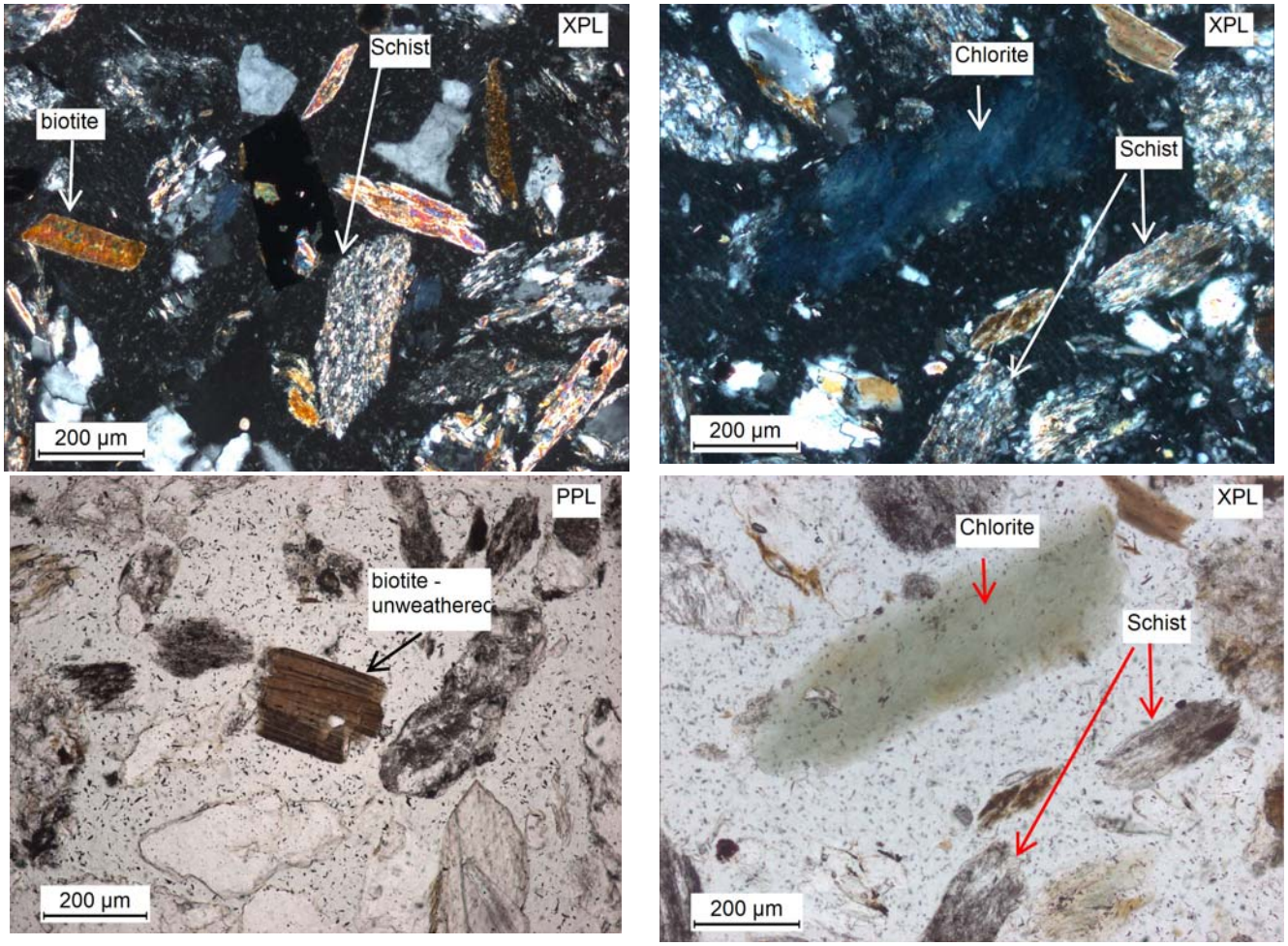

Figure 89: (A) NZR13 – biotite and schist fragments, highly fibrous, (B) NZR13 – chlorite, schist and biotite fragments in XPL, (C) NZR13 – chlorite, schist and biotite fragments in PPL and (D) NZR13 – unweathered biotite fragment.

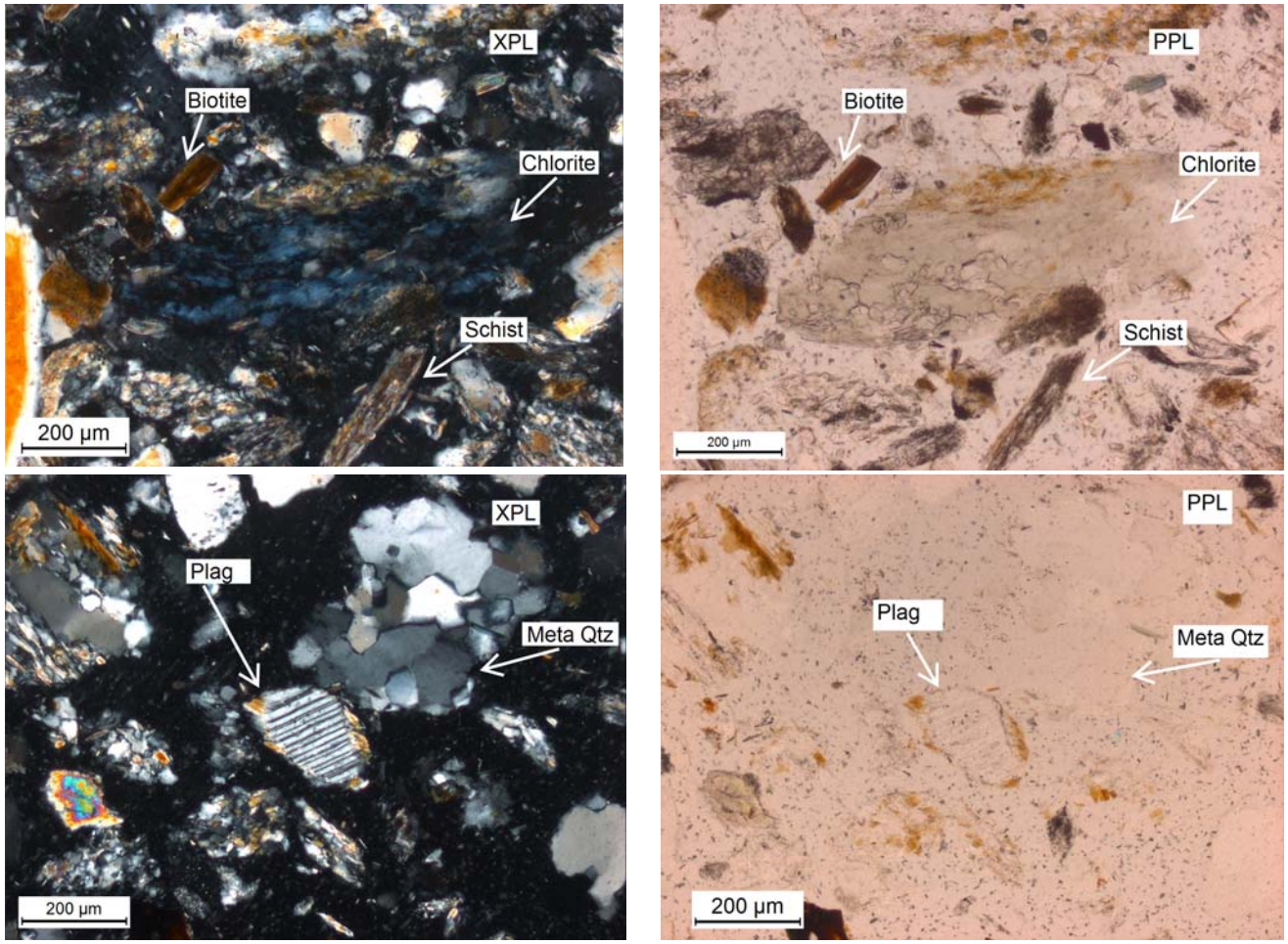

Figure 90: (A) NZR15 – Biotite, chlorite and schist fragments in XPL, (B) NZR15 – Biotite, chlorite and schist fragments in PPL, (C) NZR15 – plagioclase and metamorphic quartz fragments in XPL and (D) NZR15 – plagioclase and metamorphic quartz fragments in PPL.

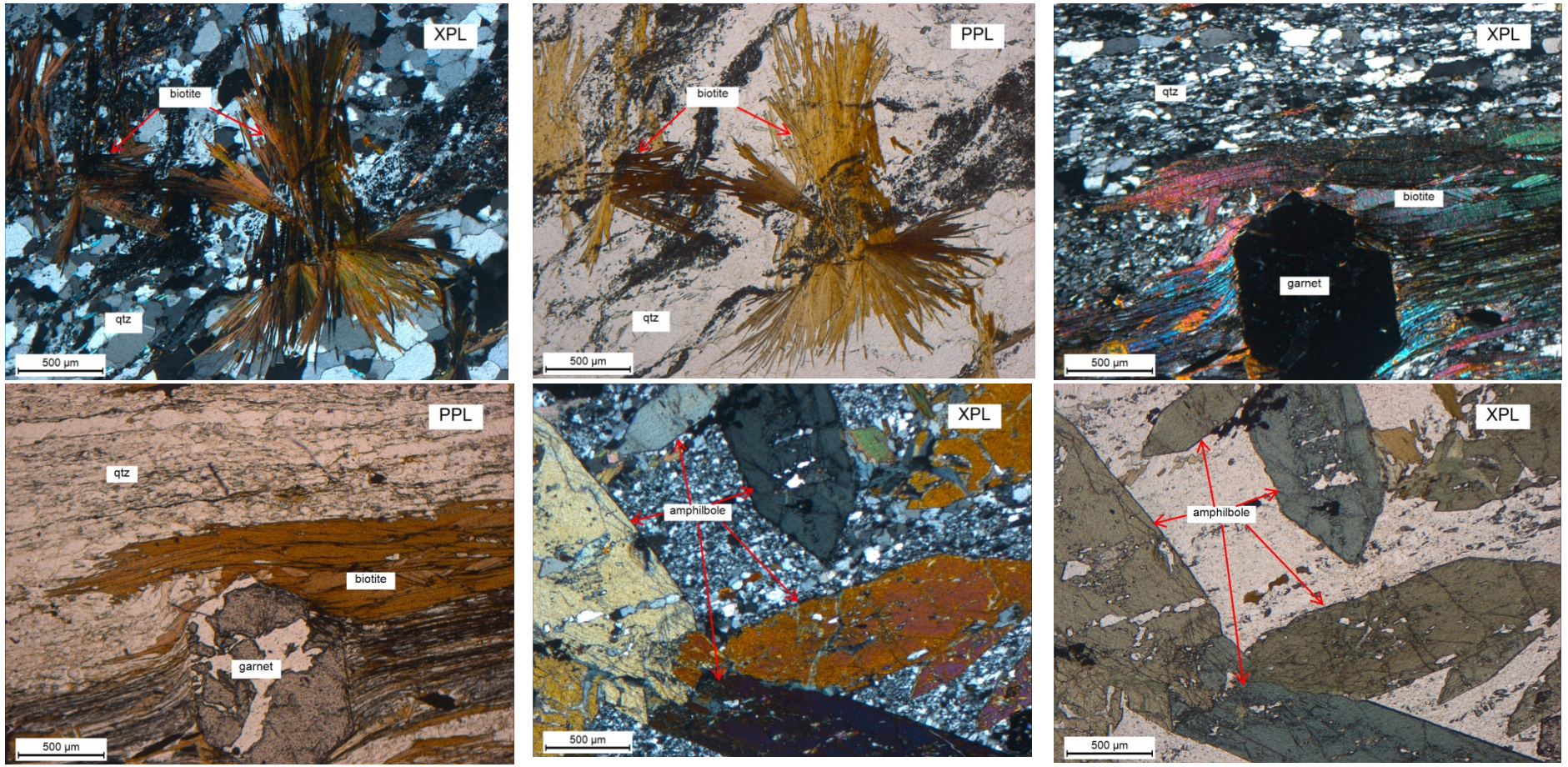

Figure 91: Bedrock hand samples - (A) biotite schist showing radial biotite in XPL, (B) biotite schist showing radial biotite in PPL, (C) garnet-biotie schist in XPL, (D) garnet-biotie schist in PPL, (E) Amphibolite schist facies, showing tabular amphibole fragments in XPL and (F) Amphibolite schist facies, showing tabular amphibole fragments in PPL.